Demonstration of anisotropy control of optical properties induced by IR fs laser irradiation in organic materials : birefringence, di-attenuation, SHG, photoluminescence

Ruyue Que

Ruyue Que. Demonstration of anisotropy control of optical properties induced by IR fs laser irradiation in organic materials : birefringence, di-attenuation, SHG, photoluminescence. Optics [physics.optics]. Université Paris-Saclay, 2022. English. NNT : 2022UPASF056 . tel-04224010

HAL Id: tel-04224010
https://theses.hal.science/tel-04224010v1

Submitted on 1 Oct 2023

THESE DE DOCTORAT

NNT : 2022UPASF056

Demonstration of anisotropy control of optical properties induced by IR fs laser irradiation in organic materials: birefringence, di-attenuation, SHG, photoluminescence

Démonstration d'un contrôle de l'anisotropie des propriétés optiques induites par irradiation d'un laser IR fs dans des matériaux organiques : biréfringence, di-atténuation, GSH, photoluminescence

Thèse de doctorat de l'université Paris-Saclay

École doctorale n° 571, Sciences chimiques :
molécules, matériaux, instrumentation et biosystèmes (2MIB)
Spécialité de doctorat : Chimie
Graduate School : Chimie. Référent : Faculté des sciences d'Orsay

Thèse préparée dans l'unité de recherche **Institut de chimie moléculaire et des matériaux d'Orsay (Université Paris-Saclay, CNRS)**
sous la direction de **Bertrand POUMELLEC**, Directeur de Recherche,
et le co-direction de **Matthieu LANCRY,** Professeur des Universités

Thèse soutenue à Paris-Saclay, le 15 Septembre 2022, par

Ruyue QUE

Composition du Jury

Annick LOISEAU Directrice de Recherche, LEM, ONERA, Université Paris-Saclay	Présidente
Sébastien FORGET Maître de Conférences (HDR), Université Paris 13	Rapporteur & Examinateur
Razvan STOIAN Directeur de Recherche, Université Jean MONNET, St Etienne	Rapporteur & Examinateur
Marie ERARD Maître de Conférences, ICP, Université Paris-Saclay	Examinatrice
Enrique GARCIA-CAUREL Ingénieur de Recherche, LPICM, Ecole polytechnique	Examinateur
Bertrand POUMELLEC Directeur de Recherche, ICMMO, Université Paris-Saclay	Directeur de thèse

ÉCOLE DOCTORALE
Sciences Chimiques : Molécules,
Matériaux, Instrumentation
et Biosystèmes (2MIB)

Titre : Démonstration d'un contrôle de l'anisotropie des propriétés optiques induites par irradiation d'un laser IR fs dans des matériaux organiques : biréfringence, di-atténuation, GSH, photoluminescence

Mots clés : laser femtoseconde ; matériaux organiques ; anisotropie ; polarisation ; luminescence ; GSH

Résumé : L'écriture directe par laser femtoseconde dans les matériaux a été étudiée en raison de ses avantages en micro-technologie. La découverte de l'effet de polarisation trouvé dans le contrôle de l'orientation de la cristallisation dans le verre d'oxydes LiNbSi a été exceptionnelle. Outre la longueur d'onde, la durée des impulsions, leur énergie et leur taux de répétition, la polarisation joue un rôle essentiel augmentant la dimensionalité du contrôle des processus à l'échelle nanométrique. De notre point de vue, nous avons étendu ce type de recherche, du monde inorganique au monde organique dans divers types de matériaux organiques parmi les cristaux et les verres. Des propriétés telles que la génération de seconde harmonique (GSH), la biréfringence linéaire (LB), le dichroïsme ou la di-atténuation linéaire (LD) ou la photoluminescence, ont été créés par irradiation laser. Toutes indiquent que, lors de ces processus, des espèces asymétriques ont été créées. Plus encore, la formation de GSH implique qu'une symétrie d'inversion a été brisée comme dans le cristal d'α-glycine. La création de luminescence a été trouvée dans de nombreux matériaux organiques après une irradiation laser femtoseconde. Cela montre une certaine généralité du mécanisme d'interaction entre le laser fs et le matériau organique. Le point culminant de cette thèse est la découverte de l'anisotropie d'excitation de la luminescence et le contrôle de l'orientation de celle-ci par la polarisation, incluant l'écriture, l'effacement et la réécriture. Cette étude est la démonstration que l'action de la polarisation de la lumière sur le contrôle de l'anisotropie peut être réalisé dans un matériau organique et à l'échelle moléculaire.

Title : Demonstration of anisotropy control of optical properties induced by IR fs laser irradiation in organic materials: birefringence, di-attenuation, SHG, photoluminescence

Keywords : femtosecond laser ; organic material ; anisotropy ; polarization ; luminescence ; SHG.

Abstract : Femtosecond laser direct writing in materials has been studied due to its advantages in micro-processing. The discovery of the polarization effect found in controlling the crystallization orientation in LiNbSi oxide glass was an outstanding finding. Besides wavelength, pulse duration, pulse energy, and repetition rate, polarization also plays an essential role in increasing the dimension of control at the nanoscale. We extended such research from the inorganic to the organic world in various kinds of organic materials among crystals and glasses. Properties such as photoluminescence, second harmonic generation (SHG), Linear birefringence (LB), Linear dichroism, or linear di-attenuation (LD) were discovered after laser irradiation. All indicate that asymmetric species have been created. SHG formation e.g. like in α-glycine crystal, implies in addition that inversion symmetry has been broken. Luminescence creation has been found in many organic materials after femtosecond laser irradiation, which seems to show a general interaction mechanism between fs laser and organic material. The highlight of this thesis is the discovery of the excitation anisotropy of luminescence and the control of its orientation by light polarization, including writing, erasing, and rewriting. This study performs a step forwards to demonstrate that the light polarization effect and anisotropy control by polarization can be realized in organic material and at a molecular scale.

CONTENU

SYNTHESE EN FRANÇAIS

L'écriture directe par laser femtoseconde dans les matériaux a été largement étudiée en raison de ses avantages en micro-technologie, tels que la conception 3D, l'implantation optique fonctionnelle, etc. Parmi les nombreux phénomènes intéressants pour la modification locale des propriétés optiques dans les matériaux, la découverte de l'effet de polarisation trouvé dans le contrôle de l'orientation de la cristallisation dans le verre d'oxydes LiNbSi a été exceptionnelle. Outre la longueur d'onde, la durée des impulsions, leur énergie et leur taux de répétition, la polarisation joue un rôle essentiel augmentant la dimensionalité du contrôle des processus à l'échelle nanométrique. De notre point de vue, nous avons étendu ce type de recherche, du monde inorganique au monde organique dans divers types de matériaux organiques cristallins ou vitreux. Des propriétés telles que la génération de seconde harmonique (GSH), la biréfringence linéaire (LB), le dichroïsme ou la di-atténuation linéaire (LD) ou la photoluminescence, ont été créées par irradiation laser. Toutes indiquent que, lors de ces processus, des espèces asymétriques sont produites. Plus encore, la formation de GSH implique qu'une symétrie d'inversion a été brisée comme dans le cristal d'α-glycine.

Une autre découverte importante est la création de luminescence dans de nombreux matériaux organiques après une irradiation laser femtoseconde. Plus précisément, après irradiation impulsionnelle à faible taux de répétition, la luminescence induite est sélective dans l'espace et n'existe qu'au point focal du faisceau laser, ce qui est utile pour l'intégration photonique en 3D. En caractérisant par microscopie confocale, la luminescence induite par le laser femtoseconde, nous avons démontré des similitudes entre les spectres d'excitation et d'émission de luminescence provenant de différents matériaux. Cette observation suggère une certaine généralité du mécanisme d'interaction entre le laser fs et le matériau organique. En outre, les paramètres d'irradiation du laser femtoseconde interviennent dans la modification des propriétés de luminescence. Par exemple, des taux de répétition et d'énergies d'impulsion modérément élevés conduisent à des spectres d'excitation et d'émission résultants de la création de centres de luminescence excités dans des bandes de longueurs d'onde plus longues.

En ce qui concerne l'origine de ces luminescences, nous pensons que le laser femtoseconde induit une carbonisation du matériau, conduisant à la formation d’agrégats de carbone graphitique (carbon dots) ou à des composés d'hydrocarbures aromatiques polycycliques ayant des propriétés luminescentes. Sur cette base, le point culminant de cette thèse est la découverte de l'anisotropie d'excitation de la luminescence. Bien que l'anisotropie d'excitation après irradiation laser femtoseconde ne soit pas évidente, elle peut être renforcée ou introduite par une irradiation laser polarisée, en continu, de faible puissance, produisant une diminution d’éfficacité d’excitation parallèle à la polarisation de la lumière d'excitation, une étape que nous appelons écriture. Nous avons découvert, ensuite, que cette anisotropie d'excitation peut être effacée et réécrite.

Nous proposons deux scénarios possibles pour expliquer ce phénomène : la rotation des molécules luminescentes asymétriques, ou un photo-blanchiment asymétrique des molécules luminescentes. Cette étude est la démonstration que l'action de la polarisation de la lumière sur le contrôle de l'anisotropie peut être réalisée dans un matériau organique et à l'échelle moléculaire.

De plus, ce manuscrit inclut des formules analytiques de calculs de la distribution spatiale de température induite par l’absorption d’un laser impulsionnel dans les matériaux transparents et son évolution temporelle. Dans ce cadre de travail, nous promouvons l’utilisation d’un paramètre qui combine les propriétés thermiques du matériau et le taux de répétition du laser. Sur la base de ce paramètre, nous montrons que l’on peut mieux comprendre et maîtriser les effets de la température, en particulier l’accumulation de chaleur, dans les processus de modification observés sensibles.

ACKNOWLEDGMENT

First, I would like to present the most sincere thanks to my supervisor Prof. Bertrand Poumellec, for his encouragement and support in my thesis and for his helps in my life. He is passionate about research, it is the source from which we started this pioneering work. I would like also to thank Prof. Matthieu Lancry, for his precious advice on laser experiments and explanations in optics. To our group colleagues, Yitao, Elisa, Benjamin, Maxime, Qiong, Jiafeng, Driffa, Julien, and Imane, many thanks for their discussions in our fields, their friendships, and their cooperation and tolerance in the life of our laboratory.

It is a pleasure to thank our colleagues and collaborators for their time and patient guidance in experiments:
M. Enrique Garcia Caurel from LPICM in Ecole Polytechnique for his precious help and discussion with Mueller matrix microscopy and spectroscopy for optical properties.
Mme. Ludivine Houel-Renault from ISMO for her numerous help with the characterization of luminescence.
M. Mebarek Temagoult from I2BC for his help on confocal microscopy about emission/excitation spectra mapping and 3D luminescence image.
M. Olivier Plantevin from LPS for polarized emission spectroscopy.
M. Romuald. Saint-Martin from ICMMO for XRD measurements.
M. Julius Nouet from GEOPS for Fourier transform infrared spectroscopy.
Mme Pascale Gemeiner from SPMS in Centrale-supélec for Raman spectroscopy.
M. Christian Herrero from ICMMO for his measurements on EPR.
Mme. Diana Dragoé from ICMMO for the measurements of XPS.
M. François Brisset from ICMMO for the measurements under SEM and the attempts on organic materials.
M. Serge AlBacha from ICMMO for the measurements of KPFM.
M. Andrew Pascal from I2BC for his attempts on Raman spectroscopy under low temperatures.

I would like also to thank my thesis examinator, Mme. Hynd Remita, for her valuable comments on the following of my thesis. Sincere thanks to my jury members: M. Razvan STOIAN, M. Sébastien FORGET Mme. Annick LOISEAU, M. Marie ERARD, and M. Enrique GARCIA-CAUREL for their precious opinions and suggestions in the reports of my manuscript and their presence for my defense, and special thanks to M. Robert Pansu for his helpful corrections in my manuscript and attendance in my defense.

I am grateful for the support provided by the Chinese Scholarship Council and University Paris-Saclay.

Finally, I am sincerely thankful to my parents, for their unconditional love and support. To my son, for keeping me company, preventing me from finishing my thesis too soon, and putting up with my bad temper in a difficult time. To my best friends Leticia and Nancy for always standing behind me, listening to me. To all my friends in France, Benjamin, Zhengyu, Weixi, Tiphaine, Bruno, Deb, Morgane, Francois, David, Irina, Caterina, Cecile, Amine, Sibylle, Chenyan, Gilbert, Chaoyan, Lixue, Jiang Dezheng, Li Ren and so on, for their company and concern.

May my work bring some value to the world.

Ruyue QUE

ICMMO, Orsay, France

01 September 2022

GENERAL INTRODUCTION

Since the invention of the femtosecond pulsed laser, it has been used extensively for the micromachining of materials due to the spatial selectivity at the micro-scale resulting from its extremely high intensity. As this technique does not usually require other processes, it is often expressed as Femtosecond Laser Direct Writing (FLDW) [1-5]. In both inorganic and organic solid materials, especially in inorganic glasses, many properties critical for integrated photonic circuits, such as refractive index change (RIC) [6-9], birefringence [10, 11], non-linear optical properties like second harmonic generation (SHG) [12], fluorescence [13], etc. have been induced by FLDW. The key laser parameters of laser-matter interaction such as wavelengths, pulse duration [14, 15], pulse energy, repetition rate, and scanning speed [16] have been well studied in terms of impact on the properties of materials.

In addition, although the polarization effect is smaller than the other previously mentioned parameters for the qualitative change of the material, it has a significant effect on the created anisotropic properties. This is a parameter that can be used to control the orientation of asymmetric objects, thereby altering the physical, chemical, or optical properties. In recent years, many studies have been carried out using laser polarization to change the orientation of nanocrystals precipitated by FLDW [17], achieving single-crystal formation in the required orientation. Polarization effects combined with scanning direction can also induce circular properties, implying the creation of chirality [18]. This valuable work contributes to the effect of laser polarization on microstructures, in particular the control of their orientation. It is a further fine control of laser-induced microstructure generation, and most of the current research is limited to inorganic glass materials.

In terms of applications, organic materials also have considerable advantages in fields such as optics and biology. From the point of view of basic research, organic compounds exist in the world as the basis of biology. Studying their interaction with lasers is a valuable exploration in any case.

Therefore, questions have been raised: the polarization effects in inorganic materials have been found and many studies have been carried out among inorganic glasses with different compositions such as LNS (Lithium Niobate Silicate) glass, LNSB (Lithium Niobate Silicate and Borosilicate) glass, etc. [17, 19], is it possible to achieve this to a larger extend in material selection such as changing inorganic substances to organic ones even though we know that their molecular bonds are completely different? What kind of organic materials to select for the relevant demonstration? How to choose the laser parameters for the interaction with organic materials without completely destroying the molecules? Under what conditions can we observe a polarization effect? Is it possible to achieve a certain degree of dependence of properties on light polarization, i.e. polarization control?

To answer these questions, this research realization has been organized in the following steps:

1, from many laser parameters, we have targeted our research on polarization. Hereby, as a continuation of the previous research on the polarization effects of lasers in inorganic glasses. This research **aims to demonstrate that a polarization effect on anisotropic properties can also be achieved in organic materials (Objective).**

2, polarization can influence asymmetric or chiral objects, either modifying the symmetry or chirality from the materials themselves or creating anisotropy or chirality by laser irradiation [20]. Therefore, **in material selection, for reasons of extensiveness, we have chosen several materials belonging to different solid types**, single crystals, and amorphous substrates, i.e., glass and polymers. Among them, the selected single crystals have optical anisotropy (e.g. linear birefringence), or optical rotation (e.g. circular birefringence), while glass and polymer are isotropic to a certain extent. By modifying their optical properties through laser irradiation (FLDW), we hope to observe polarization effects on the structures or molecules. In this manuscript, the sections are divided according to the results of the different materials after fs laser irradiation, in **Chapter III, IV, and V**.

3, before exploring the polarization effects, the critical laser parameters such as pulse energy (Ep), repetition rate (RR), and scanning speed are investigated in order to have a global view of the extent and types of laser modifications. **A thermal model has been developed to understand the temporal evolution and spatial distribution of temperature induced by fs laser pulses in relation to various parameters**, which then guide the experiments. They will be described in **Chapter II**. This investigation was also conducted experimentally at the beginning of every investigation of different materials, **obtaining the landscapes of Ep/RR plane** of various scanning speeds. In this way, we had a global vision of modifications, to define their types according to parameter range, and **to know which type can be observable in what anisotropies, and if they could be relevant to the polarization direction**. For example, in the range of laser parameters that produce a refractive index change derived from the volume change, there is no distinguishable difference in the anisotropy of this RIC in the modified region compared to the substrate, so we can hardly observe the effect of laser polarization in it. Another example is that in the modified areas with strong thermal effects, the material is largely destroyed, and the polarization effect is not considered to be apparent. But the second harmonic generation arising from laser-induced nanocrystals was discovered to have polarization dependence, as described in Cao's results [21], because for this modification (crystal precipitation from glass), the nanocrystals with different linear susceptibilities according to the optical axes, their orientation has been discovered possible to be controlled by the polarization. Therefore, the range of key parameters is necessary to be defined at the beginning of research in each material in order to characterize properly the modifications, especially the ones which can introduce breaking of symmetry, and thus to guide further investigations (to narrow the scope of the investigations).

4, **the asymmetric modifications of organic materials induced within the appropriate laser parameter range must be manifested in observable properties**, such as the ones relating to optical axis, e.g., Linear Birefringence (LB), Linear Di-attenuation or Dichroism (LD), or properties related to chirality, e.g. Circular Birefringence (CB), Circular Dichroism (CD), or non-linear effects requiring center-symmetry breaking, e.g. SHG, or polarization-dependent photoluminescence, etc. In this research, we discovered at least 4 properties, which demonstrate the creation of anisotropy from fs laser irradiation: birefringence, di-attenuation, SHG, and photoluminescence. SHG creation was observed in α-glycine, a centrosymmetric crystal. The results are described in the glycine Chapter III. The creation of anisotropic luminescence is discovered in all the 3 chosen materials (Chapter III, IV, and V), and the emission intensity varies with the excitation polarization direction. It is a kind of common effect that is described in a dedicated Chapter VI.

5, once we have shown that the anisotropic properties can be created by laser irradiation and are well observed, **the next step was to demonstrate that the polarization may control these anisotropies**. It is worth mentioning that there are other anisotropic factors besides the polarization, such as the crystal anisotropy of the substrate, and the scanning direction of the laser beam, which may affect these anisotropies as well. In this thesis work, we designed experiments to vary the polarization direction as well as the scanning direction during laser irradiation referred to the crystalline orientation of the substrate when relevant and characterized the results in an attempt to find an effect of direction. Among these anisotropic properties, birefringence, di-attenuation, SHG, and photoluminescence, **we succeeded in achieving polarization control in one property: photoluminescence. And this control can be achieved in all three chosen different types of organic materials. This finding is demonstrated in Chapter VI**.

Based on the above steps, we demonstrate the polarization effect produced by the femtosecond laser in organic materials. To summarize, step 1 introduces the aim of this study, and in Chapter I of the paper, we will investigate the most preface-related research to support the feasibility and innovation of this aim. Step 2 is to describe the reasons for material selection, which is our way of separating the main chapters to facilitate a logical presentation of the results of laser irradiation in each material, including results that meet expectations for screening out for the next experiments and others that are not significantly relevant. Step 3-5 demonstrate the experimental methodology (step 3 is to choose the appropriate laser parameters to optimize the generation of anisotropic properties, step 4 is to characterize the anisotropic properties, and 5 to control the anisotropic properties by polarization), which will be used throughout all major Chapters: III, IV, and V. In step 5, i.e. the control of anisotropic properties, not all results were successful, and those results, which were not clearly correlated with polarization were collected in the characterization section in Chapter III, IV, and V. An apparently polarization-related results discovered from all 3 materials chosen, i.e. excitation polarization-dependent photoluminescence, will be collected and discussed in Chapter VI. This summary of demonstration steps and thesis structure is presented in fig.1.

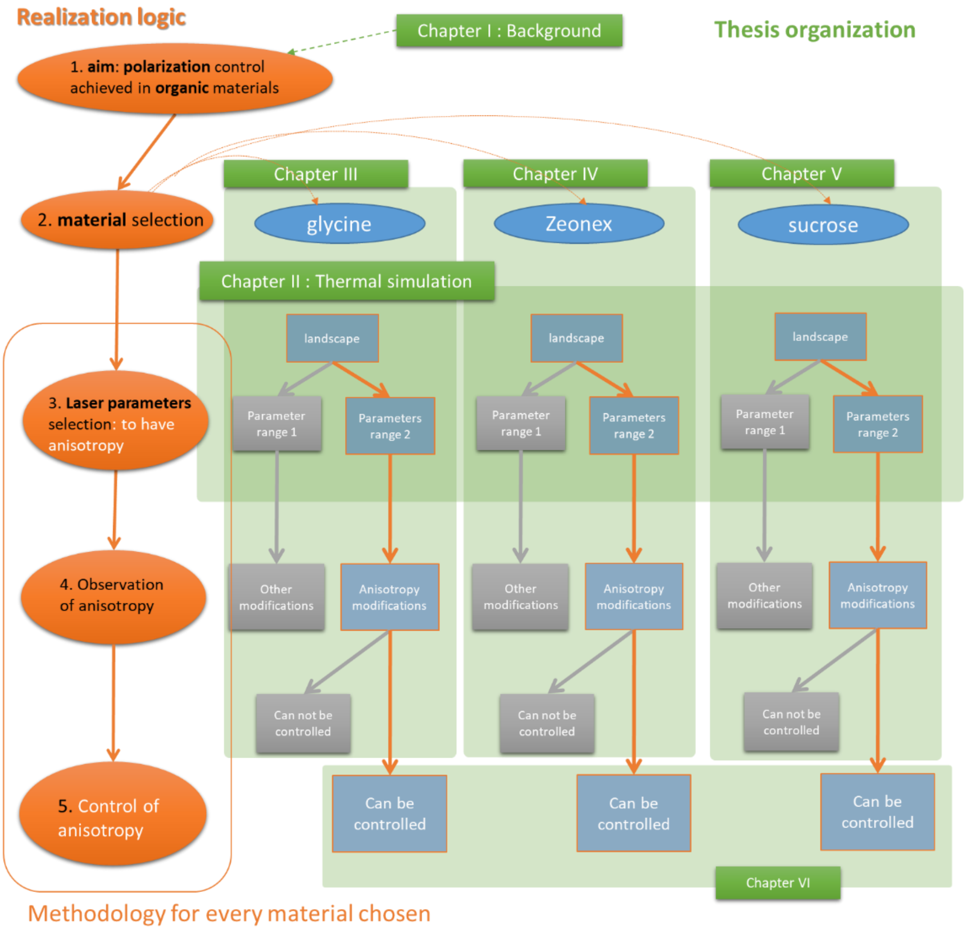

Fig.1 schematic representation of the research logic, methodology, and the corresponding thesis organization.

Chapter.I STATE OF ART OF POLARIZATION EFFECT IN LASER-MATTER INTERACTION

I.1 INTRODUCTION

I.1.1 General introduction of femtosecond laser

A laser is a device that generates and amplifies light through stimulated emission of radiation. The three critical components necessary for a laser are a pump source, a laser cavity, and a gain medium. Lasers are divided into several categories according to the type of gain medium (gas, liquid, and solid-state). The output wavelengths of lasers are depending on this gain medium or doping elements. Fig.I.1 is a practical schematic diagram showing us different lasers on the market and their corresponding wavelengths.

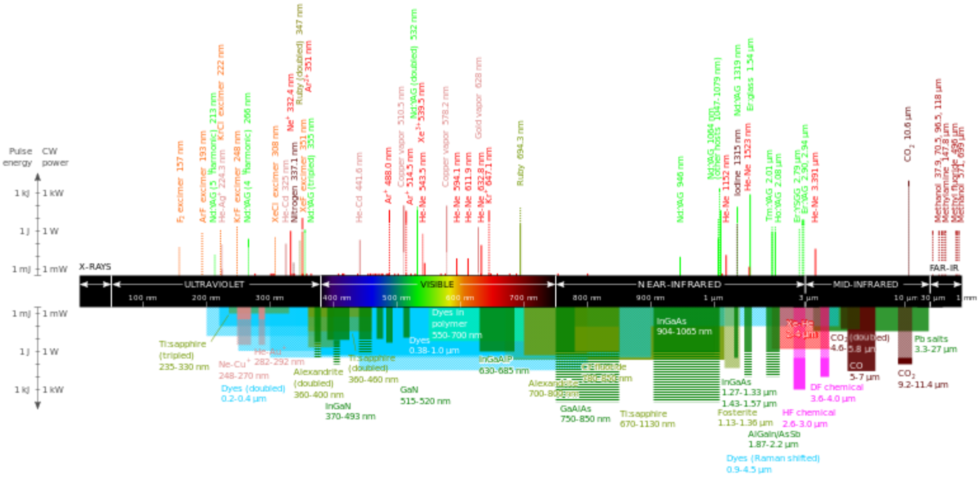

Fig.*I.1* Wavelengths of commercially available lasers. This picture is from Wikipedia and most of the data comes from Weber's book Handbook of laser wavelengths [22].

Depending on the application, the laser can operate in continuous wave (CW) mode or pulsed modes, where the optical power appears in pulses at some repetition rates [23]. to produce laser pulses, Q-switching was proposed firstly in 1958 by Gordon Gould [24], it is a well-known technique but the duration is generally on the order of ns

(10^{-9} s). To generate picosecond (10^{-12} s) pulses, the traditional method used is called mode-locking. To generate even shorter pulses such as femtosecond (fs, 10^{-15} s) laser pulses, some special mode-locking techniques including Kerr lens mode-locking (KLM), the colliding pulse mode-locking (CPM), and the hybrid mode-locking [25], etc. are required. On this basis, to fulfill the need to increase the power of fs laser pulses or to vary the wavelength, techniques such as optical parametric amplification (OPA) and chirped pulse amplification (CPA) [26] are applied.

Lasers with different pulse durations and intensities induce various processes and phenomena, as displayed in Fig.I.2. In general, for given pulse energy, the shorter the pulse duration, the higher power and light intensity the beam has. As a result, femtosecond laser exhibits advantages over conventional lasers for frontier research in physics and laser-matter interaction, inducing a variety of phenomena under different laser parameters. To better understand the processes and phenomena of fs laser-matter interactions on a time scale, next we will describe the basic mechanism.

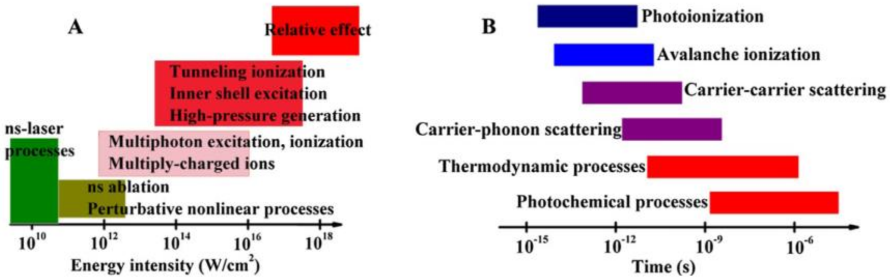

Fig.I.2. Pulsed laser-matter interaction with different energy intensity (A) and time scale of the physical phenomena associated with femtosecond laser–matter interaction (B) [27].

I.1.2 Basic mechanisms of fs laser-matter interaction

In recent years, the interaction of femtosecond laser with matter has been widely and intensively studied [28, 29]. Although the physical process of fs laser-matter interactions is not entirely clear, the following scenario is generally accepted (considering the interior of the relative transparent materials as an example). We also assume that it is similar in organic materials. Therefore, refer to fig.I.4 and also to fig.I.3 we describe the scenario in steps. When a single fs laser pulse irradiates condensed materials, the laser energy around the focus is first absorbed by the transparent material, producing electron excitation from the valence band to the conduction band in inorganic solids leading to quasi-free electron plasma. The transition is either achieved through multiphoton ionization (MPI) or by tunneling ionization (TI), depending on the Keldysh parameter γ defined in equation I.1 [30, 31], see fig.I.3 [32].

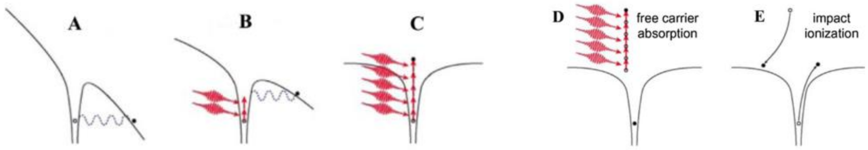

Fig.I.3. Schematic diagrams of the photoionization excited by femtosecond laser. (A) Tunneling ionization $\gamma < 1.5$; (B) mixture of tunneling $\gamma = 1.5$ and multiphoton ionization $\gamma > 1.5$, (C) multiphoton ionization, and (D, E) avalanche ionization. (Reproduced from [32])

$$\gamma = \frac{\omega}{e}\left[\frac{mcn\varepsilon_0\, I_p}{I}\right]^{\frac{1}{2}} \qquad (I.1)$$

ω is the light pulsation, e is the electron charge, m is the electron mass, c is the speed of light, n is the refractive index, ε_0 is the vacuum dielectric constant, I_p is the ionization potential, I is the light intensity. In inorganic solids, I_p is assimilated to the band gap of the solids with delocalized states, as the electrons of the conduction band are largely delocalized over a large number of atoms.

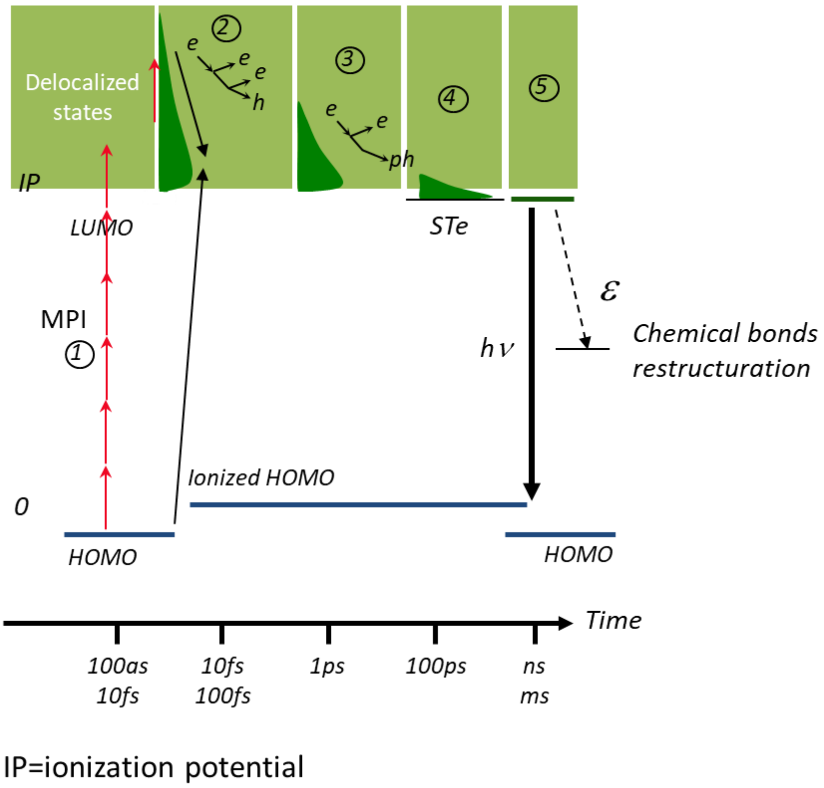

Fig.I.4 A scenario of laser-organic matter interactions. *In picture: e: electron; h: hole; ph: phonon; LUMO: lowest unoccupied molecular orbital; HOMO: highest occupied molecular orbital; IP: ionization potential; STe: self-trapped electron.*

However, organic materials are often made of small molecules. We thus use the convention of HOMO and LUMO instead of the valence band and conduction band, considering they could have discreet orbitals instead of bands. The overlap of the neighboring molecular wave functions is much weaker than the ones in inorganic solids. Band structures are rather flat and the conduction is very weak. The equivalent of the inorganic band gap would be the energy difference between HOMO and LUMO, but this gap is smaller than the energy of ionization or quasi-ionization. I_p is much larger than this gap by several eV [33]. **On the other hand, the intensity I used for organic materials is always much smaller. The Keldysh parameter eq.** $(I.1)$ **is thus larger than 1.5 so that the multiphotonic ionization process is favored.** Nevertheless, an exception to this remark is the π conjugated molecule, such as π-conjugated polymers or polycyclic aromatic compounds, graphene, etc.[34]. For them, a nano plasma can be produced along molecules.

Therefore, the nonlinear/multiphoton absorption processes (C in fig.I.3, 1 in fig.I.4) need to overcome the ionization potential (IP) to reach continuum states. Then followed by successive one-photon absorption (D in fig.I.3). The ionization is saturated, or plasma electrons are being 'heated' until their energy may overcome twice the band gap in solids with delocalized states or twice the IP in solids with the localized states (2 in fig.I.4). They are then energetic enough to trigger another excitation from the HOMO whereas the impacting electrons remain in the delocalized band. This impact ionization (E in fig.I.3) leads to the avalanche process that increases the plasma density. A bit later (at around 1ps), these electrons relax by coupling with phonons, heating the lattice (3 in fig.I.4). By this time, self-trapped electrons (STe) are formed in delocalized band states (4 in fig.I.4). Then, STe annihilate and release energy in a radiative way (light) or non-radiative way (vibrational relaxation i.e. further lattice heating or produces structure changes and converts potential energy into chemical one, etc.), consequently leading to permanent structural changes (5 in fig.I.4). However, it is only a simplified description, the induced phenomena depend on the chemical natures and physical properties of materials and also laser irradiation conditions.

I.1.3 Roles of laser parameters

As we mentioned above, many important parameters influence the process of fs laser-matter interaction, such as the laser light wavelength (λ), the pulse duration (τ) [35, 36], the pulse energy (Ep), the pulse repetition rate (f or RR), the polarization (p), the duration of the irradiation, and the numerical aperture (NA) of the focusing lens [37]. Therefore, a reasonable design of experiments must be based on these parameters and their combinations to form new structures and give rise to specific functionality in transparent materials. In this section, we will briefly describe the role of some parameters in the process. In addition, a thermal simulation based on pulse energy (Ep), pulse repetition rate (f or RR), and materials physical parameters, will be given later in Chapter II.

I.1.3.1 The wavelength, Numerical aperture (NA), and pulse duration (fixed in this work)

Wavelength (λ) represents the energy of the photon. The magnitude of the photon energy compared to the width of the energy gap between the ground state and the first excited one of the material directly determines whether the material absorbs light linearly or not, e.g. if the photon energy is smaller than the energy gap, the photon will be not absorbed, the material is transparent. However, when the light intensity is large enough, the material may absorb light non-linearly (multiphoton absorption), i.e. the material absorbs more than two coherent low-energy photons.

Alike the absorption of the material itself, the refractive index increases with the light intensity (Kerr effect). Therefore, an intense, focused beam is even more focused by such an effect (self-focusing effect [38, 39]).

On the other hand, the parameters that are of concern to us, the focus radius (w_0), and material modification threshold (I_{th}) have wavelength (λ), and numerical aperture (NA) dependencies.

Since the modifications are not only one, so there are several thresholds. One of them is called damage threshold (usually the first one) as the process is strongly dependent on light intensity. It does not correspond necessarily to damage (decomposition) but rather to the triggering of multiphoton absorption.

1) Speaking of focus beam radius (w_0), we need to mention first that since the laser amplification process occurs inside the laser cavity, the propagation of light back and forth between the two mirrors implies different modes. The mode TEM_{00} exhibits a Gaussian intensity profile. This one is generally selected by laser design. The mode maintains the same shape inside the cavity and beyond the cavity, i.e. outside of the laser. Since the geometric dependence of the fields of a Gaussian beam is governed by the light's wavelength, the focus radius of the beam waist ($1/e^2$ intensity criterion) is dependent on the laser light wavelength (λ), the beam quality factor (M^2), and the

numerical aperture (NA) [27]:

$$w_0 = 2\lambda/M^2 \ \cdot \pi \cdot (NA) \qquad (I.2)$$

where M^2 indicates how close the laser beam is to the fundamental Gaussian beam, for the Gaussian beam, M^2=1, and the larger the value M^2, the lower the beam quality is.

2) The threshold intensity (I_{th}) can be strongly wavelength dependent. For example, Jia et al studied wavelength tunable fs laser-induced damage in fused silica and CaF2 crystals. The threshold fluencies increase linearly with laser wavelength in the region of 250-800 nm, while it is nearly constant for 800-2000 nm[40].

   In addition, according to [41], the smaller light intensity I required for modifying the material is also determined by the laser pulse duration (τ), the pulse energy (Ep), and NA , it can be expected as follow:

$$I \propto Ep.NA^2/[\tau\lambda^2(1-NA^2)] \qquad (\mathrm{I}.3)$$

   However, it is important to note that the threshold intensity (I_{th}) conditionally follows this expression. For example, the dependence of I_{th} on τ has been explored for values of τ down to 10fs. For τ>10ps, I_{th} varies as $\tau^{1/2}$, indicating that Joule heating of the electrons excited at the beginning of the pulse is responsible for the optical damage [42]. For τ<10ps, I_{th} increase threefold for a tenfold increase of τ [36, 41].

I.1.3.2 Pulse energy and peak intensity

As mentioned in the basic mechanism of laser-matter interaction, when the light intensity is so high that the material can absorb light non-linearly, the multiphoton ionization rate $P(I)$ strongly depends on the intensity I as described by the following expression [43]:

$$P(I) = \sigma_k I^k \qquad (\mathrm{I}.4)$$

where σ_k is the multiphoton absorption coefficient for the absorption of k photons. Therefore, the pulse peak intensity directly determines the degree of multiphoton absorption.

Usually, in the setting of the femtosecond laser parameters, we adjust the pulse energy, what is the relation between pulse intensity and pulse energy? As described in eq. (I.3), for conditions where self-focusing is not taken into account (the Kerr effect), the pulse intensity is proportional to Ep. But this is not in agreement with the experimental observations. On the contrary, the required minimum pulse energy for nonlinear absorption, i.e. energy threshold, E_{th} is described as follows [32]:

$$E_{th} = \frac{I_{th}\tau\lambda^2}{\pi(NA)^2 + \frac{I_{th}\lambda^2}{P_{cr}}} \tag{I.5}$$

Where P_{cr} is the critical power, given by $P_{cr} = 3.77\lambda^2/8\pi n_0 n_2$, n_0 is the linear refractive index and n_2 is the nonlinear part due to the Kerr effect, the refractive index being $n = n_0 + n_2 I$. In reality, as the laser beam self-focuses, the intensity rises and eventually becomes sufficient to nonlinearly ionize electrons. The electron plasma contributes a negative refractive index change that cancels the positive refractive index change produced by the intensity-dependent index and prevents further self-focusing [32].

As I_{th} is defined by the material properties, the minimum pulse energy is defined by the relation eq. (I.5) that results from light prorogation in a non-linear medium.

Then, from a macro perspective, the deposited and absorbed pulse energy is transferred from the excited electrons to the lattice and then diffuses according to Fourier's law through the material. Therefore, higher pulse energy means higher initial temperature, the specific formulas will be given in Chapter II.

I.1.3.3 Repetition rate (frequency)

In general, the magnitude of the repetition rate, together with the thermal properties of the materials, determines the extent of thermal cumulative effects and the temperature at a steady state, leading to various modifications of properties. For example, repetition rate has been considered a crucial parameter in laser processing in inorganic glass for nanograting formation. For example, although the periodic structures, which are giving rise to birefringence and thus to retardance, are formed during the laser irradiation, the high local temperature caused by a high repetition rate may cause the self-organized nanostructure to be erased [44, 45]. With the increase of repetition rate up to the tested region of 1 MHz, retardance decreases, as shown in fig.I.5.

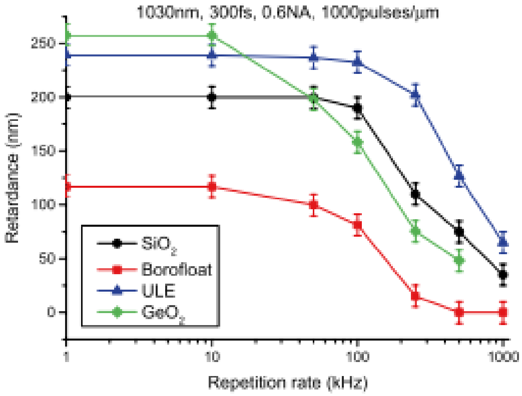

Fig.I.5 Retardance dependence with the laser repetition rate for various glasses. Extracted from [45].

I.1.3.4 Polarization

Polarizations including linear, circular, or elliptical polarizations, which can be transformed into each other, introduce symmetry breaking into laser processing. As the material is not always homogeneous (e.g. existence of dipoles) or symmetric (e.g. chirality) in molecular or structural terms, circular dichroism (CD) and linear dichroism (LD) are two types of absorption depending on the polarization. Besides, in the non-linear region, the absorption of the material can be inherently polarization dependent, e.g. the photoionization rates were approximately 3-4 times greater in fused silica for linearly polarized radiation than for circularly polarized radiation and 6 times greater in sapphire [46]. In addition to the polarization effects of the material at the absorption level, geometrically, the direction of polarization, e.g. horizontal versus vertical for linear polarization and left versus right rotation for circular polarization, will also cause the material to respond in a different orientation. Thus, it provides a specific action in the laser-material interaction in a different dimension, giving out a lot of interesting properties.

In the remainder of this chapter, we will then briefly review recent work on femtosecond laser-matter interactions including polarization effects, particularly in inorganic materials, but also in organic materials and solutions.

I.2 LASER INTERACTION WITH INORGANIC MATERIALS AND THE POLARIZATION EFFECT

The femtosecond laser can induce numerous phenomena in all kinds of transparent inorganic glasses, such as index change, migration of ions, phase separation, crystallization, nanograting, voids, etc. (these phenomena have partially overlapping definitions). Some polarization effects have been found in these phenomena. For instance, Little et al. have discovered that with the fs laser of 1kHz in fused silica, the waveguides written by circularly polarized laser exhibited refractive index contrast up to twice as large as that of waveguides written with linearly polarized radiation [37, 47]. Liu et al. demonstrated that the laser damage threshold inside fused silica is dependent on the polarization of the incident fs laser pulses. The damage threshold for circularly polarized beams is higher than that for linearly polarized beams when NA>0.4, but the reverse situation is when NA<0.4 [48].

In addition to the difference in material properties due to the type of polarization (circular vs linear), the orientation dependence of the material due to the linear polarization direction is even more exciting. Shimotsuma et al. observed periodic self-organized nanostructures inside silica glass [49], anion-doped silica glass [50], and Al_2O_3-Dy_2O_3 binary glass [51] after a Ti: sapphire fs laser or a CO_2 laser, the nanostructures are aligned perpendicular to the laser polarization direction, shown in fig.I.6. Furthermore, Cao et al. discovered in Lithium niobium silicate (LNS) glass laser-induced nanostructure, as well as nanocrystals precipitated by fs laser irradiation, are both orientable by fs laser polarization as shown in fig.I.7 [17]. It is not the only case, Muzi et al. have demonstrated the same phenomena, i.e. laser induced polarization-oriented nanocrystallization, in lithium niobium borosilicate (LNSB, B_2O_3 addition in LNS glass matrix) glasses [52].

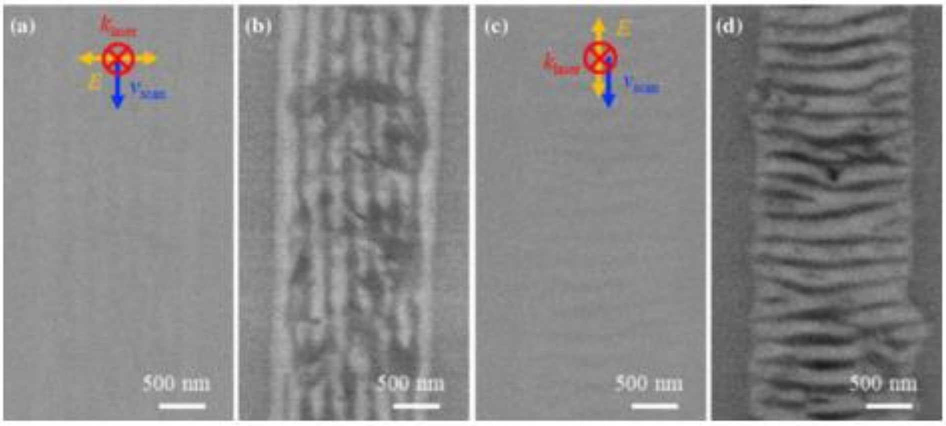

Fig.I.6 Secondary electron images (SEIs) of self-assembled periodic nanostructure in an Al_2O_3-Dy_2O_3 glass sample, cited from [51].

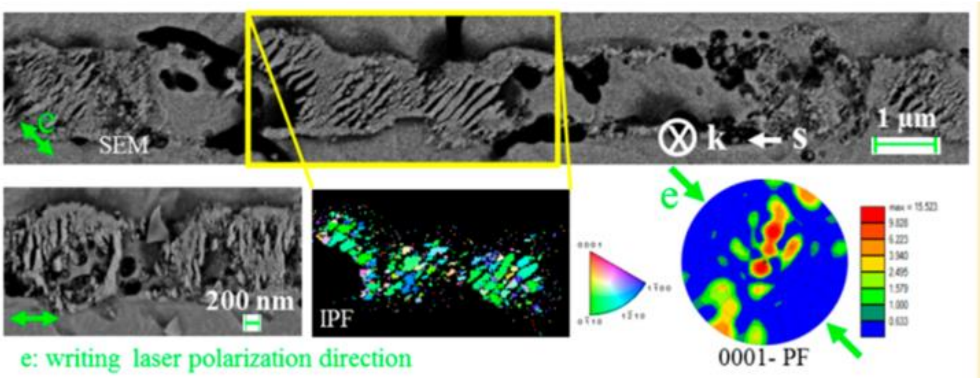

Fig.I.7 Grey pictures: secondary electron SEM images of fs laser-induced nanostructures in LNS glass at varying writing laser polarization direction (writing laser polarization direction is indicated by the green double arrows in each image). IPF (black background) and 0001-PF are the part marked by a yellow rectangle in the SEM picture. The color in the IPF is based on the $LiNbO_3$ space group (i.e., R3c), coding along with writing laser polarization direction. Extracted from [17].

In addition to linearly polarized light that can orient the laser-induced nanostructures, circularly polarized light can even induce chiral structures. For instance, Taylor et al. have produced a permanent recording of optical helicity in fused silica by circularly polarized fs laser, the chirality of the structure can be altered by inversing the circular polarization, as shown in fig.I.8 [53].

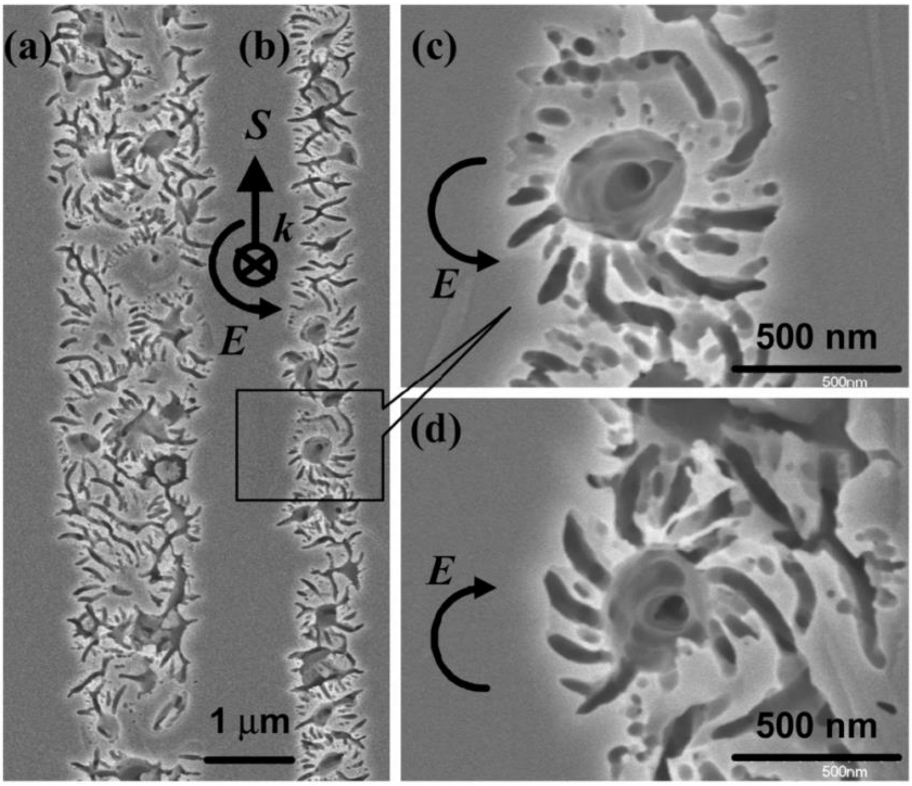

Fig.I.8 secondary electron SEM images obtained in the horizontal observation plane (a) about 4µm below the top of the modified region using Ep=350 nJ and (b) about 2µm below the top of the modified region but with Ep=200 nJ. (c) Enlarged image of one of the chiral units shown in (b) produced with right-handed CP light. (d) Chiral unit produced using left-handed CP with the same pulse energy and scan rate that was used in (c). Extracted from [53].

The above phenomenon is so common in various inorganic glasses as well as interesting, so we want to know if this phenomenon could also occur in organic solid materials. Therefore, we have reviewed recent literatures and found that among the many studies of laser interaction with organic materials, there are few studies related to laser polarization effects, let alone polarization control.

I.3 LASER INTERACTION WITH SOLID ORGANIC MATERIALS AND LIQUID SOLUTIONS AND THE POLARIZATION EFFECT

Many studies of the interaction of femtosecond lasers with organic materials have been achieved on the surface by the ablation of structures [54-57]. In recent years there are some research into changing the refractive index in bulk or organic optical fibers made of commonly used polymers such as PMMA [58], PDMS [59], CYTOP [60-62], etc. Some other research investigated laser-induced chemical changes [63]. Among these researches, some polarization dependence related papers are found: Ye et al. has discovered that in fs laser-induced Bragg gratings in PMMA, linear polarization (perpendicular to the scan direction) produced the highest refractive index contrast, while circular polarization produced the lowest [64]. Kallepalli et al. used an fs laser to induce photochemical changes in polyimide, forming absorption and luminescence properties in the visible region. The laser-treated polyimide exhibited photoluminescence anisotropy resulting from the formation of the ordered polymer upon irradiation by linearly polarized ultrashort laser pulses [63]. Some other studies have shown that a linearly polarized femtosecond laser beam can align polymer chains inducing the formation of ordered aggregates, for example via π-π stacking [34, 65, 66].

Additionally, there are some studies about polarization effects on crystallization and polymorph control using nanosecond pulsed laser irradiation in organic solution, this phenomenon was named nonphotochemical laser-induced nucleation (NPLIN). Garetz and Myerson have demonstrated pioneering research that, with a 1060nm Nd:YAG pulsed laser, the laser-induced needle-shaped crystals precipitated from supersaturated urea aqueous solutions that were initially formed, tend to be aligned parallel to the polarization of the light [67]. Yuyama et al. have successfully demonstrated the polymorph control of glycine in a D_2O solution using a linearly or circularly polarized CW near-infrared laser beam. For the supersaturated and saturated solutions, circularly polarized laser irradiation enhances γ-crystal formation, while for the unsaturated solution the laser polarization effect becomes prominent, and linearly polarized laser light at a specific power provides the maximum γ-crystal probability of 90% [68]. Sun et al. found out that in supersaturated aqueous L-Histidine, circularly polarized laser pulses tended to nucleate the orthorhombic A polymorph, whereas linearly polarized pulses tended to nucleate a mixture of the orthorhombic A and monoclinic B polymorphs [69]. Carbamazepine (CBZ) molecule in two solvents (methanol and acetonitrile), using the NPLIN technique, the irradiation of an acetonitrile solution by a linear polarized (LP) laser results in CBZ phases I and III, whereas irradiation by the circular polarized (CP) laser leads to CBZ phase III crystals, shown in fig.I.9 [70]. Furthermore, Iftime et al. demonstrate that irradiation with circularly polarized light of a film of an achiral azobenzene liquid crystalline polymer induces chirality. Circularly polarized light with opposite handedness produces enantiomeric structures [71].

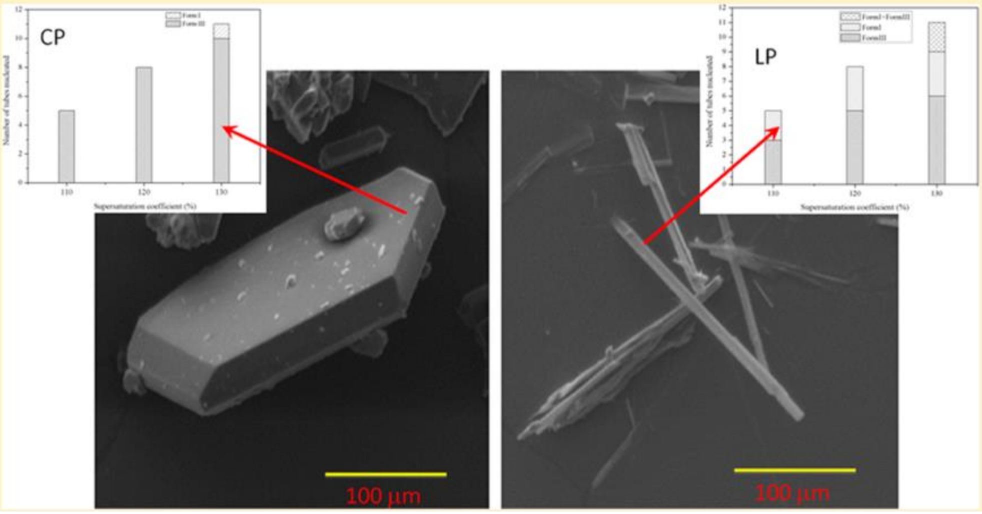

Fig.I.9 SEM micrographs of CBZ crystals produced by NPLIN in acetonitrile: (left) phase III and (right) phase I. Extracted from [70].

Above are some typical studies about laser interaction with organic material or solution including polarization influences. Most of the polarization effects in solids arise from the efficiency of the material's response to different kinds of polarizations, or for polarization control, the effects are studied only in solution. We are therefore not aware of any studies where polarization can control the direction of some anisotropies.

I.4 CONCLUSION

First, this chapter briefly introduces some background:

What is fs laser? What are the types of fs laser? How to generate fs pulses? What is the mechanism of fs laser-matter interaction? What are the necessary conditions for multiphoton ionization? What are the roles of laser parameters, such as wavelength, pulse duration, pulse energy, repetition rate, polarization, etc.? For the answers, the necessary information is summarized here for introductory purposes, detailed descriptions can be found in the cited or relevant literatures.

After that, based on the frontier literature research, we found:

1) the laser polarization effects and laser-induced asymmetry/chirality from inorganic glasses have been studied. The anisotropy/chirality can be controlled.
2) It has been pointed out that during the laser-induced crystallization process in organic solutions, the polarization affects the preferential orientation and morphology of the precipitants.
3) In organic solids, to our knowledge, some research has been conducted to study the polarization effects on properties, but few research studied the anisotropy control by the polarization.

Therefore, the demonstration of polarization effects such as preferential orientation controlled by the polarization direction during crystallization in inorganic glasses, the morphology selection by the polarization type during crystallization in organic solution, and refractive index changes in the organic solids according to the polarization type, etc. indicate and inspire that the vector properties of the light can induce anisotropy in solids and that can be controlled. They demonstrate that light force actions are feasible at the nanoscale or even at the molecular scale.

However, for different types and even different compositions of inorganic glass, the appropriate laser parameters are different, and the laser-modified properties are also not the same, e.g. the LNS glass at certain composition ratios fails to crystallize and to be orientated. Therefore, changing material from the inorganic world to the organic world is a big step, especially the intermolecular forces in organic solids are considerably weaker than the covalent bonds in inorganic glasses. Moreover, in contrast to examples of laser-induced crystallization and nanostructures in inorganic glass, no studies found that have demonstrated that lasers can induce crystallization from organic solid-state compounds, or produce **orientable** asymmetric objects (molecules or structures) in organic glass or crystals. For most organic glasses or crystals, except commonly used polymers, there is even no information about the interaction with fs laser. So we don’t have ready-made parameter ranges for reference. Our work was therefore original and challenging as we needed to find the right range of laser parameters in a wide range and try to create something to control, which is not known *ab initio*. It was a work at the frontier of knowledge.

In order not to stray too far from our goal, for example, to avoid burning the sample, we have first developed a thermal model to simulate the temperature distribution induced in the material by the laser pulses with different parameters, for guiding the experiments. It is presented in the next chapter.

Chapter.II THERMAL SIMULATION OF LASER-MATTER INTERACTION WITH ANALYTICAL EXPRESSIONS

II.1 INTRODUCTION

As we mentioned in Chapter I about the fs laser-matter interaction process, the energy deposited into transparent materials is absorbed to excite electrons by MPI or tunneling ionization or avalanche ionization, etc., after that, during the electron relaxation back to the ground state, in addition to emitting photons or storing parts of energy as chemical energy, the pulsed energy is inevitably converted into heat, which in turn raises the local temperature of the material and plays a crucial role in the transformation processes.

The objective of this chapter is to develop an analytic approximation to predict the spatial temperature distribution and the temperature development over time according to the key laser parameters combination and then to deduce important physical conclusions and semi-quantitative results without using heavy and too specific finite element calculation. This is in the spirit of Paul Dirac that declared in 1929 in the Proceedings of the Royal Society of London [72]:

"The underlying physical laws necessary for the mathematical theory of a large part of physics and the whole of chemistry are thus completely known, and the difficulty is only that the exact application of these laws leads to equations much too complicated to be soluble. It therefore becomes desirable that approximate practical methods of applying quantum mechanics should be developed, which can lead to an explanation of the main features of complex atomic systems without too much computation."

In the ultrafast laser-matter interaction process, the energy of the laser pulse that has an extremely short pulse duration (10^{-11}–10^{-15} s) is injected into a small focal volume of transparent dielectric solids. This intense laser pulse with high irradiance ($>10^{13}$ Wcm^{-2}) at the focal region stimulates a series of complex dynamic processes, such as multiphoton absorption, inverse bremsstrahlung absorption, the subsequent multiphoton ionization, tunneling ionization, and avalanche ionization in an ultrashort time scale [73]. As a consequence, the plasma with high temperature and high pressure is generated and expands rapidly at the focal zone, and results in structural modifications upon energy relaxation through the phonon–electron and electron-electron interaction.

In the low repetition rate regime, thermal accumulation is usually negligible in the processing. The temperature decreases to the initial degree before the next pulse arrives. The nonlinear nature of the light absorption confines the energy deposition to the focal volume. These advantages minimize the thermal collateral damage and heat-affected zone(HAZ) [74]. Therefore, Ultrafast Laser Direct Writing (ULDW) is suggested as a general technique to induce highly localized modifications and optical structures within/near the focus in a wide range of transparent solids [27, 41, 49, 75-77]. In this regime, denoted as non-thermal ULDW, the repetition rate is usually a few kilohertz (kHz) and the fabrication efficiency is also limited by the low pulse repetition rate.

In contrast, when the pulse repetition rate of the ultrafast laser reaches hundreds of kHz (e.g. >100 kHz in a material with diffusion time~1μs), the interval between successive laser pulses is less than the time needed for the absorbed energy to diffuse out of the focal volume. This induces localized heat accumulation effect [77-84]. In this case, energy is injected into the material by multiple laser pulses faster than they can diffuse away, and thus increases the temperature continuously in the focal zone before stabilizing. The final diffusion of the heat into the surrounding material may lead to a material melting out of the focal volume on a longer time scale. In this regime, denoted as thermal ULDW, the melted modified region is much larger than the focus size. Parallel to the wide applications of non-thermal ULDW, the localized thermal accumulation has been demonstrated to be important in the ULDW for inducing various phenomena and structures in the transparent solids and improving the performance of the fabricated devices. For example, the thermal accumulation can lead to a higher symmetry of the waveguide cross-section, reducing the propagation loss and enhancing the fabrication efficiency [78, 81, 82]. Thermal accumulation in the ULDW can also induce unique phenomena, such as element redistribution and local crystallization, which is nearly not achievable in the non-thermal ULDW [77, 85-89]. In the thermal ULDW regime, the temperature distribution can work as a driving force to redistribute the elements or reorganize the structures in the thermal melted region. The thermal accumulation effect has also been reported to be critical for the formation of periodic nanogratings in some glass systems [90]. Moreover, the thermal accumulation induces high temperatures that can produce thermally excited free electrons, which seeds the avalanche ionization and significantly enhance absorptivity [91]. As a result, more energy can be absorbed and this leads to increasing further thermal accumulation. Until now, thermal accumulation has been established to be an important assistor in many cases to help ULDW to achieve various applications in fundamental science and technological manufacturing [80, 81, 87, 91-93]. Clarifying the principle of thermal ULDW and reviewing its current stage in the applications are highly urgent and also significant for guiding future work [81, 92, 94].

For this aspect of work, Lax et al. in 1977 [95] published the first paper that described the 3D spatial distribution of the temperature rise induced by the Beer-Lambert absorption of a static Gaussian CW laser beam in cylindrical geometry. Then, Sanders in 1984 [96] described an extension of these calculations for scanning beams and gives analytic expressions. In 1991, Haba et al. [97] described the calculation of 3D spatial distribution for the Beer-Lambert absorption of a scanning Gaussian pulsed laser in cylindrical geometry. However, even if the expression is quite complete but numerically solvable, there was no extended discussion on the laser/material parameters. Then, Eaton et al. [81] in 2005 and Zhang et al. [98] in 2007 performed finite difference calculation, a simple pulsed and CW Gaussian beam in spherical geometry, preventing easy material analysis. In 2007, Sakakura et al. [84] solved the Fourier equation in the frame of cylindrical geometry for energy delivered by a Gaussian pulsed fs laser (pulse duration 220fs, repetition rate 3Hz, pulse energy<1μJ). With such a weak repetition rate, the calculation can be restricted to one pulse as the experimental measurement (a lens effect) was smaller than 1ms. However, it is not a special case and for material treatment, a large number of pulses are required. That is why Miyamoto et al. [99] in the same year, deduced analytical expressions for scanning uniform pulsed laser energy deposition in a parallelipedic volume of width 2w corresponding to the scanning CW beam diameter at 1/e and length corresponding to the absorption length ($1/\alpha$). These calculations were used also by Beresna et al. [100] and applied to a particular case i.e. borosilicate. In 2011, Miyamoto et al. [91] considered cylindrical source with full width dependent on z in order to account for the convergence of the beam or the non-linear properties including the self-focusing. In 2012 Shimizu et al. [101] used a static cylindrical Gaussian beam and Gaussian energy deposition in depth for multipulsed laser energy deposition but solved the problem numerically. Lastly, in 2019 and 2020, Rahaman et al. [102, 103] proposed an analytical solution using Duhamel's theorem and Hankel's transform method, for a transient, two-dimensional thermal model.

We summarized above research in the table below to compare with our work in this chapter:

Laser type	**mode**	**geometry**	**Source shape**	**Solving method**	**ref**
CW	static	cylindrical	Gaussian(r) Beer-Lambert(z)	analytical	Lax [95]
pulsed	scanning	3 axes	Gaussian(x,y) Beer-Lambert(z)	analytical	Sanders [96]
pulsed	scanning	3 axes	Gaussian(x,y) Beer-Lambert(z)	Analytical	Haba [97]
pulsed	static	spherical	Gaussian(r)	Finite difference	Eaton [81] or Zhang [98]
pulsed	Quasi-static	cylindrical	Gaussian(r) Beer-Lambert(z)	Analytical one pulse	Sakakura[84]
Pulsed CW	scanning	3 axes	Uniform deposition in parallelipedic	analytical	Miyamoto [99]
Pulsed	static	cylindrical	Gaussian(r)	analytical	Miyamoto[91]
pulsed	static	cylindrical	Gaussian(r) Gaussian(z)	numerical	Shimizu [101]
pulsed	scanning	cylindrical	Gaussian(r) Surface absorption	analytical	Rahaman [102, 103]
pulsed	Static/ scanning	Spherical cylindrical	Gaussian(r) Gaussian(z)	analytical	This work

Table.II.1 state of art of thermal simulation of laser-matter interaction

In short, none of the authors provide simple expressions that allow us to easily understand how each parameter of laser influences the temperatures. This is the reason why we present the analytical approach in this chapter. To follow the reading better, some key information is extracted here, giving small statements. The details, and reasons will be explained in the latter sections.

The basic assumptions considered:

- The beam is Gaussian in radial (r) and axial (z) directions.
- The pulse energy from the beam is completely deposited before the diffusion occurrence. The pulse shape is considered Gaussian also without the restriction of generality with the previous assumption.
- The physic-chemical parameters are temperature-independent.

The key laser parameters in this chapter contain:

- **Ep**: pulse energy.
  According to the principle of conservation of energy, Ep determines the maximum temperature in each pulse, regardless of the position. It also determines the amplitude of the temperature oscillations after reaching the steady state.
- $\boldsymbol{w_r}$ **and** $\boldsymbol{w_z}$: the radius of the laser pulse in the material in the radial direction and axial direction. When $w_r=w_z$, we consider that the absorption volume is spherical; when $w_r \neq w_z$, we consider the absorption volume cylindrical. Since we assume the laser beam is a Gaussian beam, the width of a Gaussian beam is defined by where the field amplitude falls to 1/e of their axial values (i.e., where the intensity values fall to $1/e^2$). When propagation in the axial direction (z), the width of the beam or spot size parameter w is a function of the position, i.e. $w(z)$. w_r is thus defined here as the Gaussian beam waist (w_0), i.e. the minimum radius in the axial direction and also z=0 set, shown in fig.II.1. From equation (I.2) we have:

  $$w_r = w_0 \approx \frac{2\lambda}{\pi.NA} \qquad (\mathrm{I}.2bis)$$

  w_r is depending on wavelength and NA.
  $w(z)$ is given by a hyperbolic relation [104]:

  $$w(z) = w_0\sqrt{1+\left(\frac{z}{z_R}\right)^2}$$

Where

$$Z_R = \frac{\pi {w_0}^2 n}{\lambda}$$

Z_R is called Rayleigh range [105]. At a distance from the waist (z=0) equal to the Rayleigh range Z_R, the width w, i.e $w(Z_R)$ of the beam is $\sqrt{2}$ larger than it is at the focus, shown in fig.II.1. Our parameter w_z, the focused fs laser beam radius in the axial direction, is defined to be Z_R, so

$$w_z = \frac{\pi {w_r}^2 n}{\lambda} \tag{II.1}$$

This value inversely proportional to NA as eq.II.1bis and fig.II.1 right shows:

$$w_z \propto \frac{n w_r}{NA} \tag{II.1bis}$$

NA influences w_z more than w_r: $w_r \propto \frac{1}{NA}, w_z \propto \frac{1}{NA^2}$.

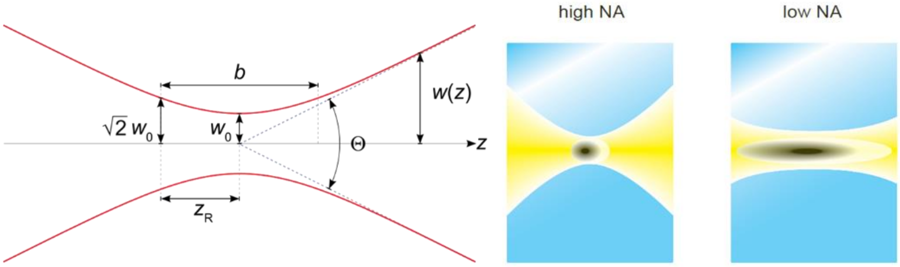

Fig.II.1 left: Diagram of Gaussian beam waist parameters. Gaussian beam width w(z) as a function of the distance z along the beam: w_0: beam waist; b: depth of focus; Z_R: Rayleigh range; Θ: total angular spread (from Wikipedia). Right: the diagram of Z_R or Z_R dependence on NA.

Therefore, these 2 parameters, which determine the absorption volume, are mainly influenced by light wavelength, NA, and refractive index. However, for ease of calculation, in the models we developed, since the beam quality refractive indices of the various materials do not differ significantly, w_r and w_z can be approximately fixed to be 1μm and 3μm for NA of 0.6 and λ of 1030nm (calculated via eq.I.2bis and II.1 with M^2=1), regardless of the materials.

However, as the absorption in our case is strongly non-linear, including multiphoton, spherical aberration, self-focusing, and excited electron defocusing, the shape of the actual absorption volume is not easy to predict. So it is often considered from experimental observations [106-108]. Here, for sake of simplicity and for deducing physical conclusions, we have assumed a Gaussian shape on the 3 variables r, z, t on the rate of energy deposition (as it can be seen below for one pulse):

$$\frac{\delta \rho_Q}{\delta t}(r,z,t) = dQ_0 \cdot exp\left[\frac{-r^2}{(w_r)^2}\right] \cdot exp\left[\frac{-z^2}{(w_z)^2}\right] \cdot 2\frac{\sqrt{\ln(2)}}{\tau \cdot \sqrt{\pi}} \cdot exp\left[-4\ln(2)\frac{t^2}{\tau^2}\right]$$

w_r, w_z is thus now and hereafter in this chapter, the waist radius at 1/e, τ is the pulse duration at Full width at half maximum (FWHM).

- **f or RR**: frequency or repetition rate of laser pulses. It is the number of pulses per unit of time.
  $\boldsymbol{\tau_p}$: pulse period which is 1/f or 1/RR.
  Considered together with the scanning speed v, RR determines the number of pulses received punctually. At each point, the irradiation time, $t \approx \frac{2w_r f}{v}$. So, the density of pulses per unit of length is $\frac{f}{v}$. Considered together with the thermal diffusion time of the material, it determines the rate of heat accumulation.

The material parameters involved:

- **ρ**: density or or specific mass.
  C_p: specific heat capacity.
  ρ and **C_p** determines the peak temperature T_{00} induced by a laser pulse. They also influence the diffusion process.
- **κ**: thermal conductivity.
  D_{th}: thermal diffusivity.
  Thermal conductivity or thermal diffusivity determines how fast the heat propagates in the material, the relationship between them is as follows:

$$D_{th} = \frac{\kappa}{\rho C_p} \qquad (II.2)$$

$\boldsymbol{\tau_d}$: diffusion time is defined by:

$$\boldsymbol{\tau_d} = \frac{w^2}{4D_{th}} \qquad (II.3)$$

It corresponds approximatively to the time for out-diffusion of 2/3 of the heat deposited by the beam at t=0 and the source geometry is considered to be spherical.

It is recalled that, in the models, ρ, C_p, κ, D_{th} as well as τ_d are assumed to be temperature-independent, and are considered to be constants in whatever spatial direction or crystal axes, varying only according to the materials.

Based on the ratio of the pulse period $\boldsymbol{\tau_p}$ to the diffusion time $\boldsymbol{\tau_d}$ we have defined a new parameter $\mathbf{R}_{\boldsymbol{\tau}}$ to numerically quantify the degree of heat accumulation, shown as follow:

$$\boldsymbol{R_\tau} = \frac{\boldsymbol{\tau_p}}{\boldsymbol{\tau_d}} \tag{II.4}$$

A large $\boldsymbol{R_\tau}$ value corresponding to a material with a large diffusivity, i.e. short diffusion times, or in the situation of low repetition rate, i.e. long pulse periods. So in large $\boldsymbol{R_\tau}$ case, there will be a low degree of heat accumulation.

Conversely, cases where the material has a small diffusion coefficient, i.e. a long diffusion time, or a short pulse period, is corresponding to a small $\boldsymbol{R_\tau}$ value, there will be a high degree of heat accumulation.

The dividing line for the $\boldsymbol{R_\tau}$ value depends on the definitions of heat accumulation.

1) If we define the heat accumulation effect as the final temperature of the material induced by multiple pulses being ε% increase of that induced by a single pulse. And this ε% relates to the temperature tolerance of the material, e.g. the temperature difference required for a phase change. This definition is actually concerned with the material properties change, in which case the $\boldsymbol{R_\tau}$ dividing line for heat accumulation is material related. For example. if we consider heat accumulation has occurred when the final maximum temperature at steady-state exceeds 7.4% of the initial peak temperature of a pulse, $\boldsymbol{R_\tau} < \mathbf{10}$. Conversely, when $\boldsymbol{R_\tau} > \mathbf{10}$, the final maximum temperature is comparable to the maximum temperature of one pulse (< 7.4%), and we do not consider there is heat accumulation. If the threshold of heat accumulation is defined by 1%, the crucial value of $\boldsymbol{R_\tau}$ will be **38**. This has practical implications, for example, to modify SiO_2 glass, the single pulse induced temperature usually is more than 2000K, in this case, a 1% increase means 20°C and a 7.4% increase means 148°C, it is more

reasonable to consider that the temperature in the steady state of 2148K to be accumulated than 2020K. Thus, $\boldsymbol{R_\tau} = \mathbf{10}$ is the better dividing line for heat accumulation in SiO_2 glass. On the other hand, in organic materials with melting temperature/decomposition temperature around 500-600K, if we consider the increase of 14-16°C which is around 3% of the maximum temperature induced by a single pulse, the dividing value of $\boldsymbol{R_\tau}$ is 15.

To conclude practically (can be adjusted by the actual situation):

- In the case of inorganic materials such as SiO_2 glass, when $\boldsymbol{R_\tau} < \mathbf{10}$, there is heat accumulation and vice versa.
- In the case of organic materials, when $\boldsymbol{R_\tau} < \mathbf{15}$, there is heat accumulation and vice versa.

2) The 1st definition of heat accumulation is the usual practical definition, here we propose a new definition of heat accumulation which is concerned only with the behavior of the temperature, e.g. whether it is linear or non-linear with respect to the diffusivity of the material and the repetition rate of the pulse.

We find that when the pulse repetition rate or material diffusion time increases within a small range ($\boldsymbol{R_\tau}$ decreases from a large value), the increase of temperature is insignificant and the slope of temperature and $1/\boldsymbol{R_\tau}$ is very small, less than one; beyond this range, as the pulse repetition rate or material diffusion time increases ($\boldsymbol{R_\tau}$ continues to decrease), the increase in temperature becomes faster until it is linearly related to the pulse repetition rate or material diffusion time. That is, linearly correlated with $1/\boldsymbol{R_\tau}$. The dividing line of this linearly correlated range, we define it as the thermal accumulation dividing line.

The first definition allows us to adapt $\boldsymbol{R_\tau}$ to the actual situation, giving the reader a concrete impression of the magnitude and range of $\boldsymbol{R_\tau}$. The second definition allows us to understand more deeply the physical meaning of temperature accumulation, i.e. whether the behavior of temperature is linearly related to $\mathbf{1}/\boldsymbol{R_\tau}$. Details will be explained later in the following sections (II.3.2.2.2 and fig.II.11). Next, we will introduce what we want to know about temperature when we consider laser parameters and material parameters.

The temperatures and other crucial information we want to predict:

Since various modifications of materials after laser irradiation are often caused directly or indirectly by thermal effects, we want to know the **temperature** in the material induced by laser irradiation, including the spatial distribution and its temporal evolution. This information can better guide us in choosing the parameters of the laser.

Firstly, when considering 1 pulse, the temperature distribution around focus (r=0) has a temporal evolution. Fig.II.2a shows that the temperature distribution around the focal point flattens out with time. fig.II.2(b) visualizes this thermal diffusion by showing the temporal evolution of temperature at the beam focus center (r=0) and 2 areas around the center (r=1µm and r=2µm).

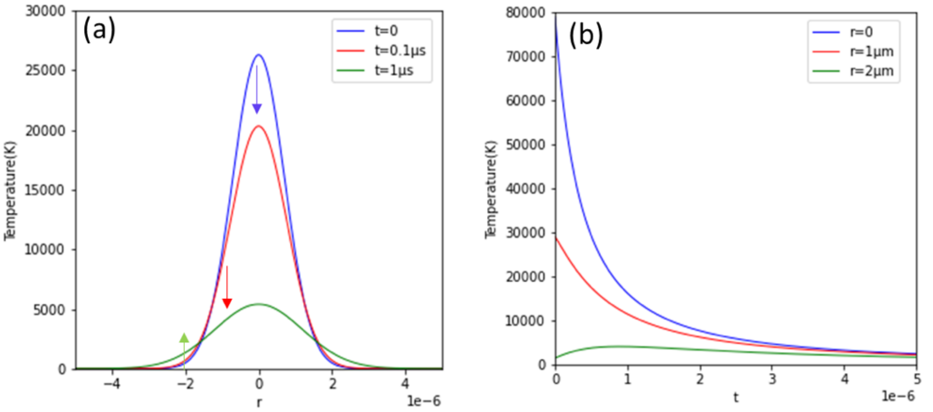

Fig.II.2 Example of the thermal simulation in SiO_2 glass: a) spatial distribution of temperature induced by 1 pulse in the radial direction at time t=0, t=0.1µs, and 1µs. b) temporal evolution of 1 pulse at beam focus center (r=0) and around (r=1µm and r=2µm) material parameters used of SiO_2 glass: absorption coefficient Ep=1µJ, A=0.3, beam width $w=10^{-6}$ m and material parameters: $\rho_{SiO2} = 2500$ kg/m^3, Cp_{sio2}=820 J/(kg.K), $k_{sio2} = 0.96\ W/(m.K)$, so diffusion time 0.534µs. profiles are plotted based on eq.II.16 and 18

The first information that we are interested in from the simulation of 1 pulse, is the maximum temperature of the pulse, i.e. the peak temperature at t=0 and r=0, called $\mathbf{T_{00}}$ which depends on the absorbed laser energy density and on the thermal parameters of the materials, which are the key parameters mentioned above: Ep, w of the laser beam, ρ and C_p of the materials.

Secondly, when considering multi-pulse irradiation, from an example of 2 representative simulation profiles (shown in fig.II.3) of the temperature at beam focus (r=0) caused by the pulses, the temperature at the center of the focal point, where the pulses are received, is not a specific value but an up and down oscillation due to the introduction of one pulse after another. This means that it will have a maximum value T_{max} (when the pulse comes), and a minimum value T_{min} (when the energy has diffused out before the arrival of the next pulse).

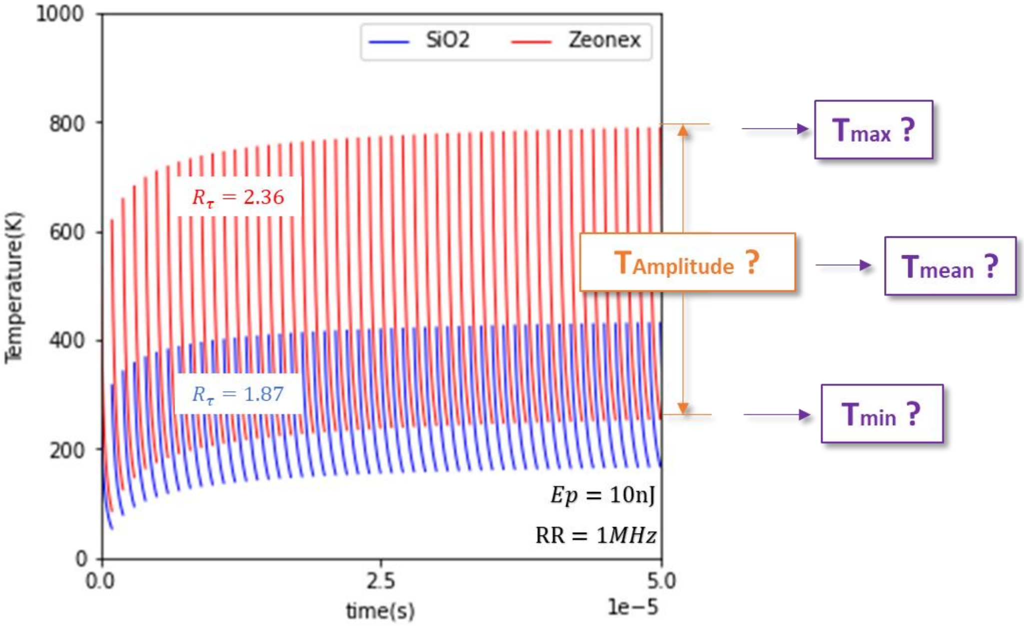

Fig.II.3 An example of temperature evolution over time by multi-pulses in SiO_2 glass and Organic polymer (Zeonex) glass with absorption coefficient A=0.3, beam width w=10^{-6} m and material parameters: $\rho_{\mathrm{SiO2}} = 2500\ kg/m^3$, *$Cp_{sio2}$=820 J/(kg.K),* $\mathrm{k}_{\mathrm{sio2}} = 0.96\ \mathrm{W/(m.K)}$ *and* $\rho_{\mathrm{zeonex}} = 1010\ kg/m^3$, *$Cp_{zeonex}$=1000 J/(kg.K) ,),* $\mathrm{k}_{\mathrm{zeonex}} = 0.597\ \mathrm{W/(m.K)}$

Therefore, since different temperatures may cause different reactions in the material, there are information and answers we want to know:

- From fig.II.3 we can see that as the temperature increases due to the incoming pulses, the temperature rises more rapidly at first, and after a period of time, the temperature increase in the material slows down. We therefore wonder whether the temperature of the material will eventually reach a limit value or it will climb slowly to infinity, as the pulses were continuously absorbed by the material.

- If there is a limitation of temperatures, including $\mathbf{T_{max}}$, $\mathbf{T_{min}}$, the average temperature during 1 pulse period, $\mathbf{T_{mean}}$, as well as the amplitude of temperature oscillation $\mathbf{T_{osc}}$, how large they will be? How and to what extent do the parameters of laser and materials affect them?
- After how long or how many pulses, the increase of these temperatures will be negligible, i.e. a steady state is reached?
- Is it the same situation out of the focus (r≠0)? What is the spatial distribution of these temperatures?

These questions and some others will be answered in this chapter and summarized in the conclusion. In this section, two models might be proposed, based on geometrical assumptions about the focus of laser irradiation, shown in fig.II.4, they are:

1) Spherical geometry, implying that $w_r=w_z$.
2) Cylindrical geometry, implying that $w_r \neq w_z$.

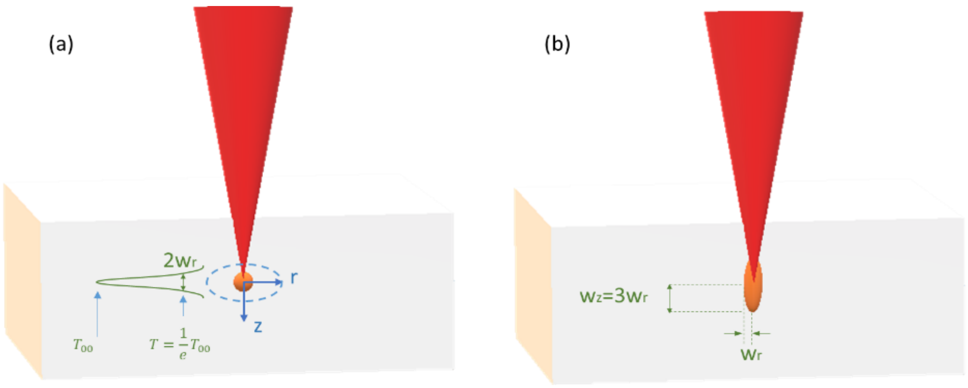

Fig.II.4 a) Spherical geometry model b) Cylindrical geometry model

Nevertheless, although we have also worked on cylindrical geometry, we report finally here, only results of spherical geometry as most of the conclusions are already deduced from this geometry and in a simpler way.

II.2 STARTING FORMULATION

II.2.1 T(r,z,t) of 1 pulse in cylindrical geometry

Firstly, we have the energy density deposition rate, which can also be seen as a deposited power volume density:

$$\frac{\delta\rho_Q}{\delta t}(r,z,t) = dQ_0 \cdot exp\left[\frac{-r^2}{(w_r)^2}\right] \cdot exp\left[\frac{-z^2}{(w_z)^2}\right] \cdot 2\frac{\sqrt{\ln(2)}}{\tau \cdot \sqrt{\pi}} \cdot exp\left[-4\ln(2)\frac{t^2}{\tau^2}\right] \tag{II.5}$$

Here, τ is the pulse duration, (e.g. $\tau = 250fs$ in this thesis work). $\frac{\delta\rho_Q}{\delta t}(0,0,0) = 2\frac{\sqrt{\ln(2)}}{\tau\cdot\sqrt{\pi}} \cdot dQ_0$ is the maximum power volume density, dQ_0 (the maximum deposited energy volume density) is described below:

$$dQ_0 = \frac{A.E_p}{\pi^{\frac{3}{2}}(w_r)^2 w_z} \tag{II.6}$$

Since only a fraction of the incident pulse energy is absorbed by the materials including a partial reflection by the electron plasma, A is mostly the reflectance of the plasma, it is prior unknown but assumed constant in this paper. If considering spherical geometry, eq. (II.6) becomes:

$$dQ_0 = \frac{AE_p}{\pi^{\frac{3}{2}}(w_r)^3} \tag{II.7}$$

To better comprehend the laser source property on space and time, fig.II.5 shows the energy distribution at t=0 in cylindrical geometry and spherical geometry. We can see from fig.II.5 the energy is more spread out in the z-direction, the maximum energy is thus lower in the cylindrical model than in the spherical one.

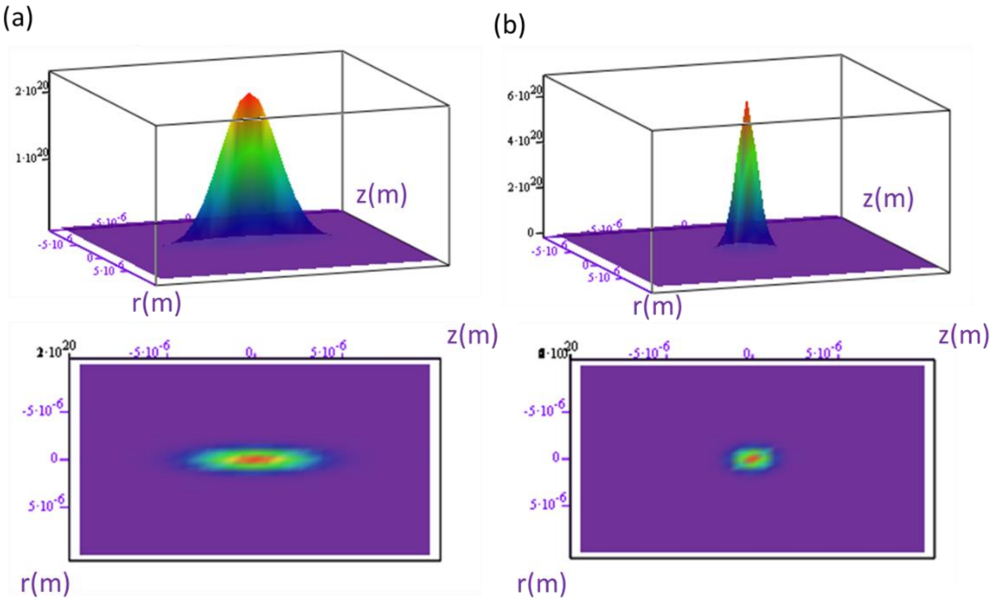

Fig.II.5 the pulse energy deposited into materials at t=0 distributing as (a) Cylindrical geometry model i.e. $\frac{\delta\rho_Q}{\delta t}(r,z,0)$ *(b) Spherical geometry model i.e.* $\frac{\delta\rho_Q}{\delta t}(r,t)$

fig.II.6 shows the temporal evolution of $\frac{\delta\rho_Q}{\delta t}$ at r=z=0, i.e. $\frac{\delta\rho_Q}{\delta t}(0,0,t)$:

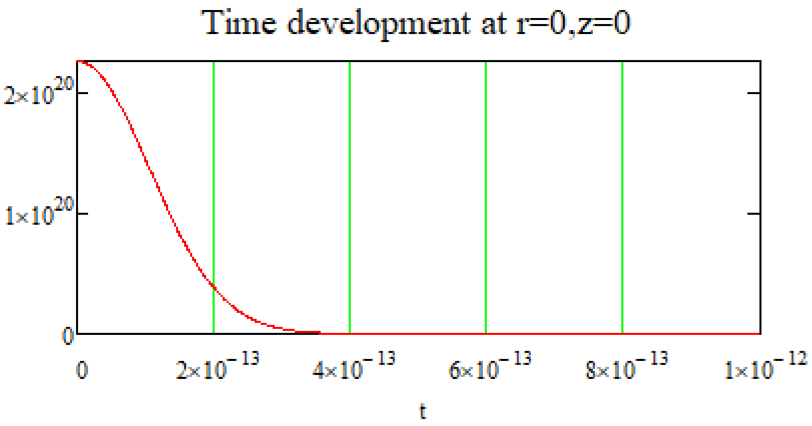

Fig.II.6 the temporal evolution of pulse energy deposited into materials at focus, r=z=0, i.e. $\frac{\delta\rho_Q}{\delta t}(0,0,t)$*, the unit of time is s; and the unit of temperature is K.*

Fig.II.6 shows the pulse duration is much less than the diffusion time, the latter is at the scale of 10^{-7}s and 10^{-6} s (see table.II.7 in the appendix). The diffusion process can be considered therefore to be well separated from the deposition process. We have thus divided the process into two periods, 1) the fs laser pulse deposition period and 2) the diffusion period. During the first period, the light energy is transferred into heat at a scale of ps, before diffusing at the scale of μs.

Once the heat or energy is deposited at a point by the laser, it diffuses into the material, following Fourier's law $\vec{q} = -\bar{\bar{\kappa}}\vec{\nabla}T$. Here $\vec{q}$ is the heat flow (energy per unit area and time). It is considered to be linearly dependent on the temperature gradient. κ is in general a tensor of order 2 which relates the gradient vector of T to the flux. Its dimension is energy (J/m^2. s. K). For glasses, macroscopically anisotropic, one supposes that this tensor is reduced to a scalar.

Using the law of conservation of energy, we obtain:

$$\frac{d\rho_Q}{dt} + \vec{\nabla}.\vec{q} = source\ terms - sink\ terms \qquad (II.8)$$

The $source\ terms$ here is the laser pulse energy written symbolically $\frac{\delta\rho_Q}{\delta t}$ ($\frac{d\rho_Q}{dt}$ is the differential form). We assume that there were no heat annihilation terms (For example endothermic chemical transformation), i.e. $sink\ terms = 0$.

Note that $\frac{d\rho_Q}{dt}$ is the energy density change rate in the diffusion period, distinct from $\frac{\delta\rho_Q}{\delta t}$, which is the energy density change rate delivered by an fs laser pulse. With the definition of specific heat capacity at constant pressure $C_p = \frac{1}{\rho}\frac{d\rho_Q}{dT}$, $\frac{d\rho_Q}{dt} = \rho. C_p. \frac{dT}{dt}$. Substituting Fourier's law, $\vec{\nabla}.\vec{q} = \vec{\nabla}.(-\kappa\vec{\nabla}T)$, with all these parts we obtain the following equation $(II.9)$ from the equation $(II.8)$ which allows us to calculate the evolution of the distribution of T by providing initial and boundary conditions.

$$\frac{dT(r,z,t)}{dt} - D_{th}.\triangle T(r,z,t) = \frac{1}{\rho C_p}\frac{\delta\rho_Q}{\delta t} \qquad (II.9)$$

Here, $D_{th} = \frac{\kappa}{\rho \cdot C_p}$, $\triangle$ is Laplace operator $\triangle = \nabla^2 = \frac{\partial^2}{\partial r^2} + \frac{\partial}{r\partial r} + \frac{\partial^2}{\partial z^2}$.

The 2 periods can be described by two equations.

1) During the pulse, a deposition of energy density takes place, but the diffusion does not have time to begin, so $D_{th} \cdot \triangle T = 0$, equation $(II.9)$ becomes:

$$\frac{dT(r,z,t)}{dt} = \frac{1}{\rho C_p} \frac{\delta \rho_Q}{\delta t} \qquad (II.10)$$

2) after pulse energy deposition, diffusion begins to operate, and the equation $(II.9)$ becomes

$$\frac{dT(r,z,t)}{dt} - D_{th}.\triangle T(r,z,t) = 0 \qquad (II.11)$$

Note that the time in $\frac{dT(r,z,t)}{dt}$ in eq. $(II.10)$ and eq. $(II.11)$ is not in the same range.

In addition, if the beam is scanning e.g. along x, $\frac{dT(x,y,z,t)}{dt} = \frac{\partial T}{\partial t} + \frac{\partial T}{\partial x} \cdot \frac{\partial x}{\partial t} = \frac{\partial T}{\partial t} + \frac{\partial T}{\partial x} \cdot v$ where v is the scanning speed [97]. The additional term $+\frac{\partial T}{\partial x} \cdot v$ is a convective term that can be neglected for the speed experienced in our experiments.

In the pulse deposition step, we set the middle of pulse deposition as t=0, so the pulse stands approximately during time t=–τ to t=τ. Integrate both sides of eq. $(II.10)$ over time, we obtain:

$$T(r,z,0) - T(r,z,-\tau) = \frac{1}{\rho C_p} \int_{pulse} \frac{\delta \rho_Q}{\delta t} dt$$

$$= \frac{dQ_0}{\rho C_p} \cdot exp\left[\frac{-r^2}{(w_r)^2}\right] \cdot exp\left[\frac{-z^2}{(w_z)^2}\right] \cdot \int_{pulse} 2\frac{\sqrt{\ln(2)}}{\tau \cdot \sqrt{\pi}} \cdot exp\left[-4\ln(2)\frac{t^2}{\tau^2}\right] dt$$

Note that $T(r,z,-\tau) = T_a$, T_a is ambient temperature.

$\int_{pulse} 2\frac{\sqrt{\ln(2)}}{\tau \cdot \sqrt{\pi}} \cdot exp\left[-4\ln(2)\frac{t^2}{\tau^2}\right] dt = 1$, so we get:

$$T(r,z,0) = \frac{dQ_0}{\rho C_p} \cdot exp\left[\frac{-r^2}{(w_r)^2}\right] \cdot exp\left[\frac{-z^2}{(w_z)^2}\right] + T_a \qquad (II.12)$$

In the diffusion step, the general form of the solutions of the equation $(II.11)$ is

$$T(r,z,t) = a \cdot \frac{b^2}{\pi \cdot \left(b^2 + 4D_{th} \cdot t\right)} \cdot \frac{c}{\sqrt{\pi \cdot (c^2 + 4D_{th} \cdot t)}} \cdot exp\left[-\left(\frac{r^2}{b^2 + 4D_{th} \cdot t} + \frac{z^2}{c^2 + 4D_{th} \cdot t}\right)\right] + d \qquad (II.13)$$

With boundary t=0, we have:

$$T(r,z,0) = \frac{a}{\pi^{\frac{3}{2}}} \cdot exp\left[-\left(\frac{r^2}{b^2} + \frac{z^2}{c^2}\right)\right] + d \qquad (II.14)$$

comparing with the equation $(II.12)$ the coefficients a, b, c, and d can be determined:

$$a = \pi^{3/2} \cdot \frac{dQ_0}{\rho C_p}, \qquad b = w_r, \qquad c = w_z, \qquad d = T_a$$

Therefore, the evolution of the distribution of T is described below:

$$T(r,z,t) = \frac{dQ_0}{\rho C_p} \cdot \frac{{w_r}^2}{({w_r}^2 + 4D_{th} \cdot t)} \cdot \frac{w_z}{\sqrt{({w_z}^2 + 4D_{th} \cdot t)}} . exp\left[-\left(\frac{r^2}{{w_r}^2 + 4D_{th} \cdot t} + \frac{z^2}{{w_z}^2 + 4D_{th} \cdot t}\right)\right] + T_a \qquad (II.15)$$

For ease of calculation, T_a will be omitted, thus in this chapter, temperature will be understood as the temperature increment above the initial sample temperature. It can thus be rewritten as:

$$T(r,z,t) = T_{00} \cdot \frac{{w_r}^2}{({w_r}^2 + 4D_{th} \cdot t)} \cdot \frac{w_z}{\sqrt{({w_z}^2 + 4D_{th} \cdot t)}} . exp\left[-\left(\frac{r^2}{{w_r}^2 + 4D_{th} \cdot t} + \frac{z^2}{{w_z}^2 + 4D_{th} \cdot t}\right)\right] \qquad (II.16)$$

where

$$T_{00} = \frac{dQ_0}{\rho C_p} = \frac{A \cdot E_p}{\pi^{\frac{3}{2}} \cdot \rho \cdot C_p (w_r)^2 w_z} \qquad (II.17)$$

II.2.2 T(r,z,t) of multi-pulses in cylindrical geometry

In the case of multi-pulses, we obtain the evolution of the temperature distribution considering the linearity of the differential equation and making up the sum of the solution for one pulse but shifted in time. For N pulses, 1st pulse comes at t=0 (n=0), the second pulse comes at t=τ_p (n=1), N$^{\text{th}}$ pulse comes at t=$n \cdot \tau_p$ (n= N-1). τ_p is the pulse period, i.e. 1/f. We thus have $T(r, z, t)$ of multi-pulses described by:

$$T(r,z,t) = T_{00} \sum_{n=0}^{N-1=\text{integer part } (t/\tau_p)} \frac{w_r^2}{w_r^2 + 4D_{th}(t - n \cdot \tau_p)} \frac{w_z}{\sqrt{w_z^2 + 4D_{th}\left(t - n \cdot \tau_p\right)}} \exp\left[-\left(\frac{r^2}{w_r^2 + 4D_{th}\left(t - n \cdot \tau_p\right)} + \frac{z^2}{w_z^2 + 4D_{th}\left(t - n \cdot \tau_p\right)}\right)\right] \qquad (II.18)$$

Or with $D_{th} = \frac{w^2}{4 \cdot \tau_d}$, it is described by:

$$T(r,z,t) = T_{00} \sum_{n=0}^{N-1=\text{integer part } (t/\tau_p)} \frac{1}{1 + \frac{t - n \cdot \tau_p}{\tau_{dr}}} \cdot \frac{1}{\sqrt{1 + \frac{t - n \cdot \tau_p}{\tau_{dz}}}} \cdot exp\left[-\left(\frac{\left(\frac{r}{w_r}\right)^2}{1 + \frac{t - n \cdot \tau_p}{\tau_{dr}}} + \frac{\left(\frac{z}{w_z}\right)^2}{1 + \frac{t - n \cdot \tau_p}{\tau_{dz}}}\right)\right] \qquad (II.19)$$

We note that the only parameters that are involved in the shape of the temperature distribution are the ratio between the period of the pulses τ_p and the diffusion times τ_{dr} and τ_{dz}. The other laser or material parameters are involved in the amplitude (T_{00} ,equation II.17).

Therefore, we introduce the parameter R_τ,

$$R_\tau = \frac{\tau_p}{\tau_d} \qquad (II.20)$$

In the cylindrical model of source and diffusion $w_r \neq w_z$, $\tau_{dz} \neq \tau_{dr}$, $R_{\tau r} = \frac{\tau_p}{\tau_{dr}}$, $R_{\tau z} = \frac{\tau_p}{\tau_{dz}}$. Equation $(II.19)$ is thus rewritten as :

$$T(r_w, z_w, t) = T_{00} \sum_{n=0}^{N-1=\text{integer part } (t/\tau_p)} \frac{1}{1 + \left(\frac{t}{\tau_p} - n\right) \cdot R_{\tau r}} \cdot \frac{1}{\sqrt{1 + \left(\frac{t}{\tau_p} - n\right) \cdot R_{\tau z}}} \cdot exp\left[-\left(\frac{(r_w)^2}{1 + \left(\frac{t}{\tau_p} - n\right) \cdot R_{\tau r}} + \frac{(z_w)^2}{1 + \left(\frac{t}{\tau_p} - n\right) \cdot R_{\tau z}}\right)\right] \qquad (II.21)$$

Here, $r_w = \frac{r}{w_r}$, $z_w = \frac{z}{w_z}$.

There are 3 variables: r_w, z_w and t, so this equation enables us to know the temperature distribution and the evolution of time.

There are also 3 parameters: N , R_τ and τ_p that influence this temperature expression. In the following sections, we will discuss the case when the number of pulses is going to infinity ($N \rightarrow \infty$), and how R_τ and τ_p influence $T(r, z, t)$ in the frame of spherical geometry.

II.3 TEMPERATURE INDUCED BY FS LASER PULSES

II.3.1 General temperature expression T(r$_w$,t)

In spherical geometry, we consider that diffusion properties and beam sizes are the same in all directions, so: $\tau_{dr} = \tau_{dz} = \tau_d$, $w_r = w_z = w$, $R_{\tau r} = R_{\tau z} = R_\tau$. T_{00} is thus $\frac{A \cdot E_p}{\pi^{\frac{3}{2}} \cdot \rho \cdot C_p (w)^3}$.

Therefore, the equation (II.21) becomes:

$$\frac{T(r_w, t)}{T_{00}} = \sum_{n=0}^{N-1=\text{integer part }(\mathrm{t}/\tau_\mathrm{p})} \frac{1}{\left[1 + (\frac{t}{\tau_p} - n). R\tau\right]^{3/2}} . \exp\left[-\frac{(r_w)^2}{1 + (\frac{t}{\tau_p} - n). R\tau}\right] \quad (II.22)$$

N is the pulse number deduced from the time t, $N - 1 = \mathit{integer\ part}\ (t/\tau_p)$.

Warning: T_{00} is independent of variables r_w, t, N, and R_τ, so it will be omitted from all the equations hereafter but note that all the temperatures we deduced should be multiplied by the factor T_{00}.

II.3.2 At the centre r$_w$=0, T(0,t)

In the center of the beam focus, i.e. $r = 0$ and $r_w = 0$, the temperature with N pulses arrived is a function that has one variable and one parameter, time t and R_τ respectively:

$$T(0, t) = \sum_{n=0}^{N-1=\text{integer part }(\mathrm{t}/\tau_\mathrm{p})} \frac{1}{\left[1 + (\frac{t}{\tau_p} - n). R\tau\right]^{3/2}} \quad (II.23)$$

Fig.II.7 demonstrates the behaviors of $T(0, t)$ with different R_τ value under 10 pulses (fig.II.7a), 20 pulses (fig.II.7b), and until 100 pulses (fig.

II.7c). N.B.: the curves are plotted according to the reduced time $N_t = \frac{t}{\tau_p}$, it is the pulse number when N_t is integer. Interestingly, this is a general simulation in which the parameters of the materials as well as the parameters of the laser are aggregated into the parameter R_τ.

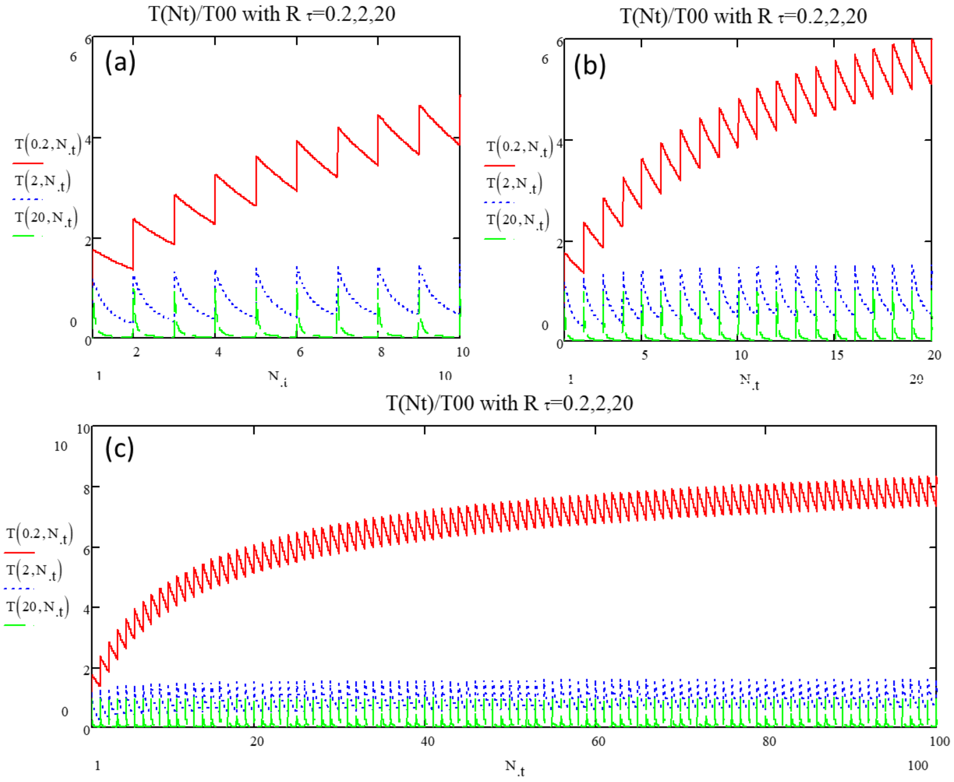

Fig.II.7 *Plot of the reduced temperature (eq.II.23) at the center in spherical geometry according to the reduced pulse number $N_t = \frac{t}{\tau_p}$ with Rτ=0.2, 2, 20 until several maximum pulse number a) 10, b) 20 and c) 100 pulses.*

In fig.II.7 we observe that:
- $T(0, N_t)$ oscillates between a minimum (T_{min}) and a maximum (T_{max}) in each period.
- The oscillation amplitude is the same, whatever R_τ.
- T seems to reach a steady state when N is large.
- The number of pulses to reach this ‘steady state’ appears very small for large R_τ and large for small R_τ. For larger R_τ, the temporal overlapping of consecutive pulse contributions is weaker, whereas there is a larger pulse overlapping when R_τ is small (heat accumulation).

II.3.2.1 T_{osc0}: oscillation amplitude

It is important to know the amplitude of the temperature oscillations (T_{osc}) because when T_{osc} is large, at the beginning of a period, the temperature may be high enough for transformation but in a too short time, and at the end of the period with a longtime duration, the temperature is too low to achieve any transformation. The middle part could be therefore the most active part for a transformation to achieve. Therefore, the value and behavior of T_{osc} give us an idea of whether the temperature change is generally around a certain transition temperature or whether it is increasing/decreasing sharply.

II.3.2.1.1 The limit of T_{osc0}

We observe oscillations of temperature in fig.II.7 due to the occurrence of pulse energy deposition within the period τ_p. Just after the pulse deposition, the temperature experiences a sudden increase and then decreases until the next pulse's arrival. The question here is: how evolves the oscillations on time according to the pulse number N for a given diffusion time? If the period is large (R_τ large), we expect independent pulses and thus the amplitude will be T_{00}. But when the pulse period is small (R_τ small), can we imagine a smaller oscillation? The next calculation gives answers.

We compare the difference between the maximum T and minimum T of the N^{th} pulse, $T_{max}(0,N)$-$T_{min}(0,N)$= $T(0, t_N)$-$T(0, t_{N+1}$-ε), ε is an arbitrary small quantity for ensuring that the number of pulses in the expression II.23 is the same. T_{max} occurs just after the deposition of the N_{th} pulse, so at the beginning of the pulse, t_N =(N-1)τ_p. T_{min} is at the end of the pulse period just before the $(N+1)_{th}$ pulse arrives. Using equation $(II.23)$, we have:

$$T_{max}(0,N) = T\left(0, \mathrm{t} = \mathrm{t_N} \ = (\mathrm{N}-1)\mathrm{\tau_p}\right) = \sum_{n=0}^{N-1} \frac{1}{[1+(N-1-n)\cdot R_\tau\,]^{\frac{3}{2}}}$$
$$= \sum_{n'=0}^{N-1} \frac{1}{[1+n'\cdot R_\tau\,]^{\frac{3}{2}}} \qquad (II.24)$$

While T_{min} will be at t=N·τ_p-ε so not containing the temperature induced by $(N+1)^{th}$ pulse, so :

$$T_{min}(0,N) = T_{min}\left(0,\mathrm{t} = \mathrm{t_{N+1}} - \varepsilon\ = \mathrm{N}\cdot\tau_{\mathrm{p}} - \varepsilon\right) = \sum_{n=0}^{N-1} \frac{1}{[1+(N-n)\cdot R_\tau]^{\frac{3}{2}}} = \sum_{n'=1}^{N} \frac{1}{[1+n'\cdot R_\tau]^{\frac{3}{2}}} \qquad (II.25)$$

Therefore,

$$T_{osc}(0,N) = T_{max}(0,N) - T_{min}(0,N) = 1 - \frac{1}{[1+N\cdot R_\tau]^{\frac{3}{2}}} \qquad (II.26)$$

When N tends to infinity, T_{osc} tends to 1:

$$T_{ocs}(0,\infty) = \lim_{N\to\infty} T_{osc}(0,N) = 1 \qquad (II.27)$$

it is the factor of T_{00} , so **the amplitude of temperature oscillation at r_w=0 will reach a maximum constant value T_{00} after some pulses**. A plot of $T_{osc}(0,N)$ of different $R\tau$ is shown in fig.II.8.

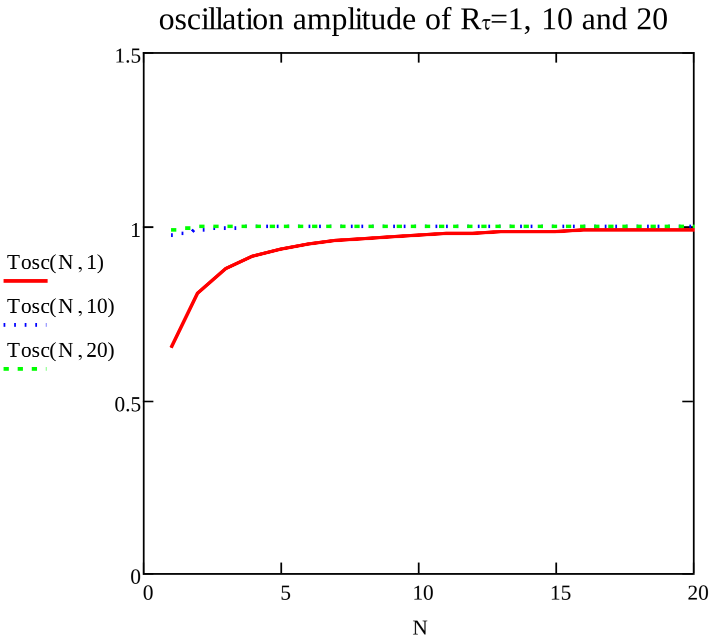

Fig.II.8 temperature oscillation $T_{osc}(0,N)/T_{00}$ (here quoted Tosc(N,R$_\tau$) evolution according to pulses and for 3 values of Rτ_τ.

From eq.(II.26) and fig.II.8, we see that the T oscillation amplitude T_{osc}

reaches a maximum value T_{00} when N goes to infinity. When N is small, it starts with a value smaller than T_{00}, and indeed small R_τ lead to small oscillations at the beginning, but when pulse number N increases, the amplitude increases until T_{00}. If Rτ is large, the amplitude is equal to T_{00} whatever N, as we expected that pulses are separated regardless of the number of pulses.

II.3.2.1.2 The effective number of pulses for reaching the limit of Tosc0: N_{sso}^{0}

The number of pulses N tends to infinity is an ideal situation. In practical, we can calculate a real number of pulses (N_{sso}^{0}) for reaching closely the oscillation limit. In notation N_{sso}^{0}, sso means steady state of oscillation, 0 means the situation when r=0. Let us consider when $T_{osc}(0, N_{sso}^{0}\ ) = (1-\varepsilon)\cdot T_{ocs}(0,\infty)$ is the limit to reach, where ε is a small quantity i.e. a few % that we can be defined based on the actual situation. Thus it is $\frac{|T_{ocs}(0,\infty)-T_{osc}(0,N_{sso}^{0})|}{T_{ocs}(0,\infty)} < \varepsilon$, set $X = \frac{1}{\sqrt{1+N\cdot R_\tau}}$, noted that 0<X<1, it becomes:

$$X^3 < \ \varepsilon$$

This yields:

$$N_{sso}^{0} > \frac{1}{R_\tau}\left[\left(\frac{1}{\varepsilon}\right)^{\frac{2}{3}} - 1\right] \qquad (II.28)$$

Since N_{sso}^{0} is the number of pulses, $N_{sso}^{0} \geq 1$, we take the integer part of its value and add 1. From fig.II.9 we can see, with ε=6%, when Rτ=1, $N_{sso}^{0} = 5.52$, so after 6 pulses the amplitude of the oscillating temperature reaches 0.94T00. When R_τ is large, e.g. R_τ =10, $N_{sso}^{0} =$ 0.552, so only 1 pulse rules the oscillation amplitude. It is easy to understand, because when R_τ=10, the pulses are separated. When R_τ is much smaller, N_{sso}^{o} increases faster, e.g. R_τ=0.1, $N_{sso}^{o} = 56$. Beyond N_{sso}^{o} of pulses, the oscillation amplitude becomes almost constant.

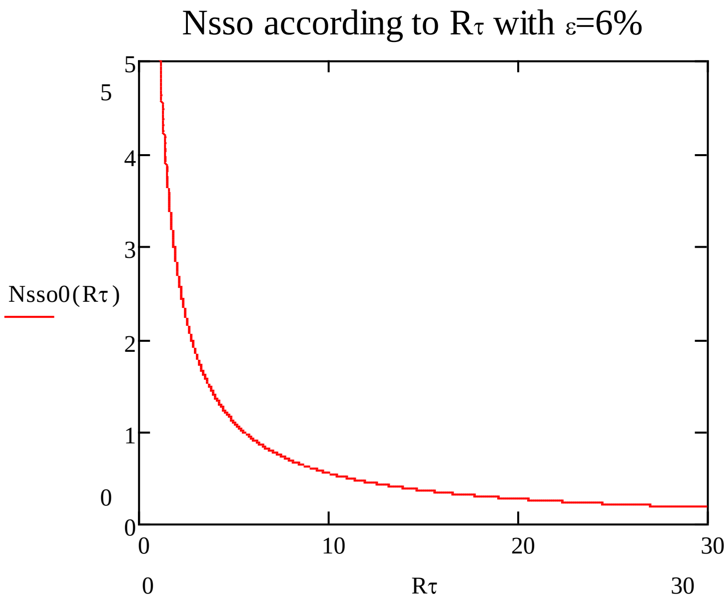

Fig.II.9 number of pulses to reach the oscillation amplitude limit N_{sso}^{0} *according to* $R\tau$*, with* ε*=6%.*

To conclude, from eq $(II.28)$, when ε is fixed, i.e. the definition of limitation is fixed**, the effective number of pulses for reaching the limit of T_{osc0} is inversely proportional to R_τ, i.e. when R_τ is smaller (slow heat diffusion or high pulse repetition rate), the pulses needed for reaching a constant oscillation amplitude is larger.**

II.3.2.2 T_{min} and T_{max}

The next question is the limitation of T_{max} and T_{min} of the oscillating temperature. Does T_{max} have a limitation?

Since the temperature is the sum of the temperature contribution induced by each pulse, as shown in eq. $(II.23)$, we need to know the convergence of this sum when the time or pulse number N increases to infinity.

A condition necessary but not sufficient is that the difference between the temperature just after N+1 pulses and just after N pulses, i.e. when t_N=(N-1) τ_p and t_{N+1}=(N) τ_p was tending to zero. It is:

$$T_{max}(0,\mathrm{t_{N+1}}) - T_{max}(0,\mathrm{t_N}) = \sum_{n=0}^{N} \frac{1}{[1+(N-n).R_\tau\,]^{\frac{3}{2}}} - \sum_{n=0}^{N-1} \frac{1}{[1+(N-1-n).R_\tau]^{\frac{3}{2}}}$$
$$= \frac{1}{[1+N.R_\tau]^{\frac{3}{2}}} \qquad (II.29)$$

Eq. $(II.29)$ is a function of N and R_τ. When R_τ is fixed, it goes to 0 when N tends to infinity. It is the same if we consider the difference of $\mathrm{T_{min}}$.

On the other hand, the sum expression eq. (II.23) can be proved to be convergent by using the p-series test, since the p value here (3/2) is larger than 1 [109].

Therefore, it is demonstrated that **the temperature induced by laser pulses will not go to infinity but to a finite value. This defines a steady state that corresponds to the equilibrium between the energy supplied by the laser and the energy diffusing out of the irradiated voxel.**

II.3.2.2.1 The limit of $\mathrm{T_{min}}$ and $\mathrm{T_{max}}$

II.3.2.2.1.1 Approximation on $\mathrm{T_{min}}$

To calculate the limit of the temperature, we start with the evolution of the minimum temperature on each period as long as N increases to infinity (so, with eq. $(II.25)$, the limit of $\mathrm{T_{min}}(0, \mathrm{t_{N+1}})$ with N tends to infinity).

Here we introduce the approximation derived from the trapezoidal rule for the calculation of integral, which is:

$$\textstyle\sum_{n=0}^{N-1} f(n) \approx \frac{f(0)+f(N-1)}{2} + \int_0^{N-1} f(n)dn \qquad (II.30)$$

Here,

$$f(n) = \frac{1}{[1+(N-n).R\tau]^{\frac{3}{2}}}$$

with an error smaller than $\frac{(N-1)^3}{12N^3} f''(n)$.

Therefore, with this approximation, we get:

$$T_{\min}(0,N) \approx \frac{1}{2(1+R\tau)^{\frac{3}{2}}} + \frac{1}{2(1+N.R\tau)^{\frac{3}{2}}} + \frac{2}{R\tau}\left[\frac{1}{\sqrt{1+R\tau}} - \frac{1}{\sqrt{1+N.R\tau}}\right] \qquad (II.31)$$

Therefore, with the information of the pulse repetition rate and diffusion time of the material, we can

With this analytical expression of $T_{\min}$, fig.II.10 shows the behavior over time or pulses with different $R\tau$:

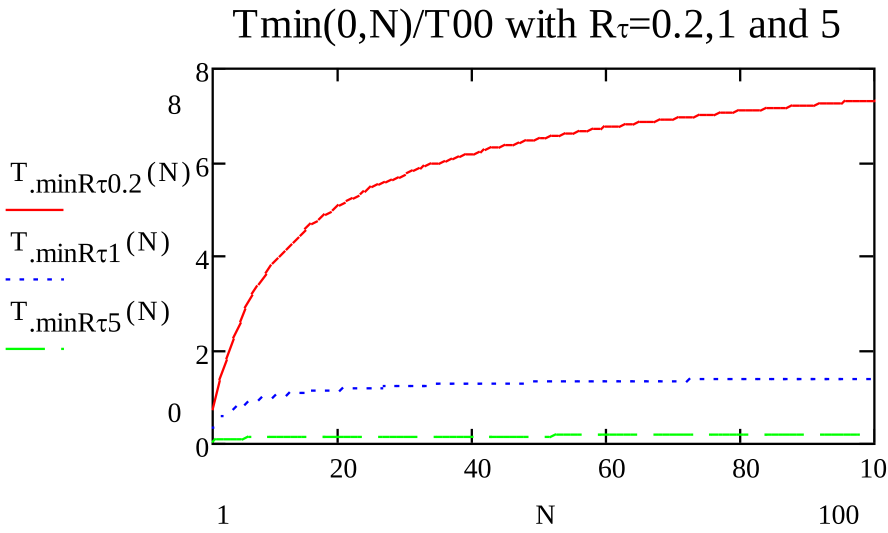

Fig.II.10 $T_{min}(0,N)/T_{00}$ evolution according to N increasing from 1 to 100 when R_τ=0.2,1 and 5

So from eq.II.31, when N goes to infinity, $T_{\min}(0,N)$ tends to:

$$T_{\min}(0,\infty) = \frac{1}{2(1+R\tau)^{\frac{3}{2}}} + \frac{2}{R\tau}\frac{1}{\sqrt{1+R\tau}} \qquad (II.32)$$

II.3.2.2.1.2 The limit of T_{max}

The same method has been applied to obtain the T_{max} limit but with the last term from the sum extracted out (due to the nature of the trapezoidal rule, there is a sharp increment in the temperature of the last pulse, which should not be averaged out):

$$\sum_{n=0}^{N-1} f(n) \approx f(N-1) + \frac{f(0)+f(N-2)}{2} + \int_0^{N-2} f(n)dn \, (II.33)$$

$$f(n) = \frac{1}{[1+(N-1-n).R\tau]^{\frac{3}{2}}}$$

We have thus:

$$T_{\max}(0,N) \approx 1 + \frac{1}{2[1+R\tau]^{3/2}} + \frac{1}{2[1+(N-1)R\tau]^{3/2}} + \frac{2}{R\tau}\left[\frac{1}{\sqrt{[1+R\tau]}} - \frac{1}{\sqrt{1+(N-1)R\tau}}\right] (II.34)$$

$T_{\max}$ can also be obtained by Tmin $(II.31)$+T_{osc}, $(II.26)$, thus:

$$T_{\max}(0,N\,) = 1 + \frac{1}{2[1+R\tau]^{3/2}} - \frac{1}{2[1+\mathrm{N}R\tau]^{3/2}} + \frac{2}{R\tau}\left[\frac{1}{\sqrt{[1+R\tau]}} - \frac{1}{\sqrt{1+NR\tau}}\right] (II.35)$$

No matter eq. $(II.34)$ or eq. $(II.35)$, when N tends to infinity:

$$T_{\max}(0,\infty) = 1 + \frac{1}{2(1+R_\tau)^{3/2}} + \frac{2}{R_\tau}\frac{1}{\sqrt{1+R_\tau}} (II.36)$$

It is easy to see that the difference of $T_{\max}(0,\infty)$ and $T_{\min}(0,\infty)$ is 1, so we don't need to plot this expression. It is also consistent with the oscillation amplitude limitation (eq.II.27) when $N \to \infty$.

When Rτ goes to 0 **(e.g. by increasing pulse frequency or with the material of small thermal conductivity)**, eq. (II.32) and eq. (II.34) approximately proportional to $\frac{2}{R\tau}$:

$$T_{\max}(0,\infty) \sim T_{\min}(0,\infty) \sim T_0 . \frac{2}{R\tau} = \frac{2AE_p}{\pi^{\frac{3}{2}} \cdot \rho \cdot C_p (w)^3 R\tau} = \frac{2AE_p\tau_D}{\pi^{\frac{3}{2}} \cdot \rho \cdot C_p (w)^3 \tau_p} = \frac{2A \cdot E_p f}{\pi^{\frac{3}{2}} D\rho C_p w} =$$

$\frac{2A \cdot P}{\pi^{\frac{3}{2}} \pi \kappa w}$ with P the average power.

We note that the temperature is now dependent on the incident laser power (P) as is the case for the CW laser and inversely dependent on the thermal conductivity (κ) whereas T_{00} was dependent on the incident pulse energy (E_p) and not dependent on the thermal diffusivity but just on the heat capacity. This is due to large time-overlapping pulses when Rτ goes to zero.

This remark allows us to explain the change of maximum temperature. For example, when using the same laser conditions, if we change the chemical compound, Rτ changes. When R_τ is large, the maximum temperature is T_{00}. When Rτ is small, it is much higher than T_{00}. The relative difference between T_{max} and T_{min} becomes small as the difference tends to T_{00}. Fig.II.11a shows this fact: $T_{\min}(0,\infty)/T_{max}(0,\infty)$ tends to 1 for small R_τ like for CW laser (no oscillations).

II.3.2.2.2 Heat accumulation concept

As mentioned in the introduction, we have two heat accumulation definitions proposed here:

1-heat accumulation is defined as the final temperature of the material induced by multiple pulses being ε% increase of that induced by a single pulse. And this ε% can be material related.

2-heat accumulation is defined to be concerned only with the behavior of the temperature, e.g. whether it is linear or non-linear with respect to the diffusivity of the material or the repetition rate of the pulse, i.e. **Rτ**.

For the 1st case,

1) the final temperature induced by multi-pulse has an increase from the temperature induced by one pulse, and this increase is not negligible compared to one pulse-induced temperature. i.e. (T_{max}-T_{00})/ T_{00} > several %. From the above analytical expressions, we know that it is T_{min}/T_{00}> several % (fig.II.11a and b blue dash profile).

2) only the temperature for comparison has been changed, the increase is not negligible compared to the final maximum temperature insead of T_{00}: (T_{max}-T_{00})/ T_{max} > several %, which is equivalent to the ratio of T_{min}/T_{max}. If T_{min} is negligible in front of T_{max}, there is no accumulation, and vice-versa (fig.II.11a and b red profile).

So the criterion can be deduced from T_{min}/T_{00} or T_{min}/T_{max} at the steady state. The two ratios are shown in fig.II.11a and if we defined the boundary between accumulation or not less than 10% (usually the case), there is no difference between these 2 criterions. Fig.II.11b adds three boundary lines at 10%, 6%, and 3% for the heat accumulation, for each case Rτ is around 7, 10, and 15, respectively.

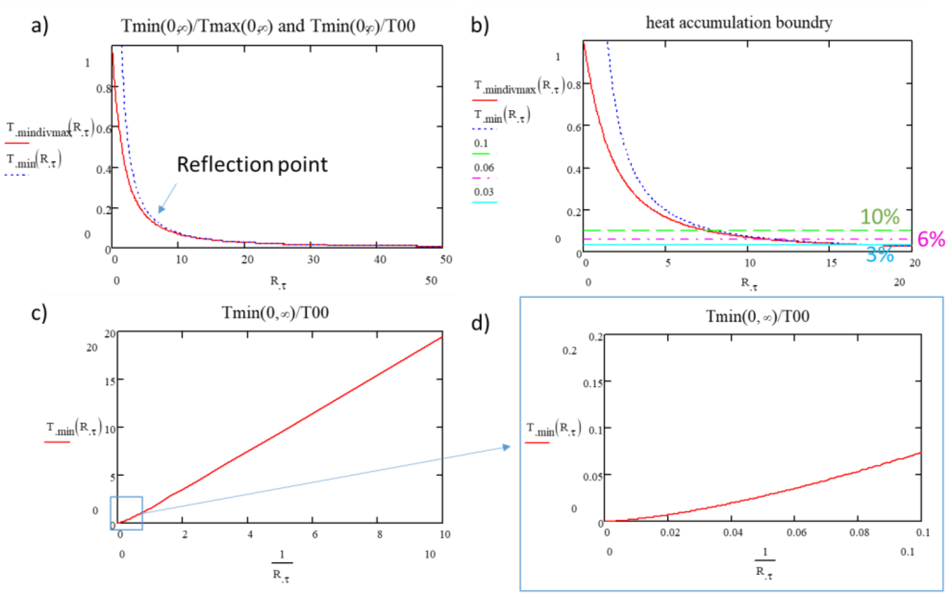

Fig.II.11 a) Plot of $T_{min}(0,\infty)/T_{max}(0,\infty)$ (red) and $T_{min}(0,\infty)/T_{00}$ (blue dash) according to Rτ from 0 to 50. b): Rτ from 0-20 and the boundary value for heat accumulation. From above, we can define correctly the heat accumulation concept. It is due to the time overlapping of consecutive pulses. c) Plot of $T_{min}(0,\infty)/T_{00}$ (red) according to 1/ Rτ from 0-10, and d) 1/ Rτ range from 0 to 0.1

Therefore, the R_τ value determines whether heat accumulation is occurring in the material. If we know the diffusion time of materials, we can deduce the pulse repetition rate required to produce thermal accumulation for each material. Note that since this defined boundary ε is continuously variable, so does this boundary of repetition rate, that we can get is a rough boundary. Some examples are shown in table.II.2 (assume the boundary of heat accumulation in SiO_2 and other organic materials according to $R_\tau = 10$ and 20 respectively, and the thermal parameters of materials can be found in table.II.7 in the appendix).

	SiO2	**glycine**	**Zeonex**	**sucrose**	**nifedipine**
RR>	187kHz	177kHz	118Khz	100kHz	30kHz

Table.II.2 approximated repetition rate needed for heat accumulation in different materials

For the 2^{nd} definition, as we can see from Fig.II.11a and b, the temperature increase shows different behaviors with the decrease of R_τ. We can clearly see from Fig.II.11a that the temperature curve has an 'inflection point': less than this R_τ value, the temperature is inversely proportional to R_τ, in fact that is, proportional to $2/R_\tau$, refering to Fig.II.11c and d. In this definition, whether there is accumulation effect, depends on the temperature behaviour and avoids the setting of a percentage (ε) of temperature increase.

II.3.2.2.3 Validity of the approximate expression

At last, let us check the validity of the approximation that we used above with integral.

For T_{min}, the error is smaller than $\frac{(N-1)^3}{12N^3}f''(n)$ with $f''(n) = \frac{15.R\tau^2}{4[1+(N-n).R\tau]^{7/2}}$ with 0≤n≤N-1 [110, 111] and have to be compared with $T_{\min}(0,\infty) = \frac{1}{2[1+R\tau]^{3/2}} + \frac{2}{R\tau}\frac{1}{\sqrt{1+R\tau}}$. The error is smaller than 1.1% for any value of Rτ, as shown in Fig.II.12a.

For T_{max}, we have an error smaller than $\frac{(N-2)^3}{12(N-1)^3}f''(n)$ with $f''(n) = \frac{15.R\tau^2}{4[1+(N-1-n).R\tau]^{7/2}}$ with 0≤n≤N-2. The error has to be compared with $\frac{T_{\max}(0,\infty)}{T_0} = 1 + \frac{1}{2[1+R\tau]^{3/2}} + \frac{2}{R\tau}\frac{1}{\sqrt{1+R\tau}}$. The error is smaller than 1.7% for any value of Rτ, as shown Fig.II.12b.

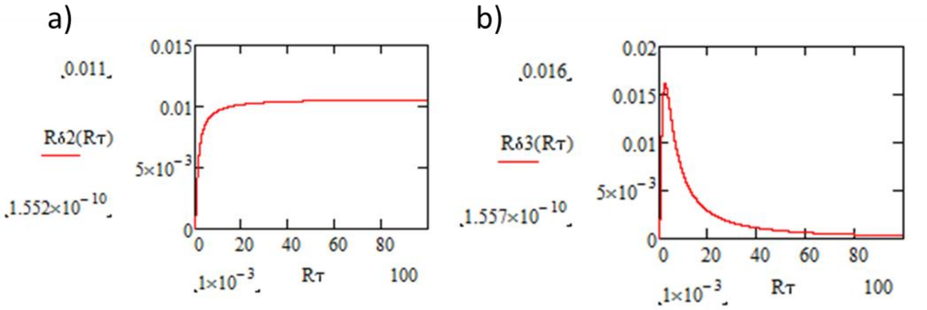

Fig.II.12 the error in using the trapezoidal rule for approximation of computing a)T_{min} and b)T_{max} versus Rτ

II.3.2.2.4 The effective number of pulses for reaching the limit of T_{min} and T_{max}

As the number of pulses increases, the contribution of the 1st pulse to the sum (eq.II.25, n=0 part) is negligible in front of the last one (n=N-1 part). Because the sum is converged to a finite value, we can determine that after how many pulses quoted here N_{ss}^0, a steady state can be considered to be reached, for which $T_{\min}(0,N)$ and $T_{\max}(0,N)$ will almost be no more N dependent.

II.3.2.2.4.1 The effective number of pulses for reaching the limit of T_{min}

The same definition as for N_{sso}, the first approximation of N_{ssmin} is obtained by solving the following assertion, with ε a small quantity:

$$\frac{|T_{\min}(0,N)-T_{\min}(0,\infty)|}{T_{\min}(0,\infty)} < \varepsilon$$

Posing $X = \frac{1}{\sqrt{1+N\cdot R\tau}}$, it reads:

$$\frac{X^3}{2} - \frac{2}{R\tau}X + \varepsilon . T_{\min}(0,\infty) > 0$$

above cubic equation has 3 roots, the interesting case is for N·Rτ>1, so 0<X<1. In this case, there is only one acceptable root, for which we have $X^3/2 \approx 0$, the X root is thus close to:

$$X < \frac{\varepsilon \cdot T_{\min}(0,\infty)}{\frac{2}{R\tau}}$$

Therefore,

$$N_{ssmin}^0 > \frac{1}{R\tau}\left[\left(\frac{2}{R\tau \cdot \varepsilon \cdot T_{min}(0,\infty)}\right)^2 - 1\right] \qquad (II.37)$$

II.3.2.2.4.2 The effective number of pulses for reaching the limit of T_{max}

With the same method, we get:

$$N_{ssmax}^0 > \frac{1}{R\tau}\left[\left(\frac{2}{R\tau \cdot \varepsilon \cdot T_{max}(0,\infty)}\right)^2 - 1\right] \qquad (II.38)$$

To better understand how N_{ss} (including N_{sso}^{0} , N_{ssmin}^{0} and N_{ssmax}^{0}) depends on $R\tau$, i.e. how many pulses are needed for reaching the steady state according to $R\tau$, and to define which N can be used practically, the different functions Nss for reaching T_{osc}, T_{min}, and T_{max} are plotted in fig.II.13 (with $\varepsilon = 0.06$).

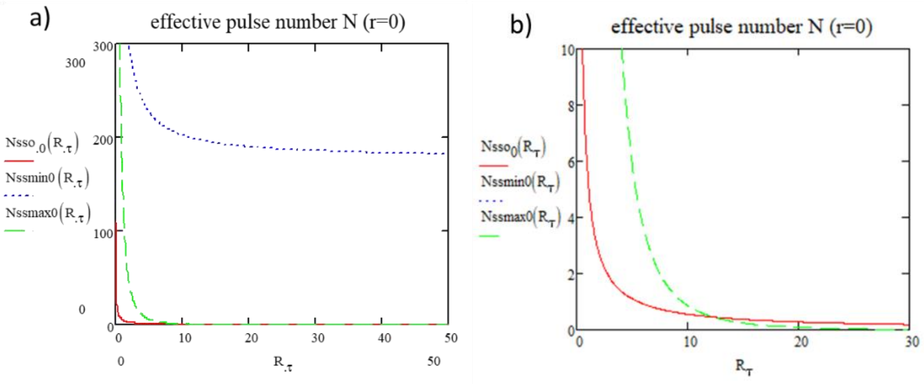

Fig.II.13 a) the effective number to reach the limit of Tosc, Tmin, and Tmax according to Rτ from 0 to 50. b) a zoom of Nsso and Nssmax according to Rτ from 0 to 30

Since the value of Tmin is almost 0 when $R\tau$ is large (no pulse superimposition), it is therefore difficult to achieve a difference of 6%, Nssmin thus is very large. For Nsso and Nssmax, the value converges to 0 when $R\tau$ is large because it can be considered at a steady state when pulses are separated. We can see that in fig.II.13b, there is a cross of Nsso and Nssmax at about $R\tau$ =12, but when $R\tau$ >12, Nsso and Nssmax are smaller than 1 which means steady state is already reached (pulses are separated). Therefore, we choose the larger effective number of pulses, $\boldsymbol{N_{ssmax}^{0}}$ (green dash profiles), as the number of pulses needed to reach the steady state. With this value, together with the laser pulse repetition rate, we know the time needed to reach the steady state.

Some examples of Nss (i.e Nssmax) value are shown in the table.II.3 (with ε=0.03 for organic materials and ε=0.06 for inorganic materials). It is clear that for some inorganic material examples in the table, 200kHz is not enough for heat accumulation. While in most organic materials, 200kHz induces heat accumulation. This is reflected in Rτ value which is <15 and Nss>1.

	SiO_2	**LNS**	**STS**	**glycine**	**Zeonex**	**sucrose**	**nifedipine**
τ_D(μs)	0.28	0.235	0.04	0.28	0.42	4.9	1.63
RR(kHz)	200	200	200	200	200	200	200
$R\tau$	18	21	125	18	12	1	3
Nss	1	1	1	1	3	641	80

Table.II.3 pulse number needed(Nss) for reaching steady state in materials, using eq.II.38

Accordingly, the time for reaching the steady state t_{ss}^0 is:

$$t_{ss}^0 = N_{ss(\max)}^0 \tau_p = \tau_D \left[\left(\frac{2}{R\tau.\varepsilon.T_{max}(0,\infty)} \right)^2 - 1 \right] \qquad (II.39)$$

The numerical plots of it, according to three materials are shown in fig.II.14.

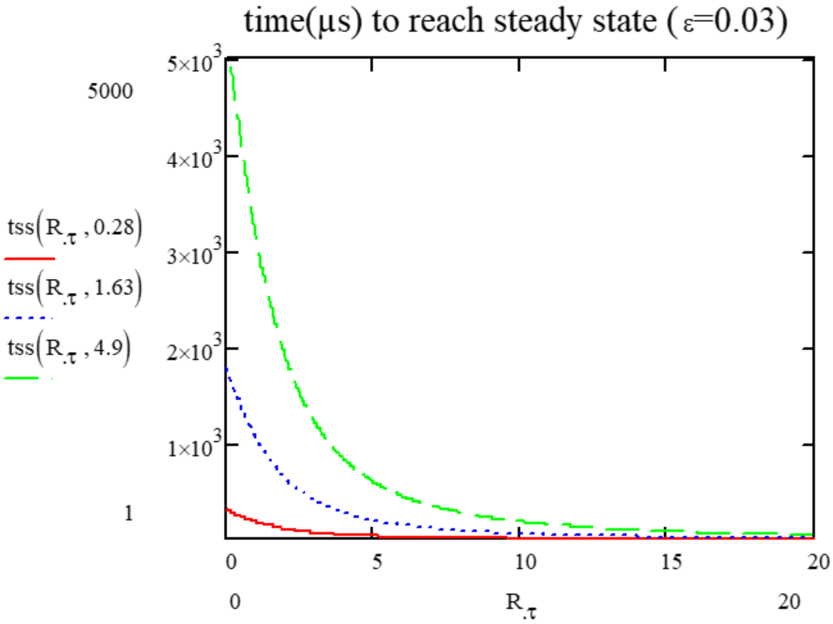

Fig.II.14 the time to reach the steady state according to Rτ for glycine(red), nifedipine (blue dash), and sucrose (green).

For Rτ small enough, the time reaches the value τ_D/ε^2 i.e. $1111\tau_D$ for ε=3%. For Zeonex glass and glycine crystal cited above with τ_D=0.28μs, and 0.42μs, this time is smaller than 1ms (e.g. red profile). But for sucrose and nifedipine, this time is 5.5ms and 1.8ms, respectively.

For Rτ large enough, This time becomes smaller when Rτ increases.

Therefore, in this thesis work, the time for reaching the steady state is always smaller than the irradiation time (2w/scanning speed) if the scanning speed is not too large (e.g. smaller than 360µm/s, estimated by the longest time in sucrose).

II.3.2.3 T_{mean}: The averaged temperature in the period

For many transformations induced by laser irradiation, fictive temperature, crystallization, erasure of previously induced structure, stress relaxation, and so on, the large temperatures occurring within a pulse period is so brief that the system has no time to significantly respond. On the contrary, for smaller temperatures occurring at the end of the period, the relaxation time is large and the system has time for responding only if temperatures are not too small (this is the case for overlapping pulses, Rτ<10). Therefore, the system responds efficiently only for intermediate temperatures in the main part of the period. On the other hand, when the pulse frequency is large, temperature oscillations are relatively small and the average value can be a guide for following the T distribution in space and its evolution. Hence, this section is devoted to finding simple expressions of average T in the function of material and laser parameters.

To be more specific, the basic underlying assumption is of the existence of a thermally activated reaction $\mathrm{A} \xrightarrow{\mathrm{k(E,T)}} \mathrm{B}$ where A is an inexhaustible matter by assumption, with a rate constant following the Arrhenius law $k(E,T) = k_0 exp\left(-\frac{E}{k_B T}\right)$ with activation energy E and T the temperature. Thus the B rate is $\frac{d[B]}{dt} = k(E,T)[A]$ and then $[B] = [A]\int_0^t k(E,T(0,t'))\,dt' = [A]\int_0^t k_0 exp\left(-\frac{E}{k_B T(0,t')}\right)dt'$. For answering to the question that which part of the period is efficient, we can plot $[B]/[A]k_0$ on a period. In the same time, a plot of the same quantity with T_{mean} shows if the mean temperature is the most adapted for managing the process. On the other hand, the plot of $[B]/[A]k_0$ versus RR show that the efficiency is always larger at low RR (Rτ large) because the activation at high temperature is efficient. However, this predominance at low RR can be decreased when the activation energy is smaller. More details are given in II.5.5.

II.3.2.3.1 General expression

We define the averaging by $\bar{T}(r,z,N) = \frac{1}{\tau_p}\int_{\substack{pulse\ period\\ at\ N}} T(r,z,t)\,dt$, this gives:

$$\bar{T}(r,z,N) = \frac{1}{\tau_p}\int\limits_{\substack{pulse\ period\\ at\ N}} T(r,z,t)\,dt \qquad (II.40)$$

II.3.2.3.2 The limit of Tmean

At the center (r=0),

$$\bar{T}(0,N) = \frac{1}{\tau_p}\int_{\frac{t}{\tau_p}=N-1}^{\frac{t}{\tau_p}=N}\sum_{n=0}^{N-1}\frac{1}{\left[1+(\frac{t}{\tau_p}-n).R\tau\right]^{3/2}}dt$$

The two summations can be permuted as they do not operate on the same variables and are independent. We get:

$$\begin{aligned}\bar{T}(0,N) &= \frac{1}{\tau_p}\sum_{n=0}^{N-1}\int_{\frac{t}{\tau_p}=N-1}^{\frac{t}{\tau_p}=N}\frac{1}{\left[1+(\frac{t}{\tau_p}-n).R\tau\right]^{3/2}}dt\\ &= \frac{1}{R\tau}\sum_{n=0}^{N-1}\left[-\frac{2}{\left[1+(\frac{t}{\tau_p}-n).R\tau\right]^{1/2}}\right]_{\frac{t}{\tau_p}=N-1}^{\frac{t}{\tau_p}=N} =\\ &= \frac{2}{R\tau}\left(1-\frac{1}{\sqrt{1+N.R\tau}}\right) \qquad (II.41)\end{aligned}$$

Result obtained without approximation. Then:

$$\lim_{N\to\infty}\bar{T}(0,N) = \frac{2}{R\tau} \qquad (II.42)$$

We note that here, the steady state temperature at the center will reach

$$\frac{\boldsymbol{2\cdot T_{00}}}{\boldsymbol{R\tau}} = \frac{\boldsymbol{2A\cdot P}}{\boldsymbol{\pi^{\frac{3}{2}}\pi\kappa w}} \qquad (II.43)$$

It is the same expression as for T$_{\mathrm{max}}$ or T$_{\mathrm{min}}$ for small Rτ. We can note that in fig.II.15 as the T$_{\mathrm{max}}$ and T$_{\mathrm{min}}$ profiles approach T$_{\mathrm{mean}}$ for small Rτ.

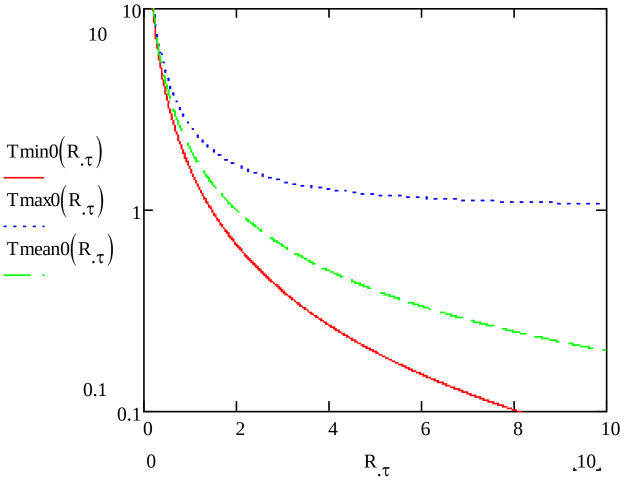

Fig.II.15 the T$_{min}$ (red), T$_{max}$ (blue dash), and T$_{mean}$ (green dash) plot according to Rτ.

II.3.2.3.3 The effective number of pulses for reaching the limit of T$_{\mathrm{mean}}$

With the same definition of the number of pulses to reach this limit, we have $\frac{|\bar{T}(0,\infty)-\bar{T}(0,N)|}{\bar{T}(0,\infty)} < \varepsilon$, N_{ssm}^{0} is obtained:

$$\mathrm{N}_{ssm}^{0} > \frac{1}{R\tau}\left[\left(\frac{1}{\varepsilon}\right)^{2} - 1\right] \qquad (II.44)$$

Therefore, the time for reaching the steady state is constant: $\tau_D\left[\left(\frac{1}{\varepsilon}\right)^{2} - 1\right] \approx \frac{\tau_D}{\varepsilon^2}$ $=1111\tau_D$ when $\varepsilon = 0.03$, which is the same as the maximum t$_{\mathrm{ss}}$ for reaching a steady state when $R\tau \to 0$ (fig.II.14). We thus again prove that when $R\tau$ is small, it is like the case of CW laser with $T_{\mathrm{min}} = T_{\mathrm{max}} = T_{\mathrm{mean}}$, and $\mathrm{N}_{ssmin}^{0} = \mathrm{N}_{ssmax}^{0} = \mathrm{N}_{ssm}^{0}$ as displayed in fig.II.16.

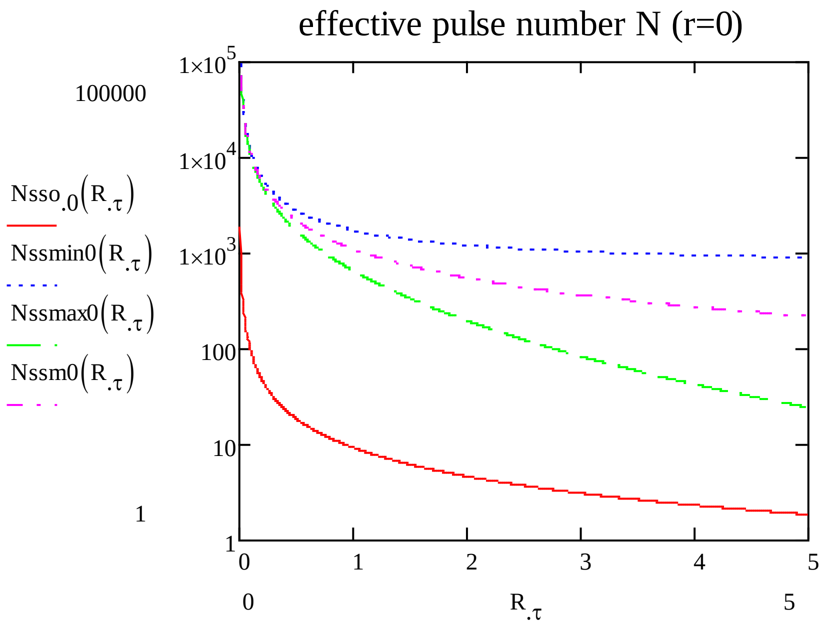

Fig.II.16 the effective number of pulses to reach the limit of Tosc (red), Tmin (blue dash), Tmax (green dash), and Tmean (pink dash) according to $R\tau$ from 0 to 5

With these analytical expressions of temperature at the steady state at the center of focus ($T_{\text{osc}}, T_{\text{min}}, T_{\text{max}}, T_{\text{mean}}$), and the needed number of pulses ($\mathrm{N}_{sso}^{0}, \mathrm{N}_{ssmin}^{0}, \mathrm{N}_{ssmax}^{0}, \mathrm{N}_{ssm}^{0}$), we have a clear view of how parameter $R\tau$ influences the amplitude of the thermal distribution. The next problem is to extend these to any place out of the center.

II.3.3 Out of center r≠0, T(r,t)

When r≠0, we come back to the expression eq. (II.22):

$$T(r,t) = \sum_{n=0}^{N-1=integer\ part\ (\frac{t}{\tau_p})} \frac{1}{\left[1+\left(\frac{t}{\tau_p}-n\right).R\tau\right]^{\frac{3}{2}}}.\exp\left[-\frac{(r_w)^2}{1+\left(\frac{t}{\tau_p}-n\right).R\tau}\right] \quad (II.22)$$

Fig.II.17 shows the temperature evolution over time for two radius r_w=1 (a and b) and r_w=2 (c and d):

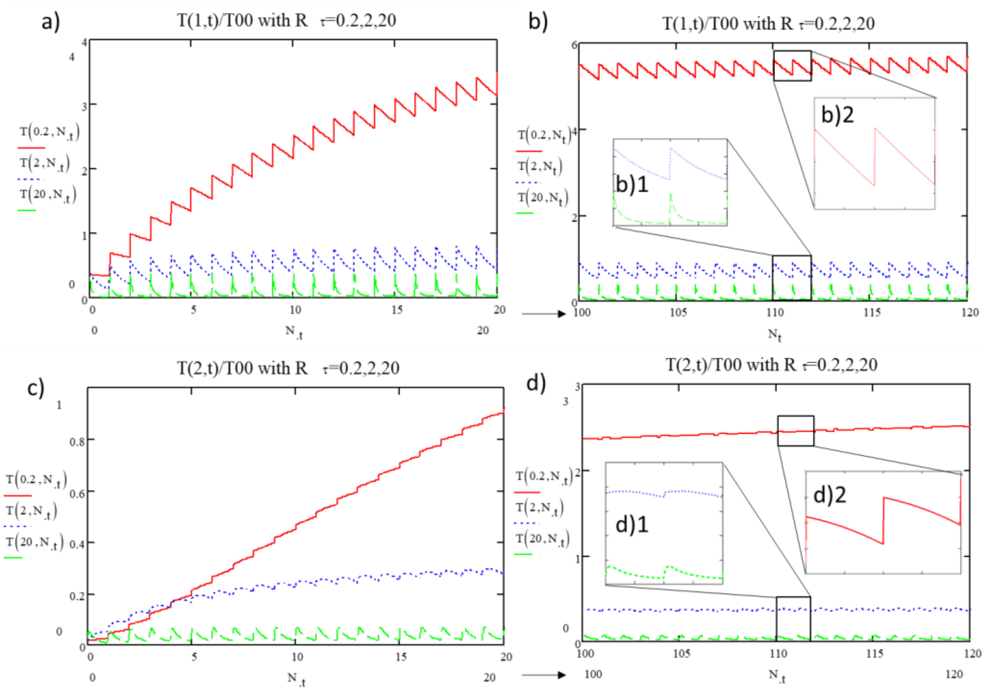

Fig.II.17: Plot of the reduced temperature (T/T_{00}) with $R\tau$=0.2, 2, 20 at a)-b) r=w_r from a) pulse 1 to pulse 20 and b) pulse 100 to pulse 120. Insert b) 1: zoom of pulse 110-112 of R_τ =2 and 20. Insert b) 2: zoom of pulse 110-112 of R_τ =0.2. c)-d) r=2w_r from c) pulse 1 to pulse 20 and d) pulse 100 to pulse 120. Insert d) 1: zoom of pulse 110-112 of R_τ =2 and 20. Insert d) 2: zoom of pulse 110-112 of R_τ =0.2.

We observe the differences between them and r=0:

- The amplitude of oscillation is less than 1 (in the unit of T_{00}). The oscillation at r_w=2 is smaller than the one at r_w=1.
- The maximum temperature is still at the beginning of the deposition of pulses at r_w=1 with these three $R\tau$, while at r_w=2 the maximum temperature is no more at the beginning.

II.3.3.1 T_{osc}, T_{min}, and T_{max}

Same as the case r=0, in general r, we compare the difference between the maximum T and minimum T of the Nth pulse to obtain the oscillation amplitude T^r_{osc}. T_{min} is considered still at the end of the Nth pulse, i.e. when t=N.τ_p without the (N+1)th pulse:

$$T_{min}(r_w, N) = \sum_{n=0}^{N-1} \frac{1}{[1+(N-n).R\tau]^{3/2}} \exp\left[-\frac{(r_w)^2}{1+(N-n).R\tau}\right] (II.45)$$

While T_{max} in some situations will be in the middle of the pulse period, we thus set x_m, $0 \leq x_m \leq 1$ to define the place where the T_{max} is. Therefore, T_{max} is at $t=(N-1+x_m).\tau_p$:

$$T_{max}(r_w, N) = \sum_{n=0}^{N-1} \frac{1}{[1+(N-1+x_m-n).R\tau]^{3/2}} \exp\left[-\frac{(r_w)^2}{1+(N-1+x_m-n).R\tau}\right] \quad (II.46)$$

This expression can be the **general expression** to describe both T_{max} and T_{min}, while T_{min} appearing at the end of the period means x_m=1, as well as when r_w=0, T_{max} appears at the beginning of the period with x_m=0.

To find the place of the maximum in the period, we searched for the root x_m of the derivative of eq.(II.46). Since the derivative of eq.(II.46) is also a sum (the derivative of a summation is a sum of the derivative of every part of it), trapezoidal rule is applied for the approximation, we get the root x_m as a function of Rτ and r_w and N, but to know only the final situation, and also for mathematically solvability, x_m is described as eq.II.47 when N tends to infinity. The x_m values according to Rτ, r_w are plotted in fig.II.18.

$$x_m = \frac{\sqrt{R\tau}.\sqrt{9R\tau + 32(r_w)^2} - 3R\tau - 8}{8R\tau} \quad (II.47)$$

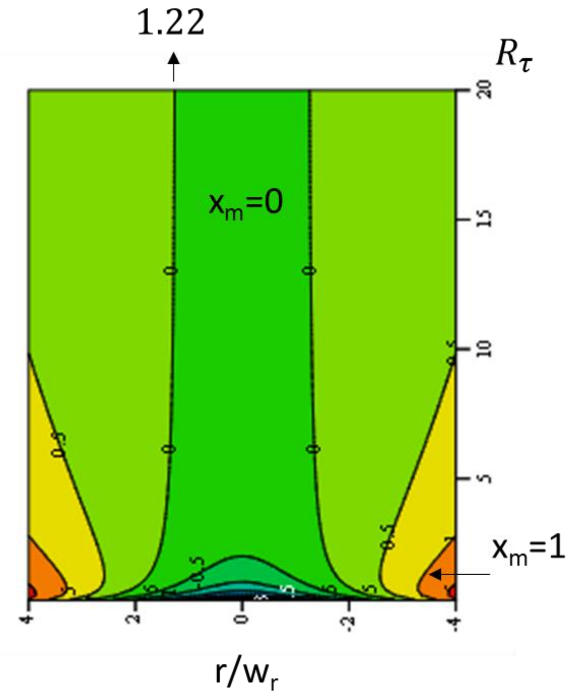

Fig.II.18 2D map of the solution x_m according to $R\tau$ and the reduced radius (r/w)

The boundary between dark green and green is $x_m = 0$, it means, in this parameter region (r$_w$, $R\tau$), the maximum of the pulse is at the beginning of the period. Note that the boundary between yellow-green and orange, is the boundary of $x_m = 1$, thus with the parameters in the orange region and red region, $x_m = 1$. Therefore, the thermal expressions will be divided into two situations:

1) $x_m = 0$, i.e. r$_w$ < $\sqrt{\frac{3}{2}+\frac{2}{R\tau}}$ or $R\tau$ is small enough (less than $\frac{2}{\mathrm{r}_w{}^2-1.5}$ when $\mathrm{r}_w{}^2 > 1.5$). In this situation, x_m can be omitted from the expressions.
2) $x_m \neq 0$, i.e. r$_w$ > $\sqrt{\frac{3}{2}+\frac{2}{R\tau}}$ or $R\tau > \frac{2}{\mathrm{r}_w{}^2-1.5}$ when $\mathrm{r}_w{}^2 > 1.5$, x_m will stay in the temperature expressions.

In fact, in order to further simplify the expression, we are looking for the condition in situation 2 that x_m can be still set to 0. Since x_m only influence the value of Tmax, and thus the Tosc, we analyze T$_{max}$ by its exact summation expression with x_m in it and the one without x_m. Fig.II.19 displays the spatial distribution of T$_{max}$ with x_m in the expression (red, eq.II.46 and eq.II.47) and the approximated one with $x_m = 0$ (blue dash, eq.II.46 with $x_m = 0$).

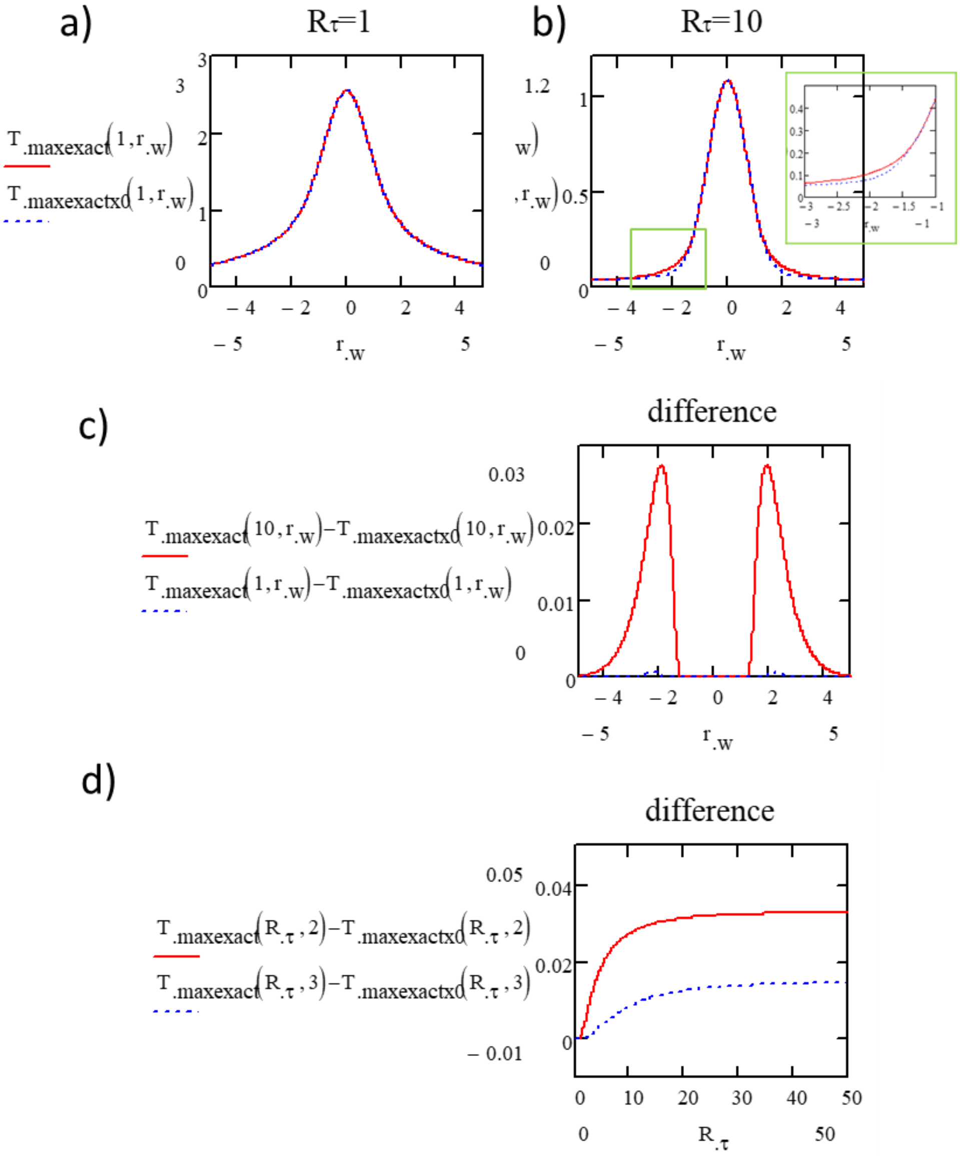

Fig.II.19 a) - b) spatial distribution of T_{max} with real expression (x_m is a function of $R\tau, r_w$) and reduce expression ($x_m = 0$). a) $R\tau = 1$ b) $R\tau = 10$ c) the difference between the 2 expressions according to r_w d) the difference between these 2 expressions according to $R\tau$.

We can see from fig.II.19a that when $R\tau = 1$, the 2 expressions have no obvious difference, i.e. even $x_m \neq 0$, the approximation by omitting x_m

in the expression is feasible. While when $R\tau = 10$ (fig.II.19b), there is a difference appearing at the place around $\mathrm{r}_w = 2$, marked by a green rectangle and zoomed. The difference is emphasized in fig.II.19c. The maximum of the difference is around $\mathrm{r}_w = 2$ and the value is smaller than 0.03 when $R\tau = 10$. However, it is not a negligible value if T_{0r} (maximum temperature induced by 1 pulse at r) is large. In addition, as $R\tau$ increases (from 1 to 10), we see that the difference emerges due to x_m, so we want to know how $R\tau$ influences this difference. Fig.II.19d shows the difference develops according to $R\tau$, so that $R\tau = 10$ is not yet the highest difference, the difference keeps increasing above 0.03 when $R\tau$ increases, however, there is a limit of it which is less than 0.04.

Therefore, using the expressions of situation 1 to approximately simulate situation 2, i.e. always **x_m=0 is feasible** practically, only to have lower Tmax and smaller Tocs at around r_w=2, the error will be less than 0.04 T_{00}. Why the largest different is at r_w=2? One reason is that when r_w is small enough, x_m is 0 as it is; while when r_w is very large, the temperature is quickly decreasing, not to mention the case when $R\tau$ is large, therefore r_w=2 is a kind of intermediate value that it is not small enough to cross the x=0 boundary, and not so far away to have low temperature.

II.3.3.1.1 The limit of T_{min}, T_{max}, and T_{osc}

For calculating the amplitude of temperature T_{osc} at r>0, due to the presence of x_m, the parts in the summation of T_{max} at this point can no longer be eliminated with the parts of T_{min} like in eq.II.26, except in situation 1. We therefore give the analytical expression for situation 1 first, and the general expression will be presented after having given the expressions for T_{min} and T_{max}.

when x_m=0, the limit of T_{osc} is described as:

$$\boxed{\begin{aligned} T_{osc}(r,N) &= T_{max}(r,N) - T_{min}(r,N) \\ &= \exp[-(r_w)^2] - \frac{\exp\left[-\dfrac{(r_w)^2}{1+N.R\tau}\right]}{(1+N.R\tau)^{\frac{3}{2}}} \xrightarrow[N\to\infty]{} \mathbf{exp}\left[-(\boldsymbol{r_w})^{\mathbf{2}}\right] \; (II.48) \end{aligned}}$$

The amplitude of the oscillations at r_w>0 is no more reaching a constant value T_{00} but $\mathbf{T_{00}.\exp[-(r_w)^2]}$. It is consistent with our observations in fig.II.17, e.g. the amplitudes are 0.368T_{00} and 0.018T_{00} at $r_w = 1$ and $r_w = 2$, respectively.

For T_{min} and T_{max}, using the trapezoidal rule for approximation as for $r_w \neq 0$, we have T_{min} from eq.II.45:

$$T_{\min}(r_w, N) \approx \frac{1}{2}\left[\frac{\exp\left[-\frac{(r_w)^2}{1+R\tau}\right]}{(1+R\tau)^{3/2}} + \frac{\exp\left[-\frac{(r_w)^2}{1+N.R\tau}\right]}{(1+N.R\tau)^{3/2}}\right] + \frac{\sqrt{\pi}}{R\tau.r_w}\left[erf\left(\frac{r_w}{\sqrt{1+R\tau}}\right) - erf\left(\frac{r_w}{\sqrt{1+N.R\tau}}\right)\right]$$

$$\boxed{\xrightarrow[N\to\infty]{} \frac{\exp\left[-\frac{(r_w)^2}{1+R\tau}\right]}{2(1+R\tau)^{3/2}} + \frac{\sqrt{\pi}}{R\tau.r_w} erf\left(\frac{r_w}{\sqrt{1+R\tau}}\right) \qquad (II.49)}$$

We call $\frac{\exp\left[-\frac{(r_w)^2}{1+R\tau}\right]}{2(1+R\tau)^{3/2}}$ part 1, and $\frac{\sqrt{\pi}}{R\tau.r_w} erf\left(\frac{r_w}{\sqrt{1+R\tau}}\right)$ part 2.

And T_{max} from eq.II.46:

$$T_{\max}(r_w, N, x_m) \approx \frac{\exp\left[-\frac{(r_w)^2}{1+x_m.R\tau}\right]}{[1+x_m.R\tau]^{\frac{3}{2}}} + \frac{\exp\left[-\frac{(r_w)^2}{1+(1+x_m).R\tau}\right]}{2[1+(1+x_m).R\tau]^{\frac{3}{2}}} + \frac{\exp\left[-\frac{(r_w)^2}{1+(N-1+x_m).R\tau}\right]}{2[1+(N-1+x_m).R\tau]^{\frac{3}{2}}} + \frac{\sqrt{\pi}}{R\tau.r_w}\left\{erf\left[\frac{r_w}{\sqrt{[1+(1+x_m).R\tau]}}\right] - erf\left[\frac{r_w}{\sqrt{[1+(N-1+x_m).R\tau]}}\right]\right\}$$

$$\boxed{\xrightarrow[N\to\infty]{} \frac{\exp\left[-\frac{(r_w)^2}{1+x_m.R\tau}\right]}{[1+x_m.R\tau]^{3/2}} + \frac{\exp\left[-\frac{(r_w)^2}{1+(1+x_m).R\tau}\right]}{2[1+(1+x_m).R\tau]^{3/2}} + \frac{\sqrt{\pi}}{R\tau.r_w}\left\{erf\left[\frac{r_w}{\sqrt{[1+(1+x_m).R\tau]}}\right]\right\} \qquad (II.50)}$$

With $\frac{\exp\left[-\frac{(r_w)^2}{1+x_m.R\tau}\right]}{[1+x_m.R\tau]^{3/2}}$, $\frac{\exp\left[-\frac{(r_w)^2}{1+(1+x_m).R\tau}\right]}{2[1+(1+x_m).R\tau]^{3/2}}$, $\frac{\sqrt{\pi}}{R\tau.r_w}\left\{erf\left[\frac{r_w}{\sqrt{[1+(1+x_m).R\tau]}}\right]\right\}$ called part 1, 2, and 3 respectively.

Note that part 1 in eq.II.49 and part 2 in eq.II.50 are smaller than the other parts, so they can be approximately omitted to simplify the expressions.

By now, with these temperature expressions, we obtain the spatial distribution of the minimum temperature and maximum temperature for a given $R\tau$, shown in fig.II.20. The temperature is oscillating between these 2 temperature profiles.

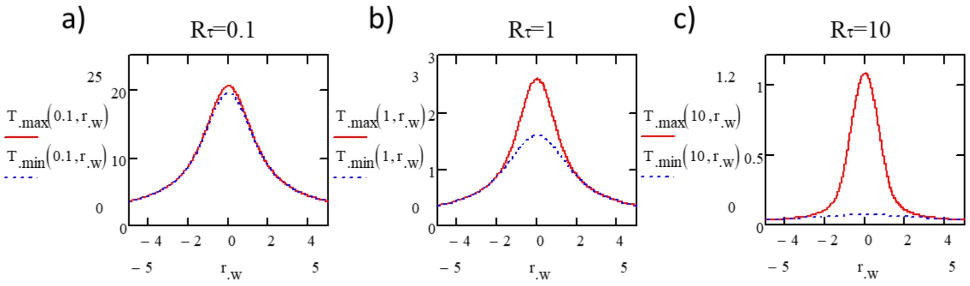

Fig.II.20. Spatial distribution of Tmin (blue dash, by eq.II.49) and Tmax (red, by eq.II.50 and eq.II.47) according to the reduced radius (r/w) when a) $R\tau = 0.1$, b) $R\tau = 1$ and c) $R\tau = 10$

From fig.II.20, we can see that when $R\tau$ is small, T_{min} and T_{max} have no big difference compared to their values, note that at r_w=0 the difference is always 1 whatever $R\tau$. We also note that when r_w>2, the difference between Tmin and Tmax is not obvious. What about with the other r_w and $R\tau$? Plots of Tosc according to r_w and $R\tau$ give the answers, shown in fig.II.21.

The general expression of T_{osc} (when N tends to infinity or larger than the effective number) is given as eq.II.50 minus eq.II.49, it reads:

$$T_{osc}(R\tau, r_w) = \frac{\exp\left[-\frac{(r_w)^2}{1+x_m.R\tau}\right]}{[1+x_m.R\tau]^{3/2}} + \frac{\exp\left[-\frac{(r_w)^2}{1+(1+x_m).R\tau}\right]}{2[1+(1+x_m).R\tau]^{3/2}} + \frac{\sqrt{\pi}}{R\tau.r_w}\left\{erf\left[\frac{r_w}{\sqrt{[1+(1+x_m).R\tau]}}\right]\right\} - \frac{\exp\left[-\frac{(r_w)^2}{1+R\tau}\right]}{2(1+R\tau)^{\frac{3}{2}}} - \frac{\sqrt{\pi}}{R\tau.r_w} erf\left(\frac{r_w}{\sqrt{1+R\tau}}\right)$$

Omitting $\frac{\exp\left[-\frac{(r_w)^2}{1+(1+x_m).R\tau}\right]}{2[1+(1+x_m).R\tau]^{3/2}}$ and $\frac{\exp\left[-\frac{(r_w)^2}{1+R\tau}\right]}{2(1+R\tau)^{3/2}}$,

$$T_{osc}(R\tau, r_w) \approx \frac{\exp\left[-\frac{(r_w)^2}{1+x_m.R\tau}\right]}{[1+x_m.R\tau]^{3/2}} + \frac{\sqrt{\pi}}{R\tau.r_w}\left\{erf\left[\frac{r_w}{\sqrt{[1+(1+x_m).R\tau]}}\right]\right\} - \frac{\sqrt{\pi}}{R\tau.r_w} erf\left(\frac{r_w}{\sqrt{1+R\tau}}\right) \quad (II.51)$$

Plots in fig.II.21a are T_{osc} according to r_w at $R\tau$ =0.1,1 and 10, accompanied with $\exp[-(r_w)^2]$ (the situation 1, eq.II.48) for comparison, the difference distribution is shown in fig.II.21(b). It is the same as the difference of Tmax as it is in fig.II.21c. It is also plotted according to $R\tau$, with r_w=2 and 3, accompanied with $\exp[-(2)^2]$ and $\exp[-(3)^2]$.

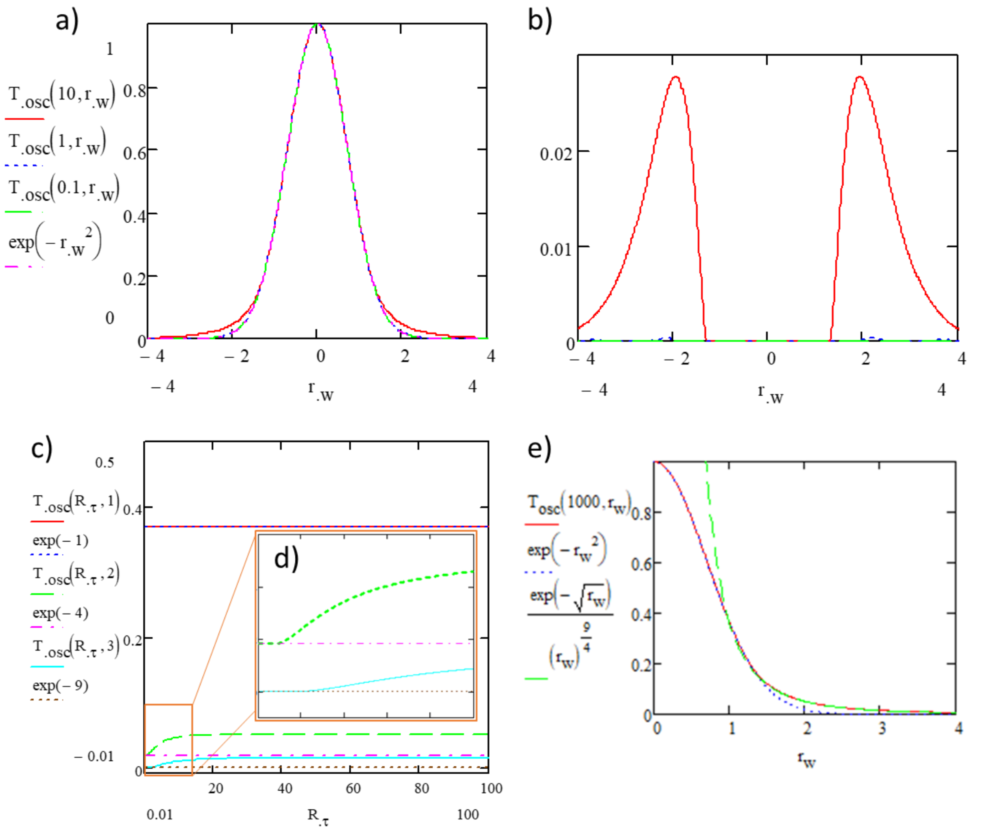

Fig.II.21. a) spatial distribution of T_{osc} with real expression (x_m is a function of $R\tau, r_w$) when $R\tau = 10{,}1$ and 0.1, and reduced expression ($x_m = 0$). b) the difference between the 2 expressions according to r_w. c) T_{osc} with real expression (x_m is a function of $R\tau, r_w$), and reduced expression ($x_m = 0$) according to $R\tau$ at $r_w = 1,2,3$. d) a zoom of $R\tau$ from 0 to 10. e) Tosc distribution when $R\tau = 1000$ (red), comparing with Tosc in situation 1(blue dash) and the maximum Tosc value when $R\tau \to \infty$ according to r_w (green).

Same as T_{max}, we note that from fig.II.21a, when $R\tau$ increases, attributed to the existence of x_m, compared to situation 1, the oscillation amplitude has only a small increase around $r_w=2$ which is sometimes not negligible. The $R\tau$ dependence is shown in fig.II.21c and d, we note that the oscillation amplitude at $r_w=2$ (green dash) and $r_w=1$ (cyan) increases when $R\tau$ increases, until a limitation. This limitation is calculated to be $\frac{\exp\left[-\frac{3}{2}\right]}{\left[\frac{2}{3}(r_w)^2\right]^{3/2}}$ when $R\tau \to \infty$ (because $x_m . R\tau \xrightarrow{R\tau\to\infty} \frac{2}{3}(r_w)^2 - 1$). Fig.II.21e demonstrates this limitation value according to r_w. Therefore, the range of T_{osc} is given by eq.II.52 and 53:

$$T_{\text{osc}}(R\tau, r_w) \xrightarrow{R\tau\to 0} \exp[-(r_w)^2] \qquad (II.52)$$

$$T_{\text{osc}}(R\tau, r_w) \xrightarrow{R\tau\to\infty} \frac{\exp\left[-\frac{3}{2}\right]}{\left[\frac{2}{3}(r_w)^2\right]^{3/2}} \qquad (II.53)$$

We note that the oscillation amplitude T_{osc} at situation 1 is $\exp[-(r_w)^2]$ which is the minimum, while in situation 2, the amplitude is larger due to the influence of x_m, with a maximum value of $\frac{\exp\left[-\frac{3}{2}\right]}{\left[\frac{2}{3}(r_w)^2\right]^{3/2}}$ at place around $r_w=2$.

II.3.3.1.2 The effective number of pulses for reaching the limit of T_{osc}, T_{min}, and T_{max}

Since x_m prevents simple expressions, and the scope of our study lies often in situation 1, the effective number of pulses for reaching the limit of Tosc, Tmin, and Tmax ($N^r_{sso/ssmin/ssmax}$) is given in the situation when $x_m = 0$.

With the same definition as we calculated in r=0, with ε a small quantity and $X = \frac{1}{\sqrt{1+N\cdot R\tau}}$, we have:

$$\frac{\left|T_{osc/max/min}(r,N) - T_{osc/max/min}(r,\infty)\right|}{T_{osc/max/min}(r,\infty)} < \varepsilon$$

Therefore, we have $N^r_{sso/ssmin/ssmax}$ solution shown below:

$$N^r_{sso} > \frac{-3.W\left[-\frac{1}{3}e^{-\frac{1}{3}\left(\frac{r}{w}\right)^2}.\left(\frac{r}{w}\right)^2.\varepsilon^{\frac{2}{3}}\right] - 2\left(\frac{r}{w}\right)^2}{3.R\tau.W\left[\left(-\frac{1}{3}e^{-\frac{1}{3}\left(\frac{r}{w}\right)^2}.\left(\frac{r}{w}\right)^2.\varepsilon^{2/3}\right)\right]} = \frac{1}{R\tau}\left(-\frac{2\left(\frac{r}{w}\right)^2}{3.W\left[\left(-\frac{1}{3}e^{-\frac{1}{3}\left(\frac{r}{w}\right)^2}.\left(\frac{r}{w}\right)^2.\varepsilon^{2/3}\right)\right]} - 1\right)(II.54)$$

This expression doesn't have an analytic root without using the tabulated function, W is the Lambert W function (defined as $\omega e^{\omega} = z, \omega = W(z)$). In practice, since $X^2 \ll 1$, by approximation, it becomes:

$$N^{\text{r}}_{sso} > \frac{1}{R\tau}\left[\left(\frac{1}{\varepsilon.\exp[-(r_w)^2]}\right)^{\frac{2}{3}} - 1\right] \qquad (II.55)$$

For N^r_{ssmin} and N^r_{ssmax}, with approximation of $\operatorname{erf}(X.r_w) \approx \frac{2}{\sqrt{\pi}}X.r_w$,

$$N^r_{ssmin} > \frac{1}{R\tau}\left[\left(\frac{2}{R\tau.\varepsilon.T_{\min}(r_w,\infty)}\right)^2 - 1\right] \qquad (II.56)$$

$$N^r_{ssmax} > \frac{1}{R\tau}\left[\left(\frac{2}{R\tau.\varepsilon.T_{max}(r_w,\infty)}\right)^2 - 1\right] \qquad (II.57)$$

The behavior of Nssr according to $R\tau$ is the same as r_w=0 (fig.II.13 and fig.II.16), but with an overall increase. We plot the Nsso (r), Nssmax (r), and Nssmin (r), at $R\tau = 18$ (e.g 200kHz for glycine) according to r_w as shown in fig.II.22a. A plot of reaching steady state time (with diffusion time 0.28µs) is plotted in fig.II.22b.

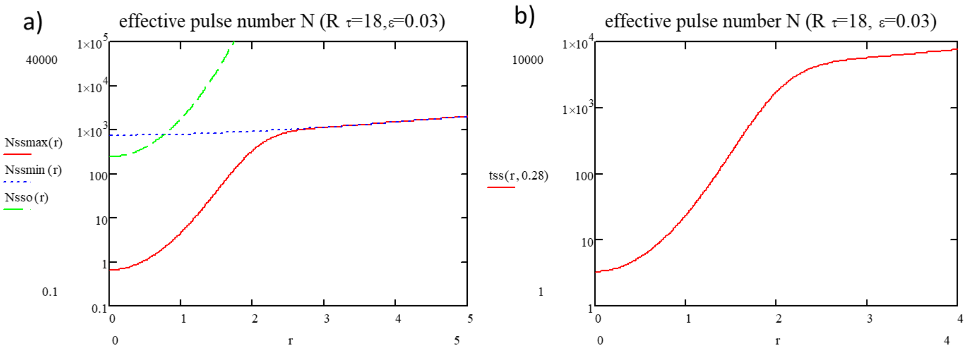

Fig.II.22 a) effective number Nssmax (red) and Nssmin (blue dash) and Nssmax (r_w =0, green) for reaching a steady state according to r_w from 0 to 5. b) effective time for reaching a steady state according to r_w from 0 to 4

Out of the center, with r_w increases, we can see from fig.II.22a that it is much harder to reach the steady state, the main reason is that the temperature out of the center is low when r_w is large, that means 0.03 of a small value is even smaller to reach just like the case of Tmin at r_w=0. The curve (red) is reaching to the Nssmin curve (blue dash) when r_w increasing, it is because beyond this radius, Tmin almost equals Tmax. From fig.II.22b, the plot of time for reaching a steady state in an example with $\tau_D = 0.28\mu s$, $R\tau = 18$, i.e. 200kHz, the time for reaching steady state is less than 10ms within 4w$_r$, which is still less than the irradiation time when we use the scanning speed less than 200µm/s.

II.3.3.2 Tmean: The T averaged on the period

II.3.3.2.1 The limit of T$_{mean}$

With the definition $\bar{T}(r,z,N) = \frac{1}{\tau_p}\int_{\substack{pulse\ period\\ at\ N}} T(r,z,t)\,dt$ (eq.II.40), we have the average temperature in a period as:

$$\bar{T}(r,N) = \frac{1}{\tau_p}\int_{\frac{t}{\tau_p}=N-1}^{\frac{t}{\tau_p}=N}\sum_{n=0}^{N-1}\frac{1}{\left[1+(\frac{t}{\tau_p}-n).R\tau\right]^{3/2}}.\exp\left[-\frac{(r_w)^2}{1+(\frac{t}{\tau_p}-n).R\tau}\right].dt$$

$$= \frac{\sqrt{\pi}}{R\tau.\ r_w}.\left[erf(r_w) - erf\left(\frac{r_w}{\sqrt{1+N.R\tau}}\right)\right]\xrightarrow[N\to\infty]{}\frac{\boldsymbol{\sqrt{\pi}}}{\boldsymbol{R\tau.\ r_w}}\boldsymbol{erf(r_w)}\ (II.58)$$

II.3.3.2.2 N_{ssm}^{r}: The effective number of pulses for reaching the limit of T$_{mean}$

The effective number N_{ssm}^{r} with approximation $\mathrm{erf}(X.r_w) \approx \frac{2}{\sqrt{\pi}}X.r_w$ is solved to be:

$$\mathrm{N}_{ssm}^{r}(r_w) > \frac{1}{R\tau}\left[\left(\frac{2.r_w}{\varepsilon.\sqrt{\pi}.erf(r_w)}\right)^2 - 1\right] \qquad (II.59)$$

From the expression above, we see that the periphery of the distribution is stabilized after the center. Calculation shows that it is increasing as r$_w$, so in most cases, with the scanning speed used in the experiments, the use of the steady state for concluding is justified.

II.4 CONCLUSION OF ANALYTICAL EXPRESSIONS

	r=0			**r≠0***		
		$N \to \infty$	$N_{ss}^{0}(\varepsilon, R\tau)$		$N \to \infty$	$N_{ss}^{r}(\varepsilon, R\tau)$
$\boldsymbol{T_{osc}(r,N)}$	$1 - X^3$	1	$\frac{1}{R\tau}\left[\left(\frac{1}{\varepsilon}\right)^{2/3} - 1\right]$	$\exp[-(r_w)^2] - X^3\exp[-(X.r_w)^2]$	$\exp[-(r_w)^2]$	$\frac{1}{R\tau}\left[\left(\frac{1}{\varepsilon.\exp[-(r_w)^2]}\right)^{2/3} - 1\right]$
$\boldsymbol{T_{min}(r,N)}$	$\frac{1}{2}[X1^3 + X^3] + \frac{2}{R\tau}[X1 - X]$	$\frac{1}{2}X1^3 + \frac{2}{R\tau}X1$	$\frac{1}{R\tau}\left[\left(\frac{2}{R\tau.\varepsilon.T_{min}(\infty)}\right)^{2} - 1\right]$	$\frac{1}{2}[X1^3\exp[-(X1.r_w)^2] + X^3\exp[-(X.r_w)^2]] + \frac{\sqrt{\pi}}{R\tau.r_w}[erf(X1.r_w) - erf(X.r_w)]$	$\frac{1}{2}X1^3\exp[-(X1.r_w)^2] + \frac{\sqrt{\pi}}{R\tau.r_w}erf(X1.r_w)$	$\frac{1}{R\tau}\left[\left(\frac{2}{R\tau.\varepsilon.T_{min}(\infty)}\right)^{2} - 1\right]$
$\boldsymbol{T_{max}(r,N)}$	$1+T_{min}(\mathrm{N})$	$1+T_{min}(\infty)$	$\frac{1}{R\tau}\left[\left(\frac{2}{R\tau.\varepsilon.T_{max}(\infty)}\right)^{2} - 1\right]$	$\exp[-(r_w)^2] + T_{min}(\mathrm{N})$	$\exp[-(r_w)^2]+T_{min}(\infty)$	$\frac{1}{R\tau}\left[\left(\frac{2}{R\tau.\varepsilon.T_{max}(\infty)}\right)^{2} - 1\right]$
$\boldsymbol{\overline{T}(\mathbf{r},N)}$	$\frac{2}{R\tau}(1 - X)$	$\frac{2}{R\tau}$	$\frac{1}{R\tau}\left[\left(\frac{1}{\varepsilon}\right)^{2} - 1\right]$	$\frac{\sqrt{\pi}}{R\tau.\ r_w}.[erf(r_w) - erf(X.r_w)]$	$\frac{\sqrt{\pi}}{R\tau.\ r_w}erf(r_w)$	$\frac{1}{R\tau}\left[\left(\frac{2.r_w}{\varepsilon\sqrt{\pi}.\mathrm{erf}(r_w)}\right)^{2} - 1\right]$

Table.II.4 analytical expressions of temperature and effective number for reaching steady state.

	r=0		**r≠0***	
	$N \to \infty$	$N_{ss}^{0}(\varepsilon, R\tau)$	$N \to \infty$	$N_{ss}^{r}(\varepsilon, R\tau)$
$\boldsymbol{T_{osc}(r,N)}$	1	$\frac{1}{R\tau}\left[\left(\frac{1}{\varepsilon}\right)^{2/3} - 1\right]$	$\exp[-(r_w)^2]^*$	$\frac{1}{R\tau}\left[\left(\frac{1}{\varepsilon.\exp[-(r_w)^2]}\right)^{2/3} - 1\right]$
$\boldsymbol{T_{min}(r,N)}$	$\frac{2}{R\tau}X1$	$\frac{1}{R\tau}\left[\left(\frac{2}{R\tau.\varepsilon.T_{min}(\infty)}\right)^{2} - 1\right]$	$\frac{\sqrt{\pi}}{R\tau.r_w}erf(X1.r_w)$	$\frac{1}{R\tau}\left[\left(\frac{2}{R\tau.\varepsilon.T_{min}(\infty)}\right)^{2} - 1\right]$
$\boldsymbol{T_{max}(r,N)}$	$1+T_{min}(\infty)$	$\frac{1}{R\tau}\left[\left(\frac{2}{R\tau.\varepsilon.T_{max}(\infty)}\right)^{2} - 1\right]$	$\exp[-(r_w)^2]+T_{min}(\infty)$	$\frac{1}{R\tau}\left[\left(\frac{2}{R\tau.\varepsilon.T_{max}(\infty)}\right)^{2} - 1\right]$
$\boldsymbol{\overline{T}(\mathbf{r},N)}$	$\frac{2}{R\tau}$	$\frac{1}{R\tau}\left[\left(\frac{1}{\varepsilon}\right)^{2} - 1\right]$	$\frac{\sqrt{\pi}}{R\tau.\ r_w}erf(r_w)$	$\frac{1}{R\tau}\left[\left(\frac{2.r_w}{\varepsilon\sqrt{\pi}.\mathrm{erf}(r_w)}\right)^{2} - 1\right]$

Table.II.5 practical approximated analytical expressions of temperature and effective number for reaching steady state.

With $X(N, R\tau) = \frac{1}{\sqrt{1+N.R\tau}}$ and $X1(R\tau) = \frac{1}{\sqrt{1+R\tau}}$. *: condition of $r_w, R\tau$ (fig.II.18)

II.5 MODIFICATIONS IN RELATION TO THE TEMPERATURE

As we can simulate the temperatures induced by laser in the materials, the purpose is to connect it to physical processes and properties in the material, such as fictive temperature, glass transition temperature, melting temperature, or the TTT diagram that defines the conditions to crystallize by nucleation creation and growth (Classical homogeneous Nucleation Theory). This section will introduce some temperature-related processes and parameters in order to better understand the applicability of temperature simulation.

Fictive temperature modification

T_f definition: Fictive temperature (T_f) is the temperature at which the equilibrium liquid structure is the same as that currently existing in the glass. In the plot of molar volume (or enthalpy) as a function of temperature, T_f can be obtained from the intersection of extrapolation along the curve of the glass and the one of the liquid in equilibrium. This temperature depends on the cooling rate. It is an imprint of the thermal history of glass preparation. Most of the physical properties including the viscosity may be dependent on the fictive temperature. It is a concept introduced by Tool et al [112-115]. The physics underlined is that when the liquid has no time to adapt its structure to the temperature, the structure is frozen. The corresponding time is called relaxation time and it corresponds to the ratio of the viscosity on the shear modulus from the Maxwell model [116]. When the relaxation time becomes larger than the time of treatment, the liquid is frozen. In practice, it is possible to compare the relaxation time curve versus the temperature and the thermal treatment curve as in Fig.II.23.

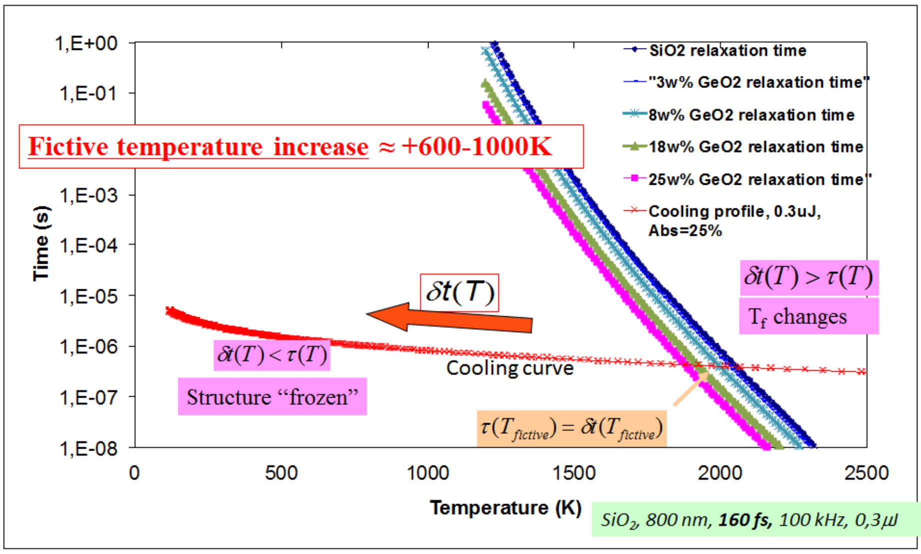

Fig.II.23: the graphic determination of the T_f for an fs laser pulse. N.B.: the cooling curve is here determined by the heat diffusion out of the irradiated area in the case of a static beam with one pulse.

The curve in red in Fig.II.23 is the temperature versus the time i.e. the treatment curve (e.g. calculated in the previous sections) but plotted as time (T) (quoted δT(T) in Fig.II.23) in order to be compared with the relaxation time τ(T), here for some classical inorganic glasses. The fictive temperature is defined from the crossing point between the two curves.

Therefore, for each value of radius around the beam axis, we use the treatment curve, we search for a crossing point of the treatment curve with the relaxation curve and the limit radius defines thus the size of the modified area. Such an area is often observed with fs-laser irradiation and leads to type I modification associated with refractive index change.

When the beam is scanning, the cooling curve is no more the spontaneous cooling down by thermal diffusion (ca µs) but the temperature spatial distribution translated at the speed of scanning i.e. much slower (ca. a fraction of s).

The use of the thermal treatment curve in the case of crystallization

In the case of the laser-induced crystallization in the scanning mode, the treatment curve is also obtained by translating the spatial temperature distribution in the direction of scanning. As shown in the Fig.II.24, the red circle schemes the T distribution Tmean(r) at the steady state. Knowing this last allows seeing what is the thermal treatment T(t) for each part of the modified line in the material.

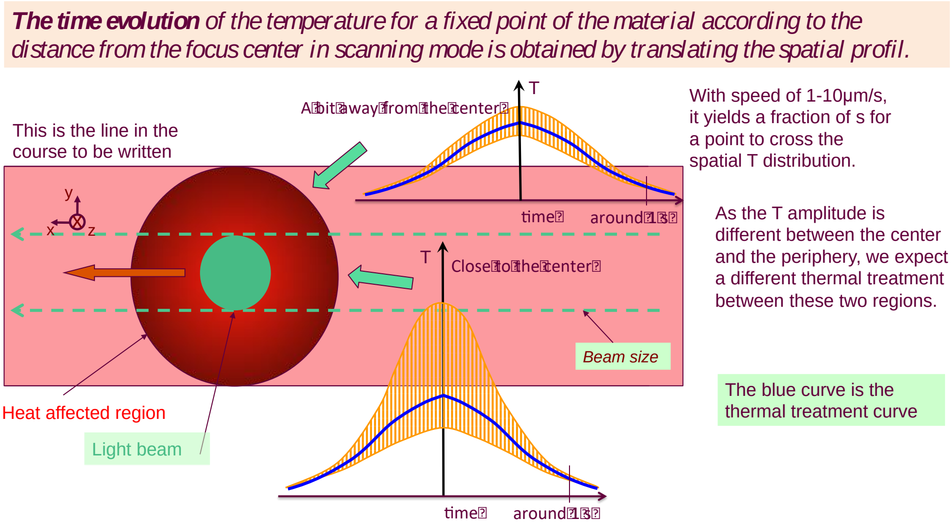

***The time evolution** of the temperature for a fixed point of the material according to the distance from the focus center in scanning mode is obtained by translating the spatial profil.*

With speed of 1-10µm/s, it yields a fraction of s for a point to cross the spatial T distribution.

As the T amplitude is different between the center and the periphery, we expect a different thermal treatment between these two regions.

The blue curve is the thermal treatment curve

Fig.II.24 the time evolution of the temperature of the different parts of the written line. The scanning beam in red along the line in pink, the thermal treatment curve in blue

Then, knowing the crystallization domain in the TTT diagram (Fig.II.25), it is possible to control the speed, pulse energy, and repetition rate in order to allow the treatment to cross the crystallization domain.

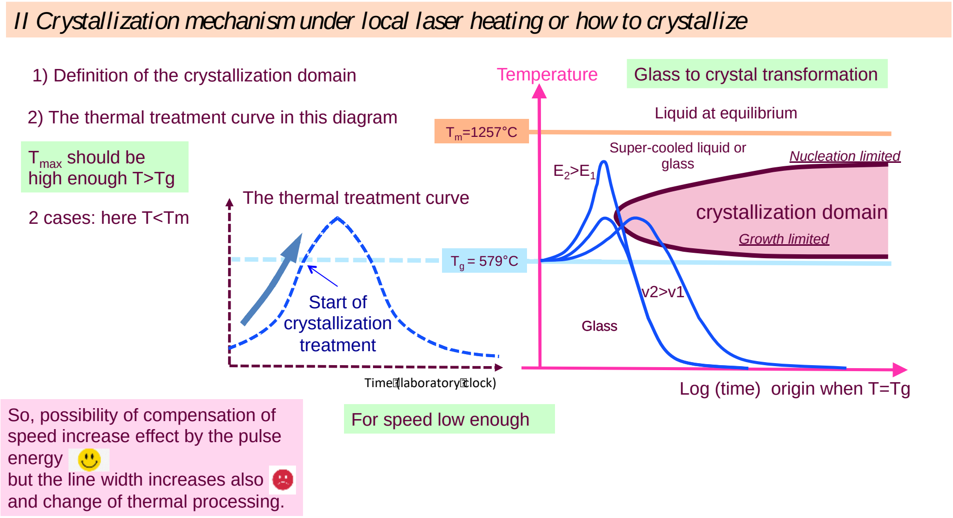

II Crystallization mechanism under local laser heating or how to crystallize

1) Definition of the crystallization domain

2) The thermal treatment curve in this diagram

T_{max} should be high enough T>Tg

2 cases: here T<Tm

For speed low enough

So, possibility of compensation of speed increase effect by the pulse energy 🙂
but the line width increases also ☹
and change of thermal processing.

Fig.II.25 The position of the thermal treatment curve comparing to the crystallization domain

This work has been presented at the conference GOMD 2022 in Baltimore 22-26 May. This knowledge has been used also in [16].

Evolution of the heat affected volume (HAV) width on RR and pulse number

We take the example from the Eaton et al. work [81] that is briefly described in Fig.II.26.

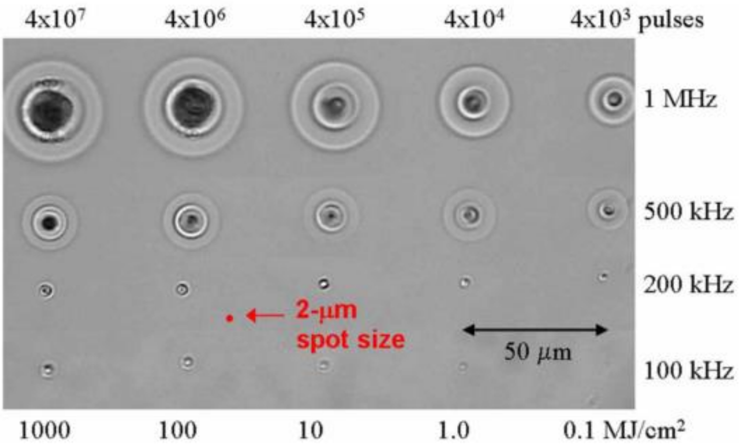

Fig. 2. Optical microscope images showing heat affected zones created in AF45 borosilicate glass with 450-nJ pulse energy from a 1045-nm femtosecond laser. Total pulse (top) and fluence accumulation (bottom) is shown for each column and the laser repetition rate is indicated for each row. Laser direction is normal to page.

Table 1. Glass properties Schott and Corning glasses [12]

Manufacturer code	Glass	Bandgap (eV)	Diffusivity (10^{-3} cm^2/s)	Density (g/cm^3)	Working point (°C)
Corning 7940	Pure fused silica	9.1	8.4	2.2	1800
Corning 1737F	Low-alkali boro-aluminosilicate	4.0	5.0	2.54	1312
Schott AF45	Alkali-free borosilicate	3.9	8.0	2.72	1225

Fig.II.26: variation of the heat affected volume (HAV) according to pulse energy and repetition rate, extracted from [81].

It is static multipulse irradiation with an fs laser. Several regions are detected but we are interested in the last one only at the largest radius. We observe that the sizes of the impacts are increasing on the repetition rate strongly but maybe not so much with the number of pulses.

The size of the most external region is assumed to be defined by a fictive temperature change. If consider the change in repetition rate at a constant pulse number, when Rτ decreases, the amplitude of the treatment curve increases and so does its width. But, we can notice that the treatment curve at the limit radius will be always the same and thus the fictive T at this limit will be always the same. Therefore, the size could be the solution of the equation II.58 mentioned in section II.3.3.2.1 for a given T_f, recalled as below:

$$\bar{T}(r,N)/T_{00} = \frac{\sqrt{\pi}}{R\tau.\ r_w}.\left[erf(r_w) - erf\left(\frac{r_w}{\sqrt{1+N.R\tau}}\right)\right] \xrightarrow[N\to\infty]{} \frac{\sqrt{\pi}}{R\tau.\ r_w} erf(r_w) = T_f/T_{00}$$

For better understanding, we have to compute first the Rτs. We find it is between 40 at 100kHz and 4 at 1MHz, just on the limit between accumulation and no accumulation. Using the equation above at the steady state, we can see that the size is varying by a factor of 10 from 40 to 4 as observed.

Now, we can compute the number of pulses for reaching the steady state for a given Rτ. For Rτ=4, we need 5x10^4 pulses at r_w=12 (as measured in Fig.II.26). The results are quite close to the observation. Before reaching the steady state, the size of the modified region increases with the pulse number, see 1MHz cases in fig.II.26.

What we can see also in Fig.II.26 is an effect at the center, different and more stressed as long as the frequency is increased. But we know that when Rτ<10, the temperature at the center increases (heat accumulation) whereas it is constant at large Rτ (no heat accumulation).

N.B.: But, we can have also an accumulation of the effect on time, i.e. some reaction development during the steady state (e.g. crystallization). So, this is interesting to know when the thermal steady state is reached, in order to input some changes to other phenomena [117].

Temperature influence on nanogratings' processing windows based on

the viscosity

The principal aim of the study of Xie et al. [118] to which we make reference to is to highlight the link between nanogratings processing window and glass viscosity behavior with temperature. Therefore, and to better appreciate the discussion in the next section, how the temperature elevation upon fs-laser irradiation impactes in an Ep – RR landscape is briefly discussed. There exist two principal situations when considering the Ep – RR landscape:

i) Low RR, increasing Ep. From the calculation in this chapter, the temperature profile distribution in space is unchanged, but the deposited heat inside the material would increase. Consequently, the maximal temperature increase (ΔT) at the pulse center also would increase, following a general form of $\Delta T \sim AE_p/\rho C_p V$. Here A is the fraction of the pulse energy absorbed by the material and effectively transmitted to the glass phonons, ρ and C_p, respectively, are the glass density and heat capacity, and V the volume within which the pulse energy is absorbed ($V = \pi^{3/2}w^3\ in\ spherical\ geometry$). It is worth pointing out that A is a function of fluence (e.g., in silica glass), and such temperature rise has already been investigated for several glass matrices including silica or Borofloat 33. As E_p is increased (and so ΔT), the spatial volume for which the temperature is beyond a transformation temperature threshold (e.g., formation of nanogratings) would be enlarged.

ii) High RR, fixed Ep. This condition is in favor of "heat accumulation regime". This effect typically results into an increase of the average temperature as we have seen that Rτ decreases, hence a decrease of the glass viscosity, in the heat affected zone. The characteristic time to evacuate the heat can be estimated as $\tau_d \approx \omega^2/4D_{th,}$. τ_d (SiO_2) ≈ 2.5 µs while τ_d (BK7) ≈ 4.3 µs. Therefore Rτ is smaller in BK7 than in SiO2 and temperature at fixed pulse energy, and repetition rate will be larger and the viscosity lower erasing the nanogratings created by the pulse itself. Consequently, the "temperature interval" to make nanogratings appears reduced in glasses such as BK7 with respect to SiO_2.

Extracted and modified from Xie et al. paper 2022 Application and validation of a viscosity approach to the existence of nanogratings in oxide glasses [118].

Nonequivalence of Ep and RR with a constant mean power

If one considers two activated processes (e.g. one could be the soft molecule transformation and the other one is destruction), with two different activation energies, the effect of the temperature will be different and one may become dominating than the other one. This can be used to push up one reaction and inhibit another.

Therefore, let us consider two extreme cases: 1) low RR and high Ep and 2) high RR and low Ep, with constant power (P= Ep*RR). Rτ reflects the degree of accumulation of pulses on different materials. In the same material, when Rτ is large (low RR, no heat accumulation, independent pulses, case 1), due to the high Ep, the oscillation amplitude is very large but the minimum temperature is close to room temperature. When Rτ is small (high RR, maybe heat accumulation, pulses are overlapping, case 2), the oscillations are smaller but the average temperature is the same of case 1. Fig.II.27 computed from the formula in this chapter shows the temperature behavior of these 2 cases. Due to maintaining the same average power, the oscillation at low frequency is three orders larger than the one at a high repetition rate.

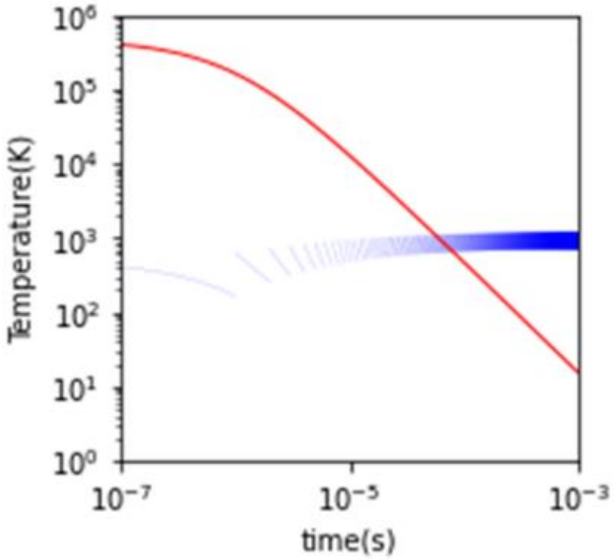

Fig.II.27: Comparison on 1ms of the temperature evolution at the center of a spherical focus for the case of Ep=2µJ, RR=1kHz (red curve, Rτ≈2000) and Ep=2nJ, RR=1Mhz (blue curve, Rτ≈2). Computation ingredients are given in the appendix.

Therefore, in the first case (red in fig.II.27, low RR, Rτ large), only a part of the period is efficient (temperature is too low at most of the time) and a part may lead to material destruction, whereas in the second case (blue, high RR, small Rτ), the temperature is more stable and can be better controlled (see fig.II.27).

For better understanding this, we cite the effects of the two following cases (see fig.II.28), along the average power line in the landscape [119]:

1) Ep=2µJ, RR=1kHz, 10µm/s, with a mean power of 2mW and pulse density of 10^8 pulses/µm
2) Ep=10nJ, RR=1Mhz, 1µm/s with a mean power of 10mW and pulse density of 10^{12} pulses/µm

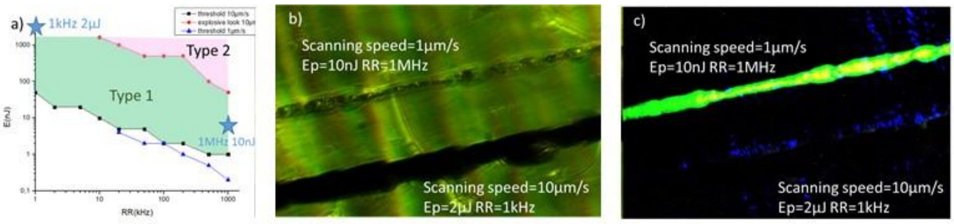

Fig.II.28: a) the positions of experiments in the landscape, b) the microscopic photo under transmission mode with natural light; c) microscopic photo of the same area of b) excited by 448nm laser and with dichroic mirror transmitting wavelength>490nm, cited from [119].

We observed that in these two situations, the luminescence is favored to form at a large frequency (and thus low Ep) even though the average power is not so different. On the contrary, the material is deeply transformed more at low frequency (and thus high Ep).

On the other hand, the width of the transformed line, which we can assume to be formed from the places where the maximum temperature overcomes some value (e.g. glass transition temperature, decomposition temperature), is smaller in the case of high frequencies than for lower ones (see fig.II.29).

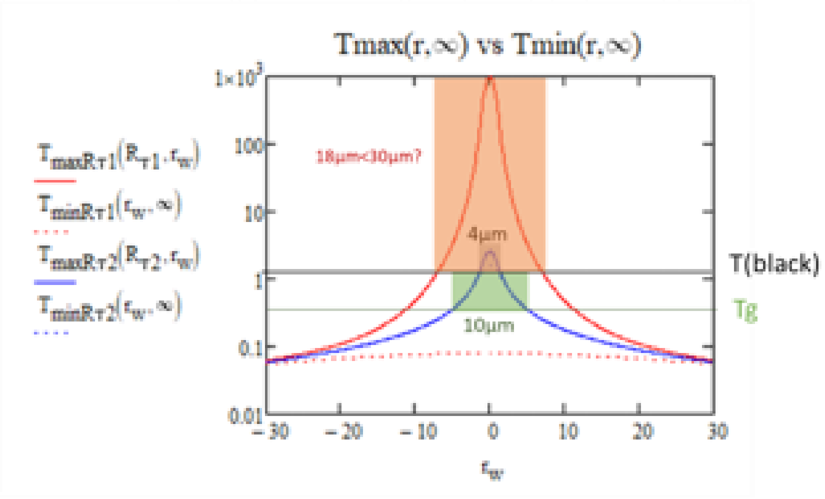

Fig.II.29: variation of the Tmax distribution around the center of the beam with Rτ at constant mean power. Note that the red curve oscillates between the full line and the dashed one, whereas the blue one oscillates much less, cited from [119].

If we consider a constant scanning speed, it means that the time per length unit is the same but of course not the number of pulses, which is several orders of magnitude larger. Therefore, we cannot easily differentiate between the effect of the temperature (very high during a short time) and the effect on the number of pulses (many pulses at a much lower temperature). To clarify this point, we considered a single first-order reaction with an inexhaustible, i.e. a reaction $A \xrightarrow{k(E,T)} B$ where A is inexhaustible matter, $k(E,T) = k_0 exp\left(-\frac{E}{k_B T}\right)$ is the reaction constant of Arrhenius type with activation energy E and temperature T. Knowing the treatment curve T(t) from the calculation of this chapter, the plot of $[B]/[A]k_0$ versus RR show that the efficiency is larger at low RR. However, this predominance at low RR can be decreased when the activation energy is smaller. We thus deduce that the activation energy of the material destruction reaction is larger than the one of molecule transformation giving rise to luminescence. This is a nice example of the possibility of reaction control through femtosecond laser parameter adjustment. Extracted from [119].

From table.II.3, we can see that the diffusion time is larger for organic compounds than for inorganic ones except for glycine. It means that Rτ is usually smaller, and the heat accumulation is more easily reached.

Therefore, the lower pulse energy is necessary to avoid a high temperature leading a complete destruction.

On the other hand, in cylindrical geometry, the size along z is larger. A few tens microns instead of one or two, so τ_{Dz} is larger than τ_{Dr} and thus $R\tau_z$ is smaller than $R\tau$, therefore thermal accumulation occurs along z more easily [120].

II.6 APPENDIX

Glossary

parameters	definitions	units
A	Fraction of reflected light by the plasma	none
α	Light absorption	μm^{-1}
ε	A small quantity of computation needs	none
τ_p	Period of the pulses	µs
τ_D	Heat diffusion time $\tau_D = \frac{w^2}{4D_T}$	µs
$R\tau$	τ_p/τ_D	none
w	Beam waist radius (at 1/e)	µm
D_T	Thermal diffusivity $D_T = \frac{\kappa}{\rho.C_p}$	m^2/s
κ	Thermal conductivity	W/(m.K)
E_p	Pulse energy	J
f	Pulse repetition rate	MHz
ρ	Density	kg/m^3
C_p	Specific heat capacity	J/(kg.K)

Table.II.6 Glossary of laser and material parameters used in this chapter

Material parameters in the simulation model

	ρ (kg/m³)	C_p (J/(kg.K)	κ (W/(m.K))	D_T (m²/s)	τ_D (µs)	Melting point (K)
STS glass	3887	410	10.1	6.34E-06	0.039	1585
LNS glass	3830	650	2.65	1.06E-06	0.235	1530
SiO_2(glass)	2200	703	1.38	8.92E-07	0.28	1983
glycine	1160,7	1266	1.3[104]	8.85E-07	0.283	506 (decomp.)
Zeonex	1010	1000	0.045	4.445E-08	5.624	553
Borosilicate (Schott D263)[121]	2510	820	0,96	4.66E-07	0.534	1324
nifedipine	1300	1000	0.2	1,54E-07	1.63	446
sucrose	1587	1243,1	0.1	5,07E-08	4.93	458 (decomp.)

Table.II.7 thermal parameters of materials

Chapter.III FEMTOSECOND LASER DIRECT WRITING (FLDW) IN α-GLYCINE SINGLE CRYSTAL

III.1 INTRODUCTION

III.1.1 Glycine crystal information

Glycine is the simplest proteinaceous amino acid, with the molecular formula $C_2H_5NO_2$. We choose it as the first attempt for some reasons. First of all, it is the only one among all amino acid molecules that without molecular chirality (the rest are levorotatory). Second, with different arrangements of the molecules, its crystalline states can have an achiral space group (e.g. α-phase $P2_1/c$), which is not optical activate, as well as chiral structure (e.g. γ-phase $P3_1$ and $P3_2$), which is optical activate. Therefore, we expect to see some change on optical properties such as a creation of optical rotation (Circular Birefringence), Circular Dichroism, secondary nonlinear effects (symmetry breaking), or some other optical properties after femtosecond laser irradiation.

Specificly, as we know, in aqueous solutions, it appears mainly as zwitterion glycine ($^{+}NH_3CH_2COO^{-}$). In the solid phase, it may be found in amorphous or in crystalline forms. When crystallizing from water solution, glycine forms three polymorphous forms α, β, and γ, as shown in fig.III.1, of which form α and γ are stable. Under the effect of high pressure, three other forms can develop: δ, ε and β' [122]. The crystalline forms differ from each other by the packing of zwitterion in the unitary cells and by the number of intermolecular hydrogen bands [123]. Since the glycine molecule is achiral, its α form crystallizes in centrosymmetric and achiral space group $P2_1/c$ [124], ruling out the possibility of optical second harmonic generation (SHG). While it undergoes spontaneous mirror symmetry breaking when it crystallizes in its chiral and non-centrosymmetric γ form or meta-stable β form (with space group $P3_1$ and $P2_1$, respectively), it will become optical active and SHG accessible. Due to these properties, the γ glycine crystal is often considered a candidate for piezoelectric and nonlinear optical applications [125-128].

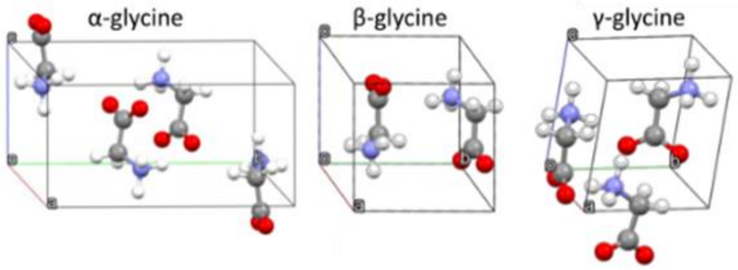

Fig.III.1 a) unit cell of α, β, and γ-glycine, extracted from [129].

Regarding the conditions under which the different crystalline forms are produced, we only have information from the precipitation in solution (as opposed to 'from solid'). It is affected by various factors, such as cooling rate, supersaturation, agitation, solvent, pH values, additives, solution concentration, impurity, and seeding [130]. The growth and characterization of α and γ glycine have already been reported by several researchers. Chongprasert et al. [131] have demonstrated that depending on the conditions (temperature, concentration, rate of cooling, and crystallization), the crystallization of aqueous solutions of glycine can provide any of its three polymorphs (α, β, γ) or a mixture of them. From water solution of pH= 2.5-10, the easiest to crystallize is α –glycine [132] while γ form can be obtained from acidic (pH< 2.5) or basic (pH > 10) solution [132] or by addition of different compounds containing alkaline monovalent ions Li^+,Na^+,K^+, $NH4^+$ in a neutral water solution [133-137]. Attempt to grow sizable β-form single crystals were not successful because of their high instability. The thermodynamic stability of these forms is decreasing in the order γ > α > β [131]. In addition, during crystallization from aqueous solutions, α-polymorph forms faster.

Some studies report about the conditions of transformation between the polymorphs, for instance, α-glycine can gradually transform into the γ-glycine at high humidity [138]. While with increasing temperature, γ-glycine is transformed into α-glycine at about 438 K, this transition is irreversible in the dry atmosphere [137].

In addition, in solution, laser-induced selective fabrication of different crystalline phases of glycine has emerged in recent years. For example, Yuyama et al. have successfully demonstrated the polymorph control of glycine in D_2O solution by a laser trapping technique using a linearly or circularly polarized CW near-infrared laser beam [68], the stable crystal polymorph of either α or γ-form were always generated at the focal spot of the solution. For the supersaturated and saturated solutions, circularly polarized laser irradiation enhances γ-crystal formation, while for the unsaturated solution the laser polarization effect becomes prominent, and linearly polarized laser light at a specific power provides the maximum γ-crystal probability of 90% [68].

In contrast to the above studies, one of our attempts is to prove that the laser-induced phase transformation of glycine can be realized in a solid state (e.g. from α phase to γ phase), and to see if the laser polarization has effects on it, or if we can create another anisotropic species, controlled by the polarization of light.

Moreover, in addition to what we have written above about the peculiarities of glycine crystals in terms of molecular structure and crystal structure, it is also of interest to us, if I may be allowed to be imaginative, because of the speculation about the origin of the chirality of life. The delivery of organic matter to primitive Earth via comets and meteorites has long been hypothesized to have been an important source for prebiotic compounds such as amino acids, nucleobases, or precursor species that contributed to the development of prebiotic chemistry, which may have led to the emergence of life on Earth [139, 140]. Significant evidence exists for an extraterrestrial origin because observations have shown the presence of many organic molecules in the interstellar medium (ISM), comets, and meteorites (e.g. [141]). In recent years, evidence and model [142] suggest that glycine forms without the need for ‘energetic’ irradiation, such as UV photons and cosmic rays, in interstellar water-rich ices, where it remains preserved, in a much earlier star formation stage. Therefore, the high temperature and pressure generated by femtosecond lasers inside it might be able to simulate the cosmic environment of the initial stages of life, as the studies having done by exposing under proton bombardment to simulate glycine under hostile environments of space radiation [123]. Clues might be found during the study optimistically.

III.1.2 Methodology

As mentioned, to demonstrate the possibility of any polarization effects, we develop the below methodology, starting from fs irradiation, based on the brief logic: modification→ observation → anisotropic properties creation → control.

Therefore, firstly, since we have almost no information on how glycine crystal responds under the irradiation of fs laser, we set a wide range of fs laser parameters, guiding by temperature simulation, to know the modification type that can be created. A landscape of RR and Ep was made with thresholds of every type that are defined by the appearance under the observation of a polarized optical microscope. With it, we have a visualized concept of modifications, which can imply different interaction processes.

Secondly, with observation through a polarized microscope, we can easily inspect the optical properties, e.g. birefringence. By sample rotation, we can have the information of its anisotropy of birefringence, from either the change of structure (e.g. crystallization, phase separation, etc.) or molecule. Some surface imaging techniques such as AFM, SEM, etc. can be used to analyse the modifications.

Thirdly, for structure change, Raman spectroscopy and IR spectroscopy are methods to characterize in general. Mueller-matrix microscopic ellipsometry can be also applied for characterizing the optical properties. If crystals are suspected to have been produced, EBSD (Electron back-scattering diffraction) can be used to identify the orientation of the crystals, except that this method is difficult for organic materials.

Fourthly, about molecule change, normally one performs mass spectroscopy and NMR for identification. However, in our case, we have difficulties with those characterizations since 1) the volume of the products created by fs laser is small; 2) the products created are hardly dissolved in any solvent, it is also a specific property. In addition, if the altered molecule has other properties, such as photoluminescence here, we image it with a confocal microscope and measure its excitation and emission spectra, as well as the lifetime. In addition, some typical peaks and characteristic peaks of functional groups in Raman and IR spectra can also provide additional molecular information.

Fifthly, for the control purpose, we list the observable properties associated with anisotropy and compare the changes in these properties by varying the polarization of the laser, to demonstrate whether they are polarization-dependent.

III.2 EXPERIMENTAL DETAILS

III.2.1 Sample preparation

III.2.1.1 Attempts of making glass

In the beginning, we envisage that glycine could be subjected to some experimentation by reference to laser-induced crystallization in inorganic glass [17, 143-146], i.e. to crystallize glycine crystal from amorphous solid instead of a solution, then probably there is a possibility to control its structure by polarization as in inorganic crystal. However, experiments, as well as reports, tell us that instead of melting, the glycine crystals begin to decompose from 230°C, producing NH_3, H_2O, and CO_2 [147]. Therefore, it is not feasible to manufacture glycine glass by heating and melting glycine crystals. We have also thought about mixing glycine powder with other polymer particles to lower the melting temperature to make glass, but we have not found a suitable composition with a similar melting temperature. There may be another possible method that has been used to make sucrose glass, named spray-drying [148-150] with equipment such as a freeze-dryer [151], but the size of the produced sample seems not adapted to our experiment. As a result, we did not succeed in making glycine glass. We therefore decided to start with a single crystal.

III.2.1.2 Crystal growth, cut, and polishing

III.2.1.2.1 Growth of glycine single crystal

α-glycine single crystals were prepared by recrystallization from a saturated aqueous solution with a slow evaporation method [133]. 25g glycine powder (Sigma, ≥99%) was dissolved in 100mL distilled water at around 50°C, or the solution with the same ratio, then it was cooled down to room temperature (around 20°C) to have a saturated aqueous solution. Seeds were harvested by slow evaporation at room temperature 2 days after. Seeds were selected and handed in the saturated aqueous solution at 40°C overnight to make them grow. The temperature was chosen for growing faster. One of the grown crystallized samples is shown in fig.III.2a. The crystals have traces of growth that are parallel to $\vec{c}$ axis, as described in [133]. The molecular arrangement of α-glycine crystal with optical axes indicates are shown in fig.III.2b and fig.III.3.

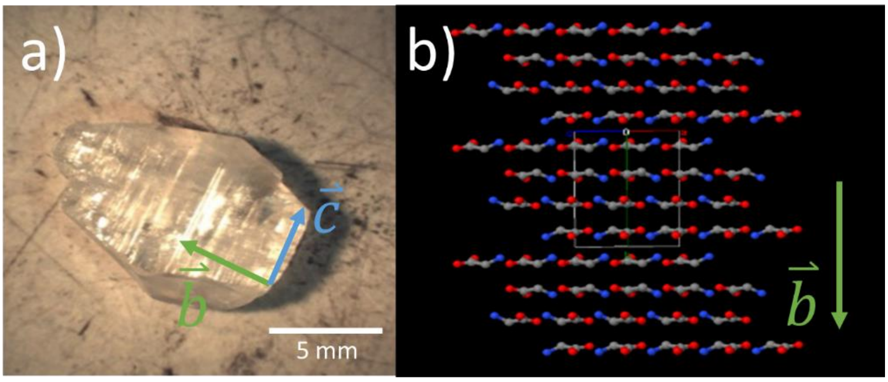

Fig.III.2 a) grown α-crystal of glycine b) the molecule arrangement in the α-glycine crystal

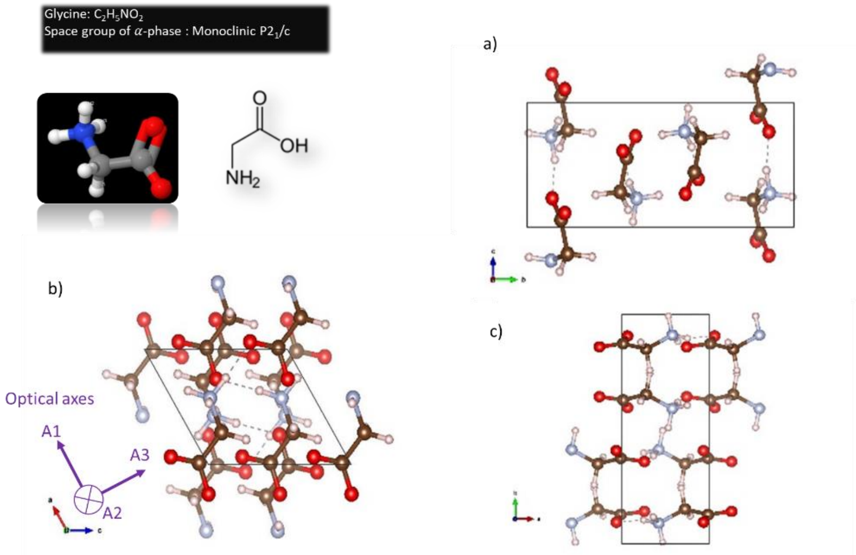

Fig.III.3 the molecular arrangement of α-glycine crystal with optical axes indicates a) the view from the bc plane b) the ac plane view d) the ab plane view γ-glycine single crystals were grown by the method described in [133]: the stable γ-form from aqueous solution in the presence of a critical concentration (>10%) of a selective additive sodium chloride. Small size crystals were grown by the slow evaporation method. The actual morphology of the crystal to the extent that it enhances the growth along the $\vec{a}$ direction of the crystal and reduces the growth along $\vec{c}$ [133].

III.2.1.2.2 Cut and polishing

For laser irradiation plateform, we need a sample in flake form. Samples were either polished or cleaved. The polishing process performed was as follows: 1) by 600-1200-2400-4000 abrasive plates 2) pure heptane with 1μm Al_2O_3 powder in a tissue plate then finished by 3) stearic acid powder.

Specifically, in α-glycine, the molecules arrange along the ac plane, i.e. (010) plane, as shown in fig.III.2b, there is no chemical bonding along $\vec{b}$ axis, so the (010) plane can be easily cleaved to obtain directly an optically smooth surface for fs laser irradiation without the polishing steps.

III.2.1.2.3 Sample conservation

All the samples, including glycine crystals, Zeonex glass, sucrose crystals, used in this thesis are conserved in a vacuumed dryer.

III.2.1.2.4 Crystal structure validation

To identify the polymorphic forms and determine the crystal parameters such as planes and axes of the grown crystals, the powder X-ray diffraction (PXRD) and single crystal XRD methods were performed.

The grown α and γ-glycine crystals were crushed to a uniform powder and subjected to powder x-ray diffractometer with Cu(Kα1) radiations (1.5406 angstroms Å) for the confirmation of the polymorphs. The powder form sample was scanned over the range of 10°-45° at the rate of 2°/min. The indexed powder XRD patterns are shown in fig.III.4. The characteristic peaks in the patterns show consistency with α and γ glycine.

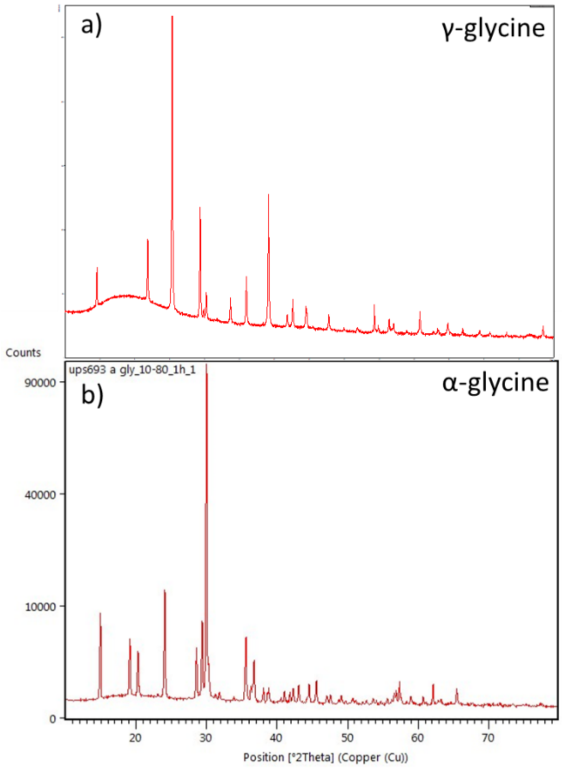

Fig.III.4 the obtained PXRD pattern of grown glycine crystal sample of a) γ-form and b) α-form

Single crystal XRD is performed by a four circles diffractometer (Kappa geometry, Bruker). Reflections were merged by SHELXL according to the crystal class for the calculation of statistics and refinement. Fig.III.5 shows the results with indicated crystal parameters, with the consistence of [133], we confirmed the cleaved plane and the growing axis. From here, we can use this as a reference to define the direction of scanning and the direction of laser polarization.

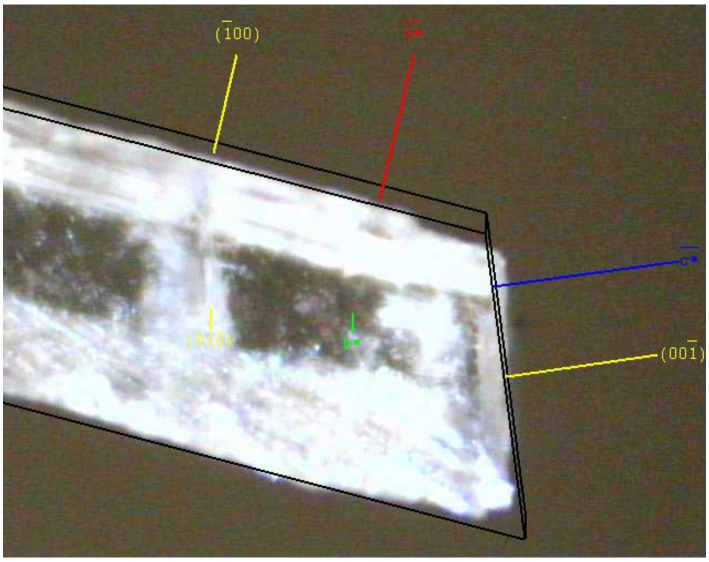

Fig.III.5 the result of XRD single crystal with the indicates of crystal indices

XRD Laue has also been performed but due to the space group being monoclinic, the identical patterns are not obvious, the result therefore is not shown here.

III.2.1.3 Energy minimum of the interband transition of α-glycine crystal

To have information about the minimum energy of the interband transition of α-glycine crystal, the absorption spectrum in Visible-UV (800nm-190nm) range was recorded by a UV-Vis-NIR spectrophotometer (*Cary 5000)*. The scan rate was 300nm/min with a data interval of 1nm and SBW (spectral band width) of 2nm. The average time was set to be 0.2 seconds. The absorption spectrum is shown in fig.III.6a which is corrected by the baseline.

The absorption starts around 5eV. With a fitting around the turning point, which is usually called Urbach tail [152], we found that the absorption α is not proportional to the exponential increase of energy $\exp(E)$, shown in fig.III.6b. Therefore, this is not a Urbach tail in the traditional sense. Instead of fitting the Urbach region by $\alpha(E) = \alpha_0 \exp(\frac{E-E_0}{E_u})$ (eq.III.1) [153], E_u is the Urbach energy, it is perfectly (chi square=5.78 x 10^{-6}) fitted with $\alpha(E) = \exp(a + bE + cE^2)$ with a=162.6, b=-64.97, c=6.508, shown in fig.III.6c. If we change this expression to the form like eq.III.1, we have:

$$\alpha(E) = \exp(a + bE + cE^2) = \exp\left(\frac{\frac{a}{c}+\frac{b}{c}E+E^2}{\frac{1}{c}}\right) = \exp(\frac{24.98-9.98E+E^2}{0.15366})$$

Therefore, we assume the absorption in the α-glycine crystal might be not behaving as the semiconductors, whose steepness of the onset of absorption near the interband edge is quantified by the Urbach energy, who implies the broadness of the density of states, associated with the disordered or low crystalline materials.

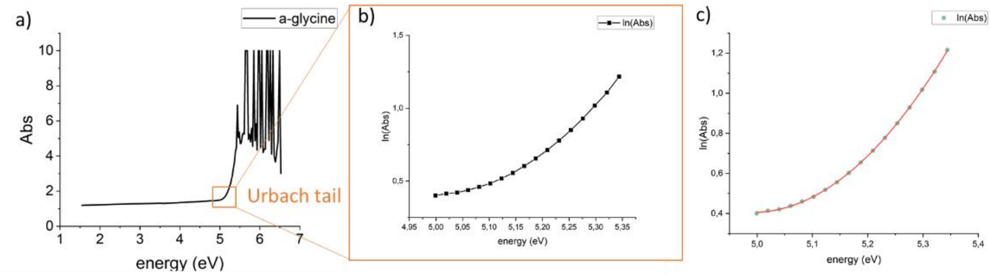

Fig.III.6 a) the vis-UV spectra of α-glycine crystal from 1.55eV to 6.52eV (800nm to 190nm), b) a zoom of Urbach edge in a range of 5eV to 5.35eV, c) fitting results of the Urbach edge.

As we have mentioned above, the ionization potentials of amino acids are around 10eV [33], from the approximative calculation of Keldysh criteria γ, with Ep=1μJ, γ=9, the process thus is multiphotonic absorption instead of tunneling. With an fs laser of 1030nm, i.e. 1.2eV, and the minimum interband of 5eV, the process in glycine crystal is approximately 5-photons absorption to overcome the interband transition and 9-photons absorption to ionize the material.

III.2.2 Laser irradiation

III.2.2.1 Laser setup

For laser irradiation, a commercial Yb-doped fiber pulsed fs laser (Satsuma, Amplitude System Ltd., Bordeaux, France) with a wavelength of 1030nm and pulse duration of 250fs was employed. The pulsed duration can be adjusted to several values. Most of the experiments in this thesis are irradiated by the pulses with duration of 250fs.

The optical path configurations are shown in fig.III.7. The reference of writing configuration is based on the green Cartesian coordinate system. Because the number of mirrors on the optical table is odd, the coordinate system changed from right-handed to left-handed. The scanning direction is along the X axis, the laser propagation is along the Z axis, and laser polarization is in the X-Y plane [144].

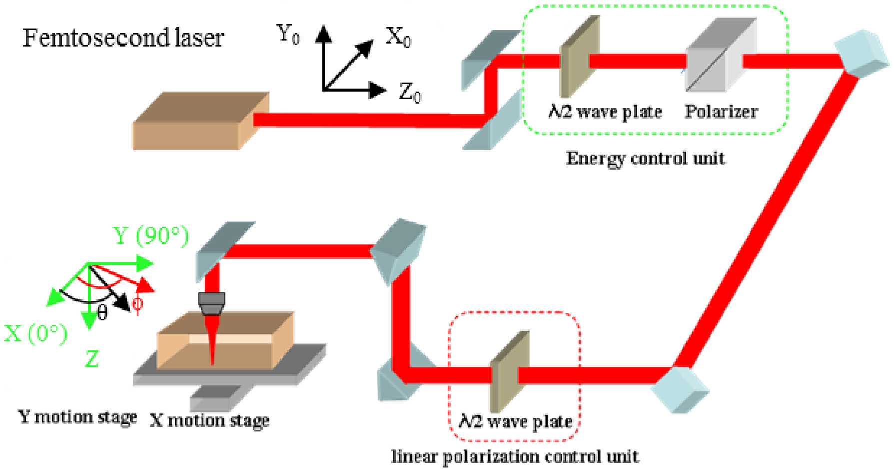

Fig.III.7 Schematic fs laser irradiation setup

Pulse energy (Ep) is controlled by a unit consisting of a λ/2 wave plate and a polarizer, the precision can be reached to 0.1nJ (there is also a limitation of the software settings). After the energy control unit, the light is linear polarized, another λ/2 wave plate is set to control the polarization. The reference of polarization according to the green coordinated was set to be: 0° is along X, 90° is along Y, degrees less than 90° is in the first/third quadrant of XY, and degrees more than 90° is in the second/fourth quadrant. The Numerical Aperture (NA) we used is 0.6.

III.2.2.2 Range of Laser parameters

The experiments start with a large range of laser parameters and narrow the interval of the parameters according to the specific interests. The pulse energy was set from 1nJ to 5µJ. The repetition rate (RR) was set from 1kHz to 1MHz. The scanning speed was set as 1µm/s to 50µm/s. polarization was set from 0° to 180°. Fig.III.8 shows the schematic diagram of our laser irradiation configuration. The samples are transparent so that the laser can be focused inside the sample. We use usually z+100µm to focus the beam below the sample surface. Due to the refractive index of the material being larger than that of air, the centre of focus is usually around 110-150µm below the surface.

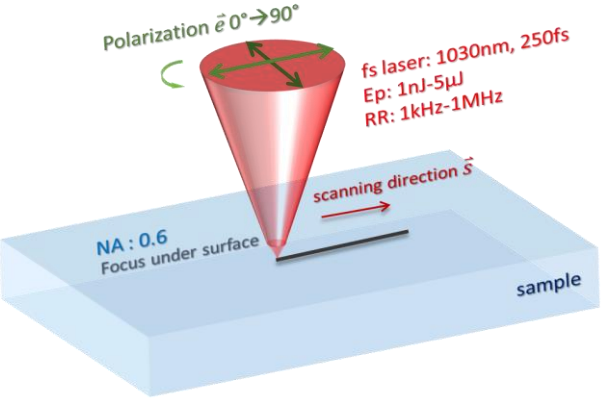

Fig.III.8 Schematic diagram of our laser irradiation configuration. The laser beam is in red, it scans the sample along the red arrow. The other laser parameters are λ=1030nm, pulse duration=250 fs, Repetition rate (RR), from 1kHz to 1 MHz, pulse energy E from 0.1µJ to 5µJ, Polarization from 0° to 180°, NA=0.6, focal beam size: ~1µm, Depth of focusing ~150 µm

III.2.3 Characterization methods

III.2.3.1 Morphology of laser-modified regions

III.2.3.1.1 Optical observation

An optical microscope equipped with a polarizer and analyzer was applied to observe the morphology in transmission mode and reflection mode. Optical properties such as linear birefringence or circular birefringence can be observed. With this method, we can detect if there is any change of the crystal axis, which mau indicate laser induced crystallization.

III.2.3.1.2 Surface and cross-section topography

Phase-shifting interferometry

As the area of laser irradiation is beneath the surface (100µm-150µm) not very deep, information can be obtained from the surface topography in order to know whether the internal structure is expanding or compressing. In addition, for some modifications that reach the surface, or the cross-section, these measurements can also be conducted if the increase/decrease of the surface does not exceed 30 µm. Phase-shifting interferometry, which relies on the wave nature of light, in particular the phenomenon of interference fringe generation following amplitude division and recombination of light from a common light source [154], is suitable for detecting a small change of the surface. Among optical areal measurement instruments, interferometry has the important property of high sensitivity irrespective of magnification [155]. In this study, interference microscopy with the Michelson interferometer was used for the measurement of the surface topography of the irradiated parts. The simplified schematic diagram of the setup is shown in fig.III.9. There are 2 sources of light, corresponding to 2 modes: monochromatic light and white light.

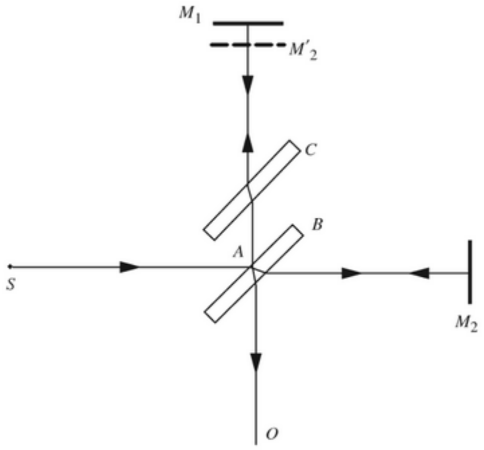

Fig.III.9 schematic of the Michelson interferometer

Atomic force microscopy (AFM)

For the same purpose, AFM is also used for the acquisition of topographical images but with better resolution. It is used to measure a cross-section of the irradiated line in the plane of scanning. The principle of AFM is to scan the surface of the sample with the cantilever fitted with a tip to obtain a 3-dimensional image with a spatial resolution ranging from a few µm (7.5 max) to nm (10 nm if the tip is a little worn). There are 2 modes: dynamic mode (tapping) and static mode (contact). In our measurement, we use only the tapping mode. The images of surface topography, phase, and amplitude were recorded with a tip (with 10nm of apex). The measurement of the oscillating deflection is performed by a laser system and a piezo servo system (Bruker Innova, 76-263kHz,1.2-29 N/m).

Scanning Electron Microscope (SEM)

Scanning Electron Microscope (SEM) along with Electron backscatter diffraction (EBSD) is expected to be applied to image the microstructure of the irradiated regions in cross-section and to measure the direction of the nanocrystals, respectively. However, because the sample cannot withstand the high voltages required for EBSD, as the pattern signal is insufficient at low voltages, and the increase can destroy material, we report here only the secondary electron images for the cross-section of the irradiated lines. The measurements were conducted in a field-emission gun scanning electron microscope (FEG-SEM ZEISS SUPRA 55 VP). The schematic diagram of an SEM is shown in Fig.III.10.

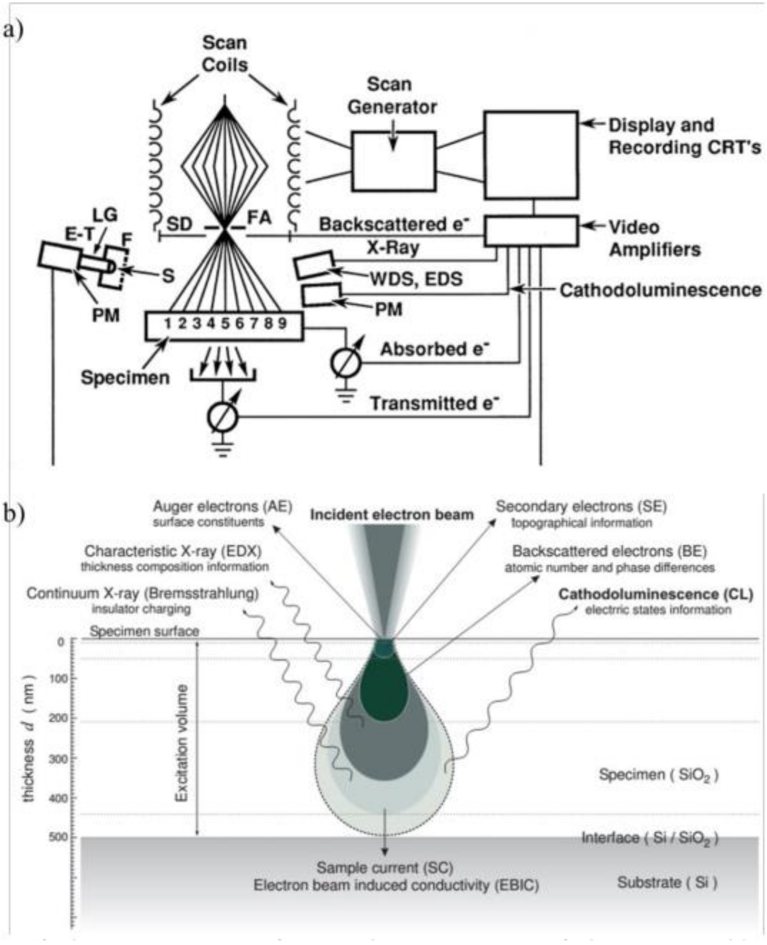

Fig.III.10 a) Schematic representations of scanning electron microscopy (SEM). FA: final aperture; SD: solid state backscattered electron detector; EDS: energy-dispersive X-ray spectrometer; WDS: wavelength-dispersive X-ray spectrometer; CRT: cathode ray tube; E-T: Everhart-Thornley secondary/backscattered electron detector, consisting of F: Faraday cage; S: scintillator; LG: light guide; and PM: photomultiplier (cited from [156]), b) processes resulting from electron bombardment (cited from [157])

III.2.3.2 Structure characterization: Raman and FTIR spectroscopy

Raman spectroscopy and FTIR spectroscopy were considered to be characterization methods to identify the transformation of the 3 polymorphic forms of glycine crystal. In Raman spectra, the differences between them are especially in low wavenumber, as shown in fig.III.11. The differences are also reflected in the infrared spectrum [123] [130], shown in fig.III.12. Therefore, we can have information on structural modification by comparing the spectra before and after irradiation.

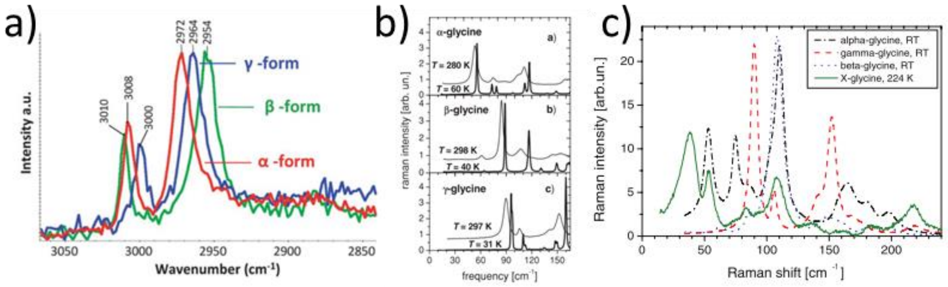

Fig.III.11 a) shifts in Raman spectra of the 3 polymorphic forms of glycine cited from [158], b) the peaks' difference according to 3 glycine polymorphs in low wavenumber 20-170cm^{-1}, cited from [159] c) the peaks' shift and intensity variation according to 3 glycine polymorphs in low wavenumber 70-250cm^{-}1, cited from [160]

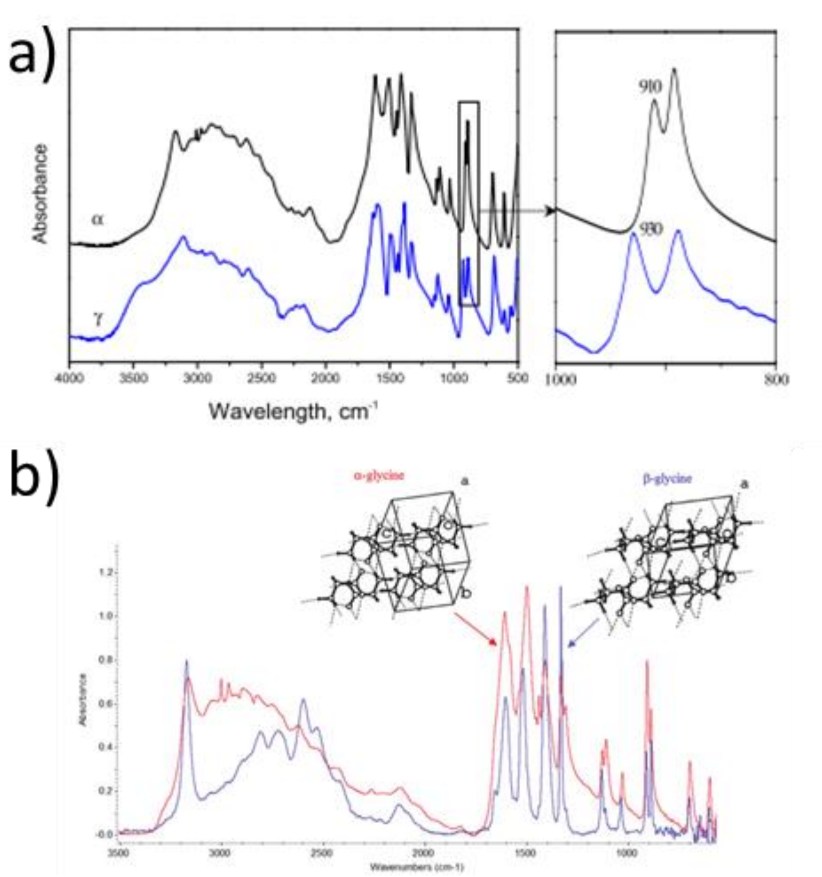

Fig.III.12 a) FTIR spectra of α- and γ- glycine, extracted from [130], b) FTIR spectra of α- and β- glycine, cited from [123]

However, for molecular modifications, information containing in a Raman spectrum or IR spectrum is not enough to identify the molecular structure. But with the existence (or not) of some feature peaks (e.g. peptide bond at 1600cm^{-1}-1700cm^{-1}, G peak at 1580cm^{-1} of graphene [161, 162], etc.), we can at least have some clues, or some supports for our conjecture based on studies. We can also make rough inferences about the possible vibration modes based on the wave numbers of the peaks in the FTIR spectrum since the peaks in the FTIR spectra reflect the vibrational absorption of the molecular bonds. For a diatomic molecule A−B, the wavenumber value can be described as follows for a simple harmonic oscillator:

$$\tilde{\nu} = \frac{1}{2\pi c}\sqrt{\frac{k}{\mu}}$$

where k is the force constant and μ is the reduced mass given by

$$\frac{1}{\mu} = \frac{1}{m_A} + \frac{1}{m_B}$$

So the difference in the IR absorption peaks recorded at the irradiated part and unirradiated part allows us to characterize the molecular or chemical bond modifications induced by the fs laser. Fig.III.13 shows the glycine crystal from the database NIST chemistry WebBook, the feature peaks associated with the vibration modes are marked on it, according to [123, 163, 164].

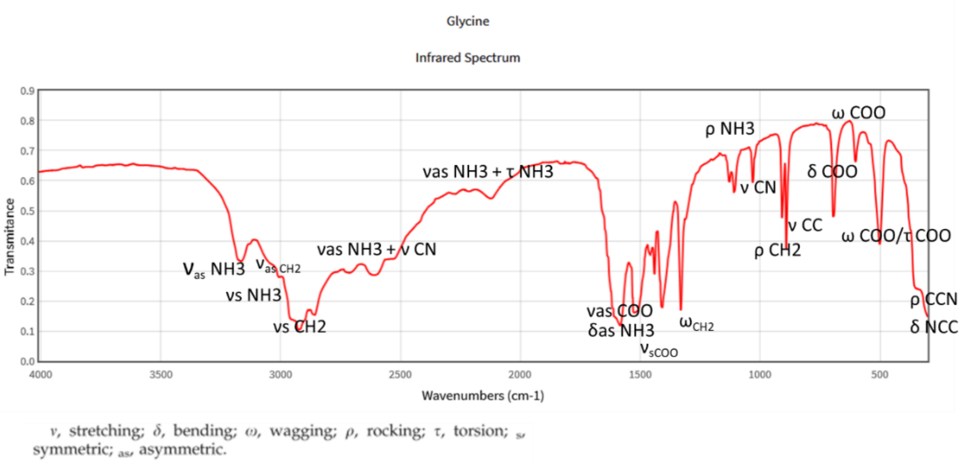

ν, stretching; δ, bending; ω, wagging; ρ, rocking; τ, torsion; $_{s}$, symmetric; $_{as}$, asymmetric.

Fig.III.13. the infrared spectrum of glycine from the database NIST chemistry WebBook, the major feature peaks are marked.

The equipment on which we performed experiments on FTIR spectroscopy is the Fourier-transform infrared (FTIR) spectrometer Frontier of PerkinElmer. It has 3 modes for obtaining signal: Transmission, reflection, and Attenuated total reflectance (ATR), and 2 modes of measurement: point mode and mapping mode. 2 detectors are equipped: one for mapping mode and one for point mode. The detector for point mode has a better sensitivity from 550-4000 cm^{-1} compared to mapping mode. In terms of identification, it is better to measure the sample in transmission mode because the IR spectra in the database generally are recorded in this way (based on sample absorption in the IR range), it is easier to compare the spectra with database in order to identify the association between absorption energy and vibration modes. If samples are measured in reflection mode, the reflection spectra were transformed into transmission spectra by Kramers–Kronig relation. However, the transmission mode is only suitable to the samples less than 10μm thick, that our samples are not able to be reached. So in this characterization, most of the experiments were applied by the reflection mode. The sample holder is KBr and sometimes a silicon glass holder. The background/baseline spectra are made by reflection on a gold plate.

III.2.3.3 Characterization of Optical properties

III.2.3.3.1 Refractive index measurement

Refractive index change (RIC) is often to be found in laser material interaction [62, 64, 165]. To know how much change in refractive index (positive or negative) and thus understand the nature of the modification (densification, porosification or elemental migration, etc.), the refractive index is measured by Quantitative Phase Microscopy (QPM). QPM is a technique to measure phase retardance to analyze the refractive index of the region after fs laser modifications. A CCD camera mounted on top of the optical microscope in transmission mode captures the sample images of the focal plane and the plane of ±3 μm to the focal plane, i.e. defocusing process. The defocusing process during measurement is automatically controlled by a piezoelectric element mounted on the objective lens (x20). The introduction of a small amount of defocus is mathematically equivalent to a differential propagation of the field. Thus, to obtain a quantitative phase image one collects an in-focus image and very slightly positively and negatively defocused images and uses these data to estimate the differential concerning the defocus of the image. The resulting data can be solved to yield the phase distribution by use of a Fourier-transform implementation [166]. In the measurement, 550nm filter with ~10nm bandwidth was introduced to select the wavelength of the non-polarized light. One limitation of the method is that the objective strength that defines the field depth thickness and the intensity gradient should be chosen in such a way that the gradient does not vary at this scale. Then, the shift of defocusing is chosen much smaller than the field depth. For instance, we chose 3μm for the x20 objective. Another limitation is that the transversal gradient should not be too fast in front of the optical resolution otherwise it is blurred.

Finally, through the phase shift Δφ of the irradiated and unirradiated region, we can easily calculate the RI difference using the expression below:

$$\Delta \mathrm{n} = \Delta\varphi \frac{\lambda_0}{2\pi l} \tag{III.1}$$

$\lambda_0$is the wavelength in vacuum, here is 550nm. l is the thickness of measurement, here is 6μm.

III.2.3.3.2 Optical properties change: Linear Birefringence Linear Dichroism Circular Birefringence Circular Dichroism

To characterize the birefringence and dichroic properties change, transmission Mueller-matrix microscopic ellipsometry with a 550nm light source was applied to the irradiated samples.

In the Mueller calculus, the polarization states of light can be represented with a four-dimensional vector, which is called the Stokes vector. Stokes parameters, which are components of the Stokes vector, describe the polarization states of the electromagnetic wave. In a Cartesian xyz coordinate system with z as the beam propagation direction, The Stokes vector, S, is composed of four Stokes components usually as I, Q, U, and V respectively. I is the total irradiance, Q describes the preference for x or y-polarization, U describes the preference for 45°- or −45°-polarization, and V for right-handed or left-handed polarization. The Stokes vectors are accompanied by a four-dimensional matrix, called the Mueller matrix, **M**, which represents the polarimetric interaction of polarized light with a given sample. The incident beam has illustrated with Stokes vector **S**$_{in}$ passes through an optical element **M** and comes out with **S**$_{out}$ as fig.III.14 shown.

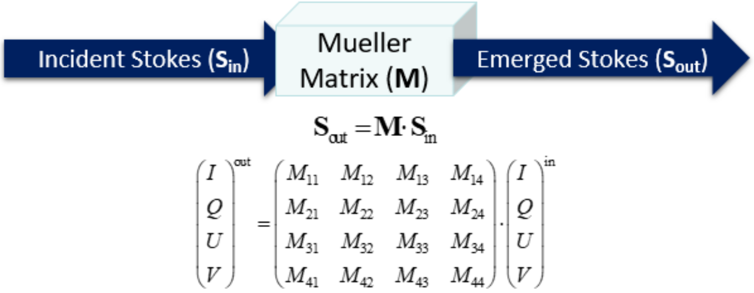

$$\mathbf{S}_{out} = \mathbf{M} \cdot \mathbf{S}_{in}$$

$$\begin{pmatrix} I \\ Q \\ U \\ V \end{pmatrix}^{out} = \begin{pmatrix} M_{11} & M_{12} & M_{13} & M_{14} \\ M_{21} & M_{22} & M_{23} & M_{24} \\ M_{31} & M_{32} & M_{33} & M_{34} \\ M_{41} & M_{42} & M_{43} & M_{44} \end{pmatrix} \cdot \begin{pmatrix} I \\ Q \\ U \\ V \end{pmatrix}^{in}$$

Fig.III.14 schematic diagram of Stokes vector passing Mueller matrix (ref)

A normalized Mueller matrix has elements denoted M_{ij} (i,j=(1,4)) and due to the normalization M_{11}=1. A differential decomposition of **M** to find its differential matrix **m** implies determining its logarithm $\boldsymbol{L}$ =ln **M** from $\frac{d\boldsymbol{M}}{dz} = \boldsymbol{m}.\boldsymbol{M}$ [167]. If **m** does not depend on z on the slice in question, i.e., **m** represents a sample that is uniform along the light propagation direction, the matrix $\boldsymbol{L}$ =**m**d_z is the cumulated differential matrix of m. m then is obtained from **m**= $\boldsymbol{L}$ /d_z, where d_z is the sample thickness. If the sample is nondepolarizing, $\boldsymbol{L}$ is Minkowski antisymmetric and contains the isotropic absorption and all linear and circular birefringence and dichroic parameters. A generalization to depolarizing sample results in this matrix logarithm $\boldsymbol{L}$, which is obtained by decomposition as $\boldsymbol{L} = \boldsymbol{L}_m + \boldsymbol{L}_u$ where $\boldsymbol{L}_m$ is Minkowski antisymmetric and $\boldsymbol{L}_u$ is Minkowski symmetric [167, 168]. Then we have the $\boldsymbol{L}_m$ matrix which is the non-depolarizing part and $\boldsymbol{L}_u$ which is depolarizing part [168]. The interesting matrix for us is $\boldsymbol{L}_m$ since it contains the optical properties.

$$\boldsymbol{L}_m = \begin{pmatrix} 0 & LD & LD' & CD \\ LD & 0 & CB & -LB' \\ LD' & -CB & 0 & LB \\ CD & LB' & -LB & 0 \end{pmatrix}$$

where LD and LD′ are linear dichroism for polarization along x–y and 45°axes, respectively. LB and LB′ are linear birefringence along x–y and 45°axes, CD is circular dichroism, and CB is circular birefringence, as shown below [169]:

LB=$\frac{2\pi}{\lambda}(n_x - n_y)l$ LB′=$\frac{2\pi}{\lambda}(n_{45} - n_{135})l$

LD=$\frac{2\pi}{\lambda}(\kappa_x - \kappa_y)l$ LD′=$\frac{2\pi}{\lambda}(\kappa_{45} - \kappa_{135})l$

CB=$\frac{2\pi}{\lambda}(n_L - n_R)l$

CD=$\frac{2\pi}{\lambda}(\kappa_L - \kappa_R)l$

It is worth noting that the quantity related to linear polarization above is not characterizing easily the optical properties as they are not obviously along the Eigen axis of the optical properties. Anisotropic properties $\mathrm{LB_T}$ or $\mathrm{LD_T}$ are obtained in amplitude by $\sqrt{LB^2 + LB'^2}$ or $\sqrt{LD^2 + LD'^2}$ and the largest axis orientation is $\mathrm{azimuth_{LB}}$ or $\mathrm{azimuth_{LD}}$ so 0.5.atan(LB′/LB) or 0.5.atan(LD′/LD).

Note that the birefringence parameters are in units of radians and are cumulated values over the optical path length and the dichroic parameters are cumulated values but dimensionless. For depolarizing media, the diagonal elements of $\boldsymbol{L}_u$ show the depolarization coefficients, diag(L_u) = (0, α1, α2, α3), which depends quadratically on the propagation distance along z.

There are 2 set-ups for getting information based on the requirements and completing the optical information collection. They are as below

1) Microscopy with one light source of 540nm
2) Spectroscopy of bulk measurement

With the 1st one, we have the spatial resolution for the sample. With the 2nd one, we have the optical properties according to a different wavelength. The resolution of this ellipsometry microscope is 1-2μm/pixel due to the setup of objective=20 times and NA=0.56. This microscope is not confocal, so the measurement result is not coming from the focused area but from the whole sample which light is coming through.

III.2.3.4 Characterization of Photoluminescence (PL) properties

III.2.3.4.1 Confocal microscopy-emission/excitation spectroscopy

Several studies have found that localized luminescence can be produced by the interaction of femtosecond lasers with polymers [13, 170], so we include the possibility of such modifications. Due to the fs laser modification of areas on the micron scale, confocal microscopy is a very effective method for observing luminescence and measuring excitation and emission spectra. Confocal microscopy, or confocal laser scanning microscopy (CLSM), is an optical imaging technique for increasing the optical resolution and contrast of a micrograph using a spatial pinhole to block out-of-focus light in image formation. Capturing multiple two-dimensional images at different depths in a sample, enables the reconstruction of three-dimensional structures (a process known as optical sectioning) within an object. This technique is used extensively in the scientific and industrial communities and typical applications are in life sciences, semiconductor inspection, and materials science. A confocal microscope structure is shown in fig.III.15.

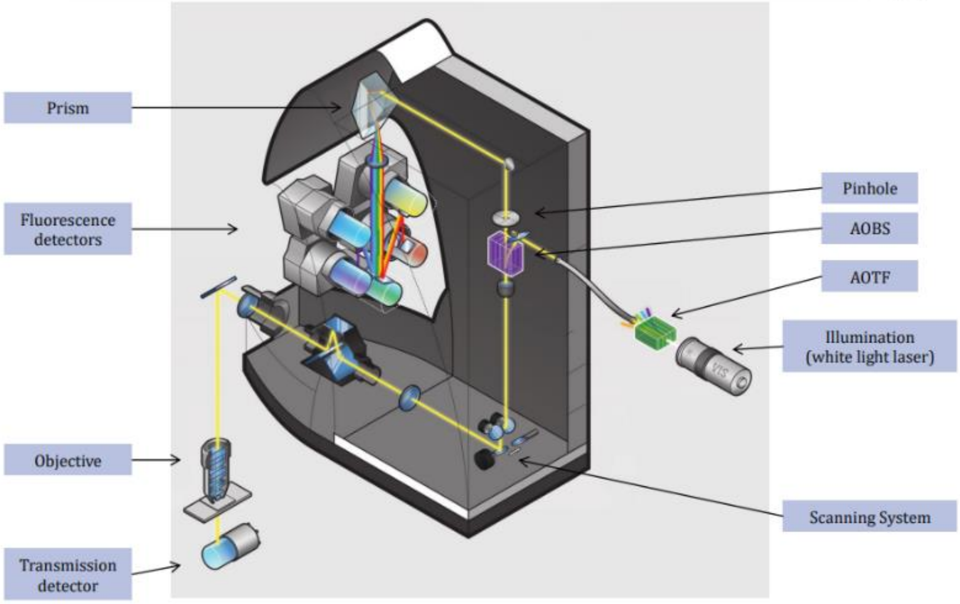

Fig.III.15 the confocal microscope composition SPX-8 Leica

Light travels through the sample under a conventional microscope as far into the specimen as it can penetrate, while a confocal microscope only focuses a smaller beam of light at one narrow depth level at a time, achieving a controlled and highly limited depth of field, as shown in fig.III.16.

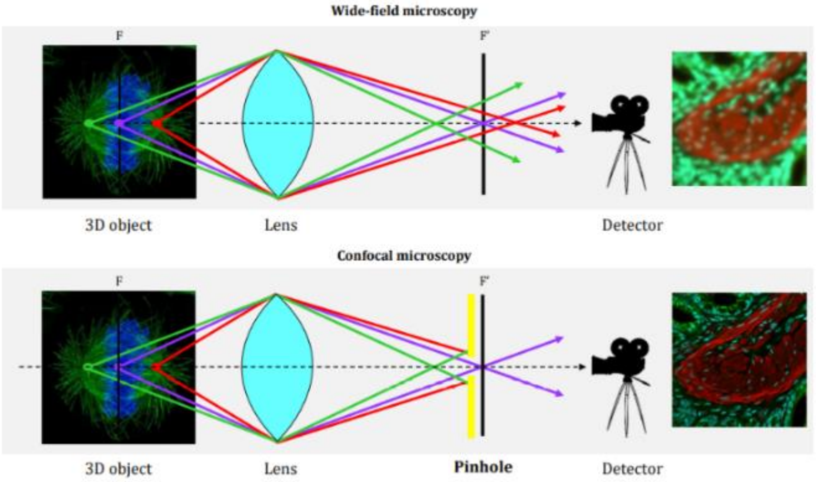

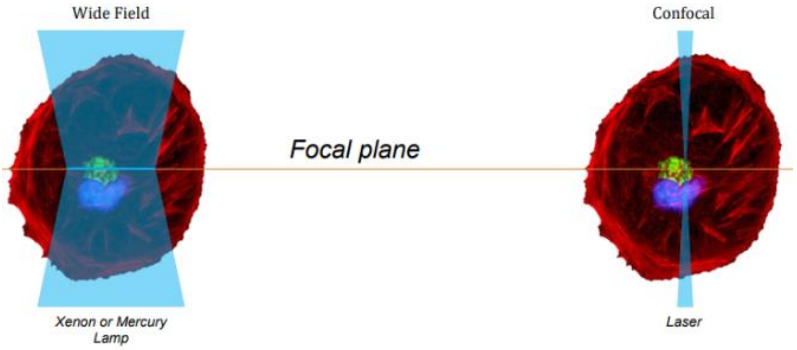

Fig.III.16 the illustration of the confocal effect

2 confocal systems were used in this thesis: one is Leica SP5 for emission spectra measurement, the other is Leica SP8-X for excitation-emission matrix measurement.

III.2.3.4.2 Details of emission spectra excited by UV and visible laser

Emission spectra in UV excitation are acquired with a commercial spectral CLSM device (TCS SP5 AOBS, Leica) equipped with Leica oil immersion apoplan objective (x20/NA 0.7) and coupled with continuous (CW) UV Ar laser (Enterprise II, Coherent), with the excitation wavelength of 351nm and 364nm. The size of confocal images is 512 × 512 pixels (1.52 x 1.52 μm), recorded on 12 bits photomultiplier with a zoom value of 1 and a pinhole value of 1 airy unit (60.66μm). Spectra are acquired in direct slow scanning mode (400 Hz) from 380 nm to 655 nm, with a 10 nm bandwidth and a 6.62 nm step-size. Data are then analyzed with Leica image-analysis software (LAS AF, Leica) to select the Region of Interest (ROI) and export the emission spectra data.

III.2.3.4.3 The excitation-emission matrix (EEM) fluorescence spectroscopy in the visible range

The excitation emission matrix measurements were performed with a confocal microscope (Leica Sp8-X) equipped with a white light pulsed supercontinuum source based on LED and Photonics Crystal Fiber, with a pulse duration of 120 fs with a repetition rate of 80MHz. The excitation wavelength was varied from 470nm to 670nm with an 8nm step. A time gate is available for collecting the light in the lap time of 12ns between two pulses. The objective used was x10 (dry, 0.4NA) and x20 (optical oil contacted with sample slide, 0.7NA). The optical axial spatial resolution with the pinhole (53.1μm) of the confocal microscope system using 10x objective, is around 564nm at λ =470nm and 674nm at λ =670 nm. The emission spectra were recorded by HyD photodetector with time gating (0-12ns) from 480nm to 740nm with 10 nm resolution. HyD photodetectors, combining PMTs and avalanche photodiodes (APDs), have better sensitivity (47% instead of 25%) and a lower level of dark noise compared to classic photomultiplier tubes (PMTs).

Excitation-emission spectra matrix or map (EEM) were recorded for each pixel of the microscope image (multispectral). This allows following the fluorescence properties variation along or across the laser written lines. More specifically, the excitation-emission map visualizes the energy level distribution of the luminophores. The number of excitation/emission centers and their positions indicate the number of the major absorption and emission energy, with which we could deduce suggestions on the energy level structure of a given PL process.

III.2.3.4.4 Radical detection: EPR/ESR

To have more information about the origin of the luminescence. Study [171] has shown that the fs pulsed laser-induced luminescence in PMMA may result from the photogeneration of emissive radicals based on an Electron paramagnetic resonance (EPR) study, so we did the same experiment to test this hypothesis.

Electron paramagnetic resonance (EPR) or electron spin resonance (ESR) spectroscopy is a method for studying materials with unpaired electrons. In the spectra, the g-value, the line width, and the spin concentration can be obtained. The g-values of EPR spectra can be used to determine whether a radical is carbon-centered or oxygen-centered e.g.. The basic equation for the electron Zeeman interaction

$$E = h\nu = g_e \beta_e B_0$$

defines the g-value, where h is the Planck constant, v is the constant mw frequency applied in the experiment, B_0 is the resonance magnetic field and β_e is the Bohr magneton. For free electrons, the g-value is

2.00232. Variations in the g-value from the 2.00232 are related to magnetic interactions involving the orbital angular momentum of the unpaired electron and its chemical environment. Organic radicals usually have g-values close to the free electron g, which depends on the location of the free radical in the organic matrix. Carbon-centered radicals have g-values that are close to the free electron g-value of 2.0023. Carbon-centered radicals with an adjacent oxygen atom have higher g-values in the range of 2.003-2.004, while oxygen-centered radicals have g-values that are >2.004 [172].

When a number of magnetic nuclei coexist in a radical and interact with the unpaired electron, the EPR spectrum will contain many lines. The magnetic field separation between two neighboring peaks in the splitting due to the same nucleus is called the *hfs*-constant of that magnetic nucleus. The hfs is a special feature of EPR and the value of the *hfs* -constant depends on the nature of the nucleus and the density of distributed on the nucleus, and the pattern provides rich information for identifying the radical. A magnetic nucleus with the quantum number I will split a single EPR line (peak) into 2IM+1 lines (peaks). For example, ^{1}H (I = 1/2) and ^{14}N (I = 1) will cause double and triple splitting, respectively.

The X-band spectra recorded in this thesis are on a Bruker ELEXSYS 500 spectrometer equipped with a Bruker ER 4116DM X band resonator, an Oxford Instrument continuous flow ESR 900 cryostat, and an Oxford ITC 503 temperature control system and were carried out under the following conditions:

Zeonex: MW freq. 9.63 GHz, MW power 1 mW, gain 50 dB, Mod. Ampl. 8 Gauss, Mod. Freq. 100 kHz at 90 K, 180 K, and 290 K.

Glycine: MW freq. 9.63 GHz, MW power 1 mW, gain 41 dB, Mod. Ampl. 4 Gauss, Mod. Freq. 100 kHz at 90 K.

With Planck constant $h = 6.62607 \times 10^{-34}\mathrm{m}^2\mathrm{kg} / \mathrm{s}$ and Bohr magneton β_e= 9.27 × 10^{-24} J /T we have:

$$g_e = \frac{h\nu}{\beta_e B_0} = \frac{71.4477\nu(GHz)}{B_0(mT)}, \nu = 9.63\ GHz.$$

III.2.3.5 Second Harmonic generation characterization

SHG amplitude is sensitive to the polarization angle of the pumping light with respect to the crystallographic orientation of materials. Therefore, we can measure the polarization-dependent SHG amplitudes to determine the anisotropy of the species and its angular distribution. Therefore, this experiment aims at obtaining information on the anisotropy orientations of new SHG species produced by fs laser irradiation in the samples.

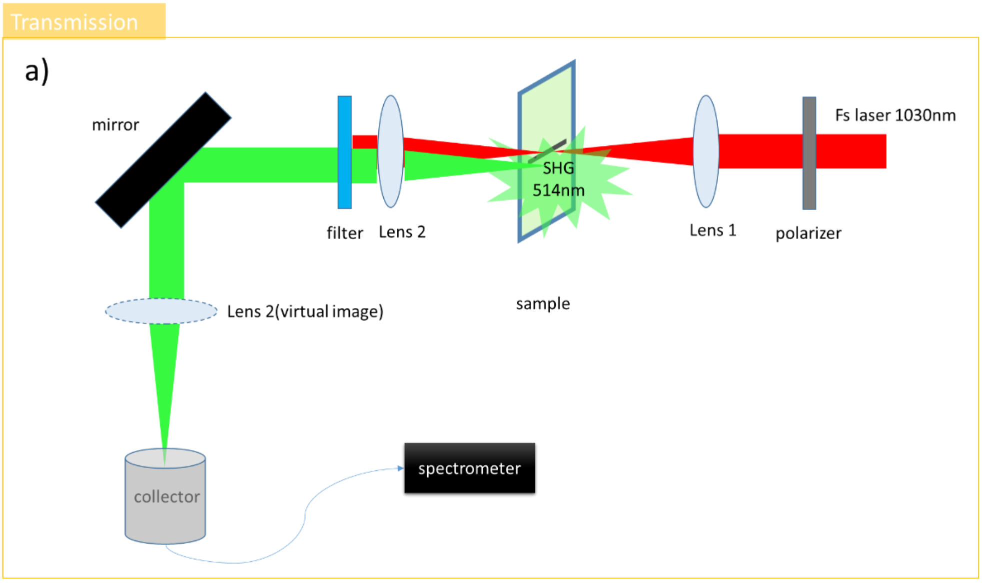

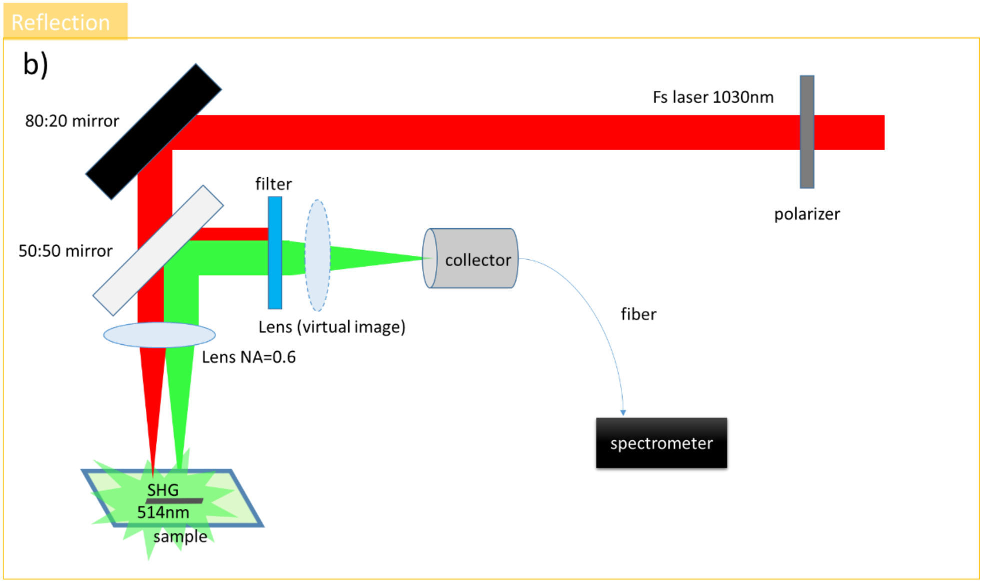

Fig.III.17 schematic diagram of the setup for SHG measurement a) transmission mode b) reflection mode

As shown in fig.III.17 the setup of characterization of SHG, the angular dependence of SHG intensity was measured in both a) transmission mode and b) reflection mode with the fundamental beam (1030 nm) propagating perpendicularly to the α-glycine sample ac plane. Generally, the SHG is times larger in transmission than reflection due to the properties of phase matching. With observation, we found the SHG induced in our sample, the reflection intensity is larger than transmission, we thus rebuilt the setup as fig.III.17b, to better collect the signals.

For each written line, we measured the SHG intensity in the XY plane according to the azimuthal angle (θ) of the probe beam polarization, up to 180° starting from the polarizer reference position in correspondence of 0°, i.e., along X. The probe beam propagation direction was set perpendicular to the XY plane and its electric field direction was parallel to this plane.

In our samples, the SHG intensity was measured in both transmission mode and reflection mode with the fundamental beam (1030 nm) propagating perpendicularly to the sample XY plane with RR=100kHz and Ep=10nJ-50nJ, avoiding any secondary permanent modification on the sample. The spot size (diameter) of the probing beam was approximately 30 μm, well overlapping each laser track. The transmitted SHG light (515 nm) was recorded after passing an IR low pass filter mounted before the spectrometer (Ocean) collector.

III.2.3.6 Molecule identification attempt with Mass Spectrometry

Since we observed fluid production and we were not sure if it was a liquid or a gas, we tried to use a sensitive gas phase mass spectrometer with heating stage equipped to detect it. A mass spectrometer converts molecules to ions so that they can be moved and manipulated by external electric and magnetic fields. The three essential functions of a mass spectrometer and the associated components are: 1) the ion source, a small sample is ionized, usually positively by loss of an electron; 2) the mass analyzer, the ions are sorted and separated according to their mass and charge; 3) the detector, the separated ions are then measured, and the results are displayed on a chart.

A mass spectrum will give information about the existence of an ion having a specific mass-to-charge ratio (m/z) and the intensity indicates the relative abundance of the ion.

The spectrometer is analyzing gas with a specific mass range of 1-100. The sample is quickly broken crossing the irradiated area and put into a confined tube connected to the vacuum chamber of the mass spectrometer (quadrupole, electron impact ionization). We monitor the spectral change and some certain masses in real-time. There is a heating system that slowly heats the tube to speed up the release of gas from the sample or maybe vaporate the produced liquid (if any).

III.3 RESULTS

III.3.1 Landscape of modifications

III.3.1.1 Thresholds and the definitions of the types of modifications

The first set of experiments is to write lines with a large range of laser parameters to investigate the different types of modifications that can be produced. Then, energy thresholds according to the pulse repetition rate between the various domains were defined i.e. what we called the landscape of the modifications. In this case, the other parameters influencing the thresholds, such as laser wavelength, pulse duration, focus depth, scanning speed, the angle between light polarization and lattice axes, or scanning direction, are fixed. In this experiment, pulse energy varied from 0.1 to 1µJ with the step of 0.1µJ, and laser repetition rate (RR) varied from 1kHz to 1MHz. when scanning speed=10µm/s, 3 types of modifications were defined by their morphology through optical microscope observations: type 1 to 3 ordered according to average power from low to high, shown in fig.III.18a.

Type 1: the first threshold is the occurrence of index change, the irradiated lines are smooth, and transparent with a width of the beam size (around 1µm). Below this threshold, no visible permanent transformation is generated. Note that this thin line, shown in fig.III.18d, is 'brighter' than the substrate. It indicates an increase of refractive index. However, during the observation, we found it can also be 'darker' when changing the observation focus.

Type 2: the second threshold is the occurrence of opaque appearance. The irradiated lines have a width of about 4µm-10µm according to Ep, as shown in Fig.III.18c.

Type 3: the type 3 modification is defined by having an irregular swelling in the irradiated lines with a width as large as 20µm, this transformation is induced only from high RR (>400kHz). It may result from a thermal effect added to the type 2 transition.

The modification thresholds of these 3 types of lines are shown with the black, red, green, and blue profiles in Fig.III.18b.

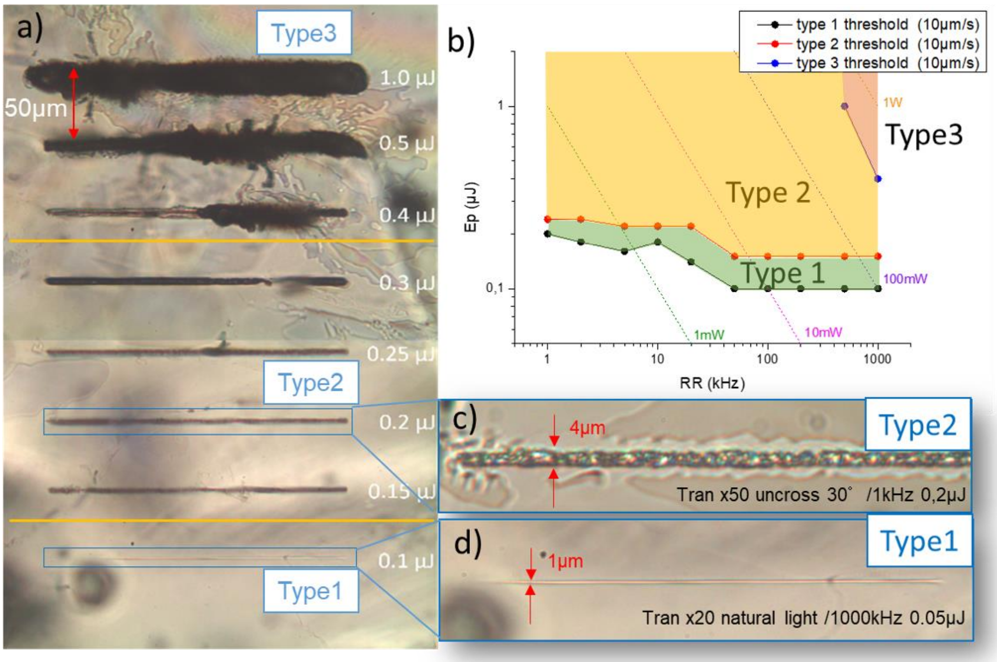

Fig.III.18 a) microscopic photo of type 1-3 modification examples (RR=1MHz, scanning speed=10µm/s) under natural light and transmission mode. b) landscape of laser irradiation in α-glycine crystal with scanning direction // $\vec{a}$ c) a zoom of type 2 line d) a zoom of type 1 line

With slower scanning speed, e.g. 1-2µm/s, we observed a new kind of modification having crystallized morphology, we call it type 4, shown in fig.III.19. The appearance of this modification is a feather-like or teeth-like solid formed along the irradiation line, or even growing out of it. It is likely to be polycrystals, as shown in the insert photo in fig.III.19a. These recrystallized polycrystals have a size around 10µm wide and 50-100µm long.

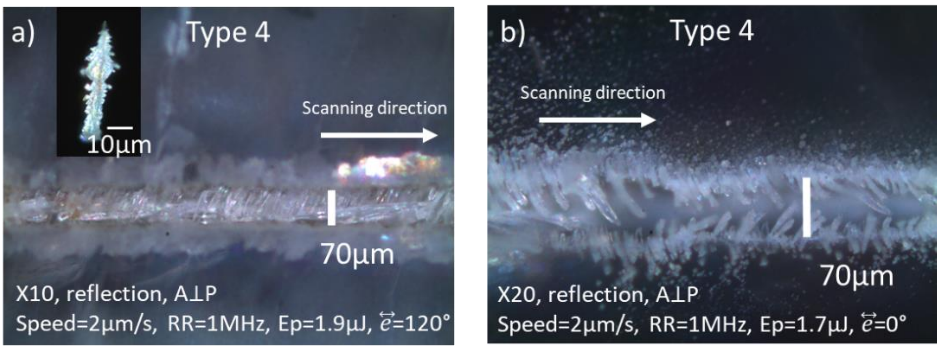

Fig.III.19 a) and b) microscopic photos of type 4 modification examples under polarized light with an analyzer perpendicular to the polarizer, in reflection mode, focus is on the sample surface. Laser irradiation parameters are marked in the photos. The photos were taken just after irradiation.

Same as type 3, this modification is induced only from high RR (>400kHz), likely resulting from thermal effect. The threshold in 1MHz is 1.2µJ. In addition, a parameter such as slower scanning speed increases the chances of generation (e.g. 2µm/s with RR=1MHz and Ep>1.2µm, which corresponds to a sure generation). Interestingly, SHG was observed during the irradiation of type 4, although it is occasionally observed in type 3, and the intensity of SHG is not as high as in type 4.

Not all type 4 modifications are extended to the surface, sometimes only parts of the surface are open. In this case, we still found recrystallization below the surface within the irradiation line, so we observed the cross-section of type 4, as shown in fig.III.20.

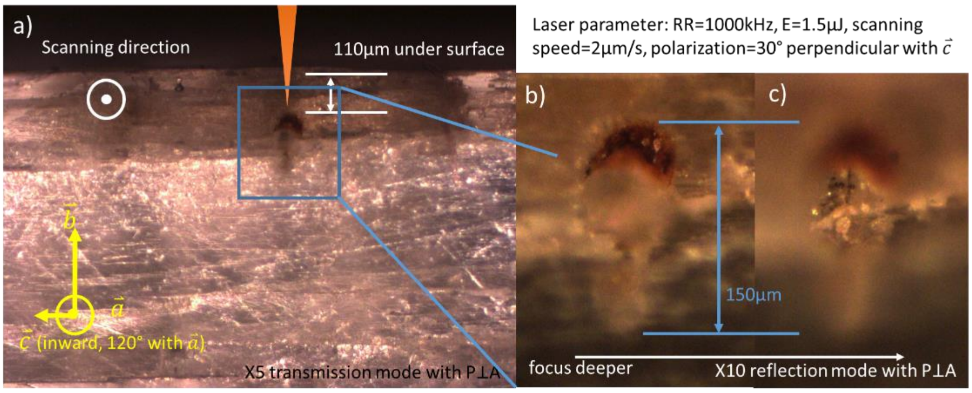

Laser parameter: RR=1000kHz, E=1.5μJ, scanning speed=2μm/s, polarization=30° perpendicular with $\vec{c}$

Fig.III.20 picture cross-section of a type 4 laser trace a) under objective with multiplication x10 b)-c) a zoom of the blue marked area with a different focus

From the cross-section observation, fig.III.20b, the cross-section of type 4 trace is a waterdrop-shape, with crystalline objects inside and in the surrounding. The top of the cross-section, i.e. closer to the laser entrance surface, is darker, implying less reflection or scattering of illumination light. This upper part may have absorbed more energy and thus had heat accumulation and produced a molecular change.

III.3.1.2 Polarization/crystal axes direction dependence of the thresholds

We investigated the dependence of the irradiation polarization direction (referring to the crystal axis $\vec{c}$) of the modification thresholds.

The sample is polished with bc plane perpendicular to the laser propagation so that the irradiated lines are on the bc plane and defined that the direction 0° is along $\vec{c}$. A group of lines with Ep and RR varying are irradiated. Thresholds of type 2 modification with the polarization of 0°/30°/60°/90° with a scanning direction of 0° are shown in fig.III.21, respectively. Note that in this experiment the laser pulse duration is 800fs so the threshold is higher than the one in fig.III.18 (250fs).

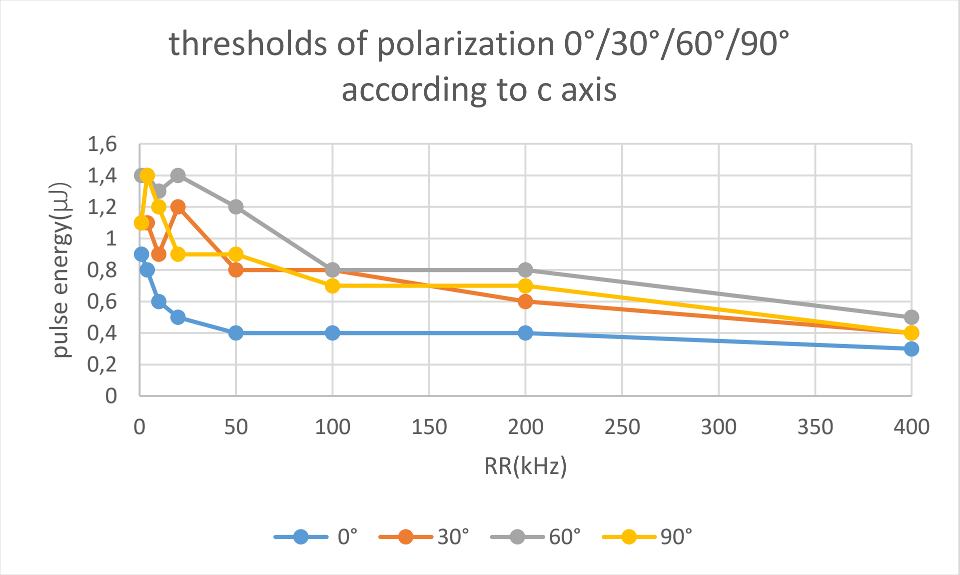

Fig.III.21 thresholds of type 2 modification of polarization of 0°, 30°, 60° and 90° to $\vec{c}$.

The morphology of irradiated lines along with fig.III.21 indicate that the threshold with polarization dependence are ranked by **60°>90°>30°>0°** (refer to $\vec{c}$).

The same experiments are performed by changing the scanning direction to -30° and 90° of $\vec{c}$. 90° of $\vec{c}$ is parallel with $\vec{b}$. Since the setting of polarization direction, 0° 30° 60° and 90° is according to system axes, transform to crystal axis reference of $\vec{c}$ is -30°, 0°, 30°, 60° in scanning direction -30° and 90°, 60°, 30° and 0° in scanning direction 90°.

Results show that In scanning direction of -30°, the threshold ranked **60°>30°>-30°>0°** (refer to $\vec{c}$); In scanning direction=90°, threshold ranked **90°>60°>30°>0°** (refer to $\vec{c}$). We thus consider that the lowest threshold for modifications in the bc plane is when the polarization is parallel to $\vec{c}$, i.e. the direction of crystal growth, compared to other directions. And the scanning direction change does not affect it.

III.3.1.3 Influence of scanning speed

As mentioned in Chapter II, at the center of focus the material absorbs energy and thus achieves thermal stability at a short time scale as μs to ms. Therefore, the slight change (e.g. 10μm/s to 2μm/s) in scanning speed does not affect the thermal effect at the center of the beam focus. However, to achieve thermal stability out of the center of focus, the pulses required are much more, i.e. the time required much longer. As a result, the scanning speed will affect these areas and some phenomena based on thermal effects (e.g. recrystallization of type 4) is favorable to occur in the case of lower speed scanning and also a decrease of threshold. Fig.III.22a) and b) shows the threshold of modification types under scanning speed of 10μm/s and 2μm/s, respectively. Note that the thresholds are more accurate due to the smaller pulse energy interval in experiment of 10μm/s, so that some of the increase in thresholds at lower energies comes simply from the larger interval of energy value.

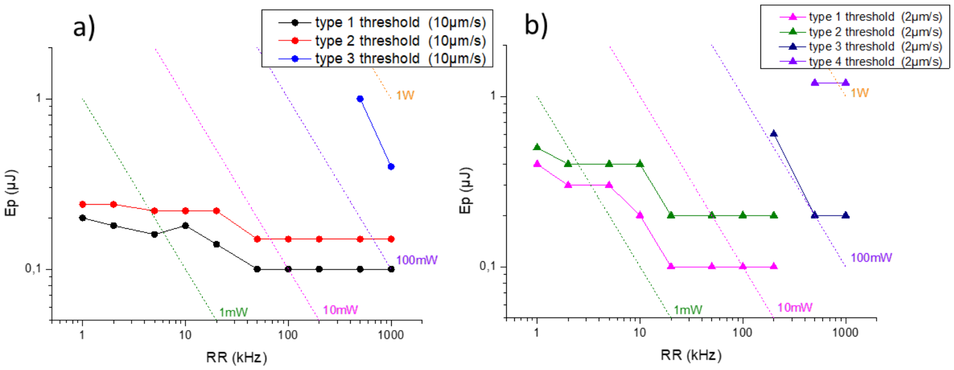

Fig.III.22 the landscape of modification types under scanning speed of a) 10μm/s and b) 2μm/s with polarization=0°

III.3.2 Topography of the surface and cross-section

Measurement of the Swelling of type 4

The surface of one irradiated line of type 4 modification (1MHz, 1.3μJ, speed=2μm/s) was measured by Phase Shifting Interferometer, results are displayed in fig.III.23. The height along x (marked in fig.III.23) shows that the teeth-like crystals in irradiated lines are about 1.8μm under the surface.

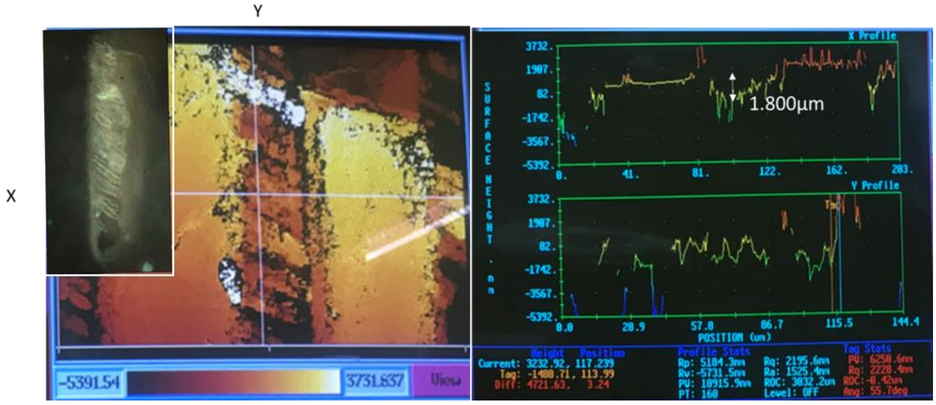

Fig.III.23 the surface topography of type 4 line (1MHz, 1.3µJ speed=2µm/s), insert photo: reflection mode with polarized light with A⊥P.

Cross-section structure measurement by Atomic Force Microscopy

One sample was cleaved along the irradiation ac plane, the irradiated area is thus exposed on the surface. A type 2 modification which is discontinuous (2µm/s, 1MHz, and 0.2µJ, fig.III.24a and b), was measured by AFM. Results show that the opaque irradiated region is a hole about 3µm-6µm deep, while the surrounding area shows a smaller height 1-3µm higher than the unirradiated region, as shown in fig.III.24d.

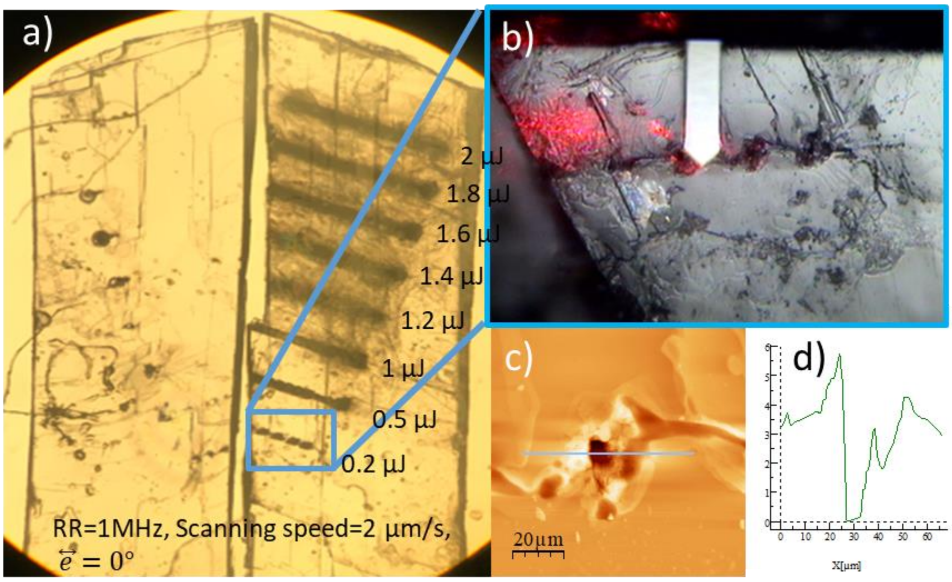

Fig.III.24 Cross-section structure measurement by Atomic Force Microscopy a) microscopic picture under natural light in the transmission mode; b) the region under AFM measurement (reflection); c) the 2D figure of height; d) the height value along the line location marked in c)

SE image of irradiated line cross-section

The irradiation lines for displaying the topography of the cross-section under SEM are along $\vec{b}$ axis. Parameters of laser irradiation: scanning speed=10μm/s, RR=200kHz, E=1.5, 0.6, 0.8, 1, 2 ,3 μJ polarization=0°, depth is around 175μm.

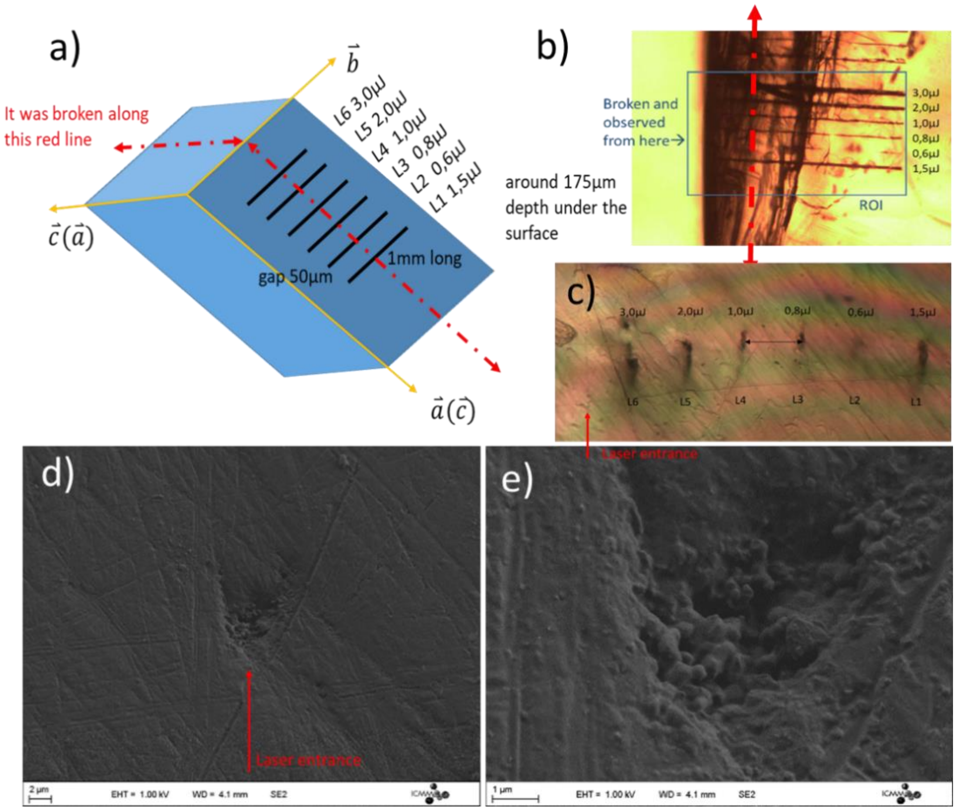

Fig.III.25 a) sketch of the irradiation lines in sample b) the microscopic picture (transmission mode, natural light, magnitude x5) of the sample which was broken with cross-section surface exposed; c) the microscopic picture of a cross-section of irradiation lines (reflection mode, natural light, magnitude x20) d) SE image of the cross-section of L1(1.5μJ) WD=4.1mm; EHT=1KV e) zoom of the cross-section

From Fig.III.25 d we can see that the shape of the cross-section looks like a triangle but with a curved bottom edge. The sketch below (Fig.III.26) helps to understand the appearance of a laser trace. It can be considered that only the head of the laser beam left a trace. Or we can suspect boldly that the intensity of the light far from the center was not enough for the transition. It is different from the one in glass, which is a waterdrop-shape and corresponds to energy dispersion.

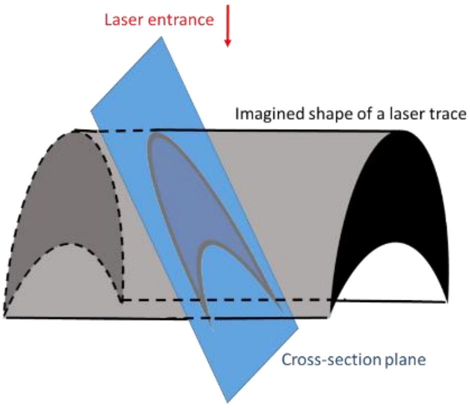

Fig.III.26 A sketch of the cross-section shape

When we look inside the laser trace (Fig.III.25 e), there are many round particle-like things inside, the diameter of them is around 0.3μm. Since it exists only inside the laser trace, it is considered to be produced by the laser.

III.3.3 Optical properties

III.3.3.1 Refractive index change (RIC)

Fig.III.27c shows the phase shift images (0.167μm/pixel) of the area (fig.III.27b) , the phase shift value Δφ represented by the grey degree bar. From a dedicated Matlab® program analysis, we get the phase shift profile shown (fig.III.27d). It allows us to estimate the phase shift amplitude between 14 rad in a type 2 line and only 0.48 rad in a type 1 line (red marked).

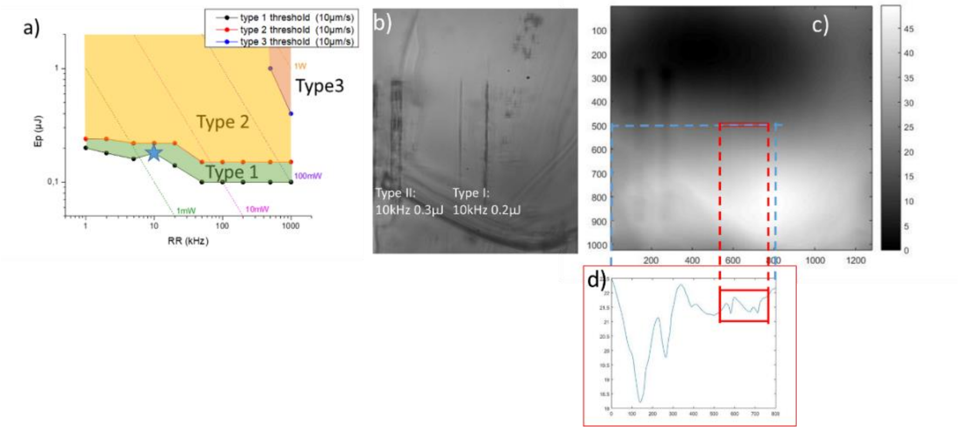

Fig.III.27 a) location in the landscape of the measured lines. The star indicates the position of the experiment in the landscape. b) Microscope photo of irradiation lines (scanning speed=1μm/s, RR=1MHz, Ep=4nJ) under green wavelength (550nm). c) The phase shift image. d) The phase shift profile along pixels at y=500 (horizontal profile). e) The phase shift profile (unit rad) along pixel y=700. The red square enhanced the profile along the red square in c).

Choosing the region marked in red in fig.III.27d for RIC calculation, we have $\Delta\varphi \approx -0.48\,\mathrm{rad}$. Since the phase shift image is coming from defocusing image $\pm 3\mu m$ up and down from the focus (fig.III.27b), 6 μm distance has been moved by a piezoelectric element, we estimate the RIC of the irradiated transparent region to be about 0.007, according to the equation.III.1 in section 2.3.3.1. A decrease in RI may indicate creation of porosity.

III.3.3.2 Optical properties: birefringence and dichroism

The Mueller matrix of type 2 irradiated lines (50kHz, 30μJ, 10μm/s, polarization=0°) was measured, and their optical properties LB, LD, CB, and CD were obtained after decomposition are shown in fig.III.28.

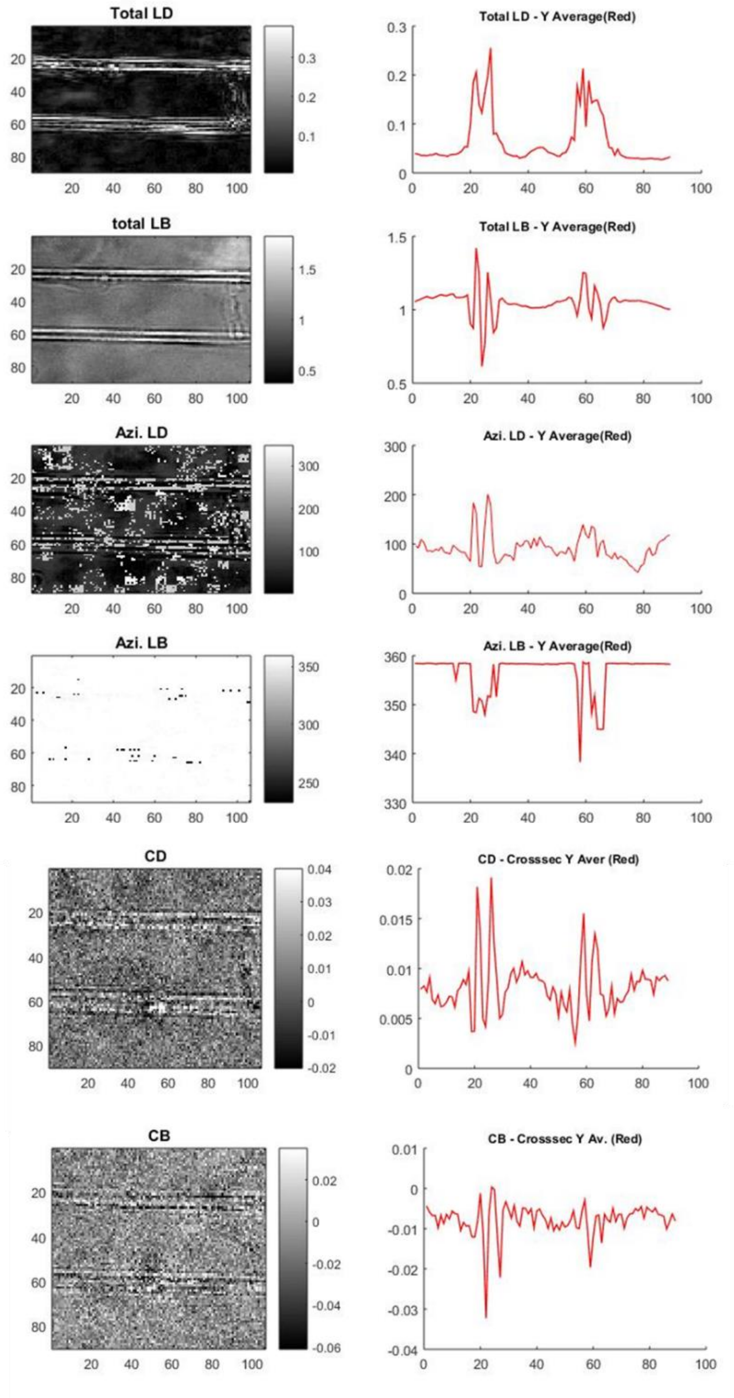

Fig.III.28 the value of optical properties of the irradiated sample with type 2 lines, red profiles are the value according to y-axis of the photo and averaged by each x. the azimuth angle (in °) is the one between the fast axis and the x-axis of the measuring system.

From fig.III.28, the total LD value of the substrate is not 0 due to the anisotropy of the ac plane, and so does the total LB. The irradiated lines have an optical properties change compared to the substrate. The total LD increase of around 0.1-0.2 rad difference and a smaller increase in the middle from the unirradiated region. It could come from light di-attenuation (absorption or scattering) in the x and y direction (refer to system) at 550nm.

The total LB in irradiated lines is distributed like a sandwich, with the edge and center of the line having less LB than the unirradiated region while the rest of the line has an increase.

The azimuth angle of the background crystal is almost 0° which means the fast axis (crystal a-axis) is parallel to the x-axis of the system. The fast axis of parts of the irradiated lines has an azimuth angle about 10° to the c-axis.

The same characterization was conducted on different irradiation lines with some other fs laser parameters, however, we did not find a correlation with polarization. The results of this section therefore remain open to question.

III.3.4 Photoluminescence

In the course of investigation of the laser-induced modifications, we found strong luminescence background of type 2 and type 3 lines in the Raman spectrum excited by 488nm laser. We know that glycine absorption starts from 250nm, which means that the fs laser-modified region (type 2 and type 3) produces new molecules. Thus we used confocal microscopy to characterize the localized luminescence from fs laser-modified lines.

Fig.III.29 display the luminescence from type 2- type 4 detected by confocal microscopy.

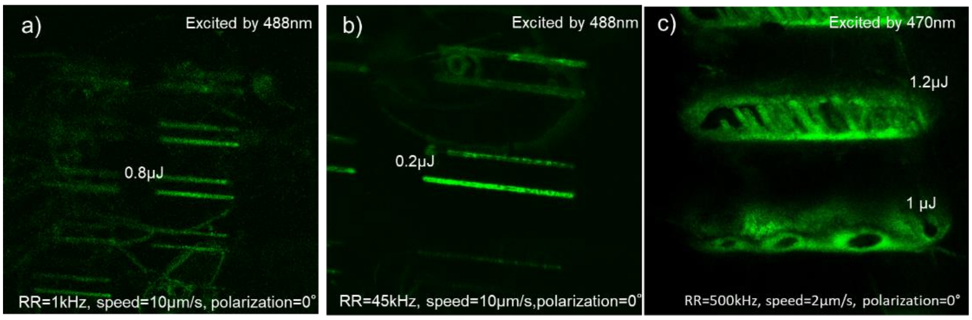

Fig.III.29 irradiation lines under confocal microscopy in luminescence mode with excitation of 470nm-488nm and detection range 500-600nm, the green color is from software effect. a) type 2 lines irradiated by low RR 1kHz, b) type 2 lines irradiated by RR=45kHz, c) type 4 irradiated by 1MHz.

Results show that PL can be created in all modification types including type 2 to type 4, no matter low RR or high RR. And once the permanent modifications are made, PL is created. We therefore believe that the production of luminescence results from direct light action of a single pulse instead of pulse cumulative effects. N.B: type 1 we detected also luminescence but the intensity is very small.

III.3.4.1 Emission spectra

Emission spectra are recorded in the irradiated lines of various laser parameters.

Fig.III.30b displays the sample with fs-laser irradiated lines under a confocal microscope in transmission mode and the display color of luminescence intensity is selected as green. Fig.III.30a reports the luminescence emission spectra under 488nm laser excitation of the regions of interest (ROIs) which were marked with rectangles of different colors. In Fig.III.30b. The spectra were recorded with a resolution of 5nm and normalized. From Fig.III.30a, we observe that the spectra of luminescent regions are peaking at around 560 nm.

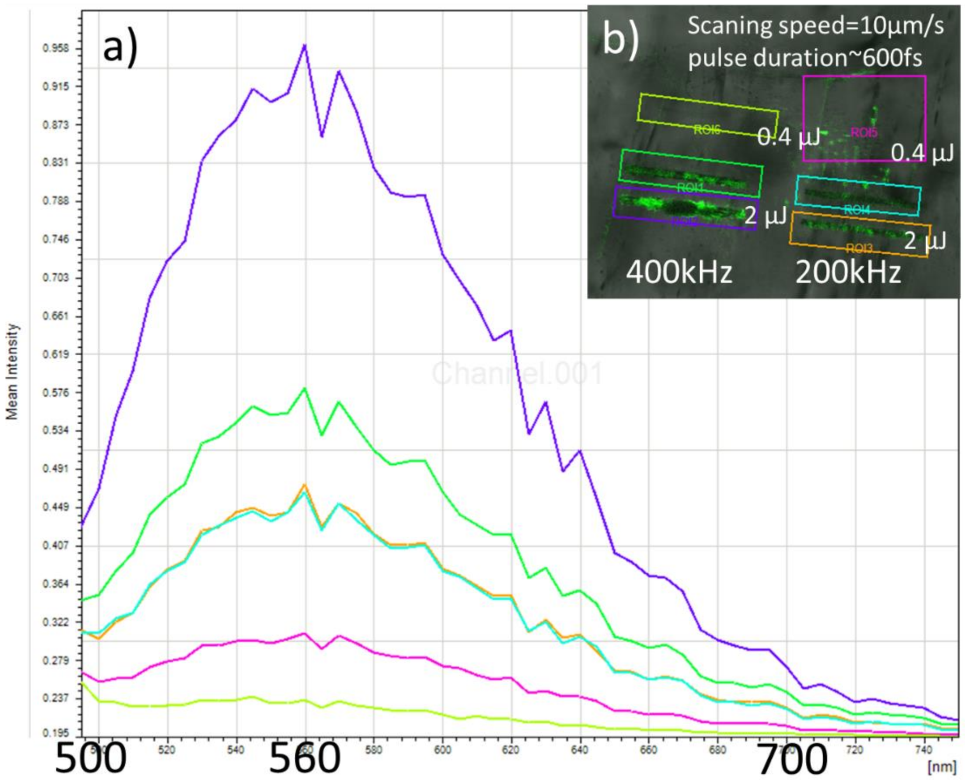

Fig.III.30 a) emission spectra of ROIs marked in b), b) irradiated lines with laser parameters indicated

The same measurements are carried out on the irradiation lines with other laser parameters, these emission spectra have only one peak as in fig.III.30a. Their maximum values are summarized in Fig.III.31.

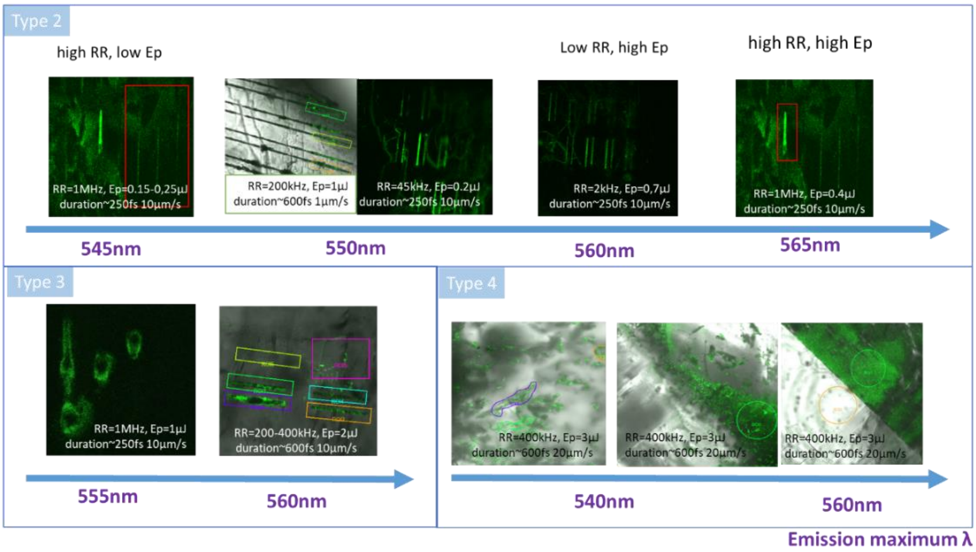

Fig.III.31 peak value of Emission spectrum in different irradiation lines, laser parameters are marked in the photo

The maximum of the emission spectrum between type 2, type 3 and type 4 modification doesn't have a big difference, e.g. the one in type 4 crystalline objects shifted around 10-20nm to the shorter wavelength. As the environment of the luminescence changes, from the confined interior, with crystallization to reach the exterior, we suggest that a small shift of emission peak may result from it.

III.3.4.2 Excitation-emission matrix in the different modification types

Fig.III.32 shows the excitation-emission spectral Matrix (EEM) from type 2 lines written at 1-2KHz and 4μJ. We see that 2 species with excitation centered at around 475nm and 520nm with a broad emission from 520nm to 630nm and 545nm to 620nm, respectively.

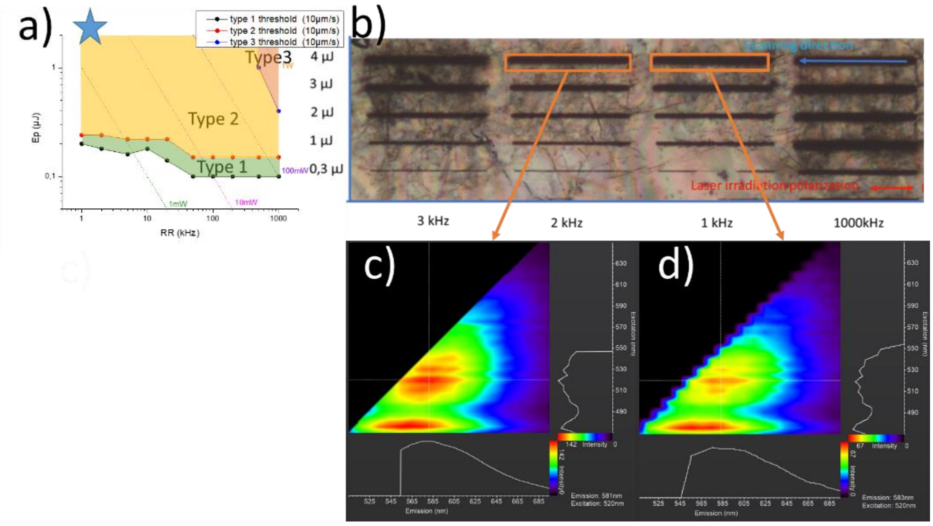

Fig.III.32 a) location with a blue star in the landscape of the investigated lines (type 2: 4µJ, 1kHz-2kHz); b) the microscopic photo of the investigated llines; c)-d) EEM from the line body written at 2kHz, and 1kHz, respectively.

The vertical axis in EEM c) and d) corresponds to the excitation wavelength from 470nm to 650nm, whereas the horizontal axis is for the emission wavelength from 500nm to 700nm. Two spectra are plotted: an emission one excited at 520nm (excitation maximum) and an excitation one detected at 581nm (emission maximum). The intensity scale is linear.

III.3.4.3 Lifetimes

The lifetimes of the luminescence were detected by Time-Correlated Single Photon Counting (TCSPC) by two-photon absorption with an IR laser (800nm). The instrument response function (IRF) was obtained with the erythrosine in a saturated potassium Iodide solution.

We observed two domains, type 2 and type 4 (parameters are marked in the landscape, shown in fig.III.33a). The luminescence spectrum is peaking at 540 nm under 488 nm excitation. The lifetime decay was recorded and it can be fitted by 2 exponential functions. 2 lifetime thus is deduced. One is around 0.4 ns and another one is around 2ns. It indicates that 2 chromophores are appearing in the irradiated parts. It is the same for type 2 and type 4 but the lifetime values are different.

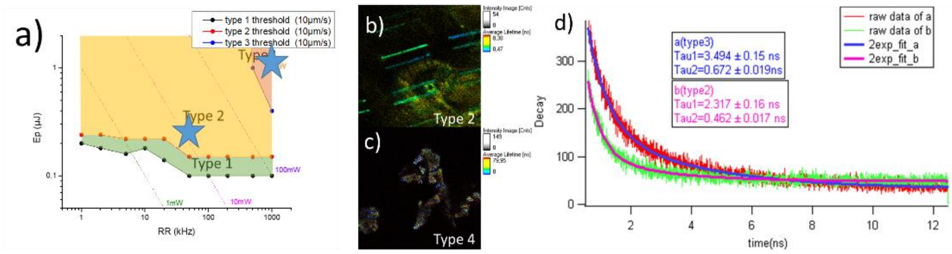

Fig.III.33 a) locations of the parameters of type 2 (sample b) and type 4 (sample a) regimes b-c) lifetime distribution of the measured areas d) the decay vs time profile of sample shown in b) and c) and its 1-2 exponential fitting.

Specifically, the measured decay y(x) can be described in the below equation, with an assumption of n lifetimes:

$$y(x) = y_0 + A_1 e^{-\frac{x}{\tau_1}} + A_2 e^{-\frac{x}{\tau_2}} + \cdots + A_n e^{-\frac{x}{\tau_n}}$$

Here, y_0 is the background, A_1 to A_n are the coefficients. τ_1 to τ_n imply the lifetimes of the chromophores. 1 exponential fitting to 5 exponential fittings has been performed as shown in fig.III.34. The 1-exponential fitting doesn't fit so well, the chi-square (chisq in b) which implies the error distribution is more than 400000. Then, we tried 2-exponential fitting which fits well with chi-square less than 250000. We tried more exponential fitting, the fitting lines are not changing much as we can see from fig.III.34 that the 2-5 exponential fitting profiles are overlapping. The chi-squares, background, A1 and $\tau_1$of them which are the same can also indicate that this decay fitted by 2 exponentials is appropriate.

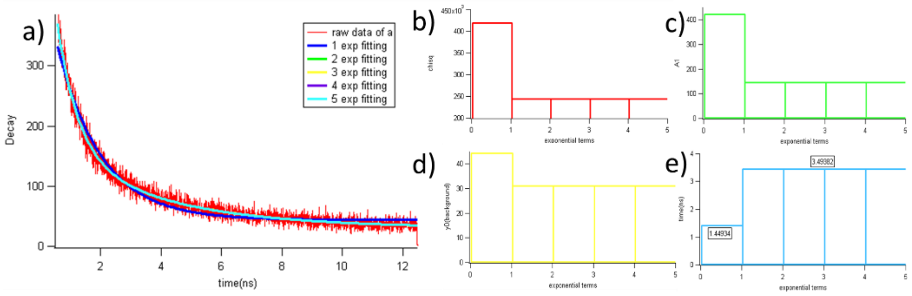

Fig.III.34 a) decay vs time profile of sample a (type4) and its 1-5 exponential fitting; b)-e) the chi-sqares, background y0, coefficient A_1, lifetime τ1 of 1-5 exponential fitting, respectively.

Therefore, we can deduce that there are 2 lifetimes of the products which means there are 2 different conformations of the chromophores. one with a short lifetime (0.4-0.7ns) and another one with a longer one (1.5-3.5ns).

III.3.4.4 Spatial Distribution of luminescence

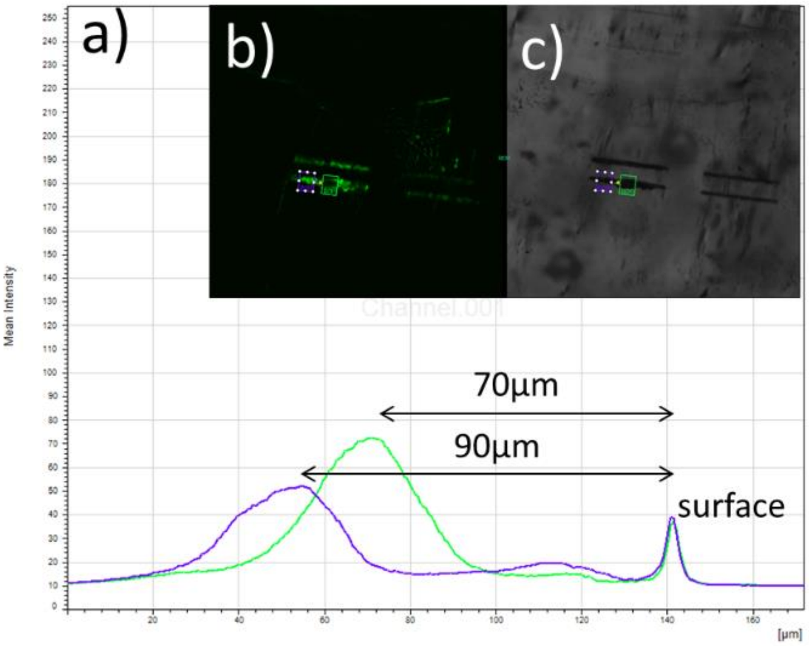

Fig.III.35 PL distribution in type 3 lines and the swelling part of type 3 line.

Fig.III.35a displays the luminescence intensity along z direction, the purple profile and green profile is correlated to the ROIs marked by purple and green rectangle. The small overlapping peaks at around 140 are a reflection of the surface, thus it defined the location of the surface. From the position of the luminescence peak at 50 and 70, we know the luminescence in the irradiation line is around 90μm while in the swelling part is 70μm beneath the surface, and the luminescence is distributed only to the internal surface, the side close to the surface where is the laser entrance. We thus suggest maybe it went through the same process as [63] in polymer: the laser-induced plasma expands outwards, a temperature gradient is formed, then the material in the focal volume is vaporized and collected on the interface.

III.3.4.4.1 3D distribution

A 3D picture of irradiated lines were scanned by a confocal microscope to show the location of the luminescent region, which was induced by fs laser irradiation.

We can see that the luminescence of type 4 lines (a to d) is located in the teeth-like polycrystals and the edge of the irradiated line, they are all on the surface. A type 3 line (500kHz, 1.1µJ) has parts of luminescence under the surface and parts of the luminescence on the surface of the sample, consistent with the morphology observed under the microscope. While in type 2 lines (e and f), the luminescence created 100µm under the surface, with 54µm deep in the z direction.

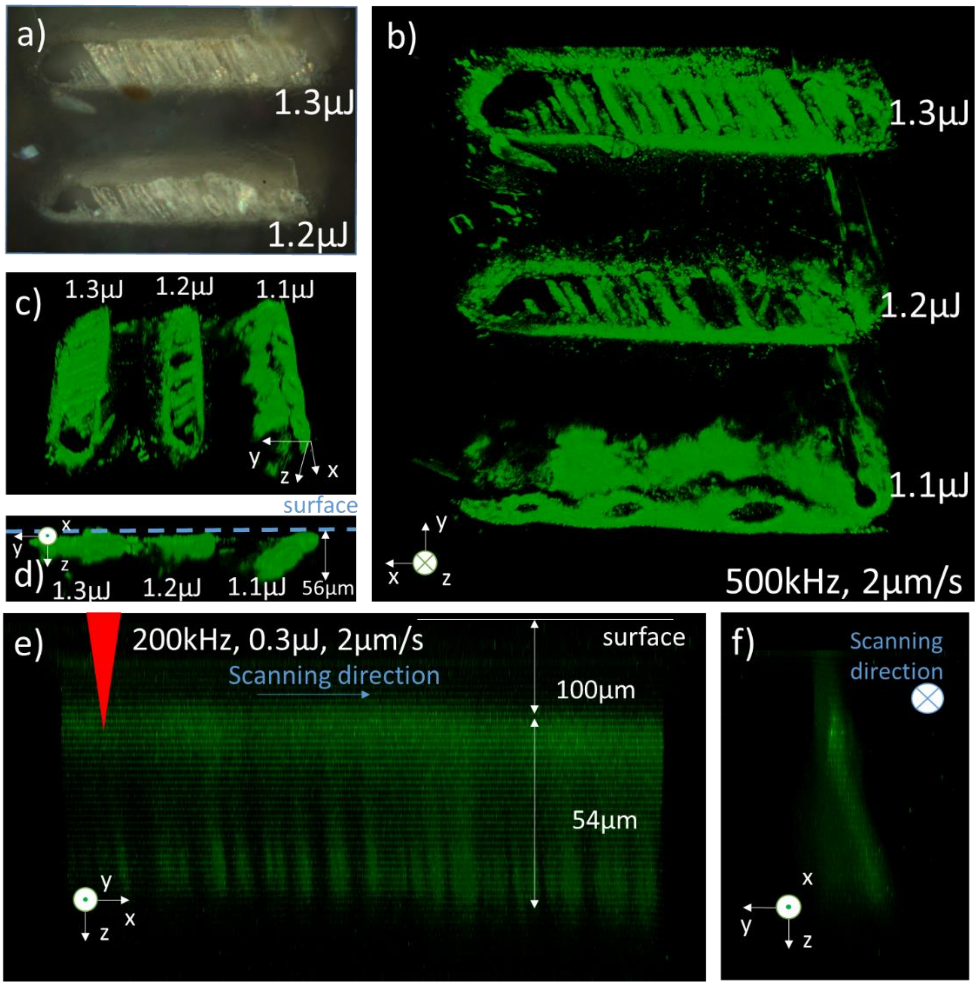

Fig.III.36 different view of the 3D PL distribution of type 2, type 3, and type 4 irradiated lines. a) microscopy photo of type 4 lines under polarized light in reflection mode with A⊥P; b) luminescent photo of type 4 lines indicated in a) plus a type 3 line; c) side view (slightly top view) of the irradiated type 3, 4 lines shown in b); d) side view of type 3, 4 lines shown in b); e) side view of 3D PL photo of a type 2 line (200kHz,0.3µJ), f) side view of 3D PL photo of the cross-section of the type 2 line shown in e) all the PL photos is under the excitation 470nm.

III.3.4.4.2 Distribution of normal PL and PL with up conversion?

Three 2D pictures of the same luminescent type 4 lines were taken under different excitation/detection conditions, in order to have some information about the distribution of the related luminophores. In fig. III.37, only excitation wavelength are different (written in fig.III.37), the detection wavelength range are kept the same (500nm to 600nm).

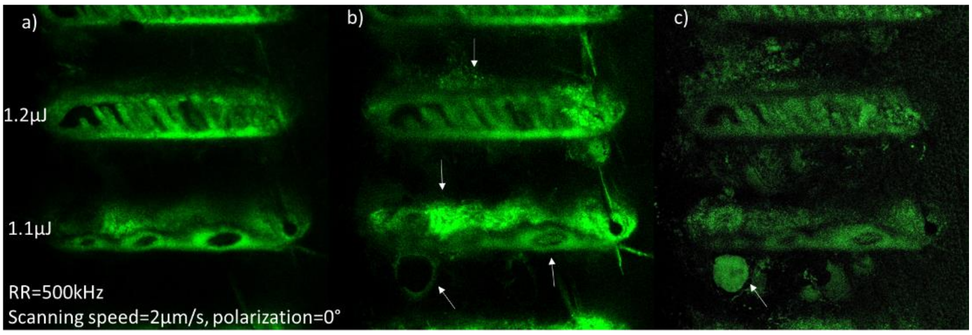

Ex:405nm
Detect 500-600nm

Ex:470nm
Detect 500-600nm

Ex:670nm
Detect 500-600nm

Fig.III.37 localization of the luminescence according to excitation wavelength: a) excitation at 405nm, b) excitation at 470nm, c) excitation at 670nm

From fig.III.37a b c, the distributions are different as some examples marked by white arrows. From luminescent 3D pictures (Fig.III.36) of the entire volumes and topography of the surfaces of these lines, we know that the elliptical features of the 1.1µJ line are the holes on the surface of the irradiated volume. The luminophore in the largest ellipsoid hole can be excited by 470nm instead of 405nm, it is maybe when excited by 405nm, the measurement distance is shorter that the center part, which is lower than the surface, is out of measurement of 405nm. More interestingly is, in fig.III.37c, this picture is taken by excitation at 670nm but detected in a shorter range 500nm to 600nm. We can observe that even though the PL intensity is lower, a round area outside of the irradiation area (white arrow in c) stands out from the other 2 pictures. Generally, the detection range is 70nm away from the excitation wavelength, so the reflection of the excitation light is considered not involved in the results. Therefore, 2-photon excitation might be one of the possibility. The other possibility could be an anti-stoke shift transition for an explanation or so-called upconversion. It is not happening often and its intensity usually to be much lower than the normal transition. The origin of this phenomenon still needs further investigation.

III.3.4.5 In solution and separated irradiated area

In order to identify the luminescent products created by fs irradiation inside the glycine crystal, we dissolved the glycine substrate into the water, the products are distributed or dissolved in the solution, making all the solution luminescent. During the dissoving process, some irradiated parts doesn’t dissolved and becames a cluster remaining in the solution, they were sepatrated out by a needle.

Fig.III.38 a and b shows the solution dissolved irradiated glycine crystal and pure glycine crystal under natural light and UV (365nm) lamp. Under natural light, the solution with irradiated products appears light yellow while the glycine water solution is transparent. Under a UV lamp, the sample solution appears blue while the glycine solution is transparent without color.

We have measured the excitation spectra and emission spectra of the solutions containing laser-induced luminescent products, results are shown in fig.III.38c.

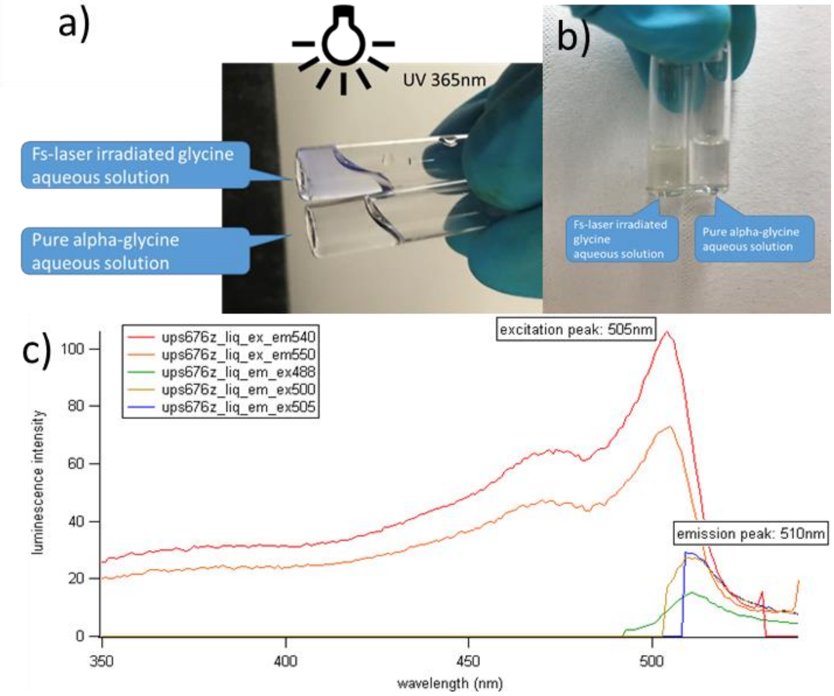

Fig.III.38 a) aqueous solution of irradiated glycine (type 4) under UV(365nm) lamp b) aqueous solution of irradiated glycine (type 4) under natural light c) excitation spectra of the solution containing laser-induced luminescent products

As can be seen from the graph, there are two excitation peaks, one is at around 470nm and the other is at 500nm, the one at 500nm is larger than the one at 470nm, it is similar to the EEM in section III.3.4.2 with an overall shift. The peak of the emission spectra at 510nm is very close to the peak of the excitation spectrum, implying a low Stokes shift. Furthermore, the different detection wavelengths give the same excitation spectrum, and the different excitation wavelengths give the same emission spectrum, implying that only one luminophore is excited in this range (488nm-505nm).

In addition, the emission spectra of a separated type 2 line excited by UV (356nm) is also recorded, fig.III.39 displays the comparison of these emissions. The peaks of the two emission spectra are different, implying a difference in the forbidden band width, so the two wavelengths excite different luminophores.

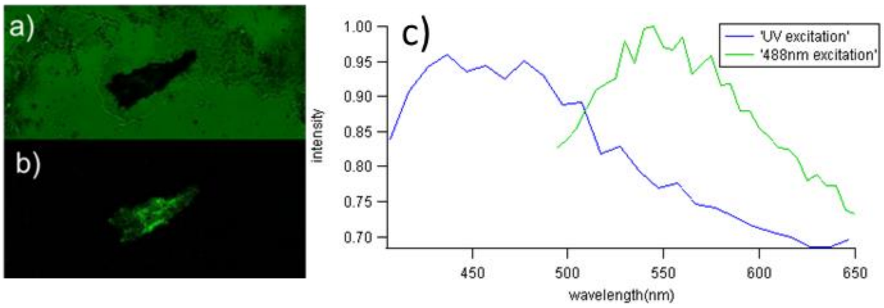

Fig.III.39 a) and b) the separated laser-induced solid products (type 4) under a confocal microscope of transmission mode and luminescent mode. c)Emission spectrum by excitation of 365nm UV (blue curve) and 488nm (green curve).

The lifetime of this separated product is characterized and fitted with 2 exponentials, indicating 2 luminophores with a lifetime of 1.98ns and 0.41ns, shown in fig.III.40.

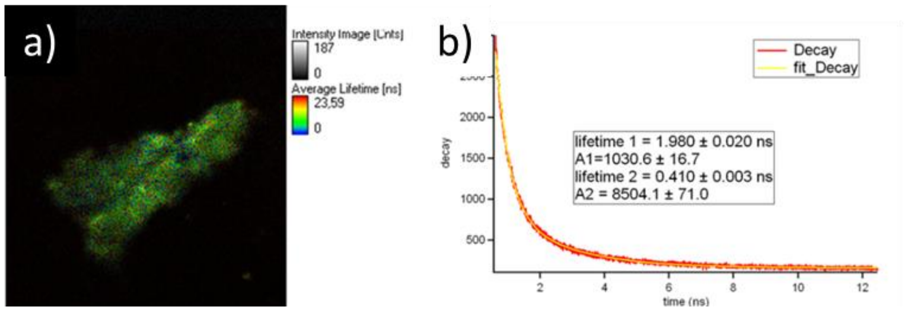

Fig.III.40 a) the lifetime distribution on a separated laser-induced solid products (type 4) b) lifetime decay with 2 exponential fitting

III.3.5 SHG property

γ-glycine crystals are considered a promising optical material because of their nonlinear properties and chirality [173]. While α-glycine is centrosymmetric which doesn't have the 2nd nonlinear properties. Therefore, it would be interesting to locally produce SHG in a centrosymmetric substrate, in order to achieve such an optical function SHG was first occasionally found in type 3 modifications during the irradiation. After adjusting the parameters, for example, by slowing down the scanning speed, we found a constant SHG generation with the modification type 4 and the SHG is located in the focus region. Therefore, the laser irradiation has broken the center symmetry. On the contrary, when irradiating the γ-glycine, there was SHG emitted not only from the region of irradiation but also from the whole crystal, shown in fig.III.41a. On the other hand, one occasion when scanning in α-glycine along the ab plane and using a high power, we also observed THG, shown in fig.III.41 b. The blue light and green light are recorded by a spectrometer to be an isolated narrow peak at 515nm and 343nm, i.e. the SHG and THG.

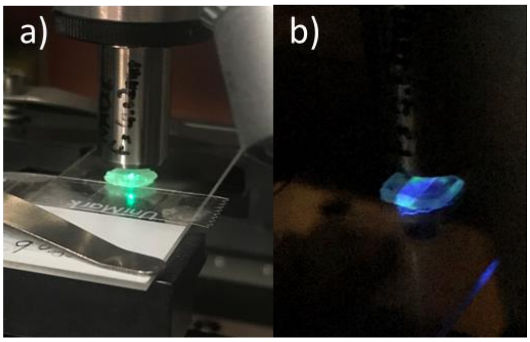

Fig.III.41 a) a γ-glycine sample during irradiation b) an α-glycine sample during irradiation (bc plane)

After irradiation, with a probe light (1030nm, with a power lower than the damage threshold) and the setup of transmission mode and reflection mode, we fould that the type 4 lines are still SHG active.

III.3.5.1 SHG polarization dependence

Fig.III.42 a) shows the SHG induced by probing fs laser with RR=100kHz and Ep=0.1μJ, Fig.III.42b) is the spectra of detected SHG.

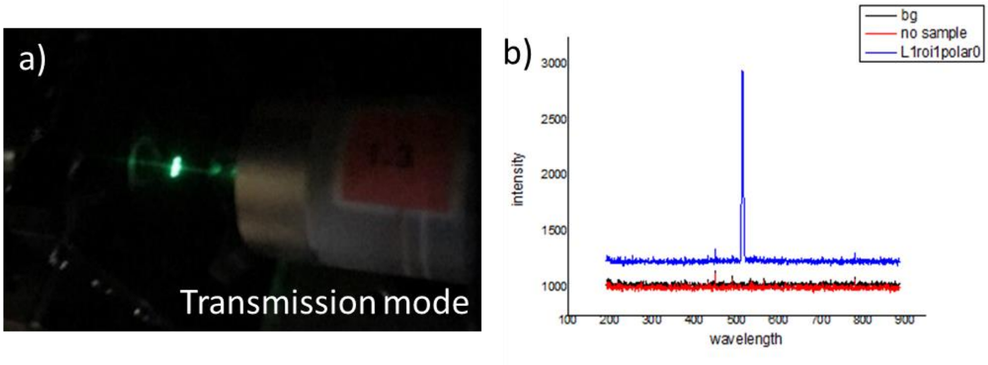

Fig.III.42 a) SHG in the irradiated sample probed by 1030nm fs laser with 100kHz,0.1μJ. b) the spectra of the emitted green light (blue) and glycine background (black) and air (red)

3 samples were characterized for different purposes:

1) Unirradiated γ-glycine crystal. Glycine crystal in the γ phase doesn't have the inversion symmetry so the SHG is highly generated. This experiment was used to test our experimental system.

2) Type 4 lines: scanning speed=2μm/s, RR=1MHz, Ep=1.2-2μJ, polarization=0°. The purpose of this experiment is to find laser parameters (Ep) that produce SHG more stable and with high polarization dependence, as the trial in [146].

3) Type 4 lines: scanning speed=2μm/s, RR=1MHz, Ep=1.2μJ, polarization from 0° to 180°. Since in experiment 2, we have found the SHG properties of type 4 irradiated by 1.2μJ to be very interesting, we tried to control the anisotropy of each SHG by changing the laser polarization, as in [174].

First, fig.III.43 shows the results of the first experiment. It should be noted here that results from these SHG measurements are from 1 point in/on the sample, unirradiated region, or irradiated region, it will be called ROI in the rest of the text, the measured area (of ROI) is the size of the probe beam, diameter about 30μm. We found that when the fs laser irradiates on γ-glycine, it had an SHG response which is sensitive to the polarization of the probe light. The contrast of polarization angular dependence is high, from 1.5×10^4 to 7×10^4.

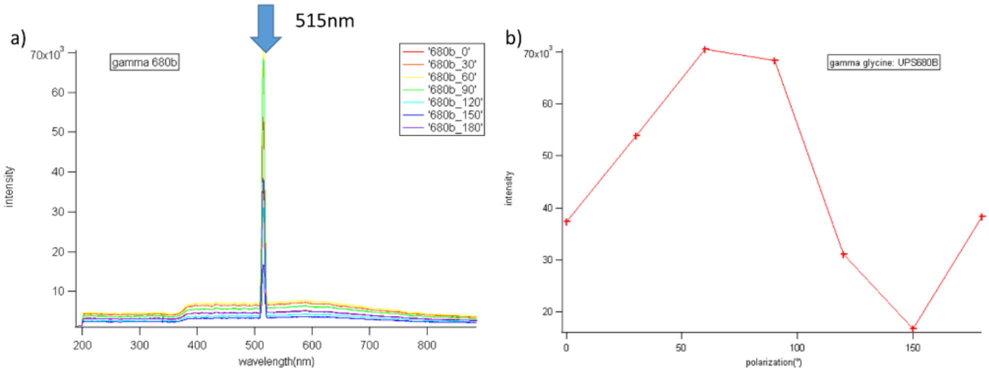

Fig.III.43 SHG angular dependence of pure γ glycine crystal

Fig.III.44 shows the results of experiment 2. Among type 4 lines irradiated with Ep=1μJ, 1.2μJ, 1.4μJ...2μJ, the one irradiated with 1.2μJ has the maximum contrast of the SHG intensity modulation. In particular, Ep>1.2µJ, the contrast decreases with energy increasing, implying that the anisotropy of the SHG-producing species is diminishing.

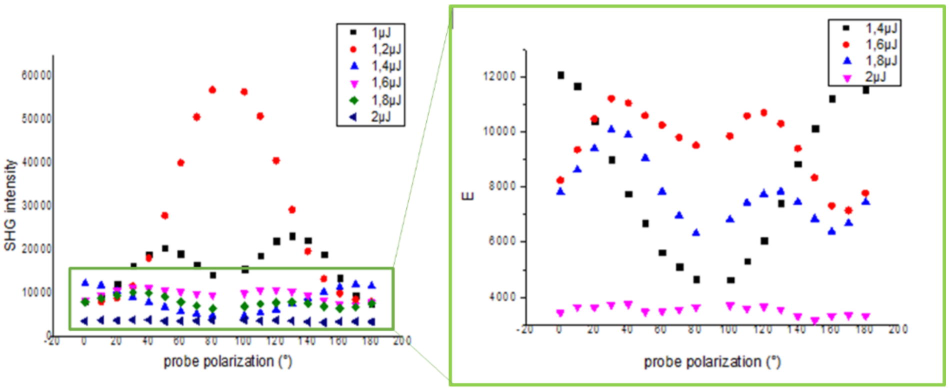

Fig.III.44 polarization angular dependent SHG intensity according to Ep variation

For reproducibility reasons, 6-8 ROIs were measured, and the normalized results of lines by 1.2µJ and 2µJ. They are shown in fig.III.45 a and b with a)bis and b)bis the original intensity.

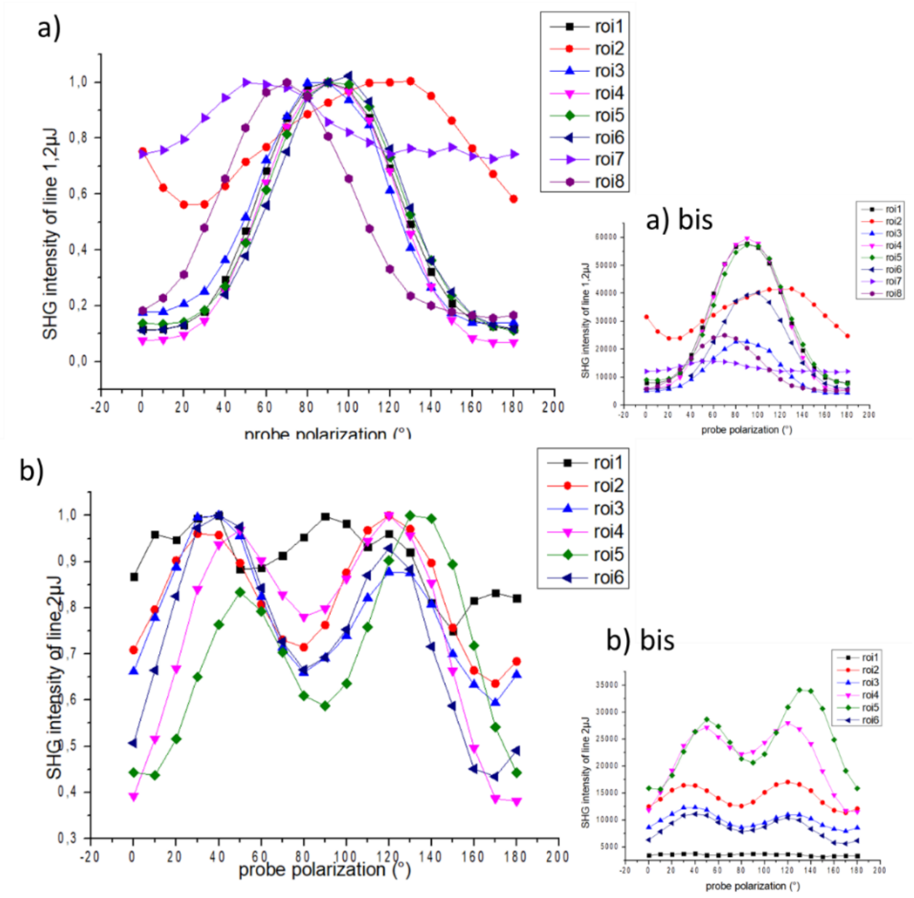

Fig.III.45 Normalized SHG intensity modulation according to the polarization of several ROIs in irradiated lines by a) Ep=1.2μJ b) Ep=2μJ, a) bis and b)bis are the original intensity

We found that the SHG generated by Ep=2μJ and 1.2μJ seems to have a modulation mode with 2 maximum and with 1.2μJ, which might imply the crystalline symmetry is different [175].

with Ep=1.2μJ the nonlinearity is having the largest contrast compared to the higher energy. We thus tried to fix this parameter and change the polarization for irradiation to see if the SHG could have a polarization correlation. The results of experiment 3 are shown in fig.III.46 below:

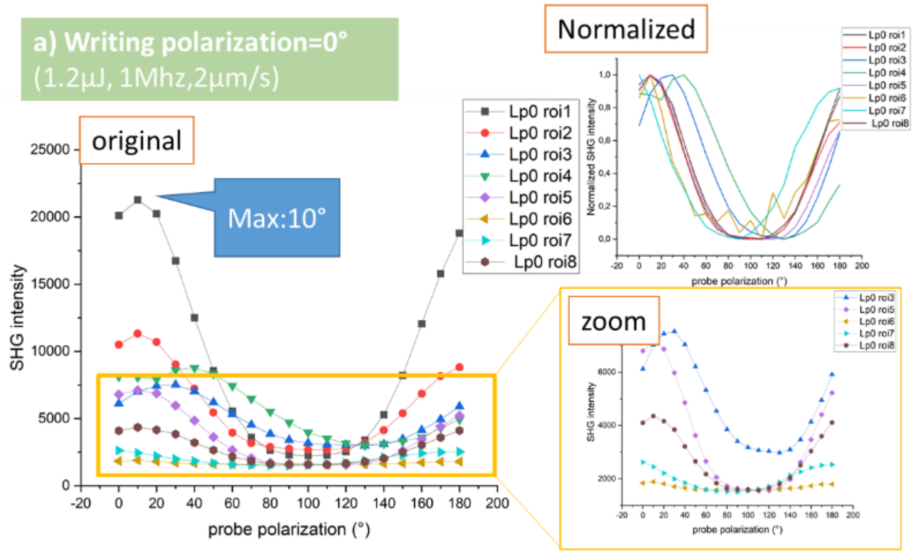
a) Writing polarization=0°
(1.2µJ, 1Mhz,2µm/s)
original
Max:10°
SHG intensity
probe polarization (°)
Lp0 roi1
Lp0 roi2
Lp0 roi3
Lp0 roi4
Lp0 roi5
Lp0 roi6
Lp0 roi7
Lp0 roi8
Normalized
Normalized SHG intensity
zoom

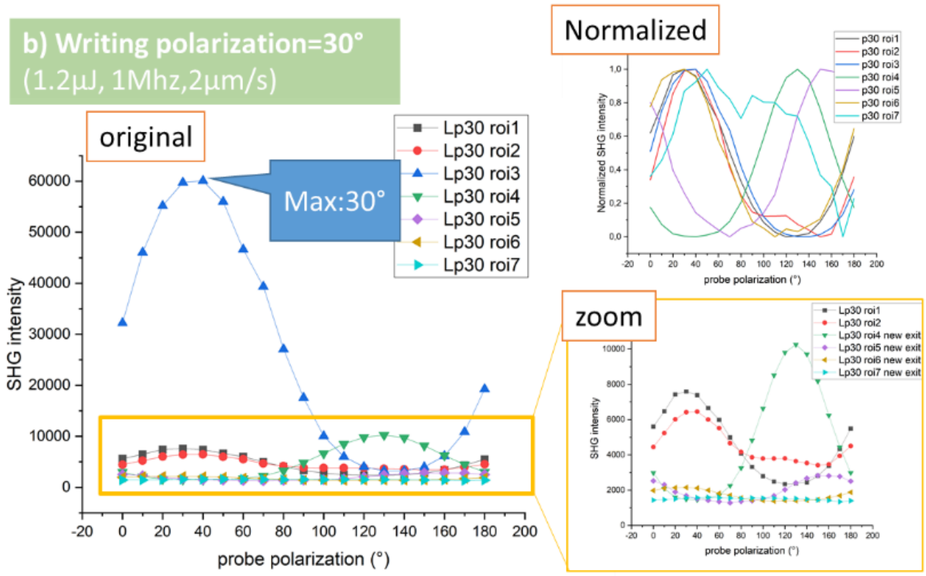
b) Writing polarization=30°
(1.2µJ, 1Mhz,2µm/s)
original
Max:30°
SHG intensity
probe polarization (°)
Lp30 roi1
Lp30 roi2
Lp30 roi3
Lp30 roi4
Lp30 roi5
Lp30 roi6
Lp30 roi7
Normalized
Normalized SHG intensity
zoom
Lp30 roi4 new exit
Lp30 roi5 new exit
Lp30 roi6 new exit
Lp30 roi7 new exit

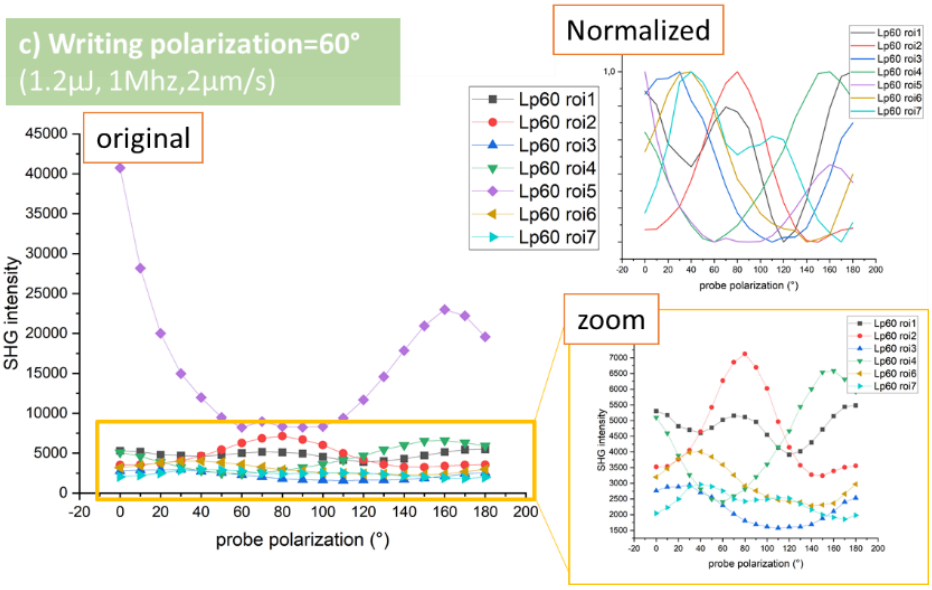
c) Writing polarization=60°
(1.2µJ, 1Mhz,2µm/s)
original
Normalized
zoom
SHG intensity
probe polarization (°)
45000
40000
35000
30000
25000
20000
15000
10000
5000
0
-20
0
20
40
60
80
100
120
140
160
180
200
Lp60 roi1
Lp60 roi2
Lp60 roi3
Lp60 roi4
Lp60 roi5
Lp60 roi6
Lp60 roi7
1,0
7000
6500
6000
5500
5000
4500
4000
3500
3000
2500
2000
1500

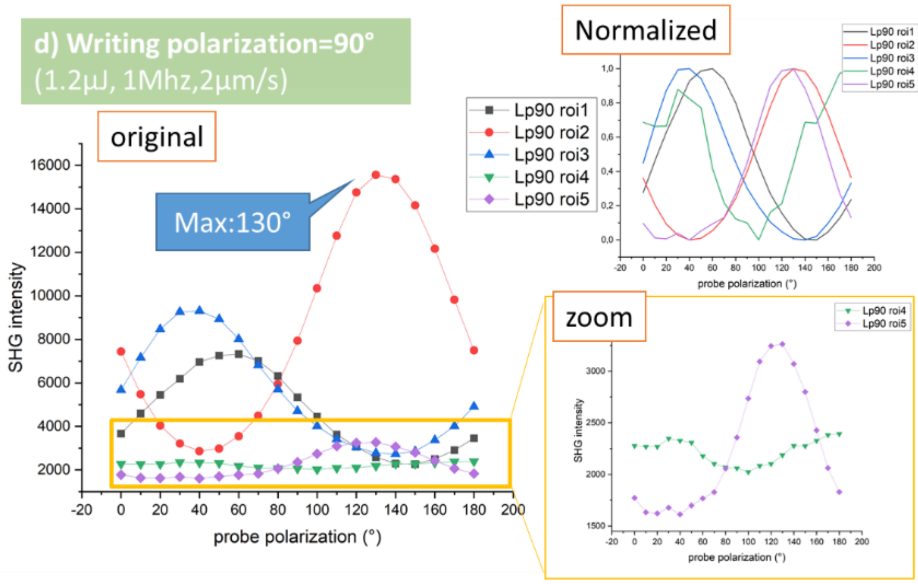
d) Writing polarization=90°
(1.2µJ, 1Mhz,2µm/s)
original
Normalized
zoom
Max:130°
SHG intensity
probe polarization (°)
16000
14000
12000
10000
8000
6000
4000
2000
-20
0
20
40
60
80
100
120
140
160
180
200
Lp90 roi1
Lp90 roi2
Lp90 roi3
Lp90 roi4
Lp90 roi5
1,0
0,8
0,6
0,4
0,2
0,0
3000
2500
2000
1500

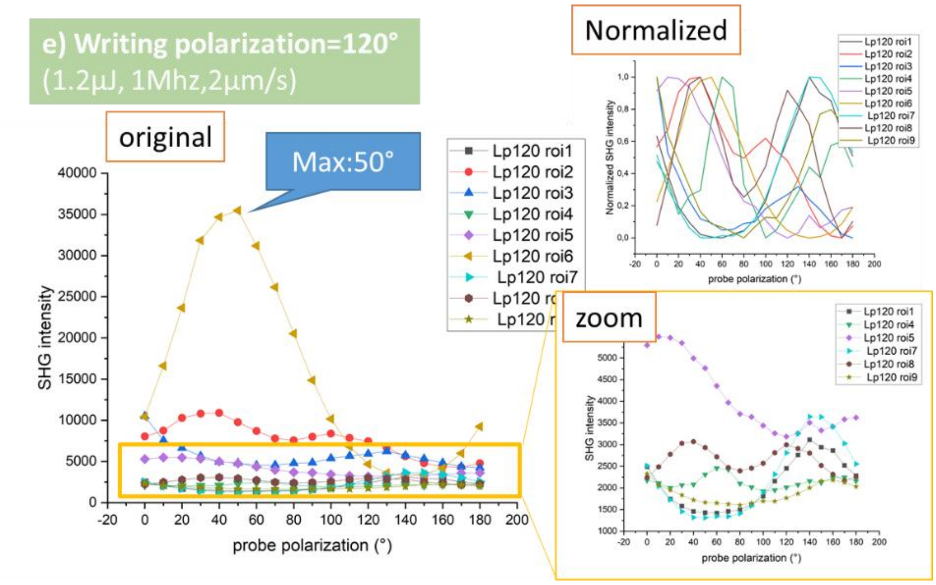

Fig.III.46 the SHG intensity according to probing polarization of ROIs in lines irradiated by 2µm/s, 1.2µJ and 1MHz, polarization = a) 0° b) 30° c) 60° d) 90 and e) 120°. In the picture, left: original SHG intensity of all ROIs extracted from spectra probed by 1030nm with 0.1µJ 100kHz exposure time 100ms and average of 5; right above: normalized SHG intensity of all ROIs; right below: a zoom of some ROIs' with SHG intensity lower than some other ROIs.

Even though we see there seems a trend in P=0° with a maximum at 0° or 10°, and in P=30° with a maximum at 30° in many results, the result does not have polarization correlation with other irradiation polarization, and the reproducibility is also not good. Therefore, attempts to control the directional dependence of the SHG by polarization were not successful.

In addition, we observed SHG decreasing when probing, thus we think that SHG is maybe not coming from the crystalline structure that we observed no visible change but might be from the molecules or microstructures non-centrosymmetric that could be influenced by light.

To see if the SHG property is constant along the line, we measured the SHG point by point (e.g. in fig.III.46 with 9 ROIs) along the line to figure out if the reproducibility along the line is good or not. There is a more efficient way to do it. We built thus a transmission setup with a probe light to cover all the lines by defocusing the beam, then we collected the SHG signal from all the lines as an image, shown in fig.III.47.

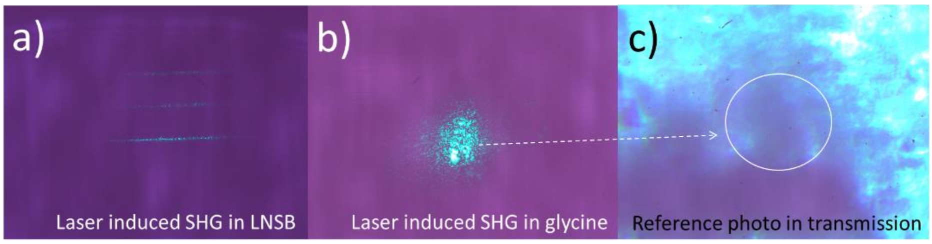

Fig.III.47 a) the SHG photo of the LNSB sample with irradiated lines [52] with the setup we built. b)-c) photo of type 4 (2µm/s 1MHz 1.9µJ) b) the SHG photo(1030nm probe light with filter); c) photo under natural light

Fig.III.47a shows the SHG distribution of nanocrystals induced by fs laser in LNSB glass. SHG is lacated in the irradiated lines. Fig.III.47b and c show the SHG distribution of type 4 modification in glycine crystal and the refered transmission photo. It seems that the SHG is not located in the irradiated lines but the surrounding. Since the SHG intensity modulation can reflect the orientation of the anisotropy, the images of SHG according to different polarizations can give us information on the formed SHG all over the region instead of measurements of points. It is easy to see if the SHG modulation is in the same trend when varying the polarization of probing light. If the SHG intensity changes the same way all over the region when observing, we can prove that the asymmetric species created along the lines are oriented in the same direction. Otherwise, it is more complicated. This experiments showed that the measured place is in the latter situation

It is worth mentioning that we have also tried using this parameter above with different scanning directions, but the results show no relation between the modulations of SHG intensity and scanning directions.

Overall, further research is needed on the orientation of SHG.

III.3.5.2 Unirradiated region

We also tested the unirradiated part, since we observed once the purple light emits during irradiation, we used a probe light with higher pulse energy Ep=0.2μJ and RR=100kHz, this parameter is under the threshold. With longer exposure time:1s, we have the result shown in fig.III.48a.

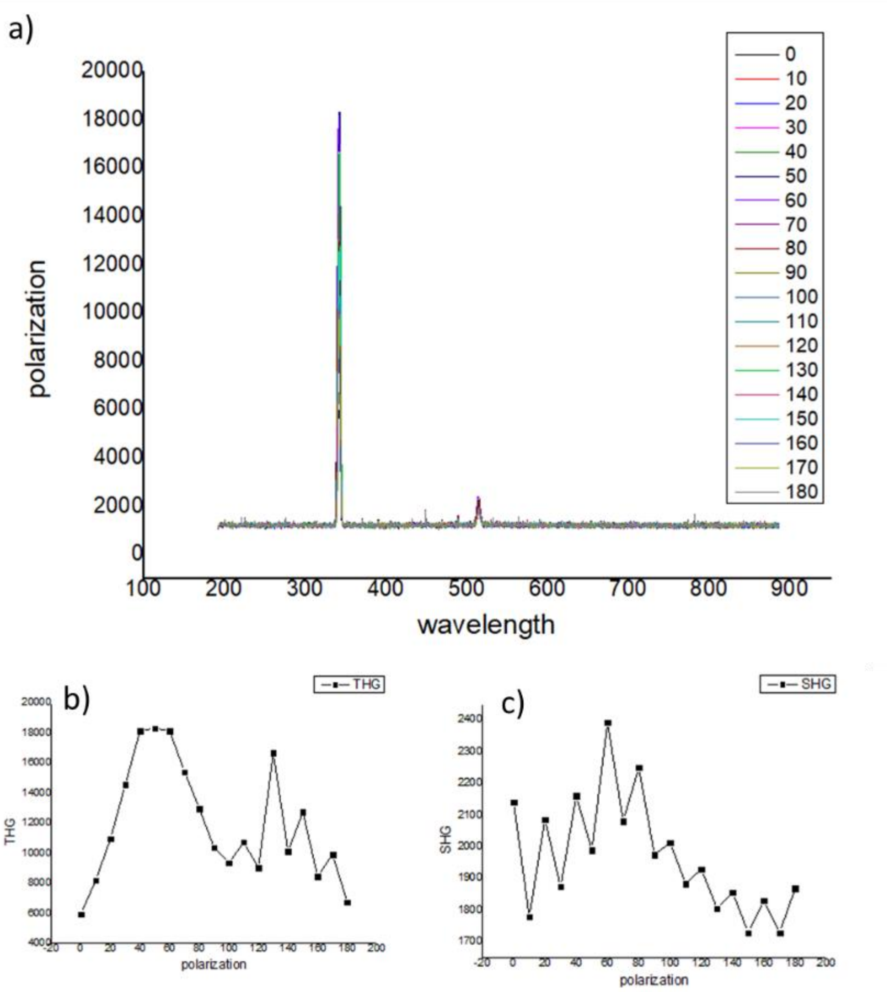

Fig.III.48 a) Spectra of alpha glycine with probe laser parameter: RR=100kHz, 0.2μJ, polarization from 0-180, 0 °Is parallel with c axis. Acquisition parameters of spectrometer: exposure time 1s, average 1 time. b) and c) the THG and SHG intensity polarization dependence

In the unirradiated part, we also find the presence of SHG, but it is much less intense compared to THG. This SHG is also much less than the one created in type 4 (it is measured under a 10 times longer exposure time: 1s). The SHG could be due to 2 possibilities: the laser-induced instantaneous anisotropy, a temporary breaking of the centrosymmetry of alpha glycine, or the SHG is coming from the interaction between THG (3ω) and the incident light (ω). The THG and SHG intensity induced in unirradiated part seems to have no polarization related, as we can see from fig.III.48 b and c.

III.3.6 Other characterizations for molecular information

III.3.6.1 Raman spectroscopy

First of all, fig.III.49 shows the polarization-dependent Raman spectra (448nm, polarized along x) of α-glycine crystal according to the orientation of its crystalline axes. The same typical peaks mean all the vibration modes exist but have polarization dependence.

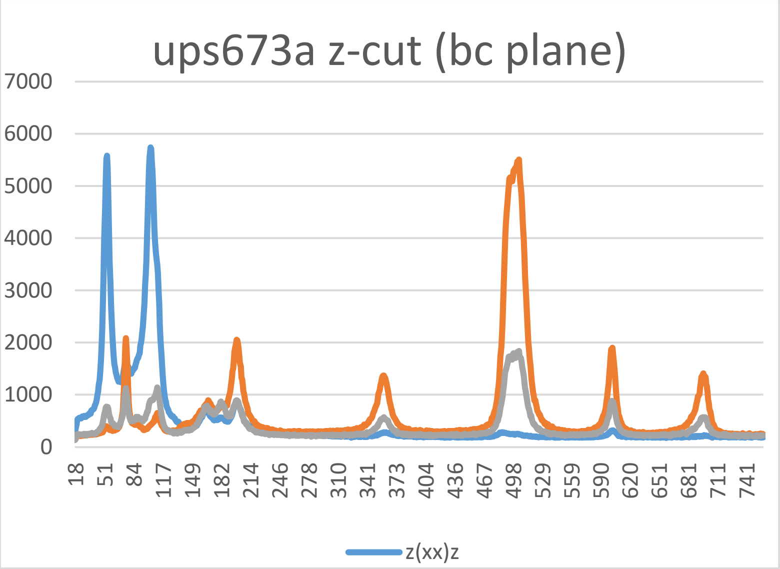

Fig.III.49 Raman spectra of α glycine from incident laser polarization along c (blue) and perpendicular to c (orange) and 45° with c (gray)

Fig.III.50 shows the Raman spectra of pure α-glycine crystal and irradiated glycine. From the type 1 profile (0.8μJ), the lower intensity of the typical peaks below 200cm^{-1} with almost the same intensity of the no peak glycine environmental background (200-750nm) implies no molecular changes but a structure distortion. Type 2 (1μJ-1.4μJ) profiles show a strong luminescence background of the spectra, with still 2 typical peaks of glycine remaining (see fig.III.50 and 51).

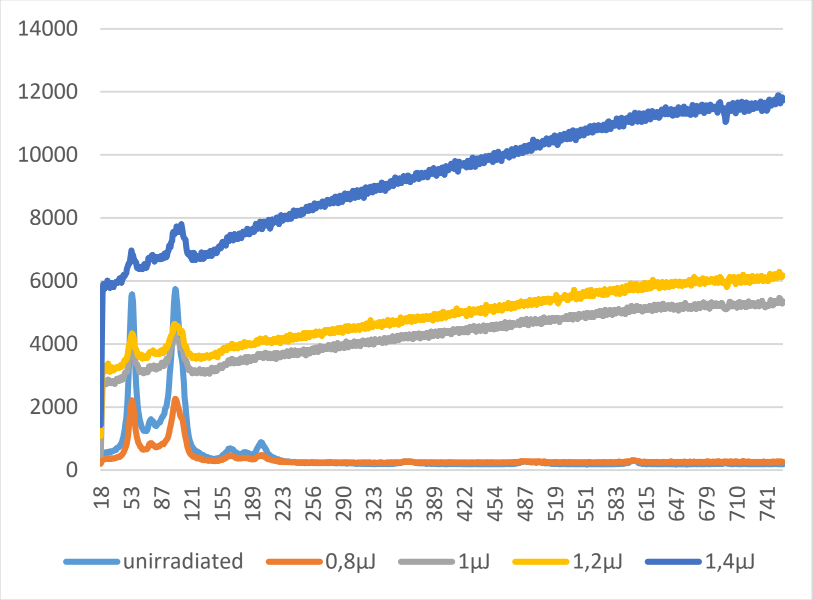

Fig.III.50 Raman spectra of unirradiated α glycine (blue, z(xx)z) and irradiated lines with different laser parameters

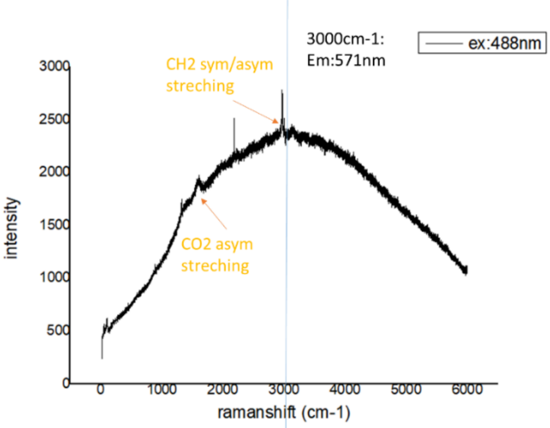

Fig.III.51 Raman spectrum of type 2 with a large range

To lower the luminescence background, Raman spectroscopy with another excitation wavelength of 633nm was applied. We measured 3 different ROIs of a type 4 line (Ep=1.7μJ, RR=1MHz, scanning speed=2μm/s and polarization=90°): ROI1 is the teeth-like crystals induced by fs laser in the irradiation line, ROI2 is the side part of the irradiation, which has birefringence under the microscope of reflection mode with polarizer perpendicular to the analyzer. ROI3 is the reference of an unirradiated glycine crystal. The ROIs and sample are shown in fig.III.52a and the Raman spectra of these ROIs are shown in fig.III.52b. Results show that with strong luminescence background, the typical peaks of glycine crystal are vanished in the irradiated part, including the recrystallized part and the side.

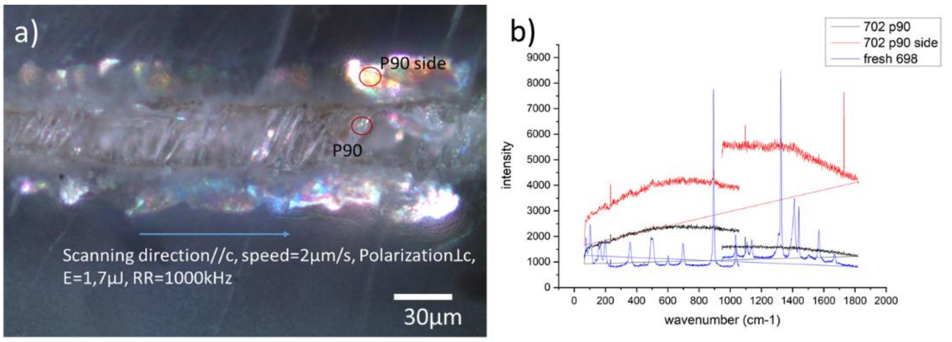

Fig.III.52 a) optical image in reflection with the positions of the measurement, b) Raman spectrum before irradiation (blue) and after.

On the other hand, we have observed a fluid-like area which is likely to be thin-film interference around the irradiated region, we speculate whether CO_2 or H_2O is resulting from a decomposition process. To have some information on the composition of these areas, some ROIs were also measured by Raman spectroscopy. The ROIs are shown in fig.III.53a and each Raman spectrum is shown in fig.III.53b.

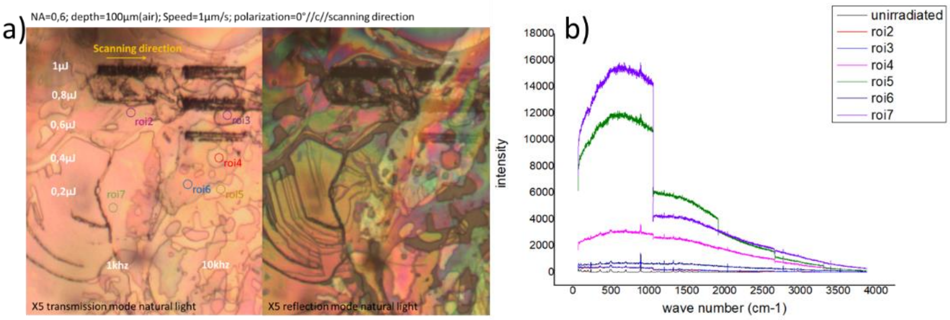

Fig.III.53 a) microscope pictures of UPS707 of irradiated lines and the indication of the ROIs we recorded the Raman spectra in b)

We noticed that there is strong luminescent background in the Raman spectra of the fluid-like region, the Raman peaks are undetectable, and so does the typical ones of water (3400-3600cm^{-1}) and CO_2 (1280cm^{-1}, 1380cm^{-1}).

III.3.6.2 FTIR

The FTIR spectra of the separated type 2 lines and type 4 crystals were measured.

Fig.III.54 shows the FTIR spectra of irradiated lines and unirrdiated parts. Fig.III.54c is a IR spectra map of the sample region of Fig.III.54 a and b. Fig.III.54a is a luminescence photo and b is a photo under reflection mode under natural light. This map containing spectra from every pixel. Fig.III.54d shows the spectra of 3 ROIs in the map. 1 and 2 are from an separated irradiated line and 3 is from the area in between. From the spectra we can see, the FTIR signal of the irradiated area is weaker due to the scattering. The solid transparent part in between (ROI3) has a better intensity. Fig.III.54e and f show the spectra measured in point mode of these ROIs and the unirradiated part. By comparing the spectra with the substrate alpha glycine, shown in Fig.III.54f, there is a very new created peak at 1218, which is always connected to C-O stretching for example the function group =C-O-C and Ethylene oxide. Since we observed some liquid in the sample after irradiation under the microscope at the same focus of irradiated lines, it is possible to have dehydration condensation reaction of glycine, so we checked the infrared spectrum of glycine dipeptide, tripeptide, polypeptides 2,5-Diketopiperazine which are often produced as degradation products of polypeptides, etc., but no identical peaks, such as from peptide bonds, are matched.

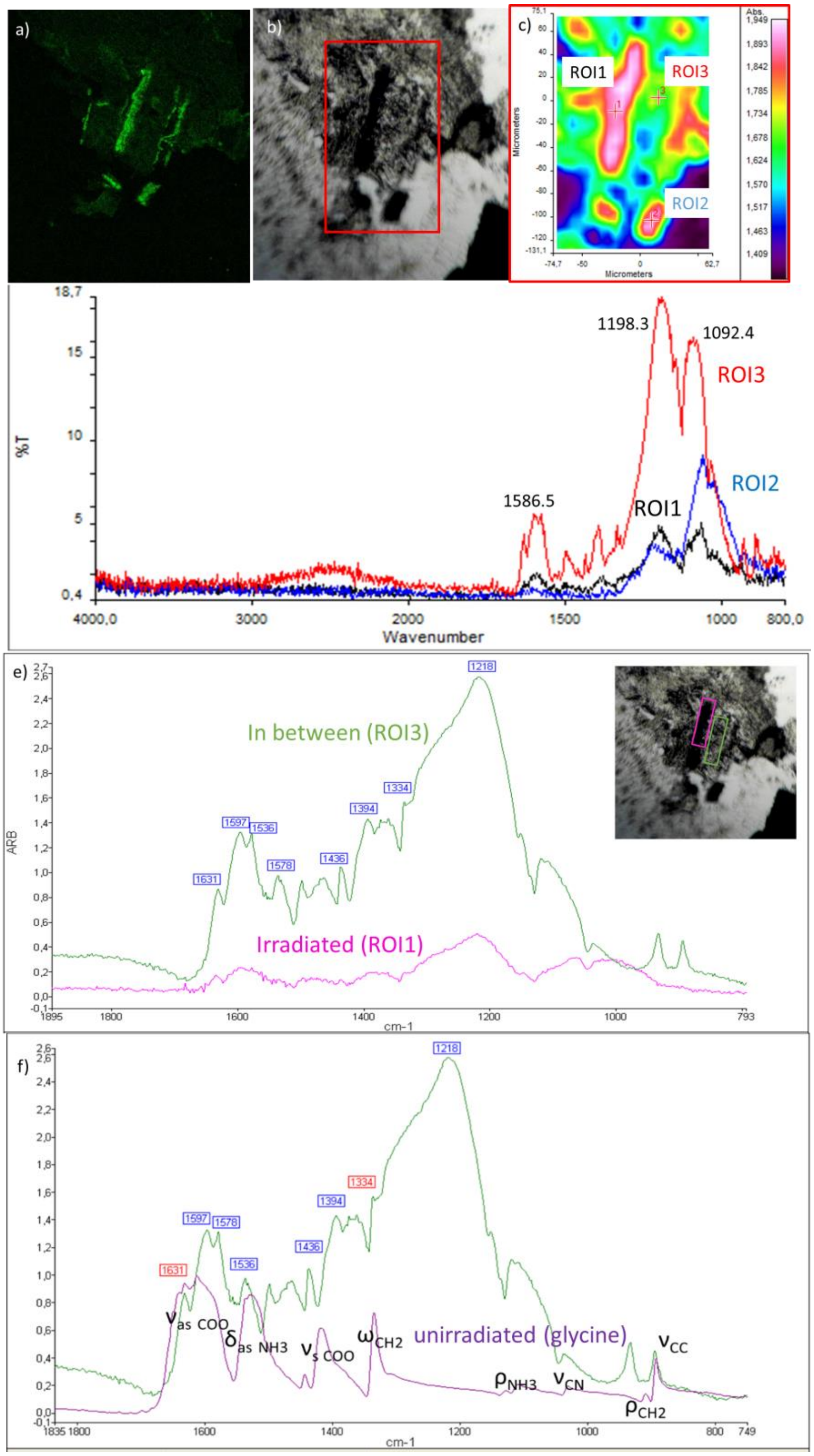

Fig.III.54 FTIR reflectance spectrum of separated irradiated lines and the transparent solid part between lines. a) luminescent photo of the separated irradiated lines under *confocal microscope b) microscope photo under reflection mode and natural light; c) average FTIR spectra intensity map of the area shown in a) and b), pink area refers to the separated irradiated lines; d) the FTIR spectra of point 1, 2 and 3 marked in c). e) the FTIR spectra of one irradiated line (pink profile) and the area between the 2 irradiated lines (green profile); f) the FTIR spectra of the area between the 2 irradiated lines (green profile) and the unirradiated area (purple profile).*

An irradiated α-glycine sample with type 4 modification was also measured: the recrystallized crystalline objects were dialed down by a clean tweezer onto the sample holder and measured the IR spectrum with transmission point mode. the spectrum is shown in fig.III.55 in red profile. By comparison, the IR spectrum of the laser-induced type 4 crystalline material was found to be 85.7 % similar to the IR spectrum of glycine. Thus, despite the laser-induced recrystallised polycrystals has luminescent properties, the main body remains glycine.

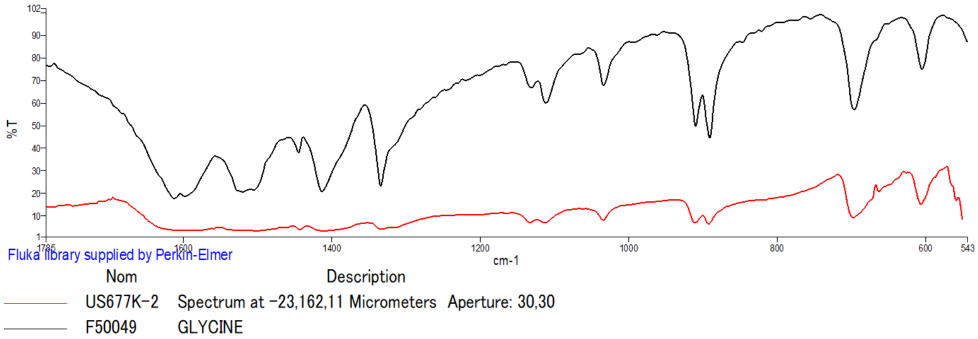

Fig.III.55 Fs laser parameters for irradiation is scanning speed=20µm/s, RR=400kHz, E_p=3µJ, Polarization=0°.

III.3.6.3 Electron Para-magnetic Resonance (EPR)

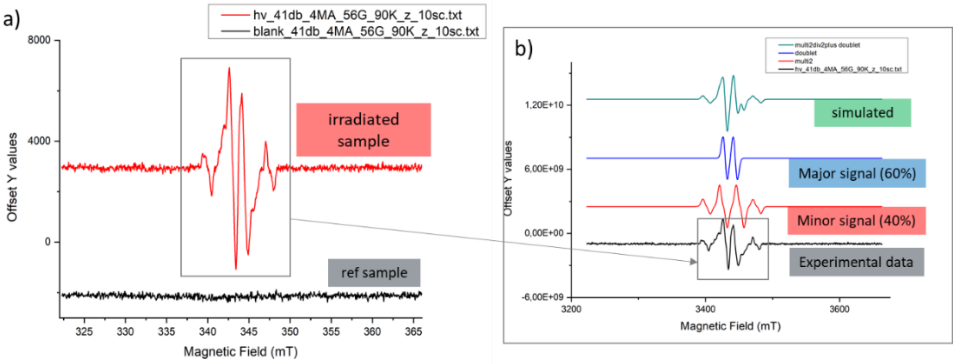

Fig.III.56. a) EPR spectrum of irradiated α glycine crystal (RR=1MHz, Ep=1μJ, speed=10um/s, red) and unirradiated α glycine crystal (black) b) simulation of the EPR spectrum of the irradiated sample. Black: the experimental data; green: simulated data; blue: the major component; red: minor component.

Fig.III.56a shows the EPR results of pure α-glycine crystal (black profile) and α-glycine crystal with an irradiated area (3mm*3mm square 4 layers, RR=1MHz, Ep=1μJ, speed=10um/s). The spectra of the unirradiated reference sample show no signal. On the contrary, similar to [176], radicals were produced in the fs laser irradiated sample.

By simulation, shown in fig.III.56b, this radical signal consists of 2 signals. The major signal (60%) corresponds to a simple radical on a proton with g value =2.0035 and A=15 Gauss which is the blue trace. The minor signal (40%) is more complicated. It corresponds to a radical centered on three equivalent protons (quartet) coupled to a different proton which splits the quartet in a doublet and it has g value=2.001 A(Ha)=25 Gauss and A(Hb)=6.1 Gauss and it corresponds to the red trace in fig.III.56b.

III.3.6.4 Mass spectroscopy

We were trying to get some information on the chemical formula of the fluid phase, we tried to measure the gas escaping from a sample by mass spectroscopy. Fig.III.57a shows the result from a broken irradiated glycine crystal and unirradiated crystal with molecular weight from 1-100 after about 2 hours. The 2 spectra looks no difference. Then we try to heat the sample slowly and monitoring the spectra evolution. Almost every mass decreases since the air is pumping out with less concentration, but 3 masses 39, 41 and 43 had been detected to be arising after we started to heat the sample, as shown in Fig.III.57b. They can be possible products of the combination of CHO such as cyclopropane but it can never be sure. Also, it can be a decomposition of the molecules with a higher weight. But actually, we found no change in carbon dioxide or oxygen.

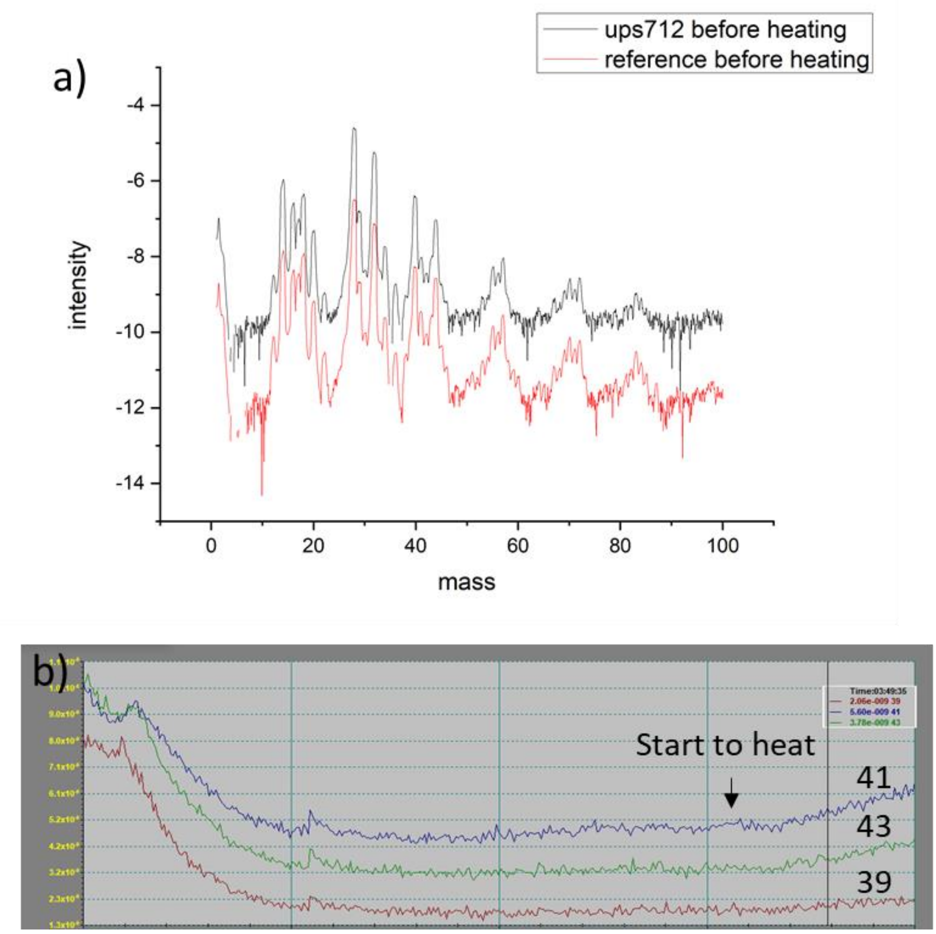

Fig.III.57 MS of a) Irradiated glycine b) α-glycine reference and c) monitoring of Mass= 39,41 and 43

III.4 **DISCUSSION**

III.4.1 Mechanism of the fs laser-glycine interaction

During the irradiation, the IR fs laser pulses produce plasma in the glycine crystal sample likely through multiphoton absorption as we have calculated. This process might be alike the process proposed by Jorge Serrano et al. [177], based on the results of laser-induced breakdown spectroscopy (LIBS), large amount of fragments formed by fs pulses advocates a direct release of native bonds and a subsequent seeding of the ionic plasma with diatomic species, contrasting with ns ablation regime, where the atomic recombination and single displacement processes dominate the contribution to diatomic radicals, as long as atomization of molecules prevails over their progressive decomposition. As the pulses vanish, and the temperature cools, the atomised molecular fragments recombine to form new molecules. Under the optical microscope in transmission and reflection, we observe a fluid phase after irradiation, as shown in fig.III.58. Specifically, in reflection, this fluid has an iridescent aspect that likely arises from thin film interference. We observed that this fluid material inside the glycine crystal disappeared over time (as shown in fig.III.58 b and c, possibly being absorbed by the crystal or pooled together with the neighborhood. We suspect that this fluid may be the water expelled by the carbon atoms in the glycine when they combine with each other. The presence of water may also explain why recrystallisation occurs under thermally effective (high frequency) irradiation, as the fact that glycine is hardly soluble in solvents other than water.

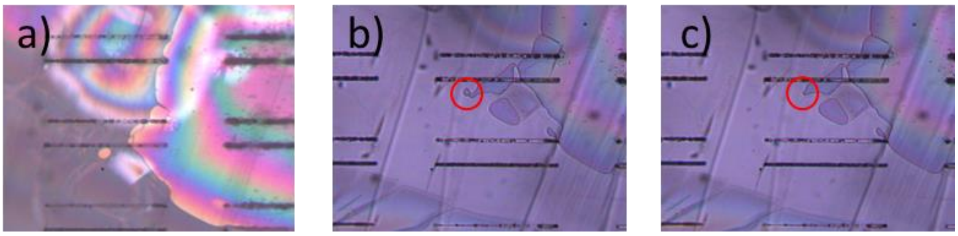

Fig.III.58 a) the microscopic photo of fluid material in glycine crystal in reflection mode. reflection b) and c) in transmission mode, the change in the fluid extent in the red circle.

III.4.2 Products

III.4.2.1 Luminescent species

Small molecules like glycine, usually don't have luminescence in visible range or no luminescence (relaxation way is non-radiative). For example, γ glycine absorbs light at 250nm and emits UV at 399nm [125]. At this wavelength, the photo energy usually excited the electron by dissociation. For this reason, $\sigma \rightarrow \sigma^*$ transition in luminescence is rarely observed. Instead, the most luminescence is found in compounds containing conjugated bonds with lower transition energy $\pi \rightarrow \pi^*$ transitions. This is due to the conjugated carbon bond lowering the gap between HOMO-LUMO.

From FTIR and EPR results, we have some discussion and suggestion below at the molecular level in the irradiated regions:

1) the type 2 lines including the transparent region between lines generated by irradiation are no more glycine, the COO-function group has been modified while the SP3 carbon bond C-C remains to a certain extent. No peptide bond formed like a favorable chemistry reaction, the fs plays a stronger role in the reaction instead of heat-triggered dehydratation.
2) The type 4 recrystallized polycrystals, even though it is luminescent, the main part of the crystal is still composed of glycine molecules. But since the glycine itself doesn't have luminescent in the visible range, we suggest that the luminophores are distributed in the recrystallized glycine with a larger carbon content compared to the glycine one.
3) An intense peak appearing at a range from 1150cm^{-1} to 1350cm^{-1} might be related to C-O stretching.
4) Proton radicals were produced, they might be one of the origin of the PL properties.

Luminescence coming from a molecule usually have multifold absorption but only one emitting wavelength, because the HOMO-LUMO relaxation transition is fixed (and unique). The reverse (i.e. one excitation and several emissions may be realized by a specie that play the role of sensitizer and then gives its energy to a series of luminophores (not absorbing). An example of a photosensitization reaction is chlorophyll dye (the sensitizer) absorbing light and then transferring the energy to another substance. From our results, it seems that there is also an excitation-dependent PL. For the wide range of emission spectra, we suggest that this may arise from the different sizes of sp2 carbon clusters, and in general, the more conjugate bonds, the longer the wavelength of light emitted, as shown in fig.III.59. It is an advantage as a wide excitation wavelength permits lower requirements of excitation lights.

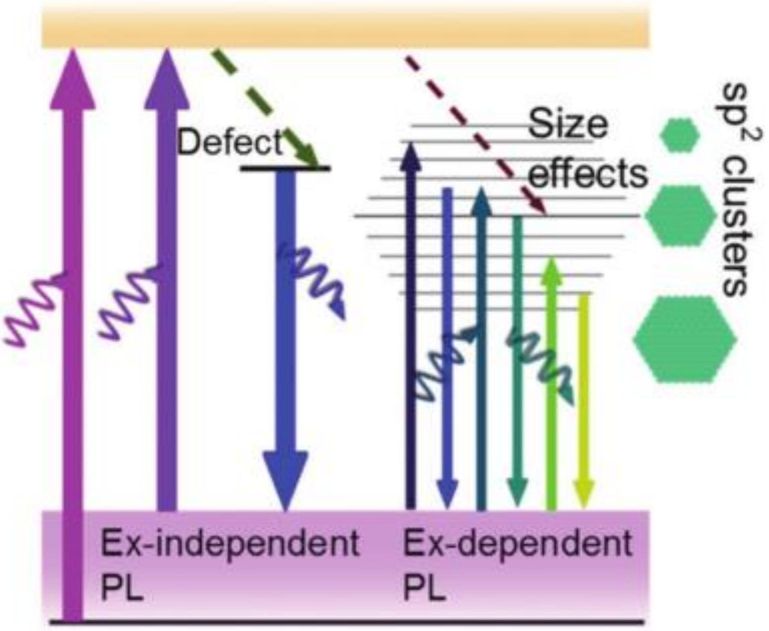

Fig.II.59: Jablonsky scheme extracted from [178]

Considering the carbon contained in glycine crystal, the produced black matter is difficult to dissolve in any solutions, we suggest that it is a kind of Carbon Dots (CDs). In general, "CDs" is a comprehensive term for various nanosized carbon materials. Fluorescent CDs contain several types, like graphene quantum dots (GQDs), carbon nanodots (CNDs), and carbon nanodots divided into carbon nanoparticles without a crystal lattice and carbon quantum dots with an obvious crystal lattice. CDs usually have luminescent properties, and the mechanisms of light absorption and emission of small fluorescent carbon nanoparticles (C-dots) are still unresolved and are the subject of active discussion. Research has shown that luminescent CDs are more likely composed of assembled individual emitters than having a collective property of nanoparticles [179].

The synthesis of CDs can be divided into 2 methods, the top-down nano-cutting methods and bottom-up organic approaches. Top-down nano-cutting generally includes cutting different bigger carbon resources such as graphene oxide, carbon fiber, fullerenes, etc. Bottom-up includes carbonization of carbohydrates, self-assembly of polycyclic aromatic hydrocarbons, and organic synthesis from small molecules. Apparently, this kind of luminescence created from glycine molecule can be sorted as the second one.

Finally, the possibilities of the source of luminescence can be concluded the followings:

i) Emissive radical(s).
ii) Different size fluorophore(s) with conjugated carbon bonds, i.e. compounds with aromatic polycyclic structure
iii) Carbon dots (CDs or C-dots) such as graphene.

Whatever the mechanism, compared to total synthesis, photosynthesis with laser irradiation is a very simple process and very fast, local and flexible.

III.4.2.2 SHG species

SHG is a two-photon process that depends on the inherent symmetry of the material and its ability to interact with an electromagnetic (EM) wave. In general, both surface and bulk SHG must be considered in the SHG process, with bulk materials without a reversal center producing much higher SHG intensities than their surface counterparts, but requiring phase-matching conditions. In SHG, the non-linear response of the bulk material and the surface is described by its non-linear susceptibility, denoted by $\overleftrightarrow{\chi}^{(2)}$, a third-order tensor describing the properties of the surface and the bulk material. Due to the dependence on the $\overleftrightarrow{\chi}^{(2)}$, α-glycine with inversion symmetry is therefore not SHG active.

The induced polarizability P(ω) of material under irradiation with an electromagnetic field E(ω)at a frequency ω. ε0 is the vacuum permittivity constant and the $\overleftrightarrow{\chi}^{(i)}$ represent the ith-order susceptibilities:

$$\boldsymbol{P}(\omega) = \varepsilon_0 \times \overleftrightarrow{\chi}^{(1)} \times \boldsymbol{E}(\omega) + \varepsilon_0 \times \overleftrightarrow{\chi}^{(2)} \times \boldsymbol{E}(\omega)\boldsymbol{E}(\omega) + \cdots + \varepsilon_0 \times \overleftrightarrow{\chi}^{(i)} \times \boldsymbol{E}(\omega)^{\boldsymbol{i}}$$

Thus the SHG term is given by

$$\boldsymbol{P}(2\omega) = \varepsilon_0 \times \overleftrightarrow{\chi}^{(2)} \times \boldsymbol{E}(\omega)\boldsymbol{E}(\omega)$$

Converting the sign of the input field $\boldsymbol{E}(\omega)$ in Eq. III.2 should also change the sign of the induced polarizability $\boldsymbol{P}(\omega)$, unless when the material has an inversion center. In this case, $\overleftrightarrow{\chi}^{(2)} = -\overleftrightarrow{\chi}^{(2)}$, and no change of sign of the induced polarizability is yielding $\boldsymbol{P}(2\omega) = 0$ and subsequent $\overleftrightarrow{\chi}^{(2)} = 0$. Conversely, for non-centrosymmetric materials, assuming the electric dipolar approximation, the rotation of the susceptibility tensor yields, $\overleftrightarrow{\chi}^{(2)} \neq -\overleftrightarrow{\chi}^{(2)}$, which in turn suggests that $\boldsymbol{P}(2\omega) \neq 0$. In this case, when the phase matching conditions are fulfilled, the bulk nonlinear susceptibility gives rise to large SHG intensities.

The SHG is forbidden in alpha glycine with inversion symmetry, we thus suspect that there are species (new molecules or glycine arrangements produced without inversion symmetry.

As we have observed, type 4 recrystallized crystals often have a feather-like fractal structure, which is often accompanied by an absence of a center of symmetry that allows second harmonic generation as shown in [180] [181]. However, experimental results show that the intensity of the SHG often decreases with laser irradiation time without any visible change in the shape of these polycrystals, so this phenomenon may be more complex.

In addition, since the slowing down of the scan speed results in a constant SHG generation with the type 4 modification, and the steady state is often reached at a longer time outside the center, the effect triggered by the change in velocity is thought to be due to thermal effects. This coincides with recrystallization.

III.5 CONCLUSION

By systematically investigating fs laser interacted with α-glycine crystal in the plane pulse energy-repetition rate, we have broadly defined the boundary or threshold of the different transformation, they are type 1 to 4 as listed below.

- Type 1: The first boundary was drawn by the appearance of permanent refractive index change, over this boundary fs laser-induced the type 1 modification. Lower RI in one depth of the scanned region than the substrate indicates slight structural distortion or porosity. Raman spectra with peaks highly consistent at the modified and unmodified region confirmed that this type 1 modification does not change the molecular structure, nor the phase transition.

- Type 2: The second boundary is defined by the occurrence of opaque material. Beyond the second boundary, the pulse energy is high enough to break the molecular bonds, changing the glycine molecules to molecules containing conjugated bonds, CDs, or radicals. Part of the new molecule(s) present luminescent properties.
- Type 3: The third boundary is defined by observing a swelling in the irradiation region. Besides the molecular changes, due to the increase in repetition rate, the heat accumulation starts to influence the region around of scanning area, resulting in a modification wider than the laser beam. The wider part is a hole and the luminescence distributes on the internal upper surface of the irradiated area.
- Type 4: The fourth boundary is defined by observing the formation of polycrystals. Although the intermediate processes are not observed, an fs laser of a high repetition rate (more than 400kHz) can cause solid-to-solid transitions, which may be related to heat accumulation effect. These crystals are confirmed to be containing glycine molecules and also luminescent molecule(s). in addition, these crystals (or surrounding) have SHG property, breaking the inversion symmetry of α glycine crystal.

In addition, the angle between polarization and crystal axes slightly influences the modification threshold: the lowest threshold for modifications in the bc plane is when the polarization is parallel to $\vec{c}$, i.e. the direction of crystal growth. and the scanning direction change does not affect it.

Fs laser-induced photoluminescence and refractive index change in organic materials were found in several polymers. Those properties induced by fs laser in crystals of small molecules such as glycine were found for the first time. We have characterized the luminescence properties. The emission/excitation matrix shows that in the visible range, the laser-induced 2 luminescent species with excitation centered at around 475nm and 520nm with a broad emission from 520nm to 630nm and 545nm to 620nm, respectively. In addition, there is another luminescent specie that can be excited by UV, because the emission peak is different than the one excited by 488nm. The lifetimes of the luminescent species excited with 2 photon absorption by 800nm are measured. Results show that there are 2 luminophores with a very short lifetime 0.4-0.6ns and another longer one 2-3ns.

We have tried to discover the origin of the luminescence and to precise the molecule formed after irradiation. Based on EPR analysis, similar to [176], unpaired electrons around proton are produced. FTIR results show that the fs laser has modified the COO- function group, sp3 carbon bond C-C somehow remains no peptide bond formed like a favorable chemistry reaction, and intense peak appearing at range from 1150cm-1 to 1350cm-1 probably related to C-O stretching. By comparing the luminescent properties, carbon-dots with aromatic polycyclic or graphene structures are the most possible products. Thus it may also have conductive properties like those described in the literature [162], making it potentially more effective concerning electronic components, and having potential application as an eco-friendly and easily accessible organic substrate for optical devices.

The important fundamental aspects of this research are: luminescence creation in organic material can be achieved by fs laser irradiation not only in polymer but also in small carbon-based molecular crystals. Since one of the luminophores, we generated, absorbs blue light and emits green light near 550nm, similar to the optical properties of GFP, and glycine is an important component of biological protein molecules, we venture to imagine that light-triggered luminophores may have similarities to luminescent proteins produced by biological evolution at the molecular level.

Although we found some interesting modifications and characterized them in some ways, we found no obvious polarization effects in them according to the fs irradiation polarization (except SHG, but it can’t be oriented by irradiation), in other words, no properties induced by fs laser irradiation has polarization dependence. Even though asymmetric species are created, their orientation is random. However, the produced luminophores induced by chemical change as the consequence of the absorption, although the process might not be influenced by the irradiation polarizations, their luminescent properties can still be anisotropic, if they are not totally symmetric. As the matter of fact, there is a polarization effect on the anisotropic luminescent properties and their control. This study will be described in chapter VI, along with the other materials.

Chapter.IV FEMTOSECOND LASER DIRECT WRITING IN ZEONEX GLASS

IV.1 INTRODUCTION

Zeonex® is a Cyclo Olefin Polymer (COP), it is an amorphous material that is very different than crystals. It is fabricated by ring-opening metathesis polymerization of cyclic monomers, followed by hydrogenation, as shown in fig.VI.1. First of all, it is considered isotropic at the macroscopic level. Compared to the widely used commercial polymer such as PMMA, PDMS, etc., it is a relatively new class of polymer that has impressive advantages in properties. We choose class 790R for experiments, the main reason is due to its glass transition temperature being 163°C which is the highest in the options. Higher glass transition temperature allows more flexible laser parameters. Besides applications such as optical lenses, display material, laboratory supplies such as test tubes, and so on, this kind of material has also been used to fabricate fibers and acts as a substrate for implementing optical functions (e.g. Bragg gratings).

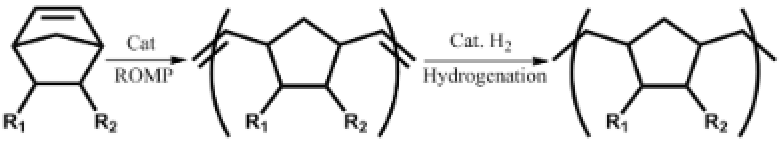

Fig.IV.1 fabrication process of Cyclo Olefin Polymer (Zeonex)

In this chapter, a published article is presented that reports our major results. In the section after the paper presentation (section IV.3), we have added some supplementary unpublished results and our understanding of them. There are the followings:

1) Some PL distribution pictures excited by different excitation wavelengths, including a wavelength longer than the emission wavelength (up-conversion?). The distribution shows that the luminophores excited by these wavelengths are located in different area of the irradiated region.
2) Raman and FTIR spectroscopy results show that the irradiated

regions have a new vibrational peak centred at 1580cm^{-1}, indicating creation of carbon double bonds.

IV.2 ARTICLE PUBLISHED IN OPTICAL MATERIALS: SPACE-SELECTIVE CREATION OF PHOTONICS FUNCTIONS IN A NEW ORGANIC MATERIAL: FEMTOSECOND LASER DIRECT WRITING IN ZEONEX GLASS OF REFRACTIVE INDEX CHANGE AND PHOTOLUMINESCENCE

Optical Materials 133 (2022) 112651

Contents lists available at ScienceDirect

Optical Materials

journal homepage: www.elsevier.com/locate/optmat

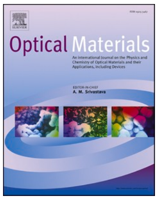

Research Article

Space-selective creation of photonics functions in a new organic material: Femtosecond laser direct writing in Zeonex glass of refractive index change and photoluminescence

Ruyue Que [a], L. Houel-Renault [b], M. Temagoult [c], C. Herrero [a], M. Lancry [a], B. Poumellec [a,*]

[a] Institut de Chimie Moléculaire et des Matériaux d'Orsay, UFR Sciences, Université Paris-Saclay, CNRS, 91405, Orsay, France
[b] CPBM, Institut des Sciences Moléculaire, UFR Sciences, Université Paris-Saclay, CNRS, 91190, Gif sur Yvette, France
[c] Imagerie-gif, Institut de Biologie Intégrative de la Cellule, Université Paris-Saclay, CNRS, 91190, Gif sur yvette, France

ARTICLE INFO

Keywords:
Organic photonics
Visible luminescent source
Direct laser writing
Cyclo olefin polymer
Femtosecond laser induced solid transformation

ABSTRACT

A Cyclo Olefin Polymer (COP), Zeonex® glass exhibits advantage for applications in photonics: high transparency from NIR to UVA, humidity insensitivity and refractive index stability. We thus studied this organic glass, made with only carbon and hydrogen to show that it can be used as a substrate for photonics. We investigated the microscale transformations induced by fs laser direct writing according to parameters: pulse energy, repetition rate, scanning speed (or time of irradiation). We pointed out two domains of modifications, one at low mean power between 0.1 and 20 mW and another above 20 mW. We called them type I and II. In type I, two basic modifications – photoluminescence (PL) creation are restricted to the irradiated volume at the scale of beam size, a large refractive index change (+0.14) appears when the pulse repetition rate is high(>500 kHz), enabling local modulation of optical properties for potential applications. Here, modification of the COP molecule is moderate and the spatial sensitivity is of the order of μm. In type II, the modification is more extended but PL is much stronger. Through correlations between the PL results, we defined signatures composed of luminophore series: S1 associated to type I, S2 associated to type II and S3 for intermediate conditions. S1 is the luminescent group, with the largest yield excitable at 475 nm with a broad emission from green to orange-yellow. S2 is remarkable with a broad excitation in the green and broad emission in yellow range. S1 and S3 results from small molecular modification but S2 is likely resulting from the disruption of COP molecule forming Carbon Dots.

1. Introduction

Electronic integration, due to its Moore's Law limits and high energy consumption, will gradually not be able to cope with the high data volume processing of the future [1]. Therefore, the hybrid integration of optics and electronics [2], as well as all optical integration [3], will become a trend, especially in the fields of telecommunications [4], displays [5], and the sensing [6–9], processing [10,11] and storage of information [12].

In terms of methodology of optical integration, the optical components required for the various applications are often space-consuming and expensive. Especially, when they are used in combination with electronic components, where they require sophisticated assembly. To address these issues, we are focusing on solutions that embed photonic functions in integrated optics in a simple but effective way, thereby simplifying system assembly and significantly reducing costs. Ultrafast photon micro-manufacturing, especially **femtosecond laser direct writing (FLDW)** is an effective method for achieving precise functional implantation in transparent materials. It currently enables to change the refractive index [13] in the material to achieve waveguides or Brag grating structures for sensing, the realization of crystalline or nano-structures [14] for optical processes such as second harmonic generation (SHG) [15–17], metamaterials design [18,19], and etching of three-dimensional structures or channels on the surface and inside of materials for chemical and biological microfluidic integration [20,21].

In terms of material selection for optical integration, researchers are always searching for transparent materials with better performance for applications such as display, optical substrates, wearable devices, etc. Organic and inorganic materials have their own advantages and

---

* Corresponding author.
E-mail address: Bertrand.Poumellec@universite-paris-saclay.fr (B. Poumellec).

https://doi.org/10.1016/j.optmat.2022.112651
Received 26 April 2022; Received in revised form 6 June 2022; Accepted 20 June 2022

Abbreviations

COP	Cyclo Olefin Polymer
FLDW	femtosecond laser direct writing
RIC	refractive index change
PL	photoluminescence
QPM	Quantitative Phase Microscopy
EEM	Excitation-emission matrix
EPR	Electron paramagnetic resonance
Ep	Pulse energy
RR	repetition rate
ROI	region of interest
KPFM	Kelvin probe force microscopy

limitations. In terms of organic materials, compared to those clear plastic commodities such as polymethylmethacrylate (PMMA), polycarbonate (PC), polydimethylsiloxane (PDMS), and polystyrene (PS), **Cyclo Olefin Polymer (COP)** is a relatively new class of polymers with better performance. COP (Zeonex®) was commercialized in 1990 and has been widely used in the fields of optics, displays, pharmaceuticals, life sciences and electronics. It is an amorphous polymer based on bi-substituted cyclo-olefin. The polymer is fabricated by ring-opening metathesis polymerization of cyclic monomers followed by hydrogenation [22], the process and the monomer structure of the final product is shown in Fig. 1.

Not to mention its advantages in other areas, in terms of optical material uses, it has outstanding benefits such as high transparency from UVA through NIR, low birefringence and impressive refractive index stability, comparing to PMMA (details can be find in website of Zeon.com). It has high modulus and high flow enable to be better shaped, making flatter and thinner substrate, so that, one of its products, 490R is considered as a good candidate of polymer optical fiber for Bragg grating sensing [7]. Lastly, in aspects of its electronic properties, COP is notable for having low dissipation factor, as well as a low permittivity. As a result, it is a very good insulator as well. Besides, it offers the lowest fluorescence of any injection-moldable thermoplastic.

In this work, we demonstrate that we can use a one-step method to create several functions including photoluminescence (PL) and refractive index increases (RIC) in a grade of COP (Zeonex 790R) with only a proper selection of laser parameters of focused femtosecond laser.

In the most modifiable regions, especially at lower scanning speed (such as 1 μm/s), the center of the line became opaque but surrounded by transparent region with a different refractive index. Quantitative Phase Microscopy (QPM) was performed in order to obtain its average refractive index value deducing that, it is possible to fabricate waveguides and gratings in this material. On the other hand, the above mentioned opaque modified center turns out to be luminescent under visible light excitation. The luminescent regions are localized within the laser focal area.

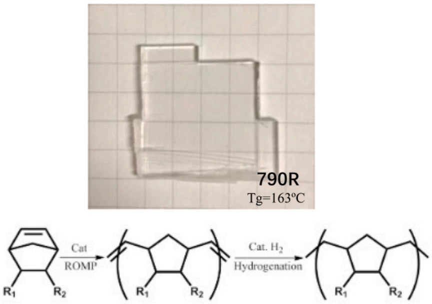

Fig. 1. Sample of COP(Zeonex®790R) and scheme of fabrication process.

Some similar studies have been recently carried out in other plastics such as PMMA [12,23,24] and PDMS [25], with demonstration of data storage. In contrast to their work, we have studied laser modifications with a wide range of parameters in order to gain a better understanding and insight of the parameter landscape. Thanks to simulation of the temperature at and out of the center of the laser focus, we have gained an in-depth understanding and attempted to explain the relationship between the morphologies of the various material transformations and pulse energy or pulse frequency.

To get an idea of the origin of the PL, EPR experiments were conducted to verify the presence of free emitting radicals as it was proceeded in PMMA [23]. We detected free (emissive) radical centered on a carbon atom, implying no H containing in the products, we can thus imagine that as previously observed in literature [26], the opaque 'black substance' may be related to carbon structure with conducting properties. We therefore foreseen the possibility that conductive traces might be written in Zeonex glass.

Both PL and RIC have potential applications in sensing, PL can also be used for data storage, display or tracking. The possible local increase in conductivity might increase the flexibility of its use when it needs to be connected to electronic-based functional components.

2. Experimental details

2.1. Materials

We received samples of Zeonex 790R from ZEON company, with purity of outgas <10 ng/g, which is significantly lower than PP and PC. This grade(790R) was chosen because its glass transition temperature Tg = 163 °C is the highest among the other grades within our range of options. With higher Tg, we increase the selectivity of laser parameters, i.e. pulse energy since we are not able to precisely manage the power less than 1 nJ. The sample was cut by a metal saw into a smaller piece with size 2 cm × 2 cm in order to be suitable for the fs laser platform. The surface was already polished (optical quality) according to the production method and had the optical smoothness for avoiding laser light scattering at the surface.

2.2. Laser irradiation

A commercial Yb-doped fiber pulsed fs laser (Satsuma, Amplitude System Ltd., Bordeaux, France) with wavelength of 1030 nm, pulse duration of 250fs was employed for the irradiation. An aspheric lens with numerical aperture of 0.6 focused the laser about 100–200 μm under the sample surface. All the irradiations were performed as a way of scanning along x axis of the platform (refer to the black coordinate in Fig. 2).

The study was processed by writing lines from a set of pulse energies from 0.5nJ to 2μJ and repetition rates from 1 kHz to 1 MHz with scanning speed = 1 or 10 μm/s without any waiting time for speed acceleration as the minimum step of our stage is 100 nm. So, it makes 100 nm or 1 μm each 100 ms. There is thus no special pulse accumulation at

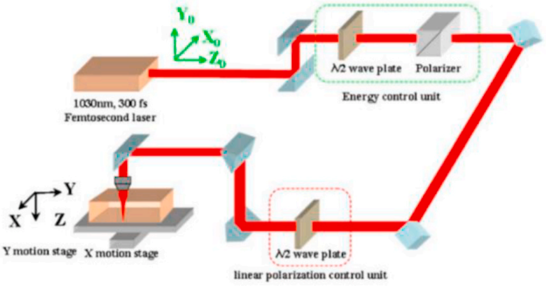

Fig. 2. Schematic of fs laser irradiation setup.

the beginning of the lines. The laser polarization was parallel to “x” scanning direction. The length of each line was 200 μm separated by 50 μm.

2.3. *Quantitative Phase Microscopy (QPM) for refractive index change (RIC) analysis*

Quantitative Phase Microscopy (QPM) is a technique to measure the phase retardance in order to analyze the refractive index of the region after fs laser modifications. A CCD camera mounted on top of the optical microscope in transmission mode captures the sample images of the focal plane and the plane of ±3 μm to the focal plane (with ×20 objective). The defocusing process during measurement is automatically controlled by a piezoelectric element mounted on the objective lens. The introduction of a small amount of defocus is mathematically equivalent to a differential propagation of the field. Thus, to obtain a quantitative phase image one collects an in-focus image and very slightly positively and negatively defocused images and uses these data to estimate the differential with respect to the defocus of the image. The resulting data can be solved to yield the phase distribution by use of a Fourier-transform implementation (see Ref. [27]). Then the phase images are converted by Matlab® program into $\Delta\varphi$ and thus, we can calculate the RIC of irradiated region Δn with equation.1 if the thickness *l* is known, in our situation here is 6 μm. 550 nm filter with ~10 nm band were introduced to select the wavelength of the non-polarized light for measurement. One limitation of the method is such that the objective strength that defines the field depth thickness and the intensity gradient should be chosen in such a way that the gradient does not vary at this scale. Then, the shift of defocusing is chosen much smaller than the field depth. For instance, we chose 3 μm for ×20 objective. Another limitation is that transversal gradient should not be too fast in front of the optical resolution otherwise it is blurred.

Finally, through the phase shift $\Delta\varphi$ of the irradiated and unirradiated region, we can easily calculate the RI difference using the expression below.

$\Delta \mathrm{n} = \Delta\varphi \frac{\lambda_0}{2\pi \mathrm{l}}$, λ_0 is the wavelength in vacuum, here is 550 nm (equation.1).

The QPM method is influenced to some extent by the intensity and distribution of the background light. The error caused to the results will be less ±3 rad if the incident light intensity, aperture diameter and the condenser are well set.

2.4. *PL characterizations equipment*

2.4.1. *Emission spectra excited from near UV*

Emission spectra in UV excitation are acquired with a commercial spectral CLSM device (TCS SP5 AOBS, Leica) equipped with Leica oil immersion apoplan objective (×20/NA 0.7) and coupled with continuous (CW) UV Ar laser (Enterprise II, Coherent), with. excitation wavelength of 351 nm and 364 nm. The size of confocal images is 512 × 512 pixels (1.52 × 1.52 μm), recorded on 12 bits’ photomultiplier with a zoom value of 1 and a pinhole value of 1 airy unit (60.66 μm). Spectra are acquired in direct slow scanning mode (400 Hz) from 380 nm to 655 nm, with a 10 nm bandwidth and a 6.62 nm step-size. Data are then analyzed with Leica image-analysis software (LAS AF, Leica) to select ROI and export the emission spectra data. Spectra are draw with OriginLab by converting x-axis from wavelengths(nm) to energy(eV) by E (eV) = 1239.8/λ (nm)

2.4.2. *The excitation-emission matrix (EEM) fluorescence spectroscopy in the visible range*

One part of the measurements was performed with a confocal microscope (Leica Sp8 - X) equipped with a white light pulsed supercontinuum source based on LED and Photonics Crystal Fiber, with pulse duration of 120 fs with repetition rate of 80 MHz. Excitation wavelength was varied from 470 nm to 670 nm with 8 nm step. A gate is available for collecting the light in the laps time of 12ns between two pulses. The objective used was ×10 (dry, 0.4NA) and ×20 (optical oil contacted with sample slide, 0.7NA). The optical axial spatial resolution with the pinhole(53.1 μm) of confocal microscope system using 10x objective, is around 564 nm at λ = 470 nm and 674 nm at λ = 670 nm. The emission spectra were measured by HyD photodetector with time gating(0–12ns) from 480 nm to 740 nm with 10 nm resolution. HyD photodetectors, combining PMTs and avalanche photodiodes (APDs), have better sensitivity (47% instead of 25%) and lower level of dark noise compared to classic photomultiplier tubes (PMTs).

Emission/excitation spectra matrix or map (EEM) were recorded for each pixel of the microscope image (multispectral). This allows following the fluorescence properties variation along or across the laser written lines. More specifically, the excitation emission map visualizes the energy level distribution of the luminophores, how many of the major absorption and emission energy levels are involved with the information of the number of excitation/emission centers and their positions, we could deduce suggestions on the energy level structure of a given PL process.

2.5. *EPR analysis*

Electron paramagnetic resonance (EPR) or electron spin resonance (ESR) spectroscopy is a method for studying materials with unpaired electrons. We studied 2 samples, one was a fresh sample for reference and another one containing a 2*2 square inscribed with 200 lines (go and return), 153 μm below the surface, by an irradiation under the following laser parameters: scanning speed = 2 μm/s (go and return), Ep = 10 nJ, RR = 1 MHz. These X-band EPR measurementsX-band EPR spectra were recorded on a Bruker ELEXSYS 500 spectrometer equipped with a Bruker ER 4116DM X band resonator, an Oxford Instrument continuous flow ESR 900 cryostat, and an Oxford ITC 503 temperature control system and were carried out under the following conditions: MW freq. 9.63 GHz, MW power 1 mW, gain 50 dB, Mod. Ampl. 8 Gauss, Mod. Freq. 100 KHz at 90 K, 180 K and 290 K.

3. Results

3.1. *Pulse energy (Ep)/repetition rate (RR) landscape: types of modification*

Fig. 3 show the morphology under microscope of the modifications produced by laser irradiation with a set of pulse energies from 0.5nJ to 2μJ and repetition rates from 1 kHz to 1 MHz with scanning speed = 10 μm/s and polarization parallel to “x” scanning direction. The length of each line is 200 μm and separation between the go and return pairs is 50 μm.

We observed that, following Ep increasing with the same RR, the effect is more intense. It is also the case at constant Ep while varying RR. For example, comparing Fig. 3 b), c) and d), when RR increases, the width of the trace increases at first and then becomes explosive and very irregular.

Fig. 3e shows the thresholds of permanent modifications that we defined by observation from Fig. 3: type I with opaque object created (as in Fig. 3a) and type II where the traces widen and become very irregular (as in Fig. 3d). We use this morphology difference to define the landscape area of type I and type II for later discussion, and to locate the position of the parameters for our next characterizations. We plotted also the iso mean power lines in Fig. 3e (dotted lines). It is worth to compare these values with those of inorganic materials for instance that are a fraction of W. Here, the mean power for achieving modifications are about 3 order of magnitude lower. This could be an advantage for some applications like 3D recording. We can also note that boundary slopes are close to the one of iso mean power (i.e. 1) although smaller (around 2/3).

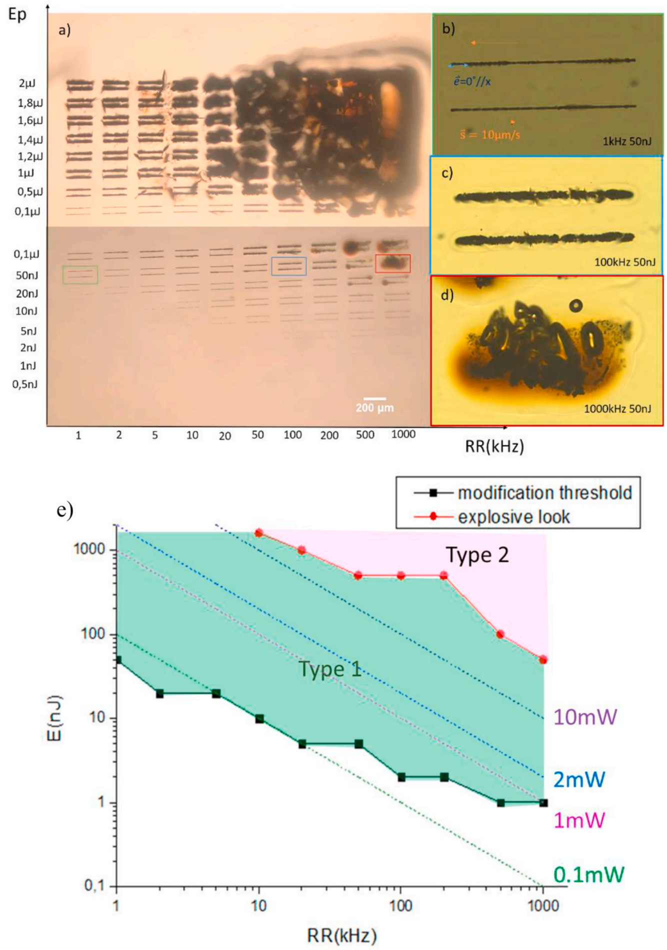

Fig. 3. Microscopic photo under natural light in transmission mode: a) morphology of the modifications irradiated by a set of pulse energy and repetition rate, b) zoom of modification lines produced by irradiation at Ep = 50 nJ, RR = 1 kHz, c) zoom of irradiated lines at Ep = 50 nJ, RR = 100 kHz, d) zoom of irradiated lines at Ep = 50 nJ, RR = 1 MHz, e) thresholds or landscape of type 1 lines (defined by appearance of dark zone) and type 2 lines (defined by line widening around 50 μm) according to Ep and RR. The dotted lines are iso mean power, the value of which mentioned on the right of the graph.

3.2. Speed influence

Changing the scanning speed (v) is to change the spatial density of pulses (RR/v) or the number of pulses received on a point taking into account the beam width ($\frac{2w.RR}{v}$, where w is the beam radius at the focus at FWHM). It is the third important parameter in the direct writing process. If the modification process is relevant of one linear reaction in term of photon energy, the fluency is relevant and it is $\frac{\mathrm{Ep}.2w.RR}{v}$.

Therefore, we designed experiments with lower scanning speed in order to increase the spatial pulses density and see the effect on the type 1 threshold. Fig. 4b shows the morphology of modifications irradiated by scanning speed = 1 μm/s under optical microscope under transmission mode for E_p ranging from 0.1 to 5 nJ and RR from 1 kHz to 1 MHz. From these results, we have plotted the type 1 threshold in Fig. 4c (red points and line) and compared it with the one obtained at 10 μm/s.

As expected, the threshold for 1 μm/s is lower than the one for scanning speed 10 μm/s, the difference is much lower than a decade (ca $10^{1/3}$) and its slope versus RR is comparable.

Beyond the threshold, in the type I region, the morphology is also different (see Fig. 4b, 4 nJ, 1 MHz). Comparing with the lines irradiated with faster scanning speed (e.g. Fig. 3b and c), we observed the transparent region with refractive index change along the irradiated lines has larger ratio in size comparing to the opaque clusters produced in the middle. Along the same mean power, this area extent with increasing RR. This is more detailed in the next section (3.2).

From the Ep/RR landscape experiments (Fig. 3), we find for some laser parameters (especially for high RR i.e. 0.5–1 MHz, and intermediate pulse energy 20–50 nJ), that at the beginning of an irradiated line scan, the modifications seem to appear in the form of type II, and we know that our laser scanning platform has no variation of speed at the beginning compared to the rest of the line. This effect is thus arising from the material revealing a particular sensitivity and an influence of the irradiated part on the not yet irradiated one.

3.3. Refractive index change (RIC)

Fig. 5c shows the phase shift images (0.167 μm/pixel) of the area shown in Fig. 5b with phase shift value $\Delta\varphi$ according to the intensity of the picture. From dedicated Matlab® program analysis, we get the phase shift profile. Two profiles are shown (10d and 10e) allowing us to estimate the phase shift amplitude between 10 and 30 rad.

Choosing the region marked in red in Fig. 5e for RIC calculation, we have $\Delta\varphi \approx 10\ \mathrm{rad}$. Since the phase shift image is coming from defocusing image $\pm 3\mu m$ up and down from the focus(Fig. 3b), 6 μm distance has been moved by a piezoelectric element, we estimate the RIC of the irradiated transparent region to about 0.14, according to equation.1 in section 2.3. This is quite noticeable indicating a large change in the structure which is like a condensation of the heavier atoms (carbon) or an aggregation of monomers.

3.4. Photoluminescence (PL) characterizations

In the course of investigation of the laser induced modifications, we found strong luminescence excited at several wavelengths from the UV range to the visible one with emission in the visible. So, we decided first to precise the landscape of these parameters for excitation in UV before studying the complete luminescence properties.

3.4.1. PL creation: fs laser parameter ranges and its distribution

First, we want to know in what range of laser parameters we can efficiently produce PL. Fig. 6 shows the energy/RR conditions for PL creation and increase. For this broad observation, PL was excited under a UV lamp around 366 nm. We can see that PL progressively appears locally in the lines after some transformations that are detected in the picture on the right. Then, increasing the energy or the RR moderately, the line broadens and in the same time PL increases. For larger energy and RR, the broadening become explosive and a PL is appearing concentrated on the periphery of the transformation.

When RR is high, PL is created when permanent modifications appeared at the lowest Ep i.e. at the threshold, at 1 MHz 1 nJ. When RR is low, the PL intensity is smaller than the one with high RR, it is hard to define the minimum Ep needed to trigger PL creation under UV lamp since the PL is so small that the detection depends on the sensitivity and excitation intensity. (However, it was confirmed under confocal microscopy that, whatever RR, PL production occurs when visible modifications appear) and stops when Ep overcomes some values.

The distribution of the laser-induced PL in the line is found dependent on laser parameters. Fig. 7 shows the strongest PL located at the periphery of the irradiated lines for high RR(500–1000 kHz). Those 3d photographs show that the PL is located at the periphery of the beginning of type I or type II lines, especially the periphery before the focus, while the PL intensity inside the line is negligible compared to the periphery at this excitation(490 nm) and detection wavelengths(500–550 nm). It should be noted that at the beginning of laser scanning (the head), a large enhancement compared to the rest of the line (the body) is recorded. This does not arise from the stage but from the material itself.

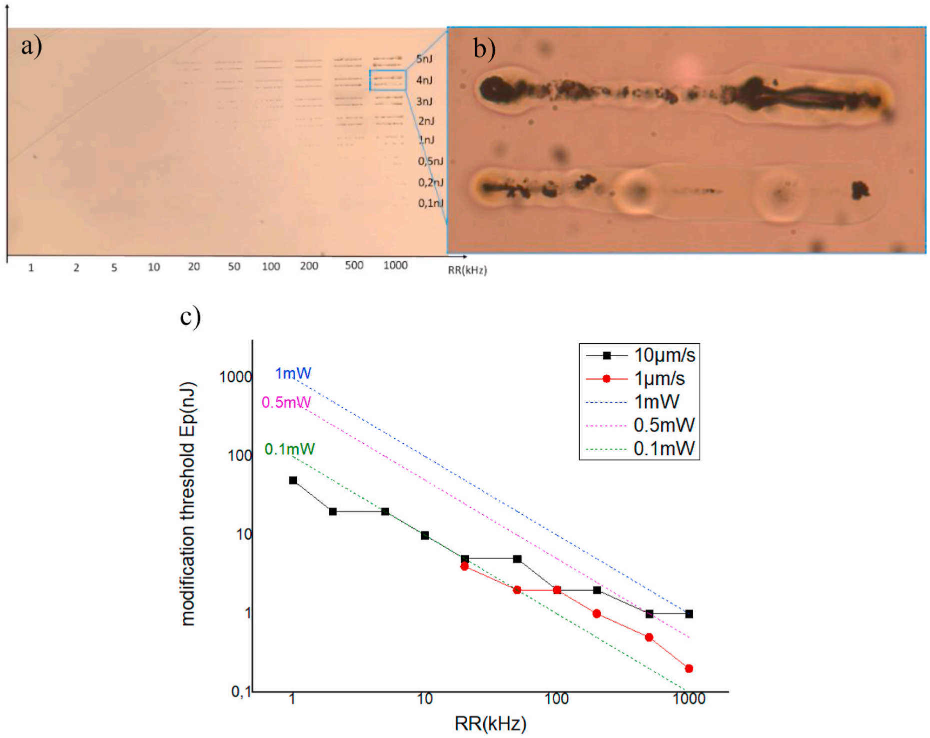

Fig. 4. A) Optical microscope image under natural light of irradiated lines (Ep from 0.1 nJ to 5 nJ and RR from 1 kHz to 1 MHz) with scanning speed = 1 μm/s.b) zoom of irradiated line (Ep = 4 nJ, RR = 1 MHz) c)the thresholds comparison of Type I modification according to RR between scanning speed = 1 μm/s(red) and 10 μm/s(black), dash lines are mean power for reference.

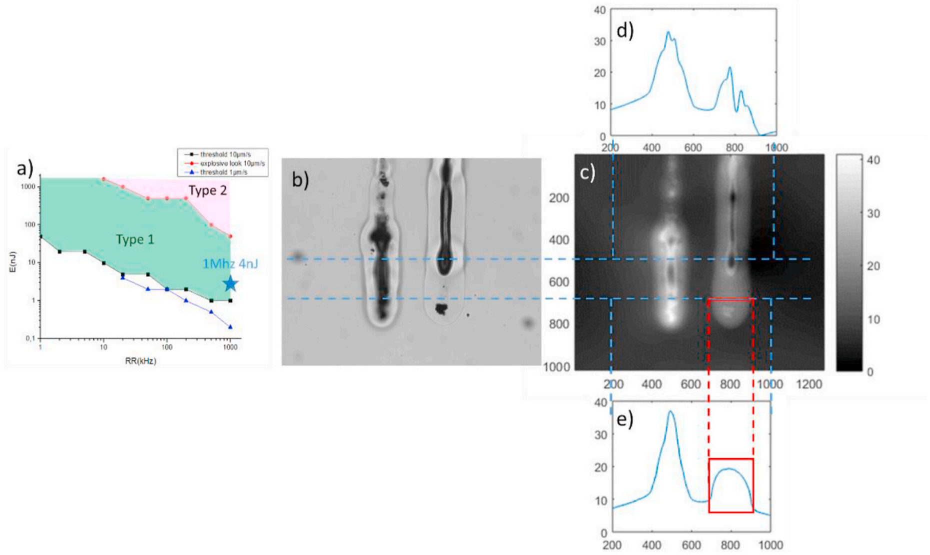

Fig. 5. A) location in the landscape of the measured lines. The star indicates the position of the experiment in the landscape. b) Microscope photo of irradiation lines (scanning speed = 1 μm/s, RR = 1 MHz, Ep = 4 nJ) under green wavelength (550 nm). c) The phase shift image. d) The phase shift profile along pixels at y = 500 (horizontal profile). e) The phase shift profile (unit rad) along pixel y = 700. The red square enhanced the profile along the red square in c).

3.4.2. *Emission spectra excited with UV according to type of transformation*

3.4.2.1. Low average power (1 mW). The confocal microscope in mode xyλ (i.e. multispectral) allows to make the difference between each line written with different parameters, but also to differentiate the body and the head of type I line. As a matter of fact, for large RR a blossoming of the head is observed that could be some premises of type II transformation.

Spectral measurements at various locations are shown in Fig. 8.

Fig. 8 d and h shows the PL intensity spectra according to photon energy for type I lines according to RR. For low RR (Fig. 8 b, c and d), the spectrum wherever it has been recorded, can be fitted with a simple Gaussian curve showing that there is only one luminophore with maximum at 2.56eV(484 nm) and FWHM of 0.58eV. It is not the case for large RR where there are differences between the different locations. Beside the center pointed out above for low RR, we found a second one with a relative weight of 0.35, centered on 2.88eV(431 nm) with FWHM of 0.28eV for 5 nJ, 0.5 MHz and a third one with a relative weight of

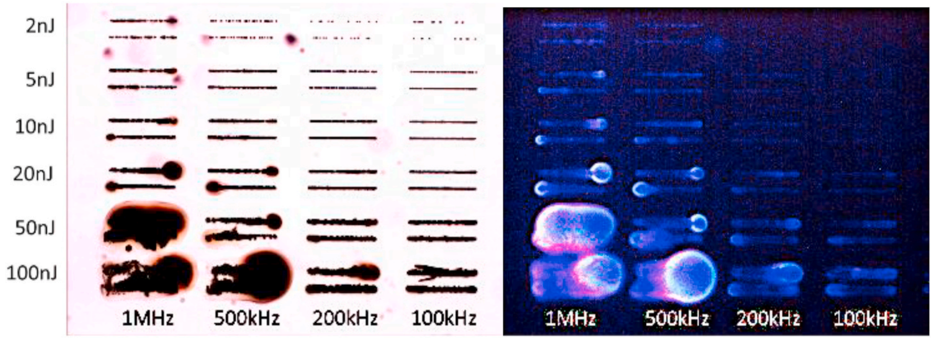

Fig. 6. Irradiated lines under natural light in transmission(left) and PL excited with UV lamp (366 nm) (right), the scanning was performed go and return for the 2 lines in a group, with speed = 10 μm/s.

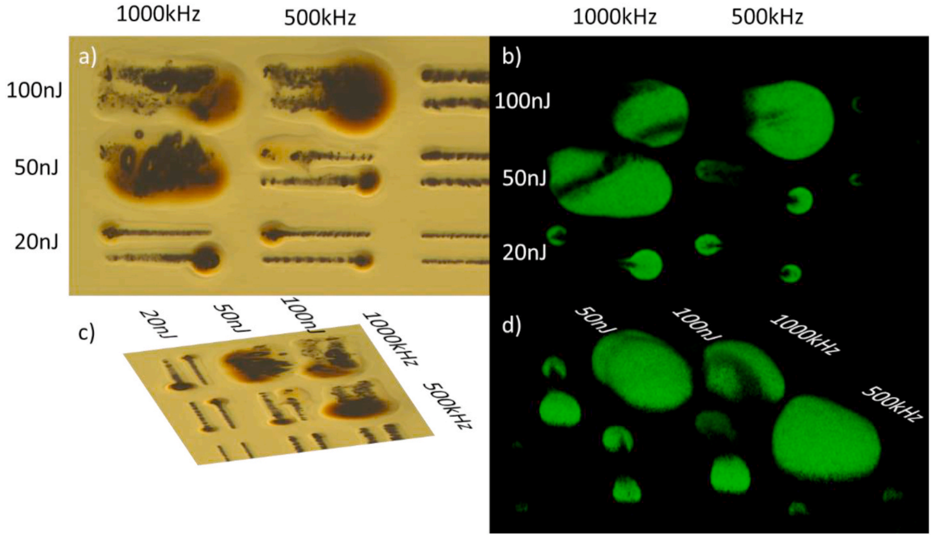

Fig. 7. A) and c) optical image under natural light in transmission mode as indication for picture b) and d). b) and d): 3D luminescent picture modelling of irradiated lines (in (a) and(c)) under excitation light at 490 nm, and detected in range 500–550 nm.

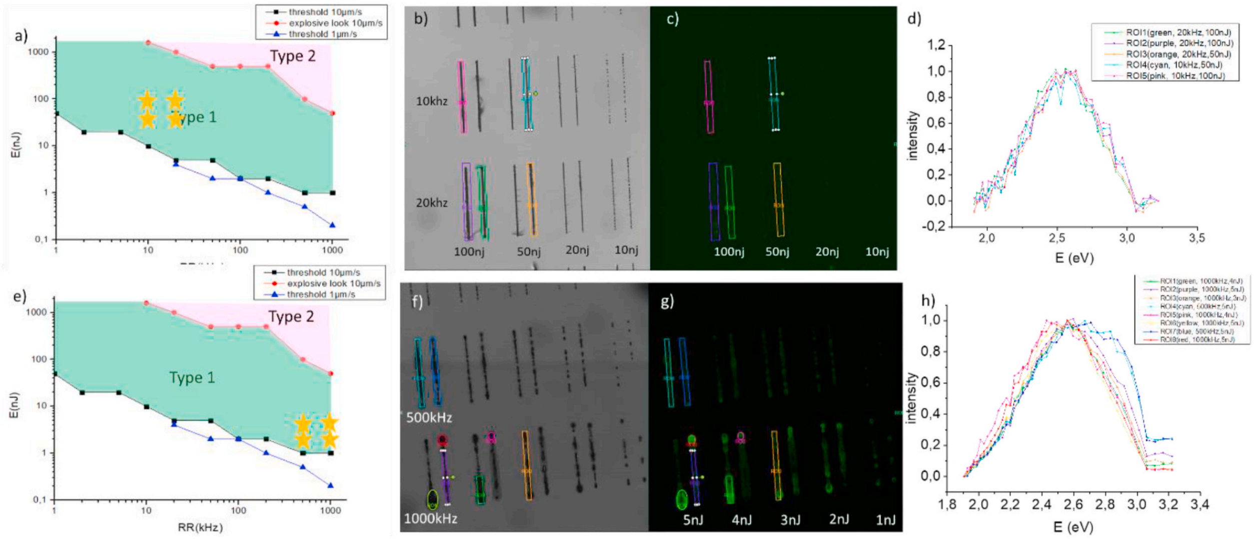

Fig. 8. Luminescence spectra of the Zeonex excited in UV. a) and e) locations of the various measurements performed in the type I regime. b)- d): irradiations at low RR. f)-h) irradiation at high RR. b) and f) optical image obtained by transmission of natural light. c) and g) luminescence images. d) and h) emission spectra of ROIs excited at 351–364 nm, which are marked in b) and f).

Table 1
The different Gaussian components found from luminescence spectra of Figs. 8 and 9.

Gaussian component parameters for low average power	2.20eV(564 nm)	2.56eV(484 nm)	2.88eV(431 nm)
	FWHM = 0.28eV	FWHM = 0.58eV	FWHM = 0.28eV
Type I (low or high RR)		1	
Type I body 5 nJ 0.5 MHz		1	0.35
Type I head 4–5 nJ 1 MHz	0.25	1	
Gaussian component position for high average power	2.28eV(544 nm)	2.63eV(471 nm)	2.92eV(425 nm)
	FWHM = 0.35eV	FWHM = 0.55eV	FWHM = 0.28eV
Type I head 50 nJ 0.5 MHz	0.44	1	
Type I (high RR) body		1	0.30
Type II		1	0.30

0.25, centered on 2.20eV(564 nm) with FWHM of 0.28eV for the head of the line written at 4–5 nJ and 1 MHz. Relative weights are collected in Table 1.

3.4.2.2. High average power (20–100 mW). Fig. 9 shows luminescence spectra of lines written at the border between type I and II regions and excited at 351 nm and 364 nm. Spectra were recorded on the body, head of type I lines and the periphery of type II line.

Although we have already noticed that the type I line exhibit some large broadening that might be of the same nature that the type II, we have found some discrepancies from luminescence characterization.

The head of one line (500 kHz, 50 nJ) type I shows a distinct shift and larger intensity from the other ROIs: fitted by two Gaussian we got maximum at 2.28eV(544 nm) and FWHM of 0.35eV. The body of a type I at high RR seems to have also 2 peaks: 2.63eV(471 nm) and 2.92eV (425 nm). Lastly, emission from the type II appears very close to the previous one. For easy comparison, we gathered the information in Table 1.

As we can see in Table 1, for low or high average power, there are always three Gaussian components to consider. Moreover, whatever the average writing power, the three components appear quite close.

So, we can establish the following correlations:

- first, at low RR and bottom of type I region, a luminophore emitting at 484 nm is produced in the body of the line,
- at larger RR or larger Ep, expansion in the head of the line develops a slightly different luminophore with maximum at 564 nm or 544 nm.
- from that point, increasing further RR and Ep, a third emission appears peaking at 425 nm in the body of the line in expansion or in type II transformation
- increasing further the energy leads to increase the proportion of luminophores emitting in the blue.

3.4.3. Emission-excitation spectral matrix (EEM) in the visible range according to the type of transformation

To understand how the luminescent property develops according to the increase of Ep, the material points that we have chosen for this study were irradiated by high RR (500 kHz-1MHz), blue lines in Fig. 10a.

Let us begin with the PL of type I body of the lines at low Ep.

Fig. 10 shows the Emission/Excitation spectral Matrix (EEM) from a line written at 1 MHz and 1 nJ. We see that a broad PL from 520 to 580 nm (at half maximum) is excited at 477 nm (blue) with a large intensity. A less intense PL is excitable at 520 nm.

To better understand the PL induced from fs laser according to Ep and RR, we recorded and analyzed the evolution of EEM of lines written from 1 nJ to 100 nJ at 1 MHz and from 20 nJ to 100 nJ at 500 kHz. This is collected in Fig. 11b.

We can see that the pattern in EEM exhibit evolution according to Ep and also to RR, until 10 nJ even in the head of the line for 1 MHz and 100 nJ for 500 kHz, the luminescence intensity is excitable around 480 nm mainly but a smaller component is excitable around 510 nm. The emission is quite broad between 520 (green) and 580 nm (yellow) as shown in Fig. 10.

Above these values, the EEM pattern transforms and a large luminescence intensity appears, excitable at 525 nm and emitting at 587 nm. We found that PL appears at the same boundary than the explosive look seen in morphology analysis under optical microscope and from which we defined the boundary of type I and type II.

A luminescence intensity excitable in the green is not the only appearance we can observe. There is also a luminescence that increases around the blue-green region (excitable at 470 nm and emission at 485 nm) as we can see in Fig. 12.

The complexity of these luminescence centers and the associated transformations led us to practice a linear decomposition of the EEM on the basis of a 3 signatures (S1, S2, S3), each signature containing probably several centers of different types. Then, luminescence properties (EEM) for different parameters or different transformation was linearly decomposed on the basis of EEM_{S1}, EEM_{S2}, and EEM_{S3}.

3.4.3.1. Definition of signatures.

- ➢ Signature 1: main broad emission from 520 nm to 580nm (half maximum) excited at 475 nm blue. Excitation with center at 520 nm was pointed out, but weaker than the ones at 475 nm, with a ratio of ex475: ex510 around 3:1 (see Fig. 13).
- ➢ Signature 2: this luminophore group has been obtained by subtracting the maximum content of S1 from EEM of 10 nJ at 1 MHz. It shows a PL at 587 nm (orange-yellow) excited at 525 nm (green). The result is shown in Fig. 13.

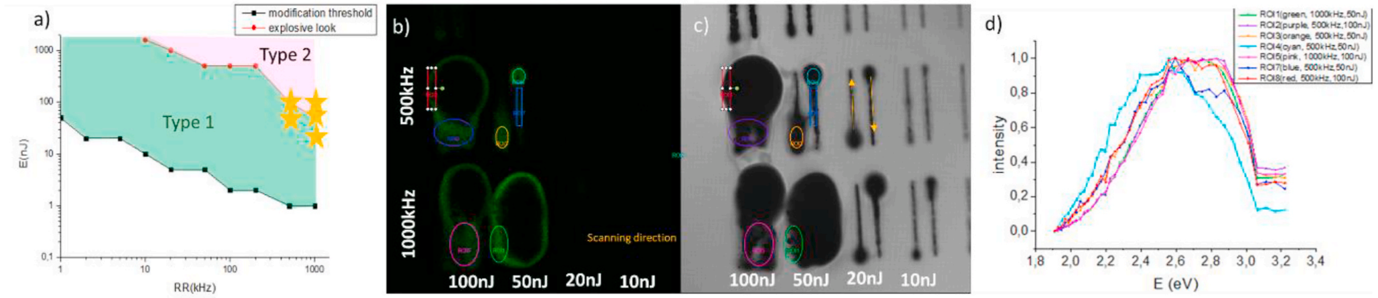

Fig. 9. (A) location of the luminescence measurement in the landscape (b) luminescence distribution along the lines. (c) natural light transmission (d) emission spectra of 8 regions of interest(ROIs) excited at 351–364 nm.

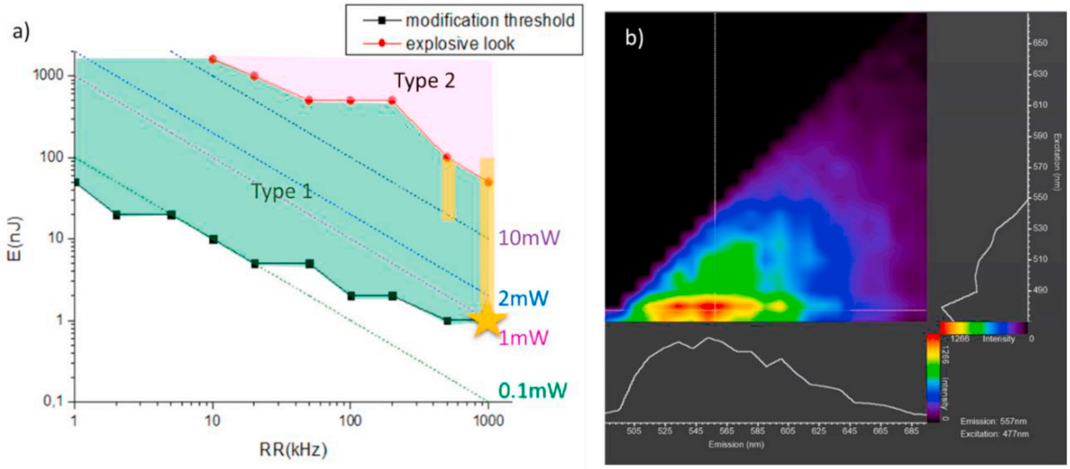

Fig. 10. A) locations in the landscape of the investigated parameter of low Ep (1 nJ, 1 MHz, yellow star) b). Photoluminescence from the line body written at 1 MHz, 1 nJ. The luminescence photograph on the left indicates the location of the measurement, it is associated to type I process. The vertical axis corresponds to the excitation wavelength from 470 nm to 670 nm, whereas the horizontal axis is for the emission wavelength from 480 nm to 730 nm. Two spectra are plotted: an emission one excited at 477 nm (excitation maximum) and an excitation one detected at 557 nm (emission maximum). The intensity scale is linear.

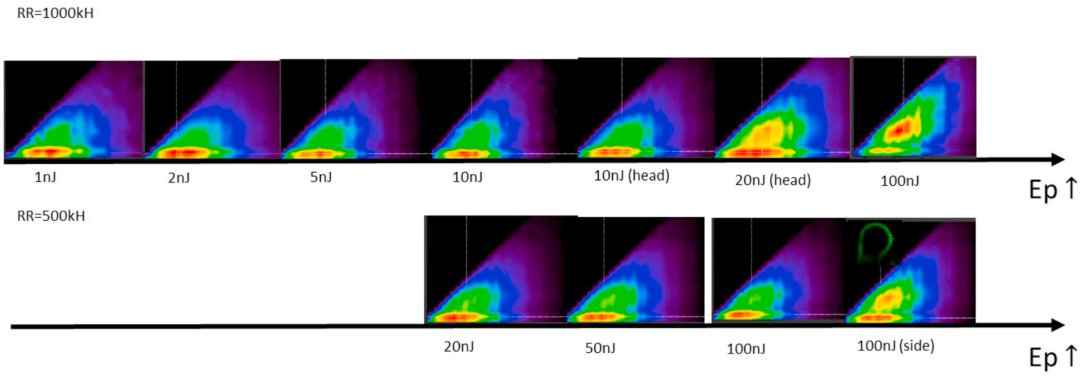

Fig. 11. EEM of lines from 1 nJ to 100 nJ in 1 MHz and 20 nJ–100 nJ in 500 kHz. Location in landscape marked in Fig. 10a with yellow bars. For all of the EEM, the excitation wavelength is between 470 nm (bottom bound) to 670 nm (up bound), the emission wavelength is from 485 nm (left bound) to 695 nm (right bound). The color scale is from dark to red for 0 to 1. The images have been normalized to 1 for easy PL analysis.

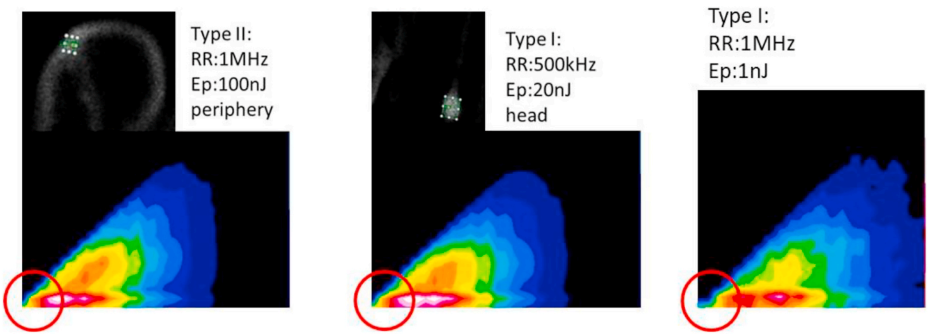

Fig. 12. The comparison of high energy transformation (head of type I and periphery of type II) with the body of type I at low energy. Note the absence of luminescence intensity at high emission wavelength for low-energy writing (1 nJ).

- ➢ Signature 3: we proceeded similarly for extracting an EEM that represents S3. We made the difference between the EEM of head and body of the line written with 20 nJ and 0.5 MHz. Results are shown also in Fig. 13. It looks like a red-edge effect for which emission wavelength follows the excitation wavelength [28,29].

Finally, performing this analysis for all lines, we were able to fill in Table 2 which gives the weight of each contribution for each laser parameters or transformations. The values of weight are obtained by a python program(scipy.optimize.leastsq()) with least square method.

From Table 2, we see clearly that the proportion of S1 that is stable for low Ep, decreases slightly when Ep increases. This is the contrary for the two other components. S2 appears when the blossoming develops and then increases largely. S3 seems to appears with the type II. This

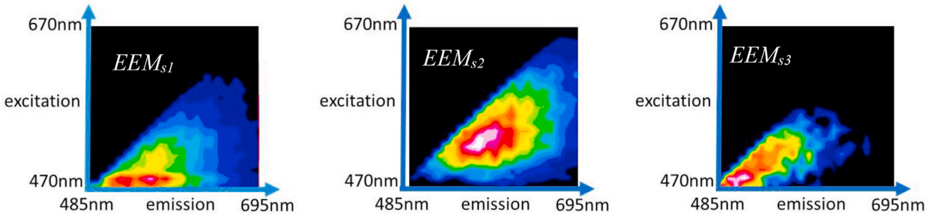

Fig. 13. From left to right EEM for 1 nJ, 1 MHz writing condition considered as signature S1 (EEMs1), EEMS2 obtained from 10 nJ(head), 1 MHz minus 0.8 EEMS1 and EEMS3 obtained by difference between head and body of 20 nJ, 0.5 MHz written line.

Table 2
Component proportions of the various EEM investigated (the value in the table corresponds to the intensity weight of each component). a) bar graph for 1 MHz, b) bar graph for 0.5 MHz.

RR	1 MHz							500 kHz					
Pulse energy (nJ)	1	2	5 Body	5 Head	10 Head	100 periphery	100 inside	20 Body	20 Head	50 body	50 head	100 periphery
Component S1	1	1.06	0.98	1.05	1.00	0.92	0.89	1.04	1.04	0.99	1.10	1.00
Component S2	0	0.03	0.01	0.10	0.31	0.19	0.64	0.12	0.12	0.03	0.22	0.44
Component S3	0	−0.03	−0.01	0.00	0.00	0.25	0.24	0.05	0.16	0.08	0.25	0.21

behavior is a bit similar with the PL excited in UV but more study is needed to achieve correlations.

3.4.3.2. Time gating influence. Due to the time-selective capabilities of pulsed laser-based fluorescence microscopy, we tried to use time gating to distinguish the lifetimes of the different centers. We found that when time gating is selected from 0 to 3.5ns, there is a high intensity around 500 nm emission while it disappears in the setting of 8.5ns–12ns. It is worth noting that from the scale, the emission intensity of the same region by a same excitation source, detection of lifetime gate of 8.5–12ns is weaker than the one of gate 0–3.5ns. the ratio is 4:1 in 0–3.5ns and 8.5–12ns. This is seen in Fig. 14 for which Type I body 500 kHz 20 nJ is composite containing S1, S2 and S3. We prove so, that the lifetime of S3 is shorter than the others.

The EEM results in Figs. 14 and 15 for Type I and Type II lines which contains S1 et S2 et S3 with lifetime gating show that the luminophore(s) excited at 476 nm and emit light at 500 nm (probably connected to S3) with a lifetime shorter than 3.5ns. These confirm the different structures of the luminescent centers.

3.5. Free radicals' creation

Fig. 16 shows the EPR results of two samples: a fresh Zeonex glass (black profiles) and an fs laser irradiated Zeonex (red profiles) and their difference (blue profiles) with three experimental values of the temperature during the EPR measurement: (a) 90K, (b) 180K, (c) 290K. The irradiation was operated at E = 10 nJ, RR = 1000 kHz and scanning speed of 1 μm/s with polarization $\vec{e}$//scanning direction $\vec{s}$.

The results show that only one peak at g = 2.003 is created by fs laser irradiation, which indicates that the unpaired electron is around C instead of H since its quantum number I is equal to 0 for the natural isotope concentration of carbon atom (^{12}C). In fact, EPR signal at g_{iso} = 2.003 (C signal) is ascribed to carbon radical [30] and this signal is a typical EPR spectrum of coked catalyst [31].In a research of fs laser irradiation of PMMA [23], the free radical formation was observed with 9 lines. A proposed explanation was the contribution of propagating radical known as a product of the photodegragation process of PMMA [32].

4. Discussion

4.1. First step of the mechanism

Using a beam of a femtosecond laser, focused in the new COP polymer Zeonex®, we were able to produce 2 types of transformations varying the laser parameters.

The first one (called type I) is a non-destructive transformation of the polymer achieved with a very small mean power (0.1 mW) compared to

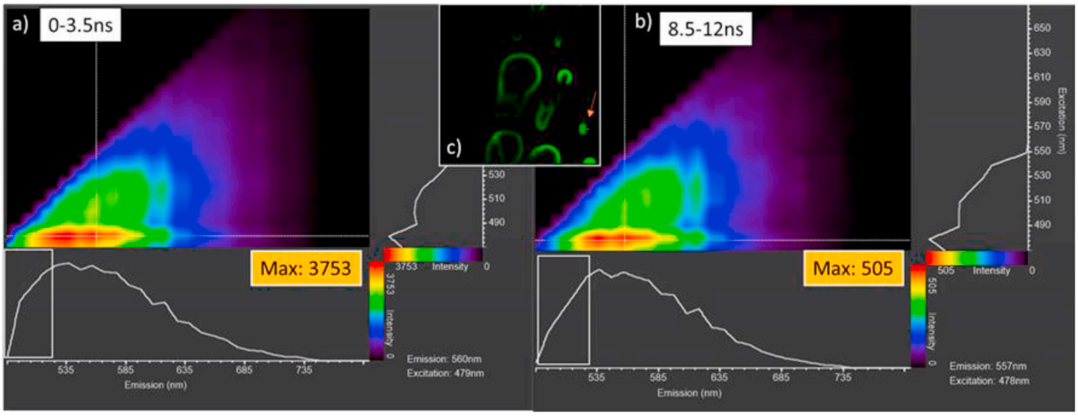

Fig. 14. A) and b) EEM of type I line head (500 kHz, 20 nJ) recorded in time gating in range of a) 0–3.5ns excitation spectrum detected at 560 nm and emission spectrum excited at 479 nm, b)8.5–12ns; excitation spectrum detected at 557 nm and emission spectrum excited at 478 nm. The white square enhanced the range of shorter lifetime. c) the ROI position accordingly.

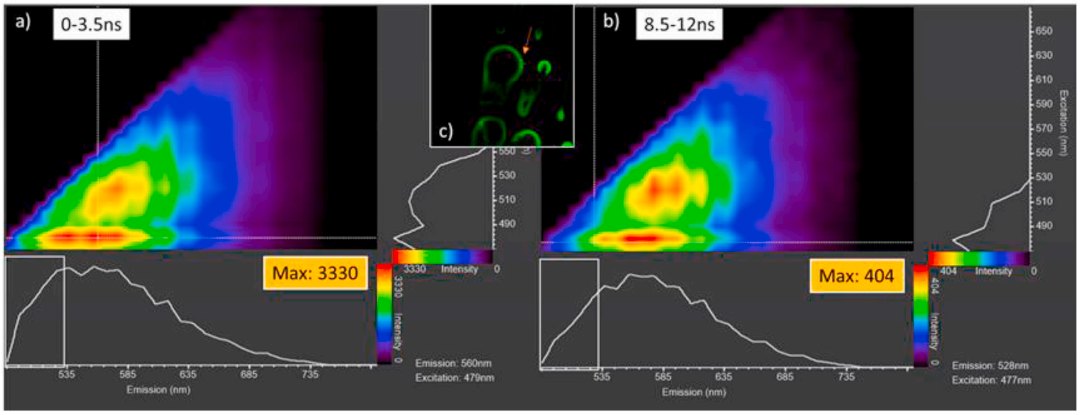

Fig. 15. A) and b) EEM of type II line periphery (500 kHz, 100 nJ) recorded in time gating in range of a) 0–3.5ns excitation spectrum detected at 560 nm and emission spectrum excited at 479 nm, b) 8.5–12ns excitation spectrum detected at 528 nm and emission spectrum excited at 477 nm. The white square enhanced the range of shorter lifetime. S2 appears also having a shorter lifetime. c) the ROI position accordingly.

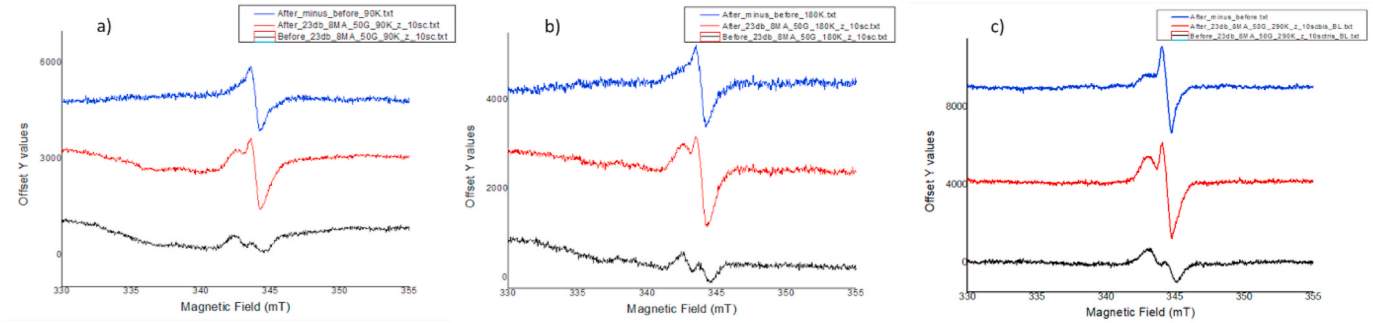

Fig. 16. The EPR results of unirradiated sample (black profile), irradiated sample (red profile) and their difference (blue profile) under measurement temperature at a)90K b)180K and c)290K

inorganic materials (ca.10 mW). However, looking at the dependence of the threshold with the laser parameters, it is not dependent on the mean power only but the weight of the inverse of the repetition rate is lower in the energy threshold (1/2 instead of 1). A creation of luminophores excitable mainly in the near UV range to blue-green, emitting on a broad range from blue-green to orange-yellow (signature S1).

The second type is destructive of the polymer molecule probably. It is explosive, clustering the carbon atoms and corresponds to a sudden large expansion in the material around the irradiation point with yellowing under natural light. It leads to PL creation of two different types, one excitable in the green and emitting in orange-yellow revealing a molecule rather well defined and another one (red-edge effect) arising from molecules varying in size like polycyclic aromatic (signature S2 and S3).

Both of the transformations are thus able to produce PL from various luminophores. Part of them appear excited from UV as it is usual for organic materials but many of them are excitable in the visible range (blue) and emit in the green-yellow with a good efficiency. The red shift in the wavelength of the emission light generally implies an increase in the number of conjugate bonds and even the size of the luminophore(s).

The richness of the PL properties produced through this method indicates a great variety of restructuration. The body of the line (type I) is luminescent mainly from blue excitation. It arises probably from a small molecular restructuration as the local volume does not change much, keeping thus the possibility of a quite local functionalization of the material at the μm scale or less. This corresponds to the creation of unpaired electrons on the backbone of COP that do not contain double bonds or combination of them as it is usual for OLED [33].

The head of the line in the type I regime is excitable from the blue range but clearly the change of the molecule is more extended as a PL efficiently excitable in the visible range is created. We can imagine that hydrogen is excluded from the molecule, giving rise to the blossoming aspect and leaving carbon atoms recombining leading to carbonized clustering and PL in the visible [33]. It is even true taking into consideration S3 PL that has an excitation/emission behavior close to a red edge effect [28,29]. Therefore, we postulate that the products are possibly to be carbonized clusters or dots, like carbon dots (CDs [34]) depending on the size of the clusters, similarly to research with laser-induced graphene electrodes from polyimide [26] or quartz crystal [35] substrates. To prove that, we foreseen to conduct Kelvin probe force microscopy (KPFM) analysis to find out if the laser irradiated lines with or without luminescence are conductive or not. However, there is a difficulty here that the fs laser irradiated line width is at the scale of micron, so there is a high probability of poor contact.

4.2. *The role of the laser parameters*

The first step of the light absorption mechanism with a high intensity femtosecond laser irradiation is a multiphoton ionization or tunneling one (Keldysh criteria $\gamma = \frac{\omega}{e}\left[\frac{\mathrm{m.c.n.}\varepsilon_0.\mathrm{E_i}}{\mathrm{I}}\right]^{1/2}$ with I being the incident intensity, and E_i the ionization energy [36]). Using [37], we fixe E_i to 7.6eV. I is fixed to 10 nJ and thus γ is found around 19. For 1 μJ, it is 1.9. When γ is around 1.5, the process is intermediate between multiphoton and tunneling and thus the intensity dependence decreases. This could be the case for type II transformation, whereas type I is rather multiphotonic before electron density saturation.

At moderate pulse energy (ca. nJ), an interlevel transition producing local unpaired transition is understandable. In the same time, the material temperature increase due to energy deposition with increasing frequency may favor homolytic bond breaking. Then, increasing the pulse energy at large pulse frequencies increases further the mean temperature that may reach the decomposed one (420 °C Zeonex documentation). But as the transformation is achieved in volume, after irradiation (1 or 0.1 s/μm), products recombine, carbon the first in the high pressure region i.e. in the space surrounding the irradiated volume. As a matter of fact, it is in this region that high density materials are frequently identified [38]. This observation would explain why PL of type II is found around the bubble like transformation.

4.2.1. The role of scanning speed

We have first to underline that changing the scanning speed does not change the temperature of the materials unless the speed is of the same order than thermal diffusion speed. This last is estimated by 2Dth/w0 where D_{th} is 3.7–5.9 10^{-7} m^2/s (Zeonex documentation) and $2w_0$ is the beam size (FWHM) of the order of 1.5 μm i.e. ca. a fraction of m/s.

On the contrary, if a non-reversible or partly reversible reaction occurs with a time constant of the order of 1/RR, the advancement degree of the transformation may progress according to the number of pulses that is $2w_0$.RR/v or simply RR/v the pulse density. It is similar to the time of irradiation.

Finally, we just fixed the speed at 1 or 10 μm/s.

4.2.2. The role of Ep and RR

Ep plays a crucial role in the absorption process. Because of the large light intensity, the absorption by non-linear process occurs in the volume of the material at the focus and not before. This is checked through a cross section, as shown in Fig. 17. The modified regions are 130 μm under the surface. At the beginning of the pulse (a few tens of fs), electrons are excited from the ground state to unoccupied levels that exhibit some degree of delocalization. The Ep dependence of the electron density is non-linear but it saturates through relaxation and then the rest of the pulse (much larger than the energy for exciting the electrons) is linearly used for heating the excited electrons that finally gives the energy to the lattice, heating it, inducing some transformation reactions. This mechanism is deduced based on the plasma saturation phenomenon shown in Ref. [39].

In particular, the temperature increase (T) is changed by Ep and RR. Then, if a transformation is thermally activated, the temperature is important. Ep and RR have an effect on the transformation.

Through the Fourier equation, the final temperature in focus is induced by a linear summation of effects of multi-pulses. The final temperature is oscillated. Ep is a coefficient that defines the amplitude of temperature oscillation T_0 in the final steady state. And the other final temperatures, such as the minimum and maximum of the temperature oscillation, as well as the average temperature, is not only proportional to this amplitude T_0, but also the coefficient of this proportion is determined by RR, to be precise, by Rτ if it is in different material. RR plays a role on heat accumulation by time overlap of the effect of pulses.

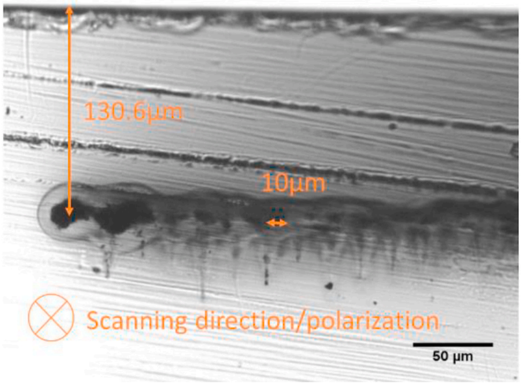

Fig. 17. Microscopic photo of the cross section of 30 irradiated lines in transmission mode under natural light with objective ×10. Irradiation Laser parameters: RR = 1 MHz, Ep = 20 nJ, scanning speed = 10 μm/s with direction perpendicular to the paper plane, in and out. Polarization is parallel to the scanning direction.

Rτ is the ratio between the period $\tau_p = 1/\text{RR}$ and the diffusion time $\tau_D = \frac{w_0^2}{4D_{th}}$ (0.4–0.7 μs for organic material), $R_\tau = \tau_p/\tau_D$. Generally, when $\tau_p < 10\tau_D$,i.e.$R_\tau < 10$, there is accumulation. In our case, the material is the same, Rτ varies from 2 to 2000 due to the change of RR. We thus have accumulation only between 0.1 and 1 MHz. Therefore, the final temperature(oscillated) in steady state is a function of Ep and R_τ. The higher Ep and smaller R_τ, the higher temperature(s), and vice versa. Details of the function please find in appendix. It is worth mentioning that the reduction of R_τ, also reduces the amplitude of the oscillations to some extent, especially in the cases out of focus. We do not make a specific analysis here.

On the other hand, if one considers two activated processes (e.g. one could be the soft molecule transformation and the other one its destruction), with two different activation energies, the effect of the temperature will be different on each of them and one may become dominating the other one. This can be used for pushing up a reaction that does not destroy the material.

Therefore, we consider 2 extreme cases: 1) high RR and low Ep and 2) low RR but high Ep with a constant power (P = Ep*RR), see Fig. 18. In general cases, Rτ we use to reflects the degree of accumulation of pulses on different materials. However, in a same material, when Rτ is large (small RR, no heat accumulation, independent pulses), due to the high Ep, the oscillation amplitude is very large and the minimum temperature is close to room temperature. When Rτ is small (large RR, some heat accumulation, pulses are overlapping), the oscillations are small and the average temperature is around the temperature produced by a continuous irradiation at the same mean power (see Fig. 18 that has been computed from the formula in appendix I). Due to maintaining the same average power, the oscillation at low frequency is 3 orders larger than the one at high repetition rate (see Fig. 18). The amplitude RR = 1 kHz is 356.10^3 K when it is 356K at RR = 1 MHz.

Therefore, in the first case (red in Fig. 18, RR small, Rτ large), only a part of the period is efficient (temperature too low most of the time) and a part may lead to material destruction, whereas in the second case (blue, large RR, small Rτ), the temperature can be better controlled (see Fig. 18).

For proving this and explaining some differences observed in this paper along the average power line in the landscape, we compared the effect of the two following cases (see Fig. 19):

1) Ep = 2 μJ, RR = 1 kHz, 10 μm/s, with mean power of 2 mW and pulse density of 10^8 pulses/μm

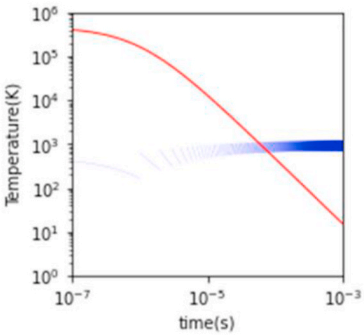

Fig. 18. Comparison on 1 ms of the temperature evolution at the center of a spherical focus for the case of Ep = 2 μJ, RR = 1 kHz (red curve, Rτ≈2000) and Ep = 2 nJ, RR = 1Mhz (blue curve, Rτ≈2). Computation ingredients are given in appendix.

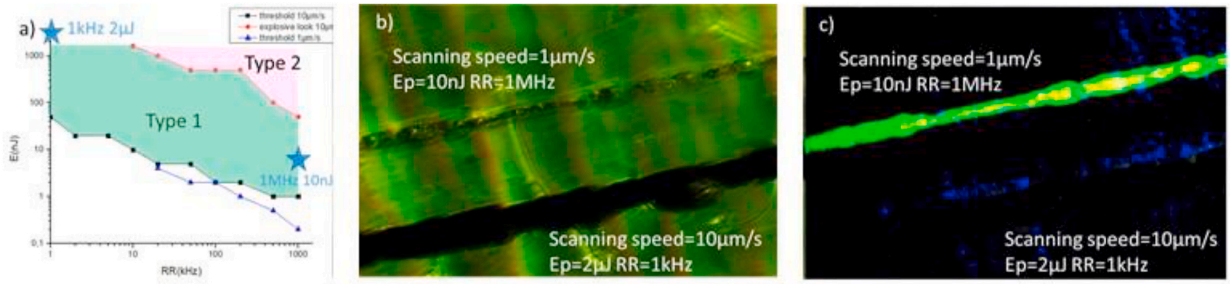

Fig. 19. A) the position of experiments in the landscape, b) the microscopic photo under transmission mode with natural light (c) photo of the luminescence excited by 448 nm laser and with dichroic mirror transmitting wavelength>490 nm.

2) Ep = 10 nJ, RR = 1Mhz, 1 µm/s with mean power of 10 mW and pulse density of 10^{12} pulses/µm

We observed that in these 2 situations which are both in modification type I area, the luminescence is favored at large frequency (and thus low Ep) whereas the average power is not so different. On the contrary, the material is deeply transformed more at low frequency (and thus high energy).

On the other hand, the width of the transformed line, that we can assume to be formed from the places where the maximum temperature overcome some value (e.g. glass transition temperature, decomposition temperature), is smaller in the case high frequencies than for lower ones (see Fig. 20).

Lastly if we consider a constant scanning speed, it means that the time per length unit is the same but of course not the number of pulses, which is several orders of magnitude larger (this is easily seen in Fig. 17). Therefore, we cannot easily differentiate between the effect of the temperature (very high during a short time) and the effect on the number of pulses (many pulses at much lower temperature). In order to clarify this point, we considered a single first order reaction with inexhaustible source (see appendix 2 for the basic assumption) i.e. a reaction $A\xrightarrow{k(E,T)}B$ where A is inexhaustible matter, $k(E,T) = k_0\ exp\left(-\frac{E}{k_BT}\right)$ is the reaction constant of Arrhenius type with activation energy E and temperature T. The plot of $[B]/[A]k_0$ versus RR show that the efficiency is larger at low RR. However, this predominance at low RR can be decreased when the activation energy is smaller. We thus deduce that the activation energy of the material destruction reaction is larger than the one of molecule transformation giving rise to luminescence. This is a nice example of the possibility of reaction control through femtosecond laser parameter adjustment.

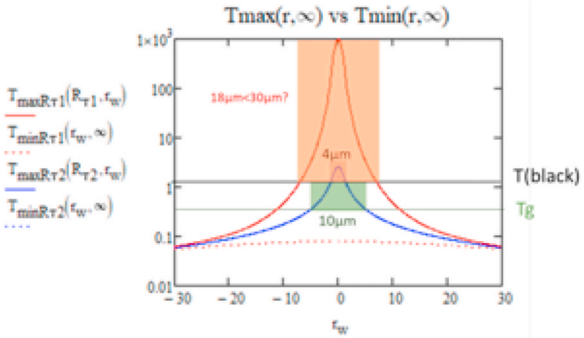

Fig. 20. Variation of the Tmax distribution around the center of the beam with Rτ at constant mean power. Note that the red curve oscillates between the full line and the dashed one, whereas the blue one oscillates much less.

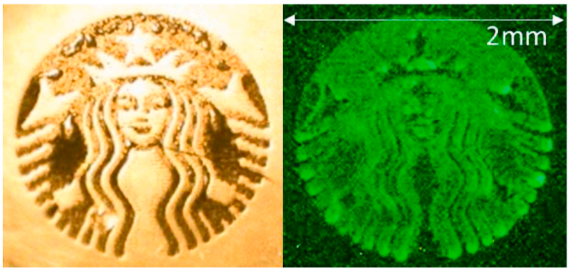

Fig. 21. 2D picture irradiated by fs laser under a) natural reflection light b) UV lamp (366 nm). Processing parameters: RR = 1 MHz, Ep = 20 nJ, scanning speed = 10 µm/s (go and return), depth(air) = 100 µm, polarization = 0°(horizontal).

4.3. *Image fabrication*

From the rationalization introduced above, we were able to elaborate an image in order to show this possibility. Fig. 21 shows a 2mm × 2 mm Starbucks® logo irradiated with RR = 1 MHz, Ep = 20 nJ and scanning speed = 10 µm/s this picture was irradiated line by line in steps of 10 µm. We found out that the resolution and contrast of created luminescence is good for reading, considering we have software limitations that leak light between white and black.

5. Conclusions

In summary, we have investigated the modifications that are induced by fs laser irradiation according to the laser parameters in Zeonex glass which is a Cyclo Olefin Polymer material used in many applications but not yet as a photonics substrate.

We found two domains of modifications that we called type I and type II. Type I denotes laser mean powers smaller than about 20 mW and larger than about 0.1 mW (several orders of magnitude smaller than for inorganic materials). This type corresponds to two types of modifications. One is probably corresponding to a change of molecular structure in the center of beam, as the specific volume is not changed significantly. Besides, the second modification still in Type I, with high RR range, a condensation of polymer molecule is induced, causing index change increase as large as 0.14, a quite interesting value for optical application (waveguiding or plate lenses). On the contrary, type II (mean power larger than 20 mW) corresponds to hydrogen/carbon separation i.e. destruction of the COP molecule and re-building of carbonized clusters like Carbon dots but also polycyclic aromatic ones. Whatever it is, in both domains, we found creation of Photoluminescence properties. In the type I domain where there is luminescence creation in the irradiated line, luminophores are mainly excitable in the near UV to blue-green range and emit on a broad range from the blue-green to yellow-orange. For type II, PL intensity is much larger and exhibits in addition to the previous PL an efficient second excitation wavelength more in the visible at 525 nm (green) leading to emission in orange-yellow (587 nm) and which is located at the edge of the modification lines, the luminophore excited in Type I are still presenting, while the luminophore content excited in green and emitting in orange-yellow decreases slightly.

EPR experiments were conducted to verify the presence of free emissive radicals as the one proceed in the case of PMMA [23]. The generation of free radicals may explain the high efficiency of luminescence, based on a number of studies demonstrating that free radical luminescence enhances internal conversion efficiency as well as external conversion efficiency [40,41]. We can also imagine as shown in literature [26], that the opaque ‘black substance’ may be related to carbonized clusters or graphite clusters which could exhibit electrical conductivity. We are currently proceeding in the characterization in order to precisely determine the nature of the luminophore species and their quantum yield.

A high contrast image was inscribed inside the glass, implying that this kind of plastic can be a promising substrate for optical processing and a potential medium for realizing either waveguiding, lenses, or localized luminescence function. Finally, we demonstrate that Zeonex glass could be a potential candidate for photonic applications.

CRediT authorship contribution statement

Ruyue Que: Conceptualization, Methodology, Validation, Formal analysis, Investigation, Data curation, Writing – original draft, Writing – review & editing. **L. Houel-Renault:** Software, Validation, Resources, Data curation, Writing – review & editing. **M. Temagoult:** Software, Validation, Resources, Data curation, Writing – review & editing. **C. Herrero:** Software, Validation, Resources, Data curation, Writing – review & editing. **M. Lancry:** Conceptualization, Methodology, Software, Resources, Data curation, Supervision, Project administration, Funding acquisition. **B. Poumellec:** Conceptualization, Methodology, Software, Validation, Formal analysis, Resources, Data curation, Writing – original draft, Writing – review & editing, Supervision, Project administration, Funding acquisition.

Declaration of competing interest

The authors declare that they have no known competing financial interests or personal relationships that could have appeared to influence the work reported in this paper.

Acknowledgments

The authors are grateful to the Zeon company for providing us samples of Zeonex® glass 790R for testing the response of this material to fs laser irradiation. The authors extend thanks to China Scholarship Council and Université Paris-Saclay.

Appendix I. Formula for temperature computation: We use an approximate model for computation an estimate of the temperature, with the following assumption

- spherical geometry,
- multi-pulse with instantaneous energy deposition in a sphere of diameter 2w
- T independent physical-chemical properties: κ, ρ, Cp, i.e. conductivity, specific density, heat capacity at constant pressure. Isotropy.

with $\tau_p = \frac{1}{f}$, $\tau_D = \frac{w^2}{4D_r}$, $R_\tau = \frac{\tau_p}{\tau_D}$, 2w is the beam diameter at 1/e

The expressions of minimum temperature and maximum temperature at the steady state shown as below eq. (1) and eq. (2). Those results are not yet published (Eq. (3) $T_{\max}(r,\infty)$ is only suitable for cases when r is small or $R\tau$ large, so that the $T_{\max}$ appears at the beginning of the period).

$$\frac{T_{\min}(r,\infty)}{T_0} = \frac{\exp\left[-\frac{(r/w)^2}{1+R\tau}\right]}{2[1+R\tau]^{3/2}} + \frac{\sqrt{\pi}}{R\tau.(r/w)} erf\left[\frac{(r/w)}{\sqrt{1+R\tau}}\right] \quad \text{eq.1}$$

$$\frac{T_{\min}(0,\infty)}{T_0} = \frac{1}{2[1+R\tau]^{3/2}} + \frac{2}{R\tau}\frac{1}{\sqrt{1+R\tau}} \quad \text{eq.2}$$

$$\frac{T_{\max}(r,\infty)}{T_0} = \exp\left[-(r/w)^2\right] + \frac{\exp\left[-\frac{(r/w)^2}{1+R\tau}\right]}{2[1+R\tau]^{3/2}} + \frac{\sqrt{\pi}}{R\tau.(r/w)} erf\left[\frac{(r/w)}{\sqrt{1+R\tau}}\right] \quad \text{eq.3}$$

$$\frac{T_{\max}(0,\infty)}{T_0} = 1 + \frac{1}{2[1+R\tau]^{3/2}} + \frac{2}{R\tau}\frac{1}{\sqrt{1+R\tau}} \quad \text{eq.4}$$

with $T_0 = \frac{A.E_p}{\pi^{3/2}.\rho.C_p.w^3}$, erf(x) is the error function, when $x < 0.5$, e.g. r is small or $R\tau$ is large, $\text{erf}(x) \cong \frac{2}{\sqrt{\pi}}x$

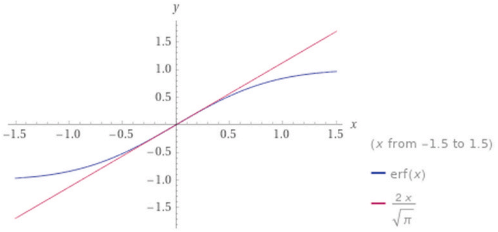

Fig. A1. erf(x) function and its approximation near zero.

The average T is:

$$\overline{T}(r,\infty)=\frac{\sqrt{\pi}}{R\tau.\ r_w}erf(r\,/\,w).\mathrm{T}_0=\frac{A.E_p.f.erf(r/w)}{4\pi.\kappa.r}=\frac{A.P.erf(r/w)}{4\pi.\kappa.r}$$

$$\overline{T}(0,\infty)=\frac{2}{R\tau}.\mathrm{T}_0=\frac{A.E_p.f}{2\pi^{3/2}.\kappa.w}=\frac{A.P}{2\pi^{3/2}.\kappa.w}$$

here Ep1 $= 1000$Ep2, so $\mathrm{T}_{01} = 1000\mathrm{T}_{02}$, $f_2 = 1000 f_1$, so $\tau_{p1} = 1000\tau_{p2}$, $R\tau_1 = 1000R\tau_2$

Table A1

physical-chemical data for Zeonex and related quantities

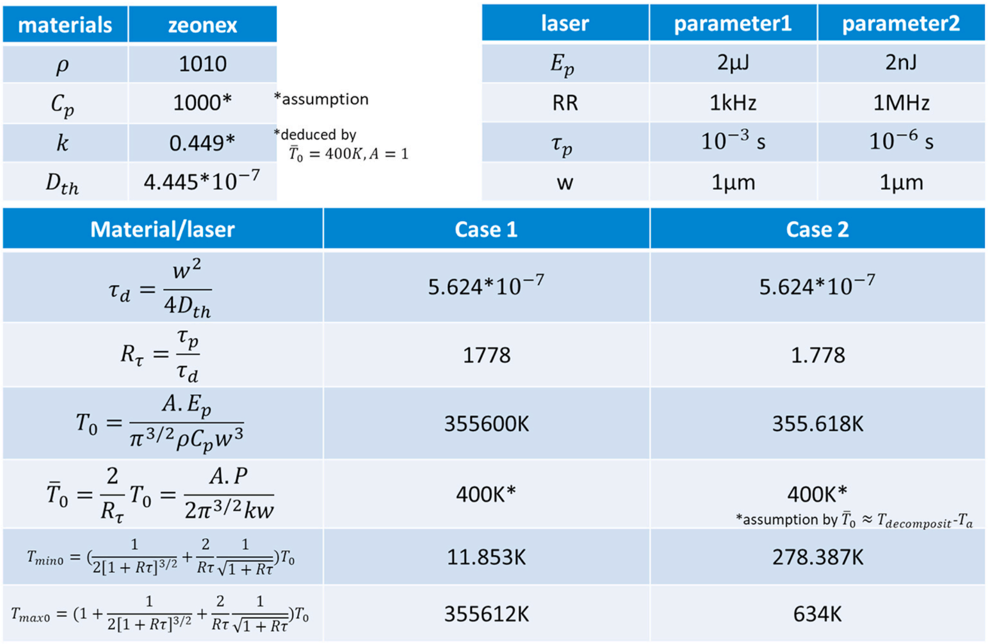

materials	zeonex	
ρ	1010	
C_p	1000*	*assumption
k	0.449*	*deduced by $\bar{T}_0 = 400K, A = 1$
D_{th}	4.445*10^{-7}	

laser	parameter1	parameter2
E_p	2μJ	2nJ
RR	1kHz	1MHz
τ_p	10^{-3} s	10^{-6} s
w	1μm	1μm

Material/laser	Case 1	Case 2
$\tau_d = \frac{w^2}{4D_{th}}$	5.624*10^{-7}	5.624*10^{-7}
$R_\tau = \frac{\tau_p}{\tau_d}$	1778	1.778
$T_0 = \frac{A.E_p}{\pi^{3/2}\rho C_p w^3}$	355600K	355.618K
$\bar{T}_0 = \frac{2}{R_\tau}T_0 = \frac{A.P}{2\pi^{3/2}kw}$	400K*	400K* *assumption by $\bar{T}_0 \approx T_{decomposit}$-$T_a$
$T_{min0} = (\frac{1}{2[1+R\tau]^{3/2}} + \frac{2}{R\tau}\frac{1}{\sqrt{1+R\tau}})T_0$	11.853K	278.387K
$T_{max0} = (1 + \frac{1}{2[1+R\tau]^{3/2}} + \frac{2}{R\tau}\frac{1}{\sqrt{1+R\tau}})T_0$	355612K	634K

Appendix II. reaction efficiency at constant scanning speed

The basic assumption is the following reaction $A \xrightarrow{k(E,T)} B$ where A is inexhaustible matter, $k(E,T) = k_0\ exp\left(-\frac{E}{k_B T}\right)$ is the reaction constant of Arrhenius type with activation energy E and T the temperature. Thus the B rate is $\frac{d[B]}{dt} = k(E,T)[A]$ and then $[B] = [A]\int_0^t k\left(E, T(t')dt' = [A]\int_0^t k_0\ exp\left(-\frac{E}{k_B T(t')}\right)dt'\right.$. The plot of $[B]/[A]k_0$ versus RR show that the efficiency is larger at low RR. However, this predominance at low RR can be decreased when the activation energy is smaller.

References

[1] K.-i. Kitayama, et al., Novel frontier of photonics for data processing—photonic accelerator, Apl Photonics 4 (9) (2019), 090901.

[2] X. Sui, et al., A review of optical neural networks, IEEE Access 8 (2020) 70773–70783.

[3] J. Feldmann, et al., All-optical spiking neurosynaptic networks with self-learning capabilities, Nature 569 (7755) (2019) 208–214.

[4] L. Piroddi, Special Topics in Information Technology, Springer Nature, 2022.

[5] K. Millard, et al., Experimental validation of SiN photonic integrated waveguide arrays at λ= 532 nm for augmented reality display applications, in: Integrated Optics: Devices, Materials, and Technologies XXV, International Society for Optics and Photonics, 2021.

[6] M.J. Ali, et al., Human body high resolution and accurate temperature FBG sensor, IOP Conf. Ser. Earth Environ. Sci. 779 (1) (2021), 012029.

[7] G. Woyessa, et al., Zeonex microstructured polymer optical fiber: fabrication friendly fibers for high temperature and humidity insensitive Bragg grating sensing, Opt. Mater. Express 7 (1) (2017) 286–295.

[8] Y.-G. Nan, et al., Ultra-fast fiber Bragg grating inscription in CYTOP polymer optical fibers using phase mask and 400 nm femtosecond laser, Opt Express 29 (16) (2021) 25824–25835.

[9] J. He, et al., Review of femtosecond-laser-inscribed fiber Bragg gratings: fabrication technologies and sensing applications, Photonic Sens. 11 (2) (2021) 203–226.

[10] H.H. Zhu, et al., Space-efficient optical computing with an integrated chip diffractive neural network, Nat. Commun. 13 (1) (2022) 1044.

[11] Z. Wang, et al., Integrated photonic metasystem for image classifications at telecommunication wavelength, Nat. Commun. 13 (1) (2022) 2131.

[12] D.L. Kallepalli, et al., Ultra-high density optical data storage in common transparent plastics, Sci. Rep. 6 (1) (2016) 1–10.

[13] J. Cao, et al., Pulse energy dependence of refractive index change in lithium niobium silicate glass during femtosecond laser direct writing, Opt Express 26 (6) (2018) 7460–7474.

[14] J. Cao, et al., Modifications in lithium niobium silicate glass by femtosecond laser direct writing: morphology, crystallization, and nanostructure, J. Opt. Soc. Am. B 34 (1) (2017) 160–168.

[15] J. Cao, et al., Femtosecond laser-induced crystallization in glasses: growth dynamics for orientable nanostructure and nanocrystallization, Cryst. Growth Des. 19 (4) (2019) 2189–2205.

[16] J. Cao, et al., Angular dependence of the second harmonic generation induced by femtosecond laser irradiation in silica-based glasses: variation with writing speed and pulse energy, World J. Nano Sci. Eng. 3 (2015) 11.

[17] J. Cao, et al., Tunable angular-dependent second-harmonic generation in glass by controlling femtosecond laser polarization, J. Opt. Soc. Am. B 33 (4) (2016) 741–747.

[18] M.L. Tseng, et al., Fabrication of Multilayer Metamaterials by Femtosecond Laser-induced Forward-transfer Technique, Wiley Online Library, 2012, pp. 702–707.

[19] K.-X. Zhang, et al., Fast fabrication of fishnet optical metamaterial based on femtosecond laser induced stress break technique, Nanomaterials 11 (3) (2021) 742.

[20] S.M. Eaton, et al., Femtosecond laser microstructuring for polymeric lab-on-chips, J. Biophot. 5 (8) (2012) 687–702, 9.

[21] F. Sima, et al., Three-dimensional femtosecond laser processing for lab-on-a-chip applications, Nanophotonics 7 (3) (2018) 613–634.
[22] M. Yamazaki, Industrialization and application development of cyclo-olefin polymer, J. Mol. Catal. Chem. 213 (1) (2004) 81–87.
[23] Z. Nie, et al., Multilayered optical bit memory with a high signal-to-noise ratio in fluorescent polymethylmethacrylate, Appl. Phys. Lett. 94 (11) (2009), 111912.
[24] Z. Nie, et al., Femtosecond laser induced photoluminescence in poly (methyl methacrylate) and three-dimensional optical storage, J. Lumin. 131 (2) (2011) 266–270.
[25] A. Alshehri, et al., Localized nanoclusters formation in PDMS upon irradiation with femtosecond laser, Opt. Mater. Express 5 (4) (2015) 858–869.
[26] M. Abdulhafez, G.N. Tomaraei, M. Bedewy, Fluence-dependent morphological transitions in laser-induced graphene electrodes on polyimide substrates for flexible devices, ACS Appl. Nano Mater. 4 (3) (2021) 2973–2986.
[27] A. Barty, et al., Quantitative optical phase microscopy, Opt Lett. 23 (11) (1998) 817–819.
[28] Demchenko, A.P., The Red-Edge Effects: 30 Years of Exploration. (1522-7235 (Print)).
[29] D.L.N. Kallepalli, et al., Ultra-high density optical data storage in common transparent plastics, Sci. Rep. 6 (1) (2016), 26163.
[30] H. Tidahy, et al., Characterisation of new Pd/hierarchical macro-mesoporous ZrO2, TiO2 and ZrO2-TiO2 catalysts for toluene total oxidation, Stud. Surf. Sci. Catal. 160 (2007) 201–208.
[31] C. Li, et al., Coke deactivation of Pd/H-mordenite catalysts used for C5/C6 hydroisomerization, Appl. Catal. Gen. 199 (2) (2000) 211–220.
32 A. Gupta, et al., Characterization of a dissociative excited state in the solid state: photochemistry of poly (methyl methacrylate). Photochemical processes in polymeric systems. 5, Macromolecules 13 (6) (1980) 1696–1700.
[33] Z. Cui, et al., Stable luminescent radicals and radical-based LEDs with doublet emission, CCS Chem. 2 (4) (2020) 1129–1145.
[34] S. Sagbas, N. Sahiner, 22 - carbon dots: preparation, properties, and application, in: A. Khan, et al. (Eds.), Nanocarbon and its Composites, Woodhead Publishing, 2019, pp. 651–676.
[35] J. Choi, et al., in: Laser-Induced Graphene on a Quartz Crystal Microbalance for Humidity Sensing. Crystals 11, 2021, pp. 289–2021, s Note: MDPI stays neutral with regard to jurisdictional claims in published.
[36] L. Keldysh, ZhETF 47, Sov. Phys. JETP 20 (1964) 1515, 1965 1018.
[37] D. Dehareng, G. Dive, Vertical ionization energies of α-L-amino acids as a function of their conformation: an ab initio study, Int. J. Mol. Sci. 5 (11) (2004).
[38] A. Vailionis, et al., Evidence of Superdense Aluminium Synthesized by Ultrafast Microexplosion vol. 2, 2011, p. 445, 1.
[39] M. Lancry, et al., Time-resolved plasma measurements in Ge-doped silica exposed to infrared femtosecond laser, Phys. Rev. B 84 (24) (2011).
[40] Z. Cui, et al., Radical-based organic light-emitting diodes with maximum external quantum efficiency of 10.6%, J. Phys. Chem. Lett. 9 (22) (2018) 6644–6648.
[41] A. Obolda, et al., Up to 100% formation ratio of doublet exciton in deep-red organic light-emitting diodes based on neutral π-radical, ACS Appl. Mater. Interfaces 8 (51) (2016) 35472–35478.

IV.3 OTHER RESULTS AND DISCUSSIONS

IV.3.1 PL distribution of normal luminescence and up conversion?

Under excitation of 491nm selected from an fs white laser, we have detected emission in the range 421-473nm, and in the range 570-620nm. The latter emission range correlated to the one already described in the above publication in fig.IV.2 signature 2 (when blossoming appears in type I), while the first one is at a shorter wavelength than the excitation.

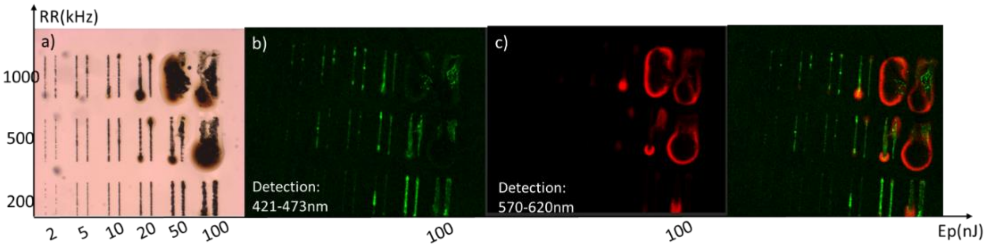

Fig.IV.2: luminescence detected under 491nm excitation in Zeonex a) transmission optical image under natural light, pulse energy, and repetition rate are indicated, b) luminescence detected in the range 421-473nm (software color green), c) luminescence detected in the range 570-620nm (software color red), d) combined picture from b and c.

From this picture, we can see that the luminescence, which was excited by the same excitation wavelength but detected in different range, located differently. The normal PL, excited by 491nm and detected in a longer wavelength range, located in all the irradiated region. In fig.VI.2, only head and periphery of the line (set color in red) are shown because the intensity of line body is much weaker. However, when excited by 491nm and detected in range shorter (421-473nm), we were amazed to discover the luminescence presenting, and only in the body of the line. The brighter periphery and head of the line haven't this kind of luminescence.

Several possibilities can give rise to shorter wavelength: an up-conversion process, a transfer energy process between molecules, or two-photon absorption. An up-conversion process is an absorption of a second photon by an excited state with or without intermediate partial relaxation. This needs an excited state with a long lifetime. The second case involves a molecule playing the role of a sensitizer. This may collect several photons from the neighborhood for reaching a high excited state. The last one is a simultaneous absorption of two coherent photons and needs high intensity. In addition, the dependence of the luminescence intensity is the square of the excitation one. Knowing the type of source used here, fs laser, this last case is credible.

As to why this phenomenon occurs only in the body of the line, we still lack understanding. But it seems due to the process of formation, that the luminescence induced by heat (red) or luminescence induced by light (green).

IV.3.2 Discovery of sp2 carbon bands by Raman/FTIR spectroscopy

IV.3.2.1 Equipment information and experimental details

We used a Raman imaging microscope (Thermofisher scientific, DXR3xi) equipped with a continuous wave laser at 780nm (infrared, DXR 780nm HP LASER). Raman spectra were recorded from 60 cm^{-1} to 3419 cm^{-1}. The laser was focused inside the sample with an x50 objective. With a pinhole of 50µm, the spot size is estimated at 1.6µm. Laser power was set from 20mW to 100mW. The collect exposure time was set from 10s to 30s and preview exposure time was set from 3-5s. The grating had 400 lines/mm with an estimated resolution of 4.7-8.7cm^{-1}. A setting of fluorescent correction was applied to the spectra. 16 spectra were accumulated.

FTIR spectra were recorded by an FTIR spectrometer Frontier of PerkinElmer. It has 3 modes for signal recording: Transmission, reflection, and ATR, and 2 modes of measurement: point mode and mapping mode. 2 detectors are equipped: one for mapping mode and one for point mode. The one for mapping mode has a good sensitivity from 690-4000 cm-1 and the detector for point mode has a better sensitivity from 550-4000 cm-1. In this section, the experimental results are from reflection and mapping mode. The sample was polished until the irradiated region was exposed to the surface.

IV.3.2.2 Results and discussion

We have measured 11 regions of interest (ROIs) irradiated with different laser parameters or the same parameters but the different areas (for checking the reproducibility), shown in fig.IV.3a Some other results are shown in fig.IV.3 b-e.

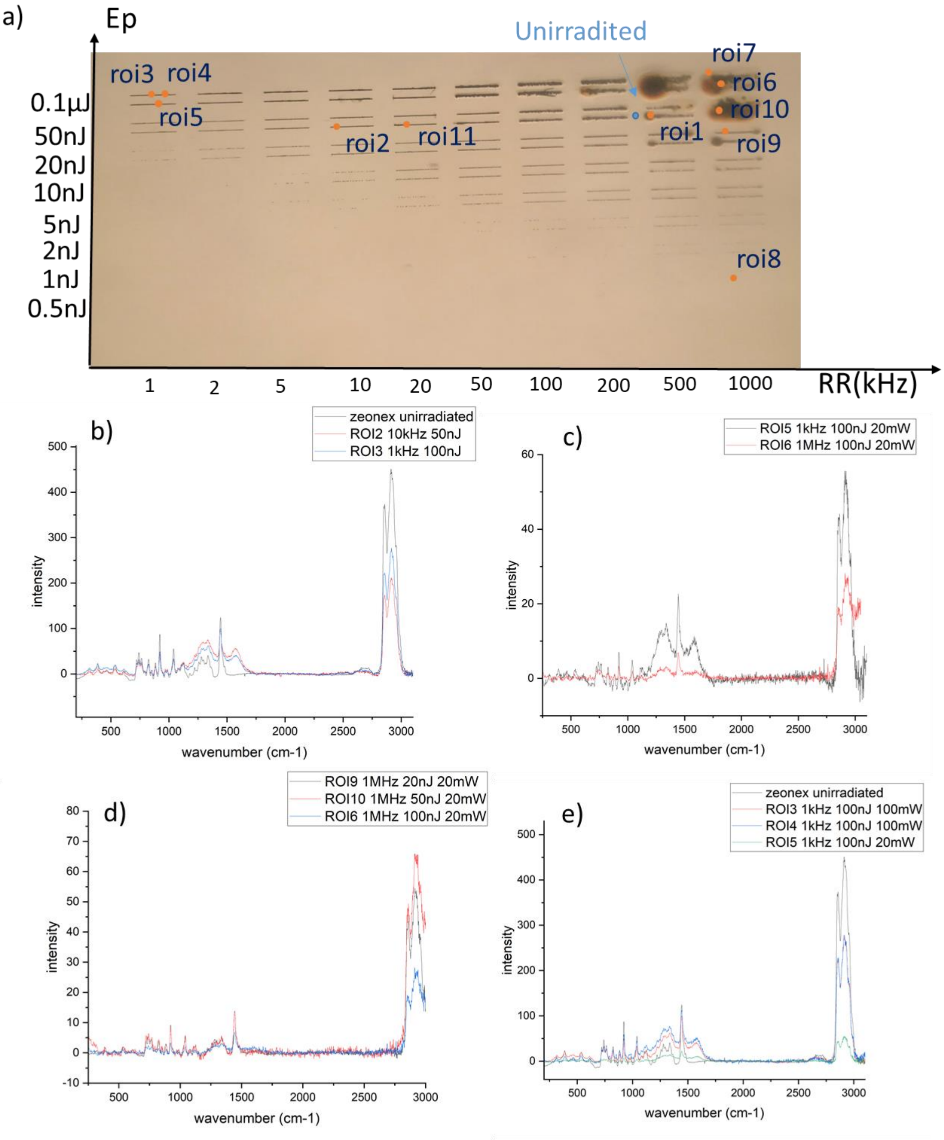

Fig.IV.3 Raman spectra of ROIs. a) the position of ROIs. b) comparison of spectra of the unirradiated region and ROI2 and ROI3. c) comparison of spectra of ROI5 and 6 d) comparison of spectra of ROI6, ROI9, and ROI10. e) comparison of spectra of unirradiated region ROI3, ROI4, and ROI5.

Firstly, from all the Raman spectra, especially the unirradiated one, the most intense peak at around 2900 cm^{-1} is from the vibration of C-H stretching (from larger wavenumber to lower one, they are CH3 asymmetric stretching, H-C-H asymmetric stretching, and H-C-H symmetric stretching). Then, the second strong structure around 1450 cm^{-1} is the H-C-H scissoring (bending), the other peaks from 100cm-1 to 1500cm^{-1} will not be described here one by one, only to notice that they are called fingerprint regions. Fig.IV.3b, shows the Raman spectrum of some irradiated regions, compared to the spectrum of unirradiated one. We note that the main CH stretching and bending peaks, as well as every feature peak in the fingerprint region, are the same, except a new obvious peak appearing at around 1580cm^{-1}. This peak is usually attributed to a carbon-carbon double bond (C=C sp2 band) [182] in-plane stretching in a ring, as it is shown in graphene and graphite as typical G-peak [161, 162, 182-185], or in Tryptophane Phe ring vibration, or Adenine Guanning ring stretching. There maybe also a stronger one around 1350cm^{-1}, or it could come from the PL background. The peak at 1350cm^{-1} can be attributed to the D-peak of graphene [161, 162, 182, 183, 185]. With the existence of G peak at 1580cm^{-1}, a graphene-like structure may have been created by fs irradiation. Besides, the D-peak creation is not so obvious compared to G-peak, indicating that the structure may be well graphited, instead of forming disordered graphitic lattice, or polycrystalline, or amorphous carbon [186]. With other Raman spectra (not all shown in the fig.IV.3), we prove that irradiated lines with parameters from 1KHz to 200kHz, graphene-like structures are created. But from fig.IV.3c, a line written at 1MHz, these 2 peaks, are found decreasing and very weak at the center for 100nJ where there are still some black parts (ROI6), whereas they all disappeared for other lines written at energy from 1nJ to 50nJ in 1MHz (see fig.VI.3d). For the periphery or the head of the line written from 20nJ to 100nJ, we can't see any peaks because PL is too strong. Fig.VI.3e shows 3 ROIs in line irradiated by the following parameters: Ep=100nJ and RR=1kHz. It shows that the reproducibility is good.

Similar results are found in the FTIR spectrum, shown in fig.IV.4.

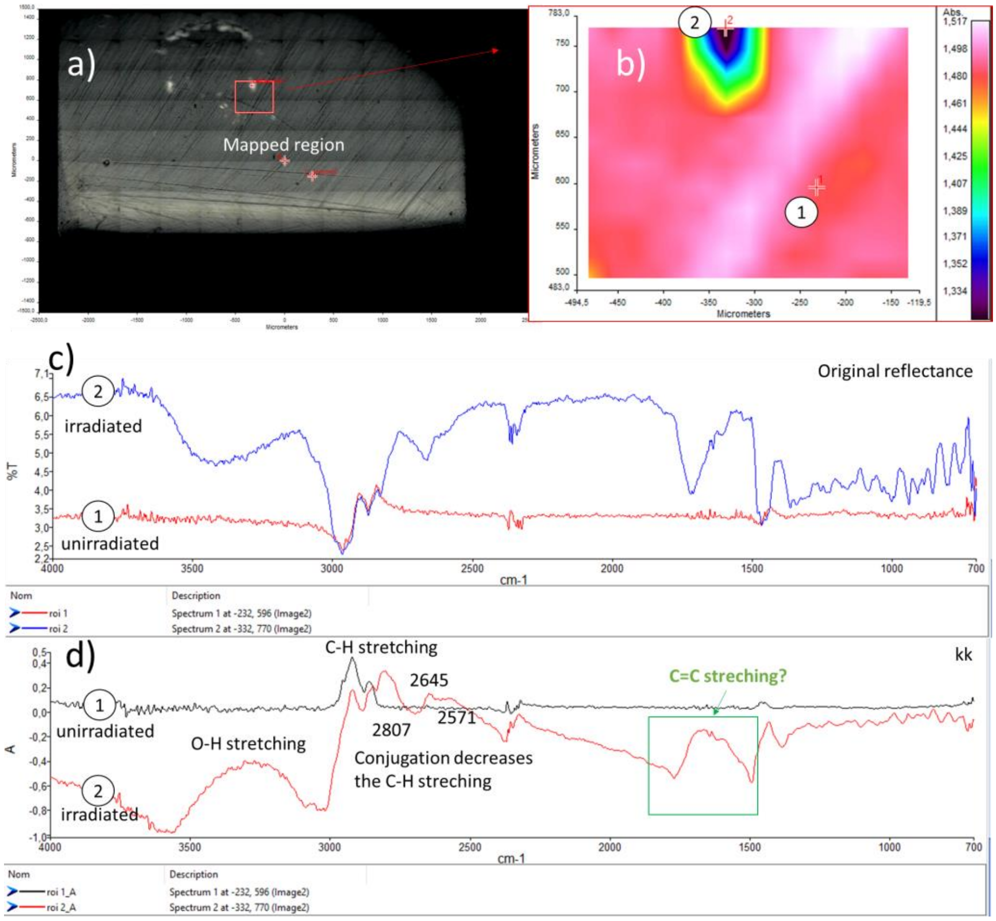

Fig.IV.4 a) mapping of the region in reflection mode b) the FTIR spectral mapping, color is given by the average reflectance intensity of the spectrum of each point. c) the original data from the reflectance signal of the unirradiated area (ROI1, red profile) and irradiated area (ROI2, blue profile). d) the absorption data obtained through Kramers–Kronig relation, roi1 (black profile), roi2 (red profile).

From the comparison of the FTIR spectra of the irradiated and non-irradiated region, we detected more than 3 peaks induced by the fs laser compared to the polymer substrate. First, the spectrum (fig.IV.4d black profile) has only several feature peaks, CH3 asymmetric stretching, CH2 asymmetric stretching, CH2 symmetric stretching around 2900cm^{-1}, and CH2 scissoring bending around 1430 cm^{-1}. The spectrum of the irradiated area (fig.IV.4d red profile), besides an obvious O-H stretching peak due to water (probably coming from the polishing process), peaks at 2807cm-1, 2600cm-1 and between 1600cm^{-1} to 1700cm^{-1} are newly generated. The first peak at 2807 cm^{-1}, in this wavenumber range, is generally considered to be still C-H absorption. Together with the two peaks next to it in higher wave numbers, we think they are the three C-H absorption peaks shifting to lower wavenumbers. There are two possibilities for shifting the absorption band position to lower wave numbers. One is when CH3 or CH2 is connected with O, i.e. Aldehydes, there is two CH absorption around 2820 cm^{-1} and 2720 cm^{-1} due to Fermi resonance. The second is the ring strain, when it is decreasing (ring size increasing), the wavenumber of C-H absorption is decreasing. Here, we tend to believe the second condition because we do not have O in the substrate and the whole modification process was inside the material, without contact with the air. Therefore, we think that more double bonds between carbons are created, forming larger cyclic/polycyclic/aromatic structures. On the other hand, the new peak between 1600cm-1 to 1700cm-1 probably could be considered as evidence of conjugated carbon bands generation, since this range is including absorption of C=C stretching/bending, but H-O-H bending is also in this range so we do not exclude this possibility either.

IV.4 CONCLUSION

In a Cyclo Olefin Polymer (COP), Zeonex® glass, we studied different types of modifications induced by fs laser direct writing, and the parametrical window (including pulse energy, repetition rate, scanning speed) for each type is generally defined. Two domains of modifications are pointed out, one at low mean power between 0.1 and 20 mW and another above 20 mW, called type I and II.

In type I, two modifications – photoluminescence (PL) creation and a large refractive index change (+0.14) were observed. PL are restricted to the irradiated volume at the scale of beam size. The large refractive index change (RIC) appears around the beam centre, especially when the pulse repetition rate is high(>500 kHz) and scanning speed is as low as 1µm/s. Type I modification is moderate and the spatial sensitivity is of the order of µm.

In type II, the modification is more extended but PL is much stronger. Through correlations between the PL results, we defined signatures composed of luminophore series: Signature 1 (S1) associated to type I, S2 associated to type II and S3 for intermediate conditions. S1 is the luminescent group, with the largest yield excitable at 475 nm with a broad emission from green to orange-yellow. S2 is remarkable with a broad excitation in the green and broad emission in yellow range.

For understanding the origin of the PL, EPR spectroscopy shows that the creation of carbon based radical. Additional experiments such as Raman and FTIR spectroscopy show the creation of a new peak around 1570 cm^{-1}, which may be corresponding to carbon double bond stretching, as known as the G peak of the graphene or graphite. Therefore, the modifications induced by fs laser direct writing might be a disruption of COP molecule, forming Carbon Dots (CDs) or more generally, a kind of polycyclic aromatic compounds.

Chapter.V FEMTOSECOND LASER DIRECT WRITING IN SUCROSE SINGLE CRYSTAL

V.1 INTRODUCTION

Sucrose, a disaccharide, is a sugar composed of glucose and fructose subunits. It is produced naturally in plants and is the main constituent of white sugar. It has the molecular formula $C_{12}H_{22}O_{11}$ and its structure is shown in fig.V.1.

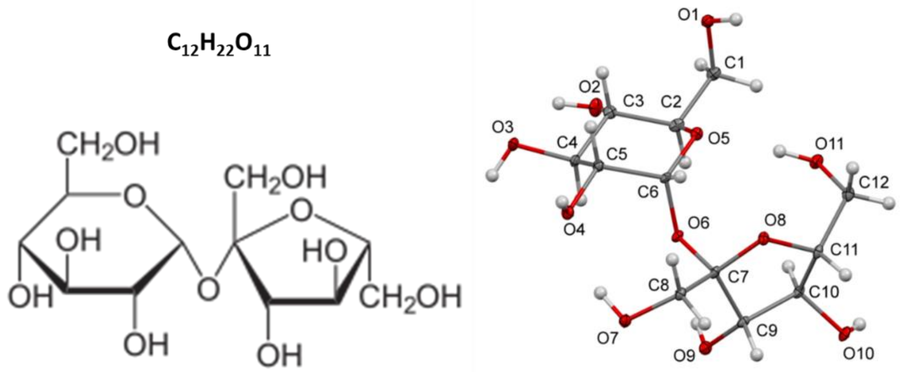

Fig.V.1 The molecular structure of sucrose

At room temperature sucrose crystallizes in the $P2_1(C_2)$ symmetry group of a monoclinic system with 2 molecules in the unit cell and the binary axis $\vec{b}$[187, 188]. It is chiral and dextrorotatory. Besides, α-glycine single crystal, with achiral molecule and achiral symmetric space group, and Zeonex, the polymer glass, sucrose is the third typical type of material, with chiral molecule and chiral space group. This structure brings about optical properties such as

1) circular birefringence (CB), i.e. optical rotation. It has 22°/cm of the plane of polarization for visible range along $\vec{a}$ axis due to the helical alignment in the crystal [189].

2) second harmonic generation (SHG) active, with efficiency 0.2 times of ammonium dihydrogen phosphate(ADP) [190]. Its origin is proposed to be the proton transfer in one specific hydrogen bond parallel to the helical axis $\vec{b}$ [191]. Recalled that SHG relative efficiency

of γ-glycine crystal was found to be 6 times higher than that of KDP [192].

3) Linear birefringence (LB), the maximal birefringence was measured to be 0.033 at 532nm [191]. Therefore, we are keen to take advantage of the various anisotropies introduced by femtosecond laser polarization to make some observable changes to its optical properties. Based on the fact that the first two materials both produced significant luminescence generation, for sucrose crystals, we expect firstly luminescence generation, in addition to other optical properties.

On the other hand, probably due to the above natural optical effects in sucrose crystal, it hasn't been considered as a substrate for photonics. However, if we can modify certain optical properties in it with a femtosecond laser, or produce luminescence, the sucrose crystals can be functionalized and play the role of a photonic substrate. In addition, compared to commercial organic substrates such as PolyMethylMethAcrylate (PMMA), PolyDiMethylSiloxane (PDMS), PolyStyrene (PS), PolyCarbonate (PC), etc. which consume petroleum and pollute the environment, this substrate has advantages such as completely environmentally friendly and indefinitely renewable as it is a bio resource. It is even eatable and thus can be used in the sugar industry for including an advertisement or entertainment messages.

V.2 EXPERIMENTAL SECTION

V.2.1 Sample preparation

As the experiments were focused on the investigation of the local interaction between the femtosecond laser with sucrose single crystals, purity was not a major consideration and, given the maturity of the sugar industry, the purity of commercially available sucrose single crystals is usually greater than 99%, so the samples used in our experiments were commercially available mass-produced sucrose single crystals with a crystallographic confirmation by XRD.

The sample was cleaved along (100) plane to have a thickness of around 1mm and polished on both sides by silicon carbide abrasive disc from 600 grit to 4000 grit and finished with a polymer tissue disc.

The polished sucrose samples are conserved in a vacuumed dryer, so does the irradiated samples.

The same problem as glycine crystal, sucrose is difficult to produce completely amorphously. Sucrose melts at about 185°C, at a low heating rate it is often accompanied by a decomposition (caramelization) [193]. Making an amorphous sugar requires a special environment, method, and equipment such as freeze-dryer [151], high compression, and spray-drying [148-150], sucrose solution drops into liquid nitrogen[194], and the resulting solid is metastable and will not surely be transparent for laser irradiation. The glass transition temperature is simulated to be around 347K (73.85°C) [151] and 72.4°C and the crystallization temperature to be 116.8°C [148]. Mixing with polyvinylpyrrolidone (PVP) with various ratios can change the glass transition temperature and crystallization temperature [148]. In this work, experiments were conducted in single crystals.

V.2.1.1 XRD for sample quality

Firstly, to validate the quality of the samples, i.e. commercial sucrose single crystals, powder XRD, Single crystal, and XRD Laue analysis were carried out.

XRD powder

A commercial single sucrose crystal was crushed to a uniform powder and subjected to a powder x-ray diffractometer with Cu(Kα1) radiations for structural analysis study. The powder form sample was scanned over the range of 10-45˚ at the rate of 2˚/min. The indexed powder XRD pattern of the grown crystal is shown in fig.V.2. Peaks in the XRD without any broadening confirm the good quality of the grown [195].

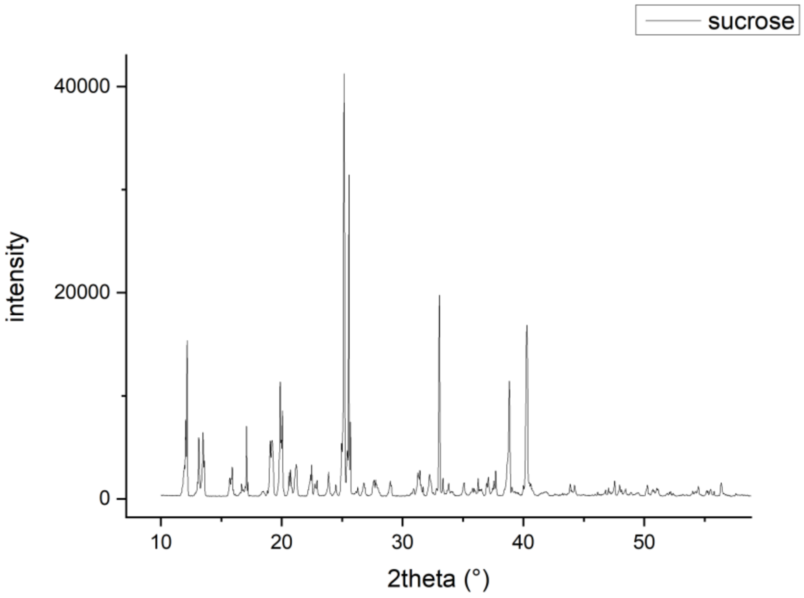

FigV.2 Powder XRD pattern of sucrose single crystal sample

XRD Laue

Although the visual appearance of the single crystal sample already resembles the standard form of sucrose single crystals, we still confirmed the crystal axes of the single crystal samples by performing X-ray Laue diffraction. The source is polychromatic with λ 0.3 Å-3Å, 30kV-25mA. The diffraction pattern is shown in fig.V.3 and with software pattern fitting, it is validated by matching the standard shape of sucrose crystal[196]. Therefore, we determine the crystal axis $\vec{a}$ by this measurement and refer the other axis according to the literatures.

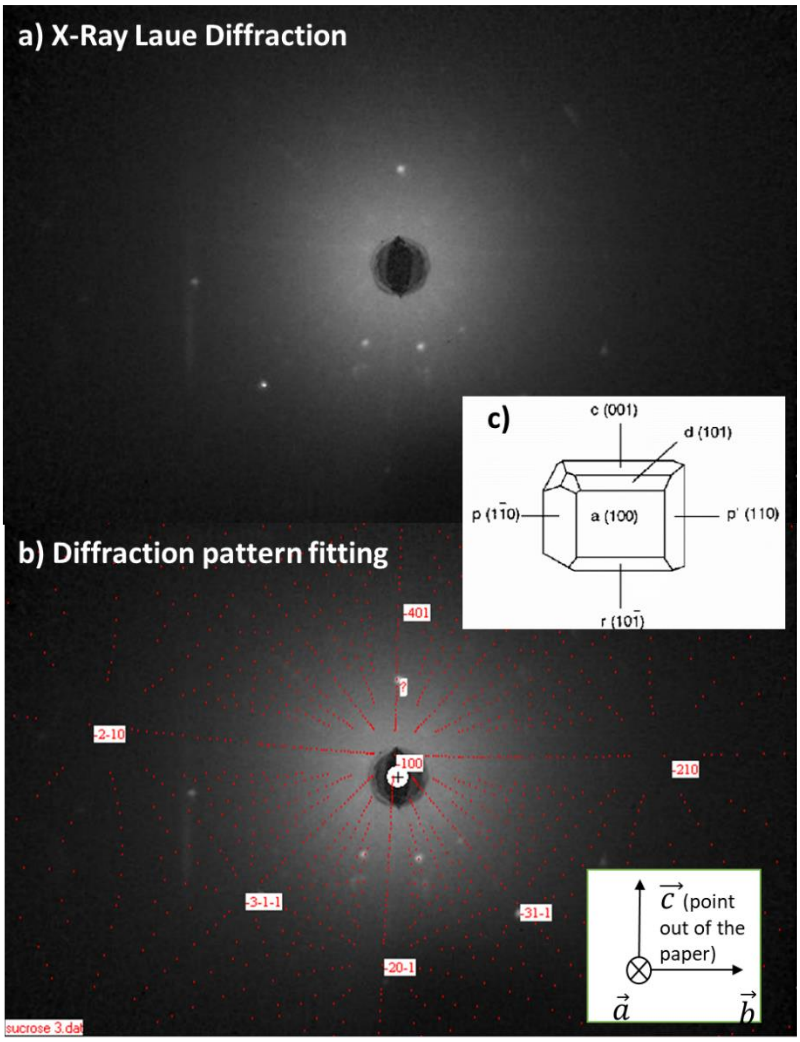

Fig.V.3 a) X-ray Laue diffraction pattern of sucrose sample b) diffraction pattern fitted by software c) standard shape of sucrose crystal showing important crystal face, extracted from[196]

Single crystal XRD

Single crystal XRD is performed by a four circles diffractometer (Kappa geometry, Bruker). Reflections were merged by SHELXL according to the crystal class for the calculation of statistics and refinement.

Fig.V.4 shows a unit cell illustrating molecular and atomic information. The measurement gives the information about cell parameters are: a = 7.7104(5) Å, b = 8.6626(5) Å, c = 10.8045(7) Å, α=90°, β = 102.922(3)°, γ, cell volume 703.38(8).

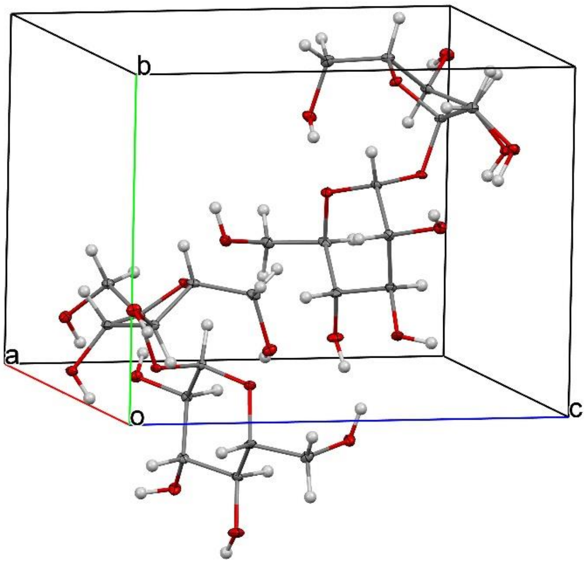

Fig.V.4 schematic diagram of sucrose crystalline unit cell

From all the structural measurements we confirmed the structure quality of the commercial single crystal of sucrose.

V.2.1.2 Absorption spectrum

Since fs laser irradiation in sucrose crystal involves the absorption of photons, the electronic band gap was confirmed by measuring the UV-Vis absorption spectrum, as shown in fig.V.5.

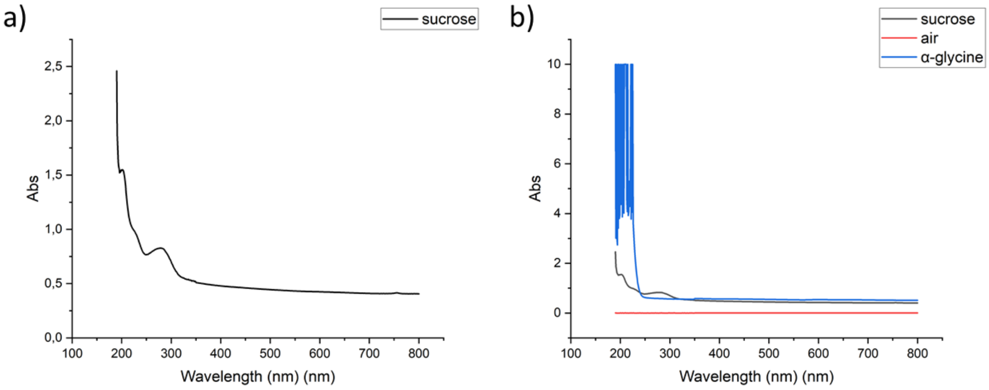

Fig.V.5 a) the absorption spectrum of sucrose single crystal sample from 190nm to 800nm; b) the spectra comparison of sucrose single crystal(black), α-glycine single crystal(blue), and background air(red).

Results show that the first absorption wavelength close to the HOMO-LUMO splitting is around 300nm, smaller than the one of the glycine, while the dissociation wavelength of sucrose is smaller than 200nm.

V.2.2 Laser irradiation

As we have confirmed the crystal parameters of the single-crystal samples, the orientation of the laser parameters will be based on the direction of the crystal axis, as shown in fig.V.6. In laser irradiation, the laser propagation is along $\vec{a}$, so the irradiation will be performed in the plane (100) with the scanning direction along $\vec{b}$, polarization is parallel to the scanning direction, which is also along $\vec{b}$.

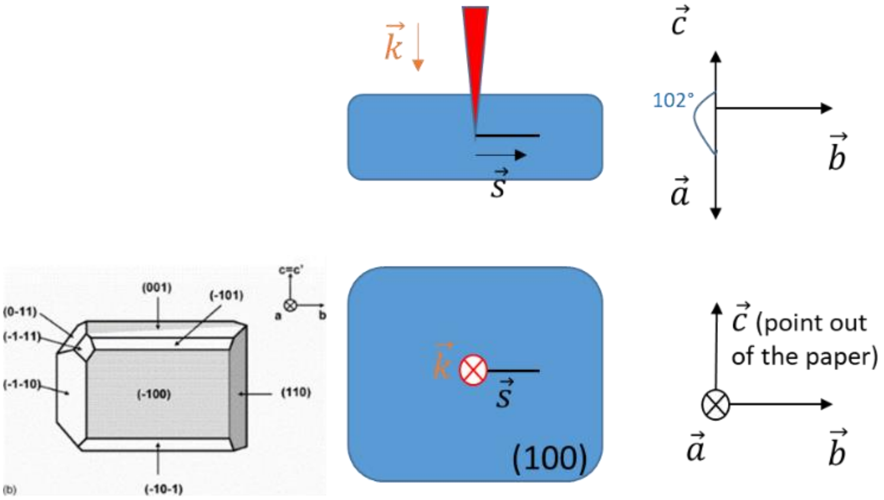

Fig.V.6 the schematic diagram of laser directions according to crystal directions, the schematic diagram of the shape of a sucrose crystal with assigned main planes is cited from [189]

After a rough temperature calculation, we set fs laser parameters in the range Ep from 0.1μJ to 2μJ, and RR from 1kHz to 1MHz. Ep=2μJ induces too high temperature at high RR so the irradiation will be stopped manually. Since the direction of scanning is no more our priority, all the irradiation lines were performed one sense from left to right, with scanning speed=10μm/s.

During the irradiation, we found that the SHG can be observed in the sample with Ep≥0.3μJ when RR=1kHz. The highest intensity is located around the focus, and all the volume of bulk is all green like in γ-glycine, shown in fig.V.7.

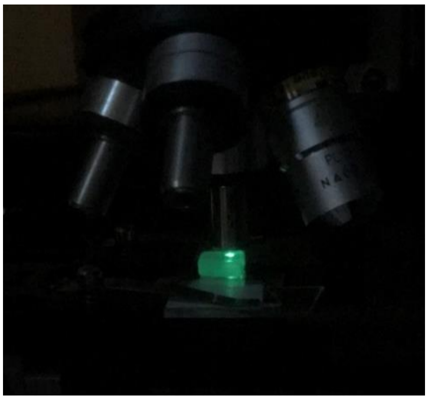

Fig.V.7 the SHG observed during irradiation with parameters Ep>0.3μJ when RR=1kHz

V.3 RESULTS

V.3.1 Modification landscape in the plane Ep, RR

As the same strategy of glycine crystal and Zeonex polymer, a set of irradiation with a wide range of Ep and RR was processed in the parameter domain avoiding the burning. The morphology of modifications is more like the ones in glycine compared to the Zeonex polymer. We defined 2 domains of modification, shown in fig.V.8 left.

Type 1: the width of the irradiated lines is uniform and of the same order as the beam size, they are opaque under the optical microscope in transmission mode without significantly volume change (the width increases with Ep, the largest~12μm).

Type 2: opaque lines with irregular explosion structures along the lines. The regions when the sample is melted at RR>100kHz are also counted in the type 2 regime.

Fig.V.8 right is the landscape collecting the remarks above.

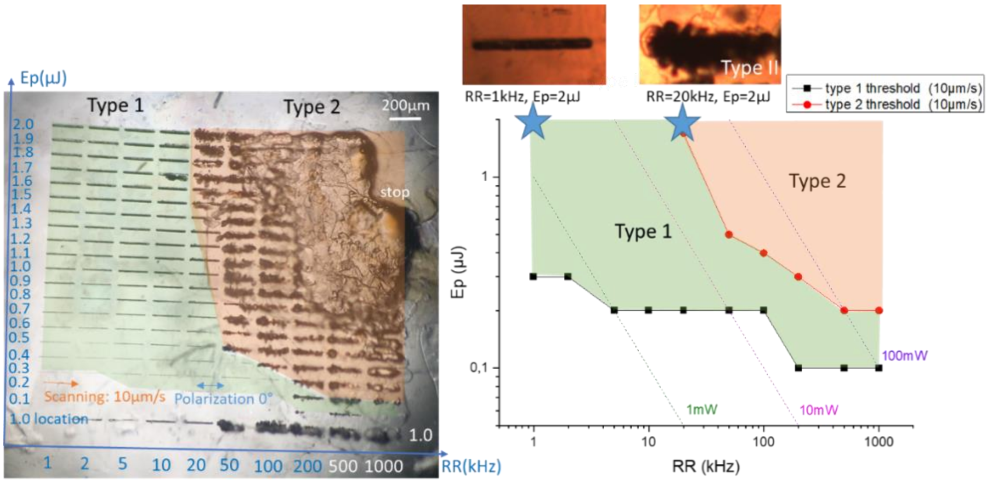

Fig.V.8 left: the irradiated lines inside sucrose single crystal under microscopy with natural light and transmission mode with x5 objective. Lines are 200µm long. Right: the thresholds for different modifications according to RR and Ep. Inserts in the right figure: the details of the different modifications: an example of Type I line and Type 2 line.

The first damage threshold is compared with the one in glycine crystal and the one in Zeonex glass, shown in fig.V.9.

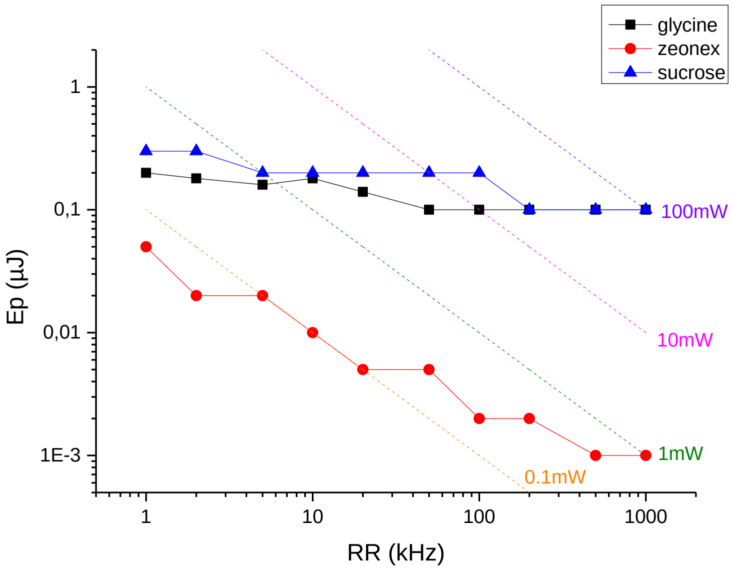

Fig.V.9 The first damage thresholds comparison of sucrose single crystal (scanning along b), α-glycine crystal (scanning along a), and Zeonex glass with scanning speed=10µm/s

From fig.V.9, we observe that the damage threshold of sucrose crystal is similar to glycine crystal, while the one in Zeonex glass is lower and has a greater slope.

The second threshold appears above 30mW and is steeper (close to a mean power dependence) showing that the modification process is different from the first, probably related to the thermal effect.

V.3.2 Photoluminescence properties (PL)

PL formation is induced by fs laser irradiation in sucrose crystal as in glycine crystal and Zeonex glass. The PL properties were characterized as in the previous sections.

V.3.2.1 Spatial distribution of luminescence

Fig.V.10 b, c and d demonstrate the irradiated lines illuminated with UV, blue or green-yellow lamp under the microscope. The transmitted light including emission and excitation light is filtered by corresponding filters mentioned below the pictures. We observe that the luminescence sources are located in the modified regions. The light around the lines is the remaining lamp light from the filter (shown in fig.V.10a).

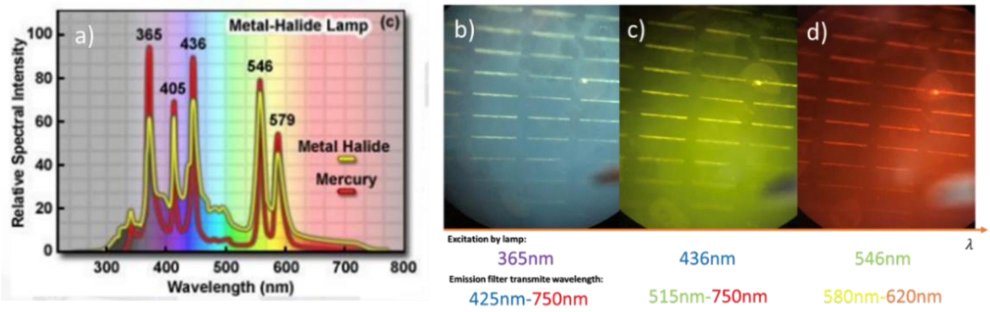

Fig.V.10 image of irradiated sucrose (type 1) under an optical microscope lightened with excitation of b) 365nm c) 436nm d) 546nm with filter cutting the excitation light. a) the spectra of the illumination lamp for observation.

Fig.V.11 are 3D images by the construction of the scanned x-y luminescent images (1024*1024) taken along z (106μm in total). the excitation wavelength is 470nm, with a detection range of 510nm-590nm. Fs laser irradiation parameters are marked on the images.

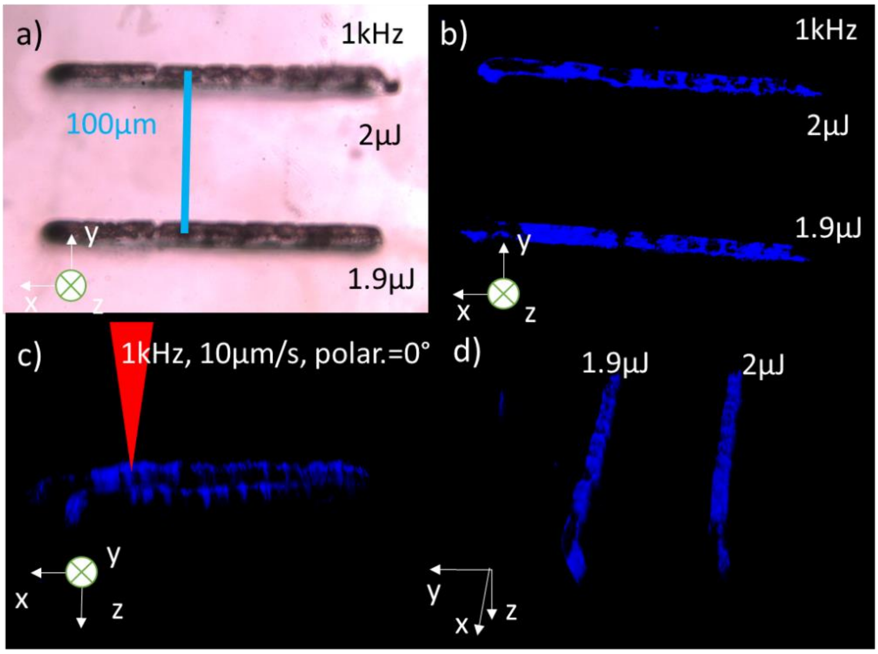

Fig.V.11 a) the irradiated lines (type I) under an optical microscope under natural light and transmission mode b)-d) 3D luminescent image of the same lines taken by confocal microscope with an excitation wavelength of 470nm and detection of 510-590nm, the blue color of lines is selected by software. b) top view c) side view of the lines d) side view along the cross-section.

From the 3D reconstruction photos, we can see that the luminescence is well confined in the black region (Fig.V.11a), and the luminescent regions along the line are discrete. The width of the luminescent line is almost the same as the opaque region, which is around 10-15μm. the length of the luminescent region in z is comparable to the width but a little more to be around 15μm.

V.3.2.2 Emission spectrum excited by 448nm continuous laser

An emission spectrum was recorded by excitation of a 448nm continuous laser. Fig.V.12 demonstrates the spectrum by converting x-axis from wavelengths(nm) to energy(eV) with E (eV) = 1239.8/λ (nm).

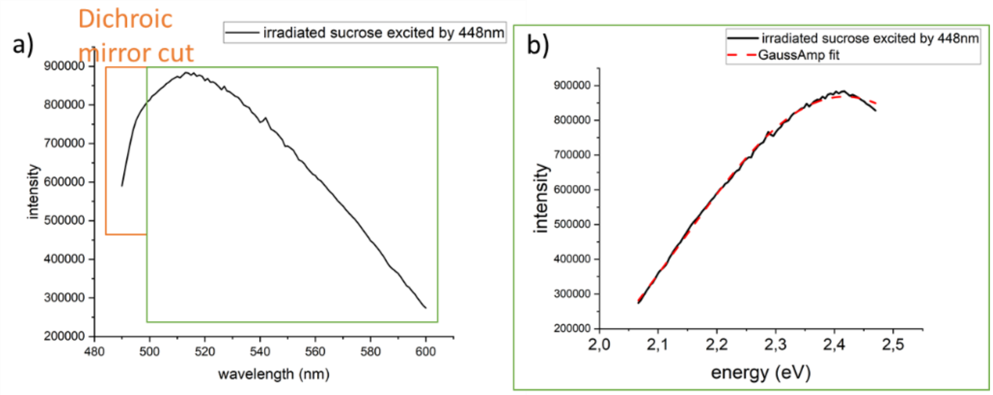

Fig.V.12 the emission spectrum of irradiated sucrose crystal excited by a 448nm continuous laser

The fitting of the result shows that the spectrum is a simple Gaussian curve as eq.V.1 with parameters shown in table.V.1:

$$I(E) = y0 + A.\exp\left(-\frac{(x - xc)^2}{2w^2}\right) \tag{V.1}$$

y0	0 (negligible)	Reduced Chi-Sqr	7.9x10^7
xc	2.409 ± 0.002	R-Square (COD)	0.99793
w	0.233 ± 0.002	Adj. R-Square	0.99788
A	870.0x10^3± 1.6x10^3		

Table.V.1 Gaussian fitting parameters of the emission spectrum

This suggests only one emitter excited at 448nm and emission spectra centered at 513nm (2.417eV).

V.3.2.3 Emission Excitation Matrix/Map

After the measurement of the PL emission spectrum, an emission excitation map was recorded as performed for glycine crystal and Zeonex polymer. Fig.V.13 shows the EEM of type 1 lines (RR=5kHz and Ep=1µJ).

Mapping was conducted from excitation from 470nm to 670nm with a step size of 8nm, the detection (HyD) begins from 485nm and ended at 700nm with a detection bandwidth of 10nm. The detection step size is 9.76nm. the lifetime gating was set from 1ns to 4.5ns.

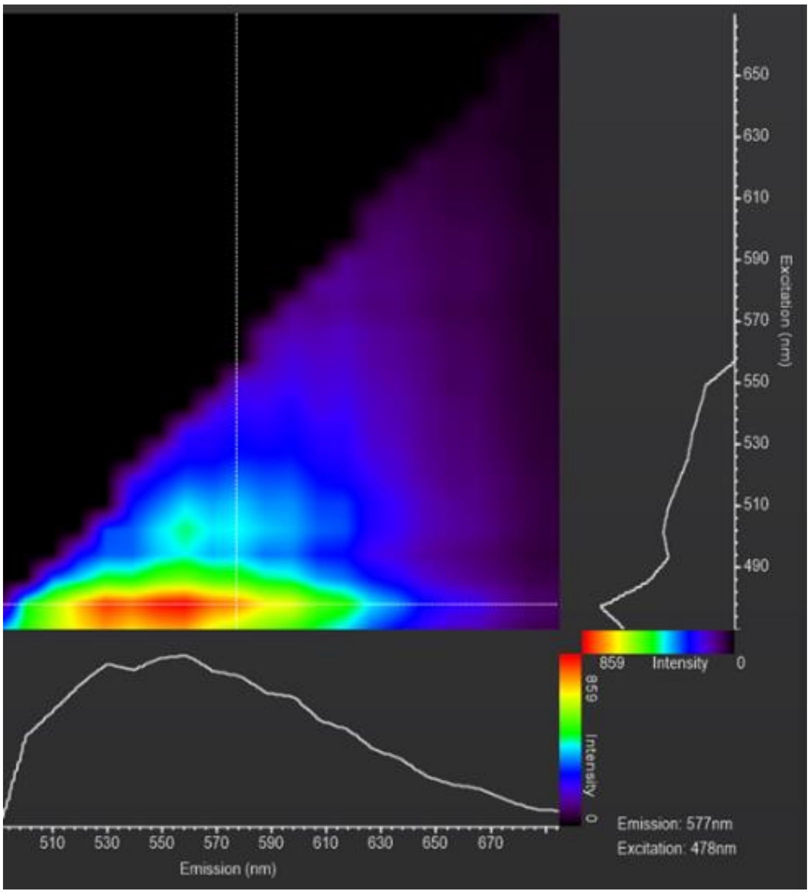

Fig.V.13 EEM of irradiated sucrose crystal RR=5kHz and Ep=1µJ (type I)

We observed a luminescent center excited at 475nm and emitting PL broadly from 510nm to 630nm. Another weaker specie with an excitation center at 500nm and an emission center at 560nm. It looks like the S1 signature from Zeonex luminescence.

V.3.2.4 PL Distribution of normal PL and PL with up-conversion

As with Zeonex glass, up-conversion seems to happen also in the irradiated area of sucrose. As shown in fig.V.14, unlike the normal stoke shift luminescent species which are all over the irradiated line(right), the species with anti-stokes shift is distributed more discretely like stars in the irradiated lines. Fs laser parameters of this modified line: 10kHz, 2µJ, 10µm/s.

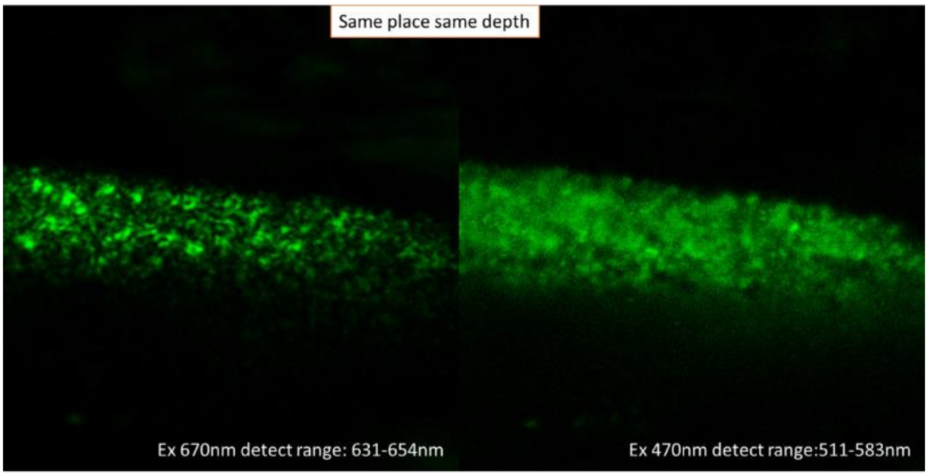

Fig.V.14 the 2D image of luminescent distribution in an irradiated line (10kHz, 2µJ, 10µm/s type I) a) the location of the species excited at 670nm and detected in the range 631nm to 654nm b) the distribution of luminophore(s) excited at 470nm and detected in the range from 510nm to 583nm.

V.3.2.5 Luminescence in the fluid produced by the irradiation

After fs laser irradiation, a fluid phase was observed around irradiated lines, shown in fig.V.15. It is observed to be luminescent as well as shown in fig.V.16.

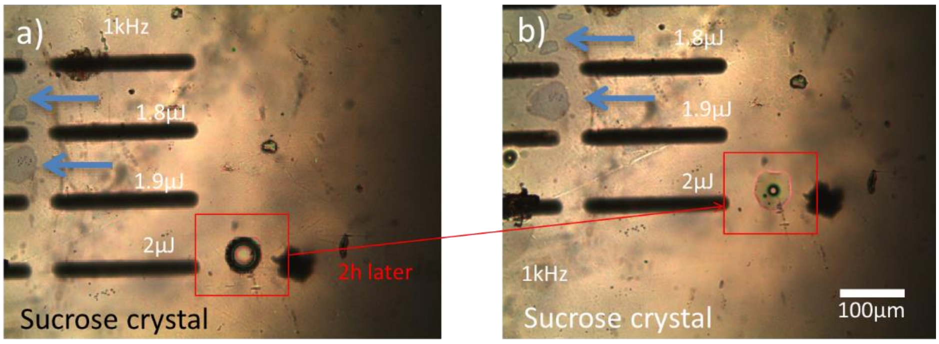

Fig.V.15 microscope image of the written lines, taken at a time delay after irradiation, fluid phase is visible. Type 1: 2µJ, 1kHz

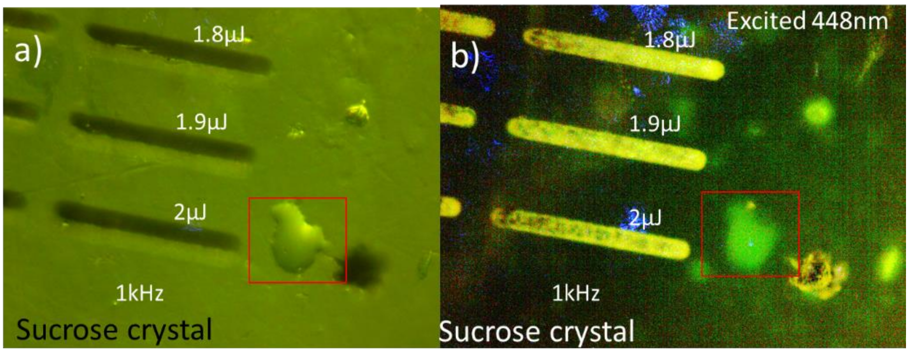

fig.V.16 luminescence under excitation at 448nm. a) microscope image in natural light, b) emitted light.

From fig.V.16, we see that the PL is well restricted to the irradiated lines (emitting in the yellow range), besides those, a fluid phase is also luminescent (emitting in the green range).

V.3.3 About Mechanism of Laser- Sucrose Crystal Interaction

Looking at the landscape in fig.V.8, the threshold for observing type 1 is weakly dependent on RR, being mainly dependent on pulse energy. On the other hand, by computing R_τ (defined in chapter 2) from the physical properties of the sucrose, we can deduce that pulses are independent until 20kHz (see table Table.V.2). For larger RR, we do not observe a behavior change. This means that the effect is just defined by the beginning of the temperature curve, probably in a physico-chemical reaction that extracts water or gas from the sucrose molecule.

RR(kHz)	R_τ
1	203
10	20.3
20	10.1

Table.V.2 R_τ value according to RR of sucrose

On the contrary, the second threshold appears closer to an effect of the mean power (hyperbolic dependence of Ep on RR) at the level of 50mW. A value close to the one that allows crystallization in the inorganic materials. It is then likely that type 2 is a physical transformation like melting (458K) or phase separation.

V.4 CONCLUSION

In summary, we have investigated the modifications that are induced by fs laser irradiation according to the laser parameters in sucrose single crystal which is chiral, optically active, and transparent in visible range even UVA, and not yet considered as a photonics substrate.

Here again, we focused on the demonstration of luminescence creation. We found two domains of modifications that we defined as type I and type II. The thresholds are smaller than the ones of inorganic materials. Type I lines appear with a width of the order of the beam, while the type II lines are blossoming in shape and the specific volume changed significantly. Nevertheless, in both domains, we found the creation of photoluminescence properties in two phases: one is attached to the solid phase and another seems moving with the liquid one. Here again, identification was still very hard. Nevertheless, it seems that the sugar crystal can be used as an optical substrate. Fig.V.17 presents some examples to display information on a sugar substrate. The information appears black under natural light but luminescent with visible colors depending on the excitation wavelengths (as shown in fig.V.10).

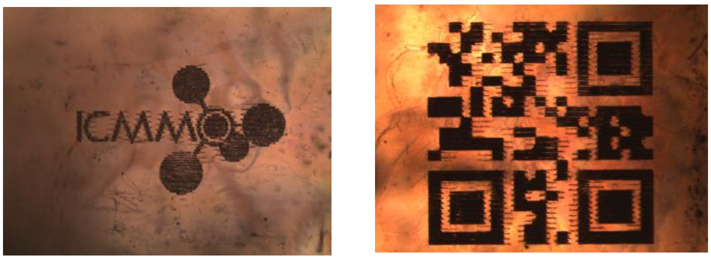

Fig.V.17: examples of inscription in sucrose crystal, a) the logo of the institute (1mmx3mm), b) a QR code (2mmx2mm)

Chapter.VI LUMINESCENCE EXCITATION ANISOTROPY AND ITS ORIENTATION CONTROL BY POLARIZED LIGHT

VI.1 INTRODUCTION

Among all the properties we discovered, characterized, and analyzed, we found that photoluminescence exhibits anisotropic property that could been controlled or respond to the polarization. One of the anisotropic properties related to photoluminescence is the **excitation anisotropy**. It means that the emission intensity is depending on the excitation polarization direction.

The local creation of luminescence with an fs laser has been discovered quite at the beginning of the application of it in the material (2007) for instance by changing the valence of transition metal [197] or rare earth [198] and due to the sphericity- of the species, there was no anisotropy. Another feature attached to the fs laser is nevertheless the possibility to create anisotropic properties that are not due to asymmetric arrangement (like it is with nanograting in silica [199] but to an asymmetric object. Especially, Podlipensky et al. [200] showed that after the precipitation of noble metal nanoparticles, it is possible to create dichroism or SHG and then, even more, to orient them with the direction of laser polarization [201].

In such a case, the absorption of the polarized light leads to the excitation of surface plasmon modes that are different along or perpendicular to the nanorod axes or nano-ellipsoid symmetry axes [202]. It is interesting to note that in these last cases, the nanoparticles are created to be spherical and then the irradiation with a polarized laser transforms them into ellipsoidal particles with orientation defined by the laser polarization.

Although the luminescence we produce with lasers is in organic matter, there is no evidence that it is necessarily spherical, so it is likely to have anisotropic properties. Therefore, we designed a set of experiments to demonstrate the existence of this effect.

VI.2 EXPERIMENTAL DETAILS

VI.2.1 Experimetal setup

To find out if the products induced by fs laser are anisotropic, a set of experiments for measuring photoluminescence were designed. As shown in fig.VI.1a, the excitation light is from a CW laser at 448nm, whose spectrum is shown in fig.VI.1b. The output of laser light was linearly polarized by a polarizer and the linear polarization direction was controlled by a half waveplate after the polarizer. Those 2 optical components are assembled as a polarization control unit, shown in orange dash square in fig.VI.1a. The origin of the polarization angle is fixed at 0°±2° in reference to the written line usually which is often parallel to the horizontal of the system but mentioned when it is vertical. After the polarization control unit, a dichroic mirror (Thorlabs, DMLP490R) reflects laser light to the objective. The power arriving on the sample was measured to be around 40µW or 10µW depending if it is exposure or measurement mode. An objective of magnification x10 was used for observation and x20 (NA=0.5) for measurements leading to an area on the sample around 160x240µm^2.

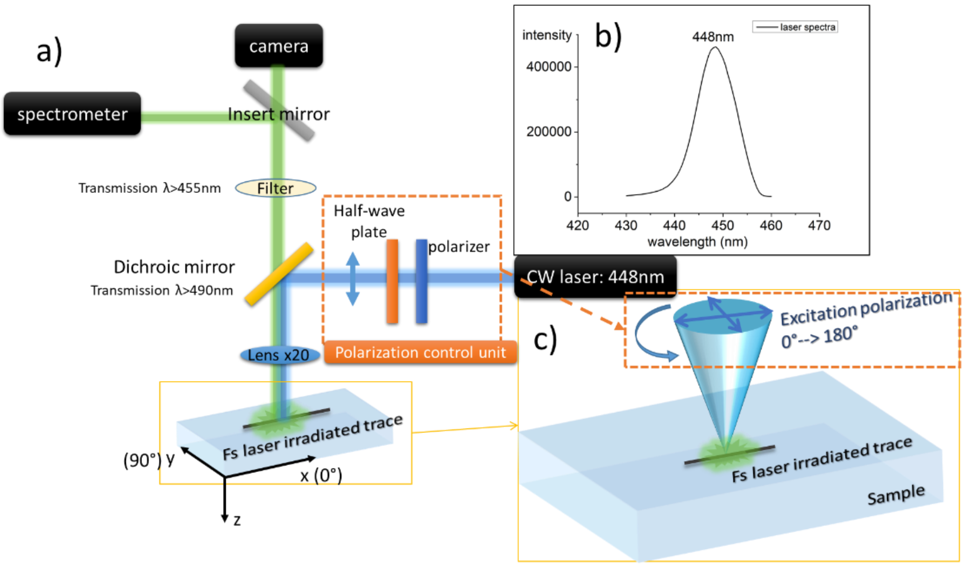

Fig.VI.1 a) schematic diagram of the measuring setup b) CW 448nm laser spectrum from 430nm to 460nm c) excitation polarization angles on the sample: polarization controlled from 0° (parallel to system x-axis) to 180°.

1) the source at 448nm is polarized by the system (polarizer and half-wave plate) and is reflected toward the objective by the dichroic mirror under 45°. Polarization convention 0° is horizontal (Shear): the reflection is close to 99-100%. For 90° vertical polarization (Parallel), the reflection is also close to 98-100%. The angular dependence of the dichroic mirror can be described as $I_{lum}(\theta) = a + b.sin^2(\theta)$, b is thus not more than -1% of a. Therefore, it is a very small polarization dependence of the incident intensity.

2) the light goes through the objective and converges to the focus in the sample. If the objective is not specially adapted for polarization, there can be some polarization dependence, especially for rays out of the objective axis. In the focus voxel in the air, compensation of polarization is achieved correctly but not out of it and the spherical aberration from the surface of the sample is not improving this with a focus that is elongated along the propagation axis. So, we can expect different polarizations along the focus in the material. This means that if one considers two points in the material, one at the focus and one out of the focus, they will be excited (irradiated) with different types of polarization.

Lastly, about exciting light, the reflection of the laser light from the sample surface is mostly cut by a dichroic mirror but its rejection is completed by the spectrum analyzer at the other wavelength.

3) The 448nm light, assumed with a given linear polarization, has now excited a luminophore and this one emits light at a longer wavelength.

The luminescence light can be partially polarized. It goes to the objective that presents the same polarization issue with 448nm and then to the dichroic mirror that works, this time, in transmission. The cut-on wavelength is at 490nm and works correctly above 500nm. The S waves are transmitted at 94-97% and the P waves at 97-100%. On the other hand, the polarization of the luminescence is likely to be only partial. So, finally, we expect a very small effect of polarization from the equipment.

The luminescence intensity is defined by the response of the material as follows:

$$I_{lum}(\theta) = [a + b.sin^2(\theta)].obj(\theta, departure\ from\ the\ focus\ \ center)$$

where θ is referenced to the "horizontal" of the system appearing also horizontal on any photographs.$obj(\theta, departure\ from\ the\ focus\ \ center)$ is the transfer function of the objective almost θ independent at the focus. Lastly, b of the order of -1%. The measurement with carboxyfluorescein confirmed this view. Residual polarization dependence is thus arising from the objective when luminescent sources are out of focus.

Then by performing repeated measurements, by turning the sample holder with the sample by 90°, we were able to correct the system anisotropy according to the polarization and to separate it from the linear polarization dependence of the sample.

Emission light was then detected by a spectrometer with 0.5s integration/point. The spectral range is set from 490nm to 700nm according to the PL of our samples. The slit was set at 15nm resolution and the data measurement step was 1nm.

VI.2.2 Sample details

The samples used in this chapter are shown below. They were all previously irradiated with an fs laser:

1) α-glycine crystal irradiated at Repetition Rate=1MHz, pulse energy=1.7μJ, scanning speed=2μm/s, polarization=0° 30° 60° 90° 120° 150°. The fs laser irradiation parameter is located in the modification landscape in fig.VI.2a.

The orientation of the line versus the crystal orientation is $\vec{a}$.

The written line is considered at 0°±1° of azimuth perpendicularly to the exciting light propagation direction and fixes thus the origin of the angle.

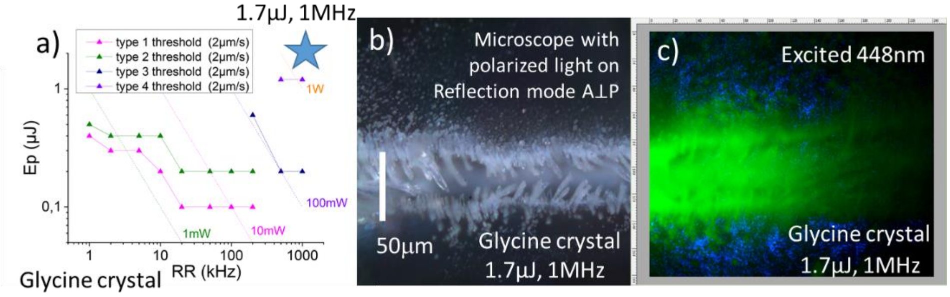

fig.VI.2: Information related to luminescence collected from Glycine sample a) the landscape including the experiment location at pulse energy=1.7 µJ – repetition rate 1MHz, b) optical image in reflection (with polarized light and crossed), c) light collected on CCD detector, sensitive in the visible. The excitation wavelength is 448nm. The blue light is the scattering of the exciting light, the green one is the luminescence.

2) Zeonex glass irradiated at RR=500kHz, Ep=100nJ, scanning speed=10µm/s, polarization=0° (see fig.VI.3).

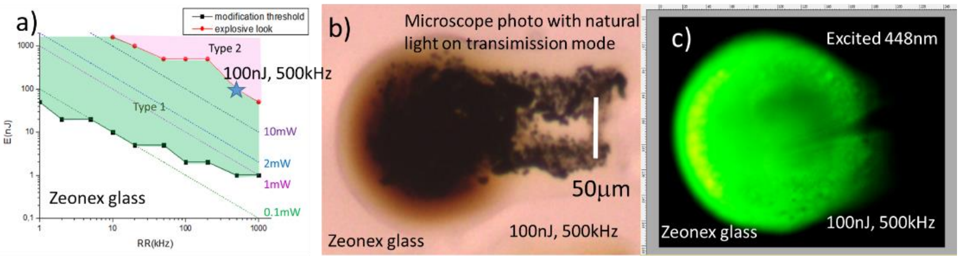

Fig.VI.3: Information related to luminescence collected from Zeonex sample a) the landscape including the experiment location at pulse energy=0.1 µJ – repetition rate 0.5MHz, b) optical image in transmission with natural light, c) excitation wavelength at 448nm, CCD detector sensitive in the visible.

2.2.3) Sucrose crystal: the fs laser parameters were chosen in the type I domain (see fig.VI.4) with speed=10µm/s.

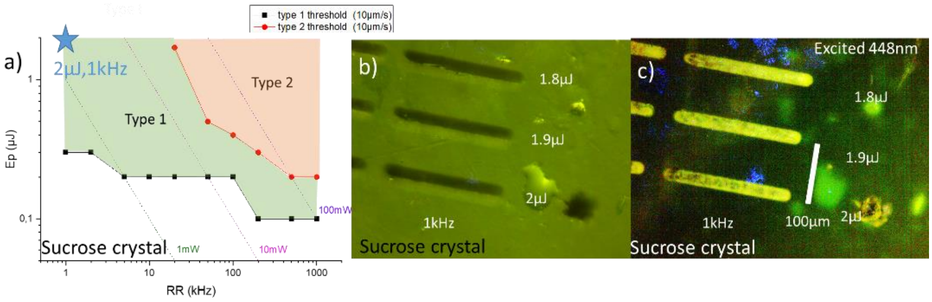

Fig.VI.4: Information related to luminescence collected from Sucrose sample a) the landscape including the experiment locations; b) optical image of the irradiated lines in transmission mode: RR=1kHz, Ep=2μJ, scanning speed=10μm/s, c) excitation wavelength at 448nm, light collected on the CCD detector sensitive in the visible

The orientation of the lines versus the crystal reference is $\vec{b}$. The written line is by convention at 0°±1°.

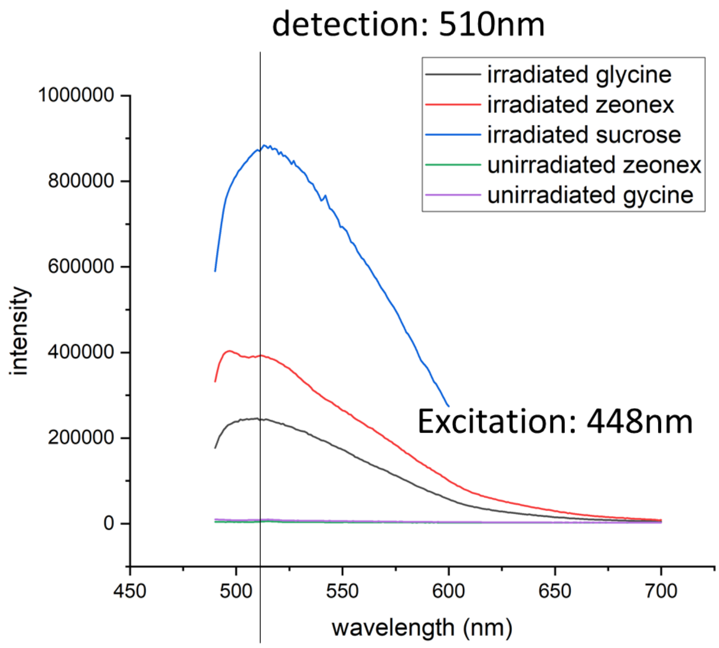

Fig.VI.5: luminescence properties (emission spectrum excited at 448nm) collected from the irradiated α-glycine sample (Ep=1.7 μJ, RR=1MHz, scanning speed=2μm/s), Zeonex glass (Ep=0.1 μJ, RR=0.5MHz, scanning speed=10μm/s and sucrose crystal sample (Ep=1.8-2 μJ, RR=1kHz, scanning speed=10μm/s)

For the irradiated areas of these 3 materials under the laser parameters introduced before, the emission spectra (fig.VI.5) under 448nm excitation have maximums around 510nm, while the unirradiated samples appear no luminescence at this wavelength. The experiments of this paper use thus this wavelength for detection.

VI.2.3 Emission spectra

In the preliminary experiment, we pointed out that the luminescence intensity changes on linear polarization and probe irradiation conditions, we had thus to investigate any change in the luminescence spectrum that may translate that several species are contributing to the luminescence under 448nm excitation. This is shown in fig.VI.6.

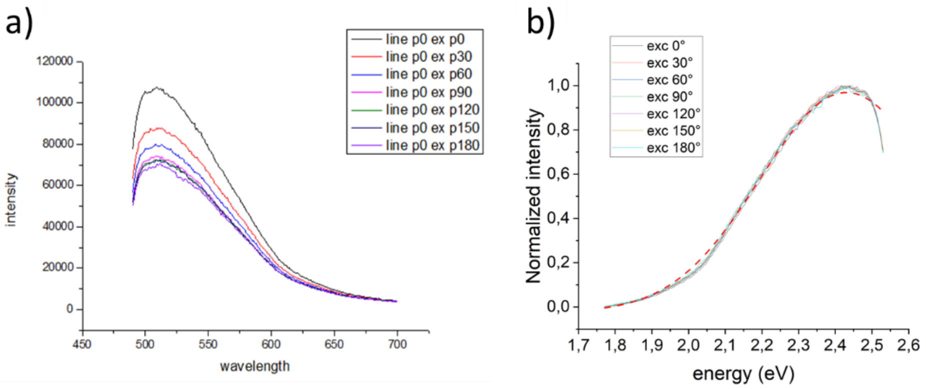

Fig.VI.6 emission spectra under excitation polarization of 0,30,60…180° and for 30s exposure duration for each polarization in α-glycine after fs laser irradiation at 0° polarization from the line direction. With 30s for each linear polarization a) raw measurements, b) renormalized, spectra according to the axis changed from wavelength to photon energy (blue curves), red dash line in b): fit with one Gaussian curve and constant background.

As we can see, there is no distortion of the spectrum (blue curves fig.VI.6b) according to probe polarization rotation and in addition, it can be fitted with one Gaussian curves contribution: with the maximum at 2. 41eV, and bandwidth of 0.22eV and at $1/e^2$ which is quite common for organic luminescence centers [203]). There is thus only one luminescence center emitting under 448nm excitation). We made the same experiment on the other compounds and collected similar results [119].

Any wavelength can be thus chosen for studying the polarization effect in the course of the bleaching and the polarization effect. We finally chose the wavelength at 510nm for our investigation as far enough from the cut-on of the dichroic mirror and close to the maximum for the three materials in consideration in this paper.

VI.3 RESULTS

VI.3.1 Bleaching

When as-cast samples of glycine alpha are irradiated at 448 nm with a power level of ca.40μW, a decrease in time of luminescence intensity is observed. One example is given in fig.VI.7. It is also detectable in fig.VI.6. This is called bleaching. We will discuss later in the paper, the possible origin of the phenomenon.

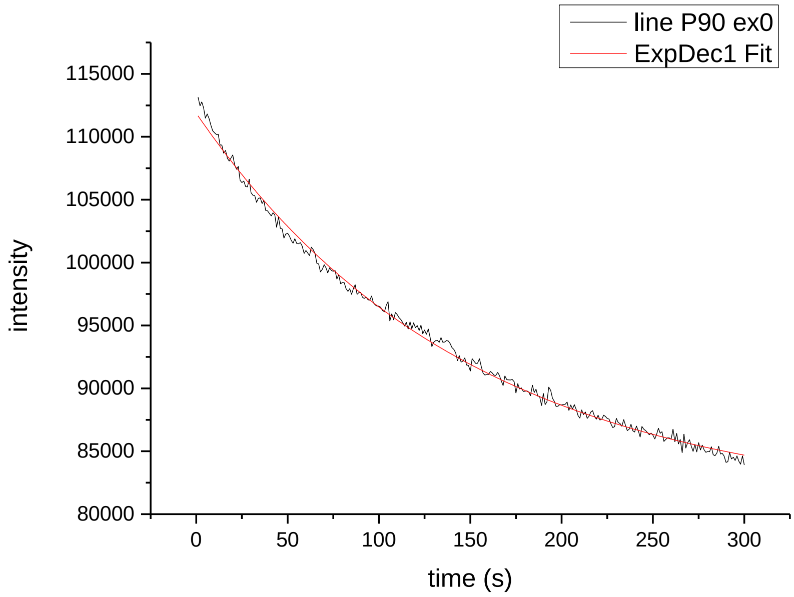

Fig.VI.7 Emission on time at 510 nm of glycine during the excitation at 448nm

From fresh sample, it can be fitted by the following expression

$$I(\mathrm{t}) = A_1 + A_2 e^{-\left(\frac{t}{\tau}\right)} \qquad (\mathrm{VI.1})$$

The obtained values of the parameters are:

A_1=81000(a.u.), A_2=31000(a.u.), τ=102s with uncertainty of 2s due to the fitting (eg. Starting time). Of course, the values of A_1 and A_2 are depending on previous exposures if there were any or on the excitation intensity or also on the place along the fs irradiated line. This shows the existence of two components: one bleachable and one not bleachable. The time decay appears to be material dependent (e.g. around 60s in Zeonex), but also dependent on the place of irradiation in the same line (e.g. 102s, 161s and 134s).

So, we are facing to a bleaching of the luminescence excited around 448nm. However, the amplitude of the bleaching seems to saturate and only a part of the signal can be bleached. The larger part of intensity is not bleachable.

VI.3.2 Excitation anisotropy after fs laser irradiation

Is there original anisotropy after fs irradiation like it is mentioned in [204]?

For that purpose, we decided to test the irradiated sample as cast without previous exposure to any light. We wanted to know if the fs laser irradiation induces anisotropy in the material i.e. if the polarization direction or scanning direction of irradiation or else the crystal orientation is involved in this preference. In this experiment, bleaching is unavoidable but proceeded to some corrections.

Bleaching correction

In such a way, we first found out that there was a modulation of the luminescence intensity with the direction of exciting polarization, with the intensity minimum at 0° and the maximum at 90° (the angle reference is one of the systems). In this experiment, the polarization of the fs laser was set at 120° of the scanning directions in order to be able to distinguish between the effect of system anisotropy and writing laser polarization. Then, to find the origin, from the instrument or from the sample, we made two measurements, one with the line oriented at 0° (ref system) and a second after rotating the sample by 90°. The results are shown in fig.VI.8 taking Zeonex as an example. On the raw data 8a, we see a modulation according to polarization rotation over a decaying curve. In 8b, after correcting by the bleaching, we see the modulation according to the exciting polarization angle. We observe that the polarization-induced modulation does not change over time.

Furthermore, comparing the two configurations of the sample with line direction at 0° and 90° of the system, the position of the modulation does not shift. It means that this modulation is mainly arising from the system (see section 2.1) otherwise, we should have seen a 90° shift of the modulation.

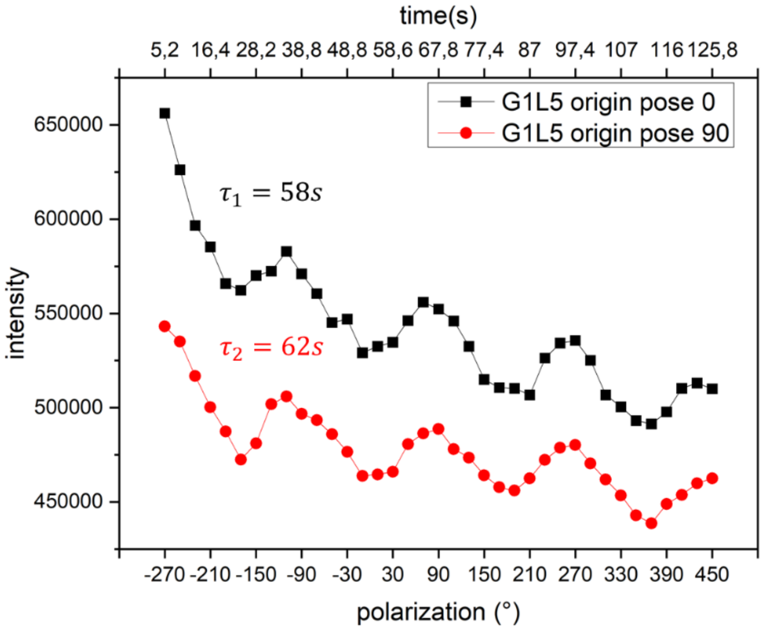

Fig.VI.8 luminescence change on time and probe laser polarization at a fresh position along fs irradiated line in Zeonex, the measument time of the 2 areas is slightly different, we chose one of it for the time reference (top abscissa)) τ1 and τ2 are the bleaching time according to the equation in the text above.

On the other hand, whereas the global intensity has decreased by about 30%, the modulation amplitude seems not to have decreased (its amplitude is about 6% of the whole signal. We can say that there are two components excited at the same wavelength, one bleachable and the other one not bleachable as is already noticed above in the fitting, but excitable at the same wavelength. On the other hand, the original anisotropy can be still hidden behind the anisotropy of the system. We thus try to find out the quantity of how much the equipment influenced the anisotropy and exclude it, do we have any anisotropy left from the fs irradiation before any further exposure to the exciting light?

For excluding the system anisotropy and a clear measurement of the original anisotropy eventually induced by fs laser irradiation, we thus used a combined approach described below.

Fitting approach

In recording the luminescence from an as-cast sample of glycine, the decrease of intensity is dominant on the effect of polarization change whatever the origin (instrument or sample material) in the condition of the recording above (slow recording speed, for a large signal to noise ratio). We have also seen that the modulation according to excitation light polarization is not sensitive to bleaching at a level smaller than about 10%. So, if there is a material anisotropy (excitation dichroism), it is hidden by the instrument one.

To find the parts of non-bleachable-isotropic, non-bleachable-anisotropic, bleachable-isotropic, and bleachable anisotropic, we consider the following equation (VI.2) that accounts for all cases. θ is the exciting light polarization direction in the system reference, θ_0 is the position of the minimum of the modulation versus the same reference. The two configurations of measurements (one with line direction horizontal is quoted 0 and the other with line direction vertical is quoted 90 in the θ_0 parenthesis).

We note that for A3>>1, and θ_0 (0) =θ_0 (90), the modulation is defined by the system anisotropy i.e. the modulation does not shift. If θ_0 (0) ≠θ_0 (90), we see the effect of other sources of anisotropy. If A3 is of the order of 1, there is also an isotropic source. Note also that A2 is material-related only, not A3 or A1.

$$I(\mathrm{t}) = A1\left(1 + A2.\,e^{-\left(\frac{t}{\tau}\right)}\right)\left(1 + \mathrm{A3}.\,sin^2(\theta - \theta_0)\right) \qquad (\mathrm{VI.2})$$

We thus used a fitting procedure for separating all the effects.

The results are shown in fig.VI.9 and the values are given in table.VI.1. A1 is just a total amplitude coefficient. It is sensitive to the position in the optical system. The variation of 9% is normal. It will be not involved in the next analysis. The variation of A3 (the anisotropic response) is weak and consistent with the fact that the anisotropic part is the same whatever the sample orientation. The variation of θ_0 is weak and leads to conclude that the main part is the anisotropy arising from the system. Otherwise, if it was attached to the material only, it would rotate by 90°($\pi/2$). So, the remaining variation of 7°(0.107rad) may be arising from a weak contribution from the materials. A2 (the bleachable response) is changing significantly but has no physical contribution because this variation arises from a time shift of about 30s on the origin of the time taken between the two experiments. By the way, A2 is dependent also on the time scale and of course on the previous illumination of the material. If we consider that the first experiment has been performed without previous irradiation, the bleachable fraction can be estimated. We thus can fill in table.VI.2, with the proportion of the different contributions.

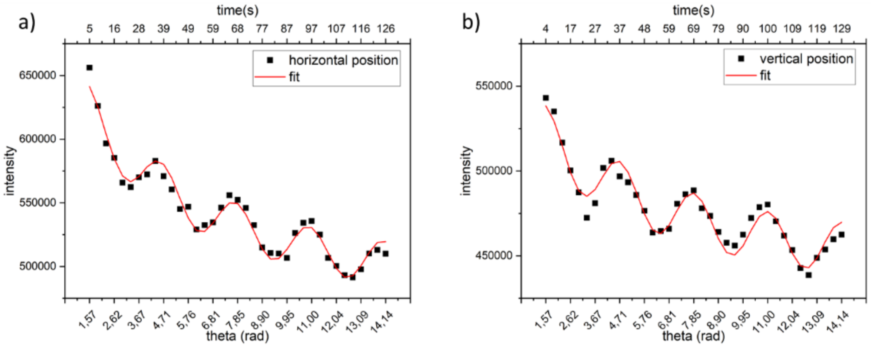

Fig.VI.9: Fitting of the data in fig.VI.8 on time and polarization angle. a) the fitting for the black curve (0°), b) the fitting for the red curve (90°)

coefficients	***Horizontal position***	***Vertical position***
τ	*58.31054*	*62.03553*
$A1$	*469828.01877*	*430032.74927*
$A2$	*0.30409*	*0.18395*
$A3$	*0.06866*	*0.06787*
θ_0*(rad)*	*-0.09099*	*0.0166*

Table.VI.1 the fitting coefficients of the emission intensity by equation VI.2.

properties	***contributions***
Total	*100.0%*
unbleachable iso	*71.8%*
Bleachable iso	*21.7%*
unbleachable aniso	*4.9%*

Bleachable aniso	*1.5%*

Table.VI.2 The component composition deduced by fitting coefficients

It is worth noting that the anisotropic part contains both system and material contribution. The material anisotropy can be deduced quantitatively by the analysis of $\theta0$. But we see here that material anisotropy (the bleachable anisotropy part) is smaller than the system anisotropy which reaches only 4.9% as expected from section 2.1. If we consider that the bleachable part is from the material, the related anisotropic part is 1.5% of the total and 7% of the total bleachable luminophores (1.5%/23.2%).

To minimize the effect of bleaching, laser intensity has been set low enough such as 10μW, and the measuring time was also minimized to be 1s for the measurement of one polarization.

The final question on this part is to bring out some information regarding the origin of the luminophore.

We thus recorded the anisotropy from as-cast samples.

we recorded from one glycine sample: same scanning direction, along 0° or x. the different irradiation polarization directions of 0°,30°,60° 90° and 150°. scanning direction 0°// $\vec{a}$ axis. Almost all the results show the absence of anisotropy after fs irradiation contrary to what Kallepally et al. [204] found in the imidine compound at 0.65 μJ, 2 kHz, 0.2 NA, 4mm/s. These authors also did not detect bleaching of luminescence with excitation at 360 nm, a wavelength that targets luminophores excited in UV.

Intermediate conclusion

We started with as-cast samples from the fs irradiation. We tested different lines written at different pulse energy. We measured the luminescence under polarized 448nm excitation, and follow the emission intensity at 510nm for glycine, Zeonex, and Sucrose samples. Each time, we found that the emission intensity is not or is weakly dependent on the excitation polarization direction (using moderate excitation intensity). So, we can conclude that there is no anisotropy from as-cast fs laser irradiated samples.

VI.3.3 Creation of excitation anisotropy in a given direction

We observed the probe polarization dependence (excitation anisotropy) of the luminescence after a period of irradiation of the order of a few minutes with the same excitation wavelength under a given polarization. **We found that the intensity is modulated with a maximum in the direction perpendicular to the pre-exposure polarization, or a minimum in the direction to the pre-exposure polarization. The probe time of each polarization is about 1s.**

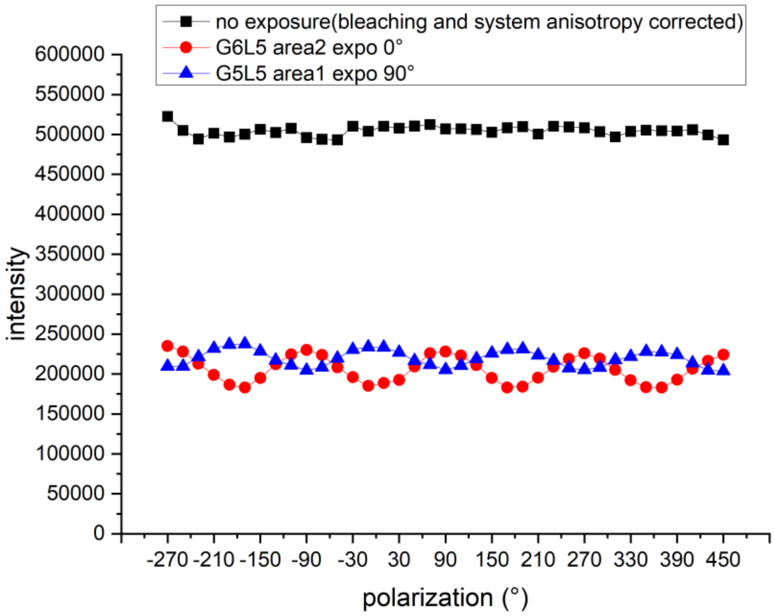

Fig.VI.10: Excitation polarization anisotropy in Zeonex sample of luminescence excited at 448nm and collected at 510nm. Black curve: as-cast sample. Red curve, pre-exposure: 2min at 0°, Blue curve: pre-exposure: 2min at 90°. The fs laser irradiation conditions are given in section 2.2. The blue and red curves are the intensity at 510nm with excitation polarization at 90°, 110°, 130°, etc. with 20° step, and back to 90°, repeated 4 times.

Fig.VI.10 shows the excitation anisotropy measurement obtained in Zeonex glass, just after fs laser irradiation (black curve). The emission intensity is almost constant i.e. not modulated according to the probe polarization direction, but after exposing the sample to light at 448nm under polarization at 0° or 90° during 2 min, the emission intensity is modulated according to the excitation polarization (blue and red curve). We can see from fig.VI.10 that after exposure for 2 min under 0° light, the luminophore has always the minimum at 0° while the intensity maximum is at 90°. But after exposure under 90° polarisation for 2 min, the emission behaviour is the opposite.

We have repeated the experiment with other as-cast areas, using a pre-exposure with other polarization angles (see fig.VI.11), we have got each time the emission intensity maximum at 90° from the direction of pre-exposure polarization. This has been seen in the three samples investigated in this paper. The example in Glycine is given in Fig.VI.11. We propose to call this period: the writing step of a luminescence anisotropy.

Here, we can define for further use, a quantity often considered in luminescence studies: the Excitation Polarization Degree (EPD) which is defined as $EPD = \frac{I_{max}-I_{min}}{I_{max}+I_{min}}$ where I means luminescence intensity that is not analyzed and indices max and min are according to the azimuthal angle of the excitation polarization [205]

Its value varies with the duration of the pre-exposure, but weakly with the direction of the pre-exposure polarization. In fig.VI.11, it amounts between *0.030-0.038 in terms of EPD in glycine.*

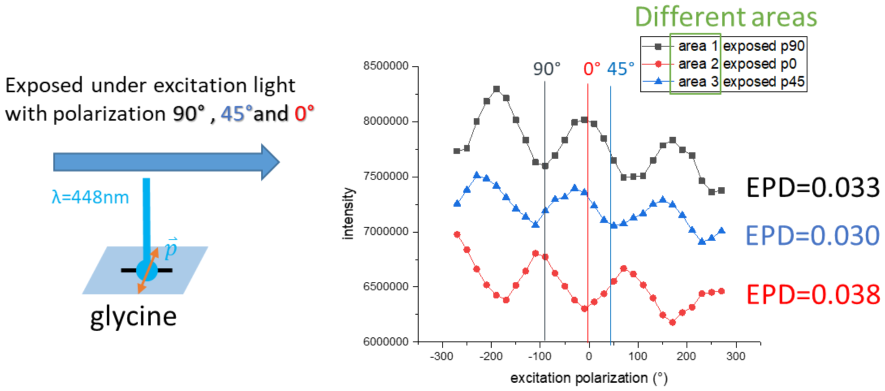

Fig.VI.11: excitation anisotropy written in glycine crystal, PL excited at 448nm and detected at 510nm from different areas after 2 min pre-exposure with 0, 45, 90° polarisation. fs laser irradiation conditions: 1MHz, 1.7µJ.

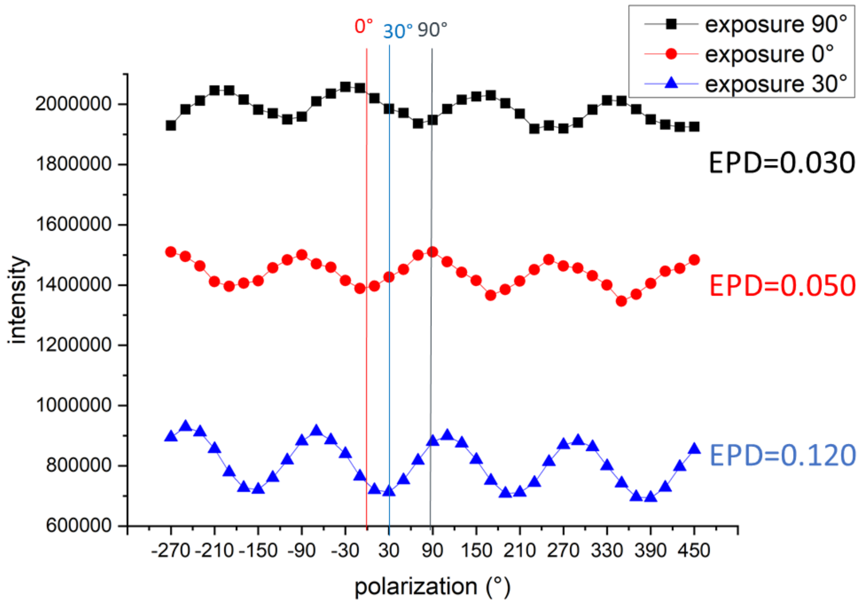

Fig.VI.12: excitation anisotropy written in Zeonex (pre-exposure with different polarization: 0°, 30°, 90° during 2 min, fs laser irradiation conditions: 500kHz, 10-50nJ.

We note that after exposure at 448nm under a given polarization direction, the minimum emission intensity happens each time at this orientation, see fig.VI.12. So the luminescence intensity modulation can be described clearly as a function of excitation polarization. The EPD's are 0.050, 0.12, 0.030 for 0°, 30°, and 90° respectively in fig.VI.12. In fig.VI.11, they are 0.038, 0.030, 0.033 for 0°, 45°, and 90° respectively.

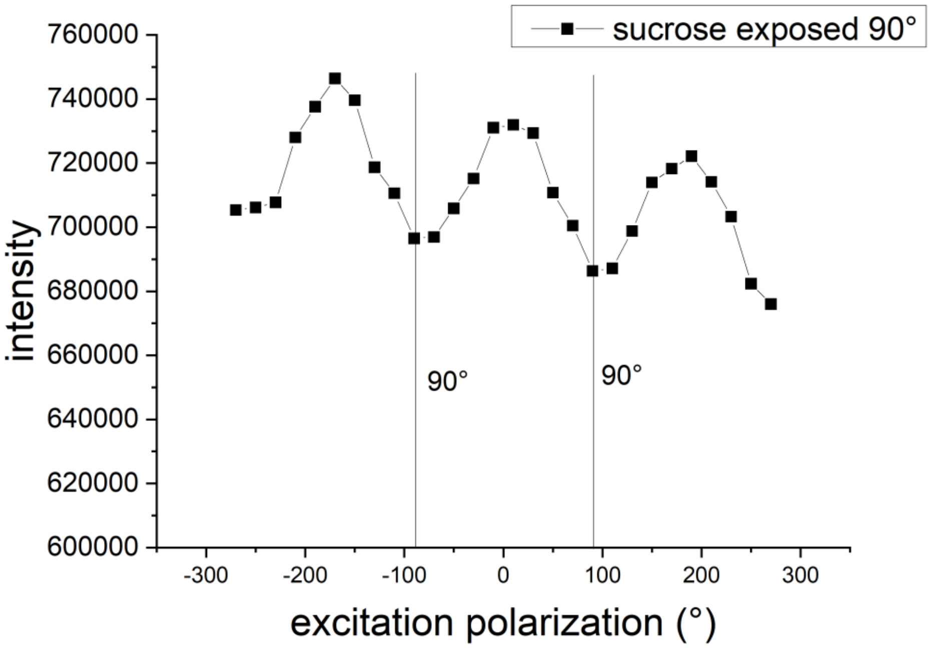

Fig.VI.13: the inscription of excitation anisotropy by irradiation with 448nm light polarized at 90° during 2min in sucrose. Fs laser conditions: RR=1kHz, Ep=2μJ, scanning speed=10μm/s

The same experiment is shown in fig.VI.13 in sugar. The EDP is found at 0.033. Note that the EPD value will increase during bleaching due to the denominator $I_{max} + I_{min}$ decreases.

By comparison of the three experiments, we can see that the writing efficiency is of the same order although the molecular structure, the long-range order and the chemical compositions are quite different.

We found that the anisotropy of the PL has a dependence on the pre-exposure polarization, where **the minimum is always at the direction of exposure polarization and the maximum is at the angles perpendicular to the exposure polarization**.

VI.3.4 Re-orientation of the excitation anisotropy

More interestingly, this anisotropic property can be rewritten by re-exposition to another polarization.

We found that after imprinting anisotropy in an area in a given direction if one performs a second exposure with another direction of polarization, the emission intensity minimum is then changed to be at the new polarization direction of the excitation light. This demonstrates that the luminescence anisotropy can be re-oriented. Such an experiment is shown in fig.VI.14 in Glycine.

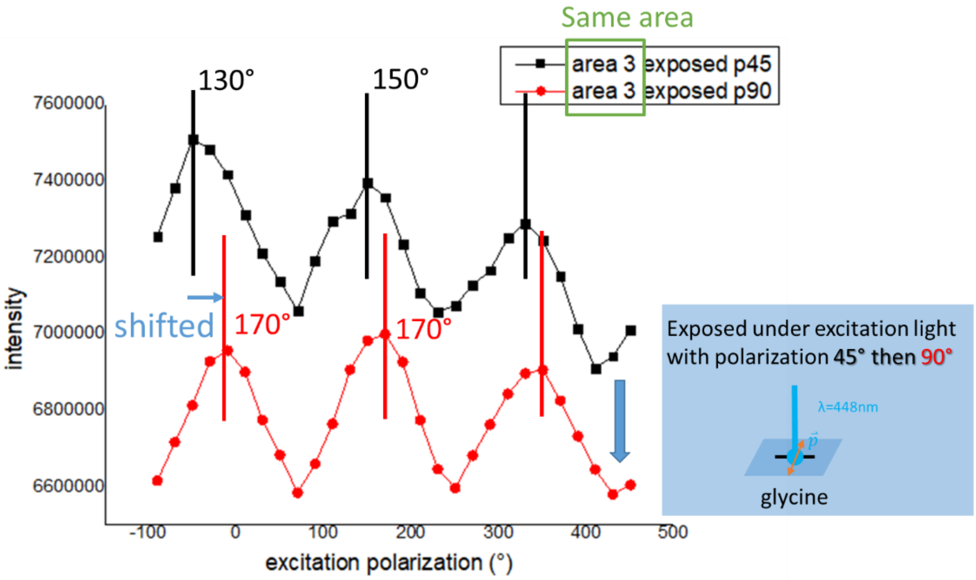

Fig.VI.14: a re-inscription experiment in Glycine. Irradiation is at 448nm. The first exposure is at 45° and the second at 90°with about the same period of time. The modulation amplitude is about the same

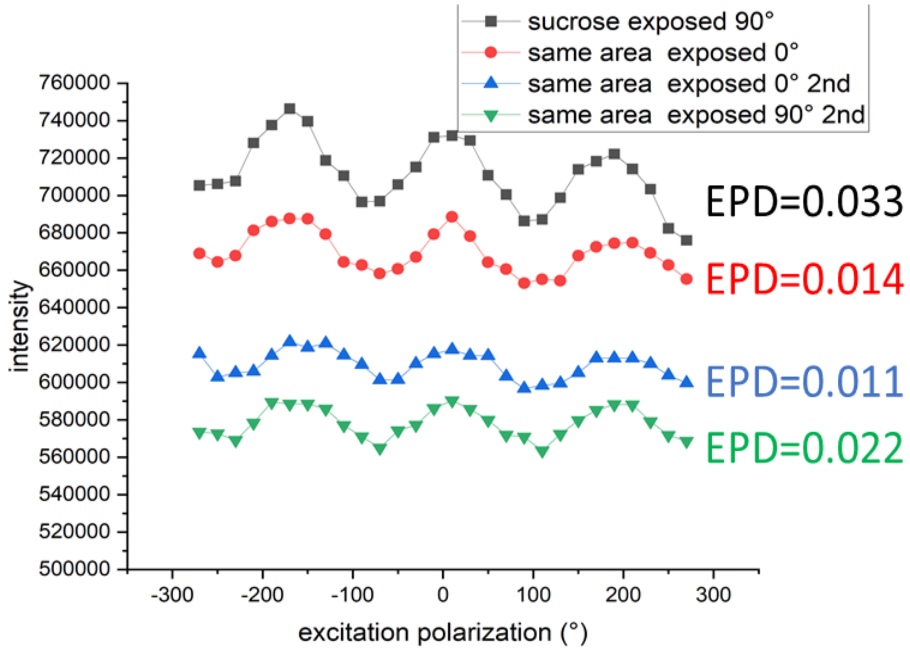

Fig.VI.15: In sucrose crystal, inscription experiments in four steps

A more complex experiment is described in fig.VI.15 in sucrose in order to show that re-inscription can be repeated and the evolution of the modulation amplitude. There are 4 steps:

1- pre-exposure at 90° 300s.
2- second exposure of 50s at 0°, the amplitude has decreased, because the EPD value decreases even though its denominator $I_{max} + I_{min}$ decreases. We can say, it is normal since we expect an opposite modulation.
3- a third exposure of 300s at 0°, the modulation is even smaller and a bit shifted.
4- Exposed under 90° again, the amplitude re-increases again with the minimum at 90°.

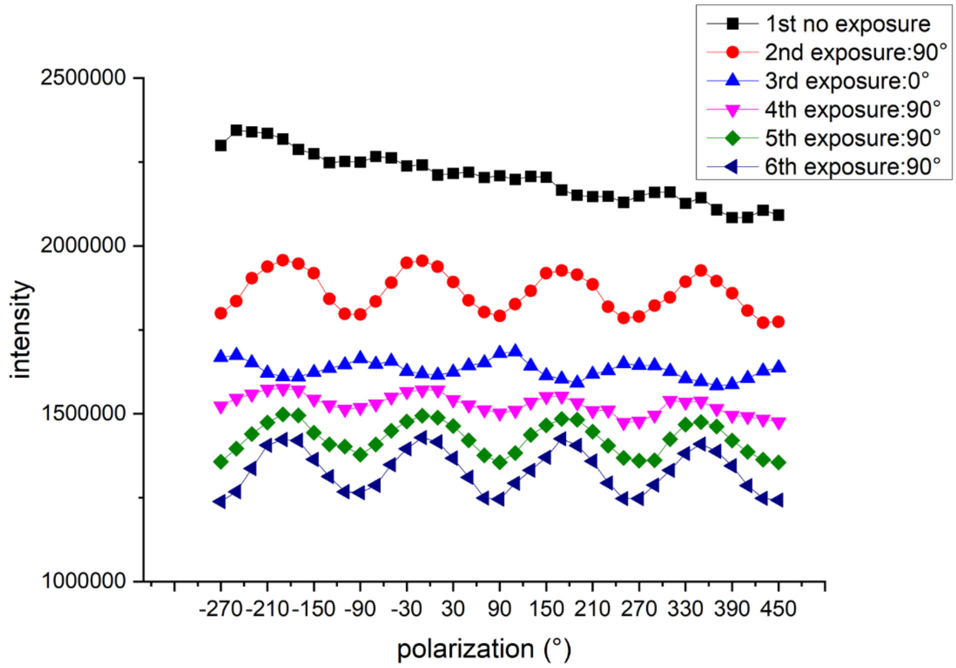

Fig.VI.16: series of rewriting in Zeonex glass with 448 nm with a period of exposure of 300s

A second experiment with a series of exposure have been performed in fig.VI.16. It is like fig.VI.15 but in another material and data extraction.

The steps are:

1- the intensity measured according to excitation polarization without exposure
2- pre-exposure at 90° 300s, we have the modulation with minimum intensity at 90° as expected.
3- second exposure of 300s at 0°, the modulation changes to the opposite.
4- a third exposure of 300s at 90°, the modulation changed back as expected.
5- exposed at 90° again, the amplitude increases with the minimum at 90°.
6- exposed 90° again the amplitude increases even more.

We note in fig.VI.15 and 16 that the anisotropy associated with the pre-exposure is easier to be written into unexposed areas, whereas it takes a relatively longer time to erase the previously written information and write new information to the areas that have already been exposed. We note also that the modulation amplitude after inversion can be reproduced with the same amplitude.

VI.4 DISCUSSION

We have thus shown that there is a negligible anisotropy of luminescence from 448nm excitable luminophores, produced by fs laser irradiation in the series of compounds investigated in the conditions of restructuration of the compounds. However, the subsequent exposure of the fs irradiated sample to polarized exciting wavelength shows bleaching with a time constant of the order of 60s in Zeonex or 147s in glycine. On the other hand, **whatever the compound, an excitation anisotropy is created that presents a minimum in the direction of the polarization**. Furthermore, **this anisotropy is re-orientable by further exposure at the same wavelength**. What can be the origin of such a property?

Bleaching

Bleaching is known in the literature. It appears as a process connected to a reaction occurring after the absorption step. It is a way of relaxation of the excited state. This can be seen in the absorption spectrum by the disappearance of the whole homogeneous band (width defined by the lifetime of the excited level) in an inhomogeneous band due to variation of the central wavelength arising from the disordered environment. Sometimes called hole burning [206]. Luminescence intensity is constant on time under continuous excitation when the luminophore population is constant (inexhaustible) or recycled. When, the absorbing part related to luminescence (excitation band) is connected to relaxation by transformation into another species, the collected signal decreases.

On the other hand, under a short pulse excitation, the photo-excited state rapidly relaxes at the ns scale for most of the materials, especially organic ones for which the luminescence lifetime is around ns [207]. Therefore, a longer decrease (here on the scale of minutes) under continuous excitation means that there exists a second channel like it is schematized in the picture below (see fig.VI.17).

On the other hand, the bleaching experiment brings out two components: one bleachable and one non-bleachable. On the other hand, the emission spectrum shows only one luminophore. They could be two possibilities for rendering consistent these two observations:

1 – two species absorb at the same wavelengths? One is the luminophore giving rise to the emission spectrum displayed in fig.VI.6 and another specie also absorbs but transfers its energy to the luminophore. This is the role of a sensitizer that is commonly used in inorganic materials [208] [209]. This last would be bleachable.

2 - the excited species transforms into another (probably thermally) B species as in the scheme below. Furthermore, the bleaching is only partial and in addition, it is reversible. So, this means that the B species has a reversed reaction giving back to A.

The saturation is accounted for by the equilibrium between A and B.

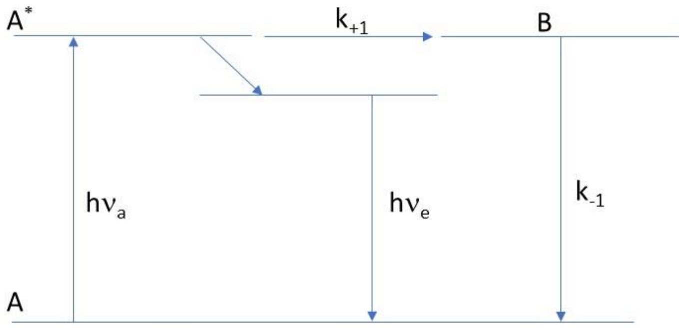

Fig.VI.17 quasi chemical scheme for accounting for the luminescence time behaviour

$A \underset{k_e(h\nu_e)}{\overset{k_a(h\nu_a)}{\rightleftarrows}} A^* \xrightarrow{k_1(T)} B \xrightarrow{k_{-1}(T)} A$, with $k_a(h\nu_a)\, and\, k_e(h\nu_e)$ the rates of excitation and emission, respectively, and $k_1(T)\, and\, k_{-1}(T)$ the thermal reaction rate between A and B.

As the luminescence is proportional to $k_e(h\nu_e)[A^*]$, the computation of the concentration of A* ($[A^*]$) according to the various reaction rate yield the answer knowing the reaction rates.

Anisotropy

What properties should have the luminophores for expecting an anisotropy on excitation?

For understanding this, we should know first what the mechanisms at the origin are of luminescence.

Luminescence is the light emission resulting from the relaxation of a matter after an excitation (from the ground state to an excited state) by various processes (photon for photoluminescence, electron for cathodoluminescence, friction for triboluminescence, etc.). In this paper, we are interested in photoluminescence.

The luminescence may arise from a molecule (local process, the states are localized on the molecule) or from a crystal or a glass (delocalized process, the states are here the collective ones of the solid). The intensity of the luminescence is defined in quantum mechanics by the number of excited states and by the coupling between the excited state and the ground state through the single electron dipole operator $\widehat{D} = \vec{e}.\vec{r}$ within the electric dipole approximation, where $\vec{e}$ is the polarization of the light and $\vec{r}$ the electron coordinate. It can be shown (see Appendix 1) that for observing an anisotropy on the luminescence excitation according to the exciting light polarization, a luminophore should be asymmetric and asymmetrically distributed according to the point group of the luminophore.

Why the modulation is never total?

Normally, we can expect a transition with the same symmetry as the dipole operator. Otherwise, when this one is oriented at 90° from the previous one, it is zero. However, it is never the case for many reasons, in particular:

-The transitions exhibit a bandwidth and if the molecular distortion is not large enough, the shift of the band is not enough for avoiding the superposition of the two bands having orthogonal polarization.

-The molecular orientation distribution asymmetry is not strong enough (the texture is not perfect), and here also, even if there is no overlap of the bands, each band will experience just a change in intensity.

So, finally, the angular dependence can be expressed as $A_1+A_2.\cos^2(\varphi-\varphi_0)$ where φ is the polarization direction in the frame of the system and φ_0 the direction of molecule dipole for which luminescence intensity is maximum. It is worth noting that φ_0 is along a principal axis of the molecule but not necessarily one of the highest symmetries.

In our case, when pre-exposure polarization is at an angle φ_1, we get $\varphi_0=\varphi_1+90°$. There are two possibilities for explaining this result:

1) the luminophore principal axis along which the effect of polarization force (exerted during the pre-exposure) is the largest, is perpendicular to the principal axis along which the luminescence excitation is the largest.

2) the luminophores having the principal axis along the pre-exposure polarization are transformed into another species.

proposal 1: the asymmetric objects rotate on the effect of a torque produced by the interaction of the pre-exposure polarization with a non-parallel molecular dipole moment. We read $\vec{\Gamma}_{DC} = DCpart(\vec{P}_\omega \wedge \vec{E}_\omega)\ with\ \vec{P}_\omega = \varepsilon_0 \bar{\bar{\chi}} \vec{E}_\omega$ the stable orientation is defined by the minimization of the potential energy $W_{DC} = DCpart(-\vec{P}_\omega.\vec{E}_\omega)$. So, the dipole becomes parallel to polarization.

In this case, the modulation shifts from one angle to the other, but the amplitude does not change.

proposal 2: the orientation distribution of the asymmetric luminophore is modified by the transformation of the molecules that are aligned along the axis that have the largest absorption/excitation. The exposure changes thus the population. The angular modulation of the luminescence intensity decreases and becomes asymmetric. Note that this mechanism is associated with bleaching.

The total luminescence can be expressed as below:

$$I_{total} = \int_{\theta_1} f\big(t, N(\theta_0, \theta_1)\big). N(\theta_0, \theta_1). R(\theta, \theta_1). d\theta_1 \qquad \text{(VI. 3)}$$

θ_1 is the direction of luminophores, f is the bleaching function, the efficiency of which depends on N the orientation species distribution, θ_0 is the asymmetry of the distribution due to previous exposures; R is the response of the luminophore that depends on the polarization direction θ and of the luminophore.

Imaging starting from a spherical distribution, it becomes flattened ellipsoidal in the polarization direction because luminophores have been erased in this direction. So, the luminescence intensity in a plane is modulated according to the azimuthal direction with a minimum in the pre-exposure polarization direction. When a second pre-exposure is performed, the ellipsoid is distorted and the azimuthal response in the same plan as before should have a complex shape like:

$$\big(\mathrm{A1} + \mathrm{A2}. \cos 2(\varphi - \varphi 1)\big)\big(\mathrm{A1} + \mathrm{A2}. \cos 2(-\varphi 2)\big) \qquad \text{(VI. 4)}$$

It is not the case for proposal 1.

Other remarks

For proposal 1: the rotation is made through the effect of an electromagnetic torque based on linear susceptibility. This torque is weakly wavelength dependent i.e., non-resonant interaction.

For proposal 2: the transformation of population distribution is achieved by structural object transformation, and this involves necessarily a resonant absorption which is thus wavelength dependent.

Fig.VI.16 is in favour of proposal 2 because with rotation (proposal 1), one should obtain the maximum shifting and it is not (the modulation amplitude decreases). However, with proposal 2, one should see a complex modulation and it is not. So, more characterization of the dynamics is necessary for reaching a clear conclusion.

Additional characterization is also to make the same experiment (orientability test) but for another luminescence, excitation wavelength corresponding to a maximum of excitation e.g. 476nm for Zeonex (absorption of another luminophore [119], and detection for 557nm or so). The objective is to see if several luminophores are exhibiting the same property.

Besides these 2 models of controlling the molecule orientation, the study of [210] (proposal 1) provides a new way of thinking in which the polarization can control the fluorophores apart from quenchers if they exist.

VI.5 **CONCLUSION**

We point out that the laser-induced PL in the three investigated materials is isotropic when it is just created from the fs laser irradiation. However, it can be efficiently rendered anisotropic by pre-exposure with resonant polarized excitation light in the excitation band that is common in our materials at 448nm. In addition, if we call this control the coding of polarization in the materials, this anisotropy can be recoded if we exposed the luminous part to another polarization direction during a time longer than the first coding.

The asymmetric luminophore creation by fs appears possible in very different materials with different chemical compositions and different crystallographic structures i.e. PL creation in materials containing CHON (glycine), CHO(sugar), and CH (Zeonex), so the necessary condition of luminophore creation here is C and H, or maybe only C?

The next question is: is it possible in any organic material? It is not obvious to address this question without a complete characterization of the luminophore. We can just add that another group observed the same [211]. However, it is not the same result compared to Kallepally et al. [204] because it is not the same excitation wavelength (360nm instead of 448nm) and thus not the same luminophore. Can we deduce that the luminophore with this last absorption is the most bleachable and supports the asymmetry orientation control?

The luminophores are in the solid, why can be oriented by continuous laser light with power as low as ~1.25W/cm2? The answer could be that it is not solid but the luminophore is weakly bound or it is not exactly oriented (proposal 1) but the distribution of orientations is dis-symmetrized through the bleaching (proposal 2).

Last remark but not least that can be done is that this is obtained in very different materials, and this pushes us to think that a common species is at the root of this phenomenon. Therefore, as mentioned by a paper about Zeonex[119], the destruction of the molecule and re-building of carbonized clusters like Carbon dots, as well as polycyclic aromatic ones may be the root of the PL property described in this paper.

VI.6 APPENDIX: THE MICROSCOPIC ORIGIN OF THE EXCITATION ANISOTROPY

The luminescence intensity is:

$I_{lum} \sim N_{f_e} \left| \langle f_e | \widehat{D} | g \rangle \right|^2 \delta\left(E_{f_e} - E_g - h\nu_e\right)$ where N_{fe} is the volume density of the excited states, $|g\rangle\ and\ |f_e\rangle$ the wavefunctions of the ground and the excited states, respectively, E_g and E_f their energy level, hν the photon energy and δ(.) the delta function translating the energy conservation. $\langle f_e | \widehat{D} | g \rangle$ is a spatial integral.

The number of excited states is, in turn, defined by a similar expression: $N_{f_e} \sim \alpha . I . N_c \left| \langle f_a | \widehat{D} | g \rangle \right|^2 \delta\left(E_{f_a} - E_g - h\nu_a\right)$ that translates the absorption of the photon by the matter. α is a branching ratio smaller than 1 if there are several possibilities for the excited state to evolve non-radiatively (electron-phonon coupling, physical or chemical reactions). N_c is the number of absorbing levels per unit volume and *I* is the light intensity amplitude. The dependence of I_{lum} with ν_e is the luminescence spectrum and its dependence with ν_a is the excitation one.

The space integrals values may depend on the electric polarization orientation (perpendicular to the propagation axis) either for exciting light or for the emitted one. However, in this paper, we do not analyze the emission and thus the luminescence intensity is just dependent on the polarization of the exciting light.

On the other hand, the space integral value is dependent on the spatial symmetry of the integrand $f_e . \widehat{D} . g$ that should contain a totally symmetric part according to the space group in order to be non-zero (ref. Cotton Chemical application of group theory Interscience 1963, Falicov Group theory and its physical applications1966). In this paper, as we are dealing with molecular solids, the spectroscopic transitions are local, and the space group can be reduced to point one. Furthermore, the symmetry of the above integrand is deduced by the multiplication of the symmetries (irreducible representations) of each part i.e. of g, $\widehat{D}$, and f_e [212]. Finally, considering a sample reference frame x, y, z and propagation along z, for observing an effect of light polarization along x and y, the sample may present some different symmetries along these directions. In this case, N_{fe} has to be rewritten as such and leads, in particular, to Malus law:

$$N_{f_e} \sim \alpha . I . \delta\left(E_{f_a} - E_g - h\nu_a\right) \int_{\psi} \left|\left\langle f_{a,\psi} \middle| \widehat{D}(\theta, \psi) \middle| g \right\rangle\right|^2 dN_c(\psi) \qquad \text{(VI. 5)}$$

with θ the azimuthal angle of the polarization, ψ is the orientation of the luminophore, $dN_c(\psi)$ is the elementary population in the ψ direction. $f_{a,\ \psi\ \psi}$ represent the absorbing wavefunction in the luminophore symmetric coordinates, $\widehat{D}(\theta, \psi)$ is the dipole operator including the polarization oriented following θ written in the luminophore coordinates. Note that $\widehat{D}(\theta, \psi)$ presents a non-symmetricity (like anti-center symmetry) and g wave function is symmetric usually (for non-magnetic materials).

Therefore, if f_a is not asymmetric and does not contain a part of the same symmetry than $\widehat{D}(\theta, \psi)$, the integral $\left\langle f_{a,\psi} \middle| \widehat{D}(\theta, \psi) \middle| g \right\rangle$ is null. There is thus no luminescence excitation. If f_a contains a part of the same symmetry as $\widehat{D}(\theta, \psi)$, the integral depends on θ and ψ, but if, in addition, the orientation population distribution is spherical, reflected in $N_c(\psi)$, we have $dN_c(\psi) = N_c . d\psi$ and the integral $\int_{\psi} \left|\left\langle f_{a,\psi} \middle| \widehat{D}(\theta, \psi) \middle| g \right\rangle\right|^2 dN_c(\psi)$ is not dependent on θ. There is also no anisotropy (e.g. liquid or glass phase).

In conclusion, anisotropy is detected only when asymmetric luminophores are asymmetrically orientally distributed.

GENERAL CONCLUSION

Femtosecond laser direct writing (FLDW) starts with multiphoton ionization and induces various permanent modifications on the relaxation way within solids and especially inorganic materials. These modifications depend on various laser parameters such as repetition rate, pulse energy, scanning speed, polarization, etc., and cause changes in optical and physical properties. This technology defines a flexible manufacturing platform suitable for integrated photonic circuits such as data storage, optical neural network computing, sensing, etc. Due to the explosive growth in the amount of data and information exchanged, this will eventually lead to an ever-increasing demand for photonic devices that require more nuanced and complex laser processing. This has therefore stimulated the need for optical integration. However, most research using this technique has been proceeding in inorganic substrates, functionalization inside organic materials is not so common, especially when light polarization control is included. This background is the basis for my thesis work.

Before this work, in several previous studies, one could control the orientation of the crystalline crystal axis based on the direction of polarization. This was pioneering work and meant that we achieved control of light on the nanoscale, using the polarization of light. However, this result has not been demonstrated in organic solids because the way how the molecules are linked in organic solids is very different from the ones in inorganic ones. The challenge of this work is thus to first gently induce the creation of anisotropic objects, and hereby to spatially control their optical properties (e.g. orientation).

In this thesis, the modifications inside several different organic materials by focused fs laser pulses have been investigated systematically according to morphology, structures, and optical properties especially photoluminescence, SHG, etc. by confocal microscopy, Raman, FTIR, EPR spectroscopy, excitation polarization controlled spectroscopy and so on. Novel phenomena such as orientation controllable of laser-induced anisotropic luminophores, as long as some other optical properties such as refractive index change, SHG formation, linear birefringence, and linear dichroism were discovered.

The main results of this work will be concluded from 2 points of view:

1) The fs-laser-induced moderate modifications in selected organic materials according to laser parameters have been extensively investigated. We have constructed simple thermal analysis models for the judicious selection of laser parameters.

2) In addition, one common laser-induced property in these materials, i.e. photoluminescence is deeply studied by spectral comparison and even anisotropy control.

By this point, we have progressed in two directions of research. Firstly, fs laser irradiation produces a wide variety of property transformations according to a set of parameters. This is a pioneering work that the readers may consider as an overview of laser-induced transformations in chosen materials but can imagine extending to similar properties in other organic materials. Each property has potential applications and can be studied further for the future integration of optical functions. In the meantime, our analytical functions for simulating temperature induced by laser are also a handy tool for any material. Secondly, confined to the interest in the demonstration of polarization control in organic materials, we have chosen only one anisotropic property, PL, to investigate in more depth, which interestingly is not limited to one material but to all the three we have chosen, which is a great encouragement for future research.

OVERVIEW OF THE FS-LASER-INDUCED MODIFICATIONS IN SELECTED ORGANIC MATERIALS

Depending on the pulse energy Ep (0.1nJ- 4μJ), on the repetition rate (1kHz -1MHz) at 1030 nm, 250 fs with a scanning speed=10 μm/s (most of), focus depth ~150 μm, and NA = 0.6, the fs laser-induced modifications have been studied in 3 kinds of organic materials: glycine single crystal, Zeonex polymer glass, and sucrose single crystal.

Firstly, the first damage thresholds of each material are illustrated in

Fig.1 left. The threshold of glycine crystal is comparable to the sucrose one. The threshold of Zeonex polymer is significantly smaller than glycine and sucrose crystals, and in high RR the reduction is even up to a hundred times. The power laws are also different: close to hyperbolic for Zeonex but almost independent for the crystals. This indicates different processes of modifications.

Indeed, different regimes/types defined by varies morphologies are induced in every material, suggesting different transformations. Thresholds of every type in each material are shown in fig.1 middle. The three figures on the right hand side of fig.1 are illustrations of some examples of every type.

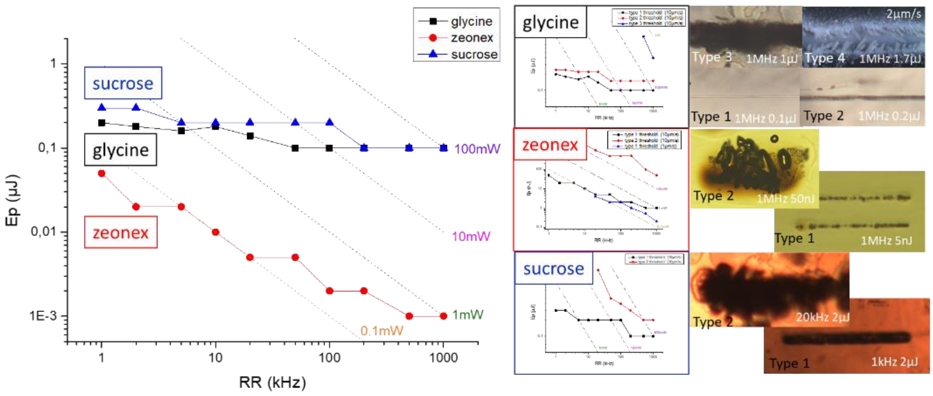

Fig.1 left: damage thresholds of glycine, Zeonex, and sucrose. middle: thresholds of different modification types in glycine, Zeonex, and sucrose. Right: examples of different modification types in glycine, Zeonex, and sucrose.

Secondly, for each material, the various modifications have different properties. It has thus to be concluded by materials than to see if common features can be pointed out and this reiterates the organization of the present thesis.

Glycine

4 types of modifications can be made according to Ep, RR, and scanning speed. Based on laser power, from low to high, we define type 1, 2, 3, and 4. Because for high RR, the Ep has been found to have a larger influence than RR, the threshold thus cannot easily be defined by the value of mean power, we thus defined them by their

morphology:

Type 1: the first threshold is the occurrence of refractive index change, irradiated lines are smooth, and transparent with a width of the beam size (around 1µm). Below this threshold, no visible permanent transformation is generated. In this regime, most of the glycine molecules are not modified. However, the reduction in refractive index might indicate creation of porous structure.

Type 2: the second threshold is the occurrence of opaque objects, irradiated lines have a width of around 6µm. Instead of total decomposition, we proposed that glycine molecules have been changed to some Carbon dots and some polycyclic aromatic molecules with conjugated carbon bonds, and fluid (gas or liquid) have been produced in this modification as well. Fs laser multiphoton ionization produces an electron plasma in the material followed by relaxation, and the transition is completed before energy is transferred to the lattice.

Type 3: the type 3 modification is defined by having an irregular swelling in the irradiated lines with a width as large as 20µm, this transformation is induced only from high RR (>400kHz). It may result from a thermal effect added to the type 2 transition.

Type 4: this is a modification with feather-like or teeth-like solid growth along the irradiation lines. It is likely to be polycrystals. These recrystallized polycrystals have a size of around 10µm wide and 50-100µm long. Same as type 3, this modification is induced only from high RR (>400kHz), likely result from thermal effect. In addition, a parameter such as slower scanning speed increases the chances of generating (e.g. 2µm/s with RR=1MHz and Ep>1.2µJ, which corresponds to a sure generation). Interestingly, SHG production seems to be associated with type 4, although it is occasionally, but not always, observed in type 3, and the intensity of SHG is not as high as in type 4. Similar PL in type 2 has been pointed out also in this modification, we thus believe that a type 2 transition was created before a type 4 transition.

Properties induced by various modifications

RIC: In type 1 and type 2 modifications, we both observed the refractive index decrease, it is around 0.007 and 0.0365, respectively. The reduction in refractive index may result from the generation of gas or liquid, but maybe also from the disorder introduced by the irradiation.

PL: We found the creation of photoluminescence properties with all types, except type 1 where the intensity is very small. Luminophores can be excited from the UV to orange range. In visible EEM, it appears 2 species, which are located in 1) excitation blue-green range (475nm) with emission on a broad range from blue-green to yellow-orange and 2) excitation at 512nm with emission centered at 565nm. This is shown in fig.2b.

SHG: SHG is created in type 4 modifications. It is angular dependent on the fundamental light polarization but no clear origin of it has been identified.

Zeonex

We found two domains of modifications that we called type 1 and type 2. Type 1 denotes laser mean powers smaller than about 20mW and larger than about 0.1mW (smaller than glycine and sucrose, and several orders of magnitude smaller than for inorganic materials):

Type 1: it appears for laser mean powers smaller than about 20mW and larger than about 0.1mW (several orders of magnitude smaller than for inorganic materials), without significantly volume change. Two kinds of modifications correspond to this type. One is corresponding to a change of molecular structure in the center of the beam and the second, with high RR, a densification of the polymer occurs, causing a refractive index increase as large as 0.14, a quite interesting value for optical application (waveguiding or flat lenses).

Type 2: induced by fs laser with mean power larger than 20mW corresponds to hydrogen/carbon separation i.e. destruction of the COP molecule and re-building of carbonized clusters like Carbon dots but also polycyclic aromatic ones.

Properties induced by various modifications

RIC: refractive index change was observed at the surrounding of the irradiated lines whatever types. However, in type 1, with higher RR and slower scanning speed, the spatial ratio between the refractive index change around and the opaque molecular change at the center becomes larger. One position was measured to have a RI increase as large as 0.14, which is quite an interesting value for optical applications (waveguiding or flat lenses).

PL: We found the creation of photoluminescence properties in both types of domains. In the type I domain where there is luminescence creation in the irradiated line, luminophores are mainly excitable in the near UV to blue-green (centered at 475nm) range and emit on a broad range from the blue-green to yellow-orange, as shown in fig.2c. Particularly, when excited by UV at 365nm, the emission light can be seen as white, by positioning the emission spectra in a chromaticity diagram. For type II, PL intensity is much larger and mostly located at the upper surface of the modification lines. In addition to the type 1 luminophore (ex.475nm), it exhibits an efficient second excitation wavelength in the visible at 525nm (green) and leads to emission in orange-yellow (587nm).

Sucrose

In a single sucrose crystal with space group $P2_1$, irradiation is processed in the (100) plane and with scanning direction along b. Two domains of modifications were defined.

Type 1: the width of the irradiated lines is uniform and in the order of the beam size, they are opaque under the optical microscope in transmission mode without significant volume change. A luminescent liquid is found next to the irradiated region. We investigated only this type.

Type 2: opaque lines with irregular “exploded” structures along the lines, they are likely induced by high temperature produced in the condition of heat accumulation. More liquid and gas were observed in this type of modification. The regions when the sample is melted at RR>100kHz are also counted in the type 2 regime.

Properties induced by various modifications

PL: we found photoluminescence creation in type 1 modification. It is well confined to the line. Arising from several luminophores, one of them can be excitable in the blue (448nm) and emits light with a maximum around 510nm, and excited in the blue-green range (centered at 475nm) and emits on a broad range from the blue-green to yellow-orange, as shown in fig.2d.

COMMON LASER-INDUCED PROPERTY: ORIENTATION CONTROLLABLE PHOTOLUMINESCENCE

Spectral similarity

The fs laser-induced PL properties are similar in the selected organic materials. This is demonstrated in the emission spectra excited by 488nm (fig.2a) and the emission excitation map excited by visible laser (ex: 490nm - 640nm, detect: 490-700nm) (fig2 b, c, d).

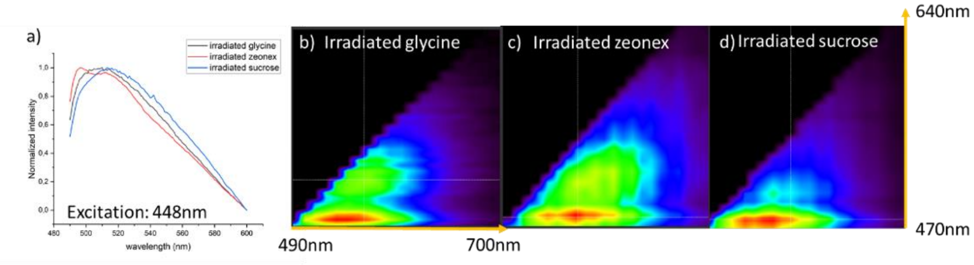

Fig.2 a) emission spectra of irradiated glycine, Zeonex, and sucrose when excited by 448nm CW laser. b)-d) the EEM of irradiated glycine (type2), Zeonex (type1) and sucrose (type1).

Similar emission and excitation spectra predict similarity in energy level structure, and this can be extended to the type of molecules or molecular structure. However, the elemental compositions of the three materials are CHON for glycine, CHO for sucrose, and CH for Zeonex, therefore, we believe that the luminescent active part may be associated only with carbon. The next question is thus: is this formation of luminophore(s) possible to be in any organic material? Since this phenomenon is arising from very different materials, this pushes us to think that a common species is at the root of the luminescence properties: the destruction of the molecule and re-building of carbonized clusters like Carbon dots but also polycyclic aromatic ones may be at the root of the properties.

Orientable anisotropic luminescence(s)

In addition to the similar luminophore(s) induced by the fs laser, another main discovering is the possibility to orient this luminescence anisotropy by the polarization of light in these selected materials. We point out that the laser-induced PL in the three investigated materials appears isotropic when it is just created from the fs laser irradiation. However, it can be efficiently rendered anisotropic and well-oriented by pre-exposure with polarized 448nm excitation light. The orientation is associated with the pre-exposure polarization, and this process is called coding. In addition, this anisotropy can be recoded if we exposed the luminescent part to another polarization direction during a time longer than the first coding. The luminophores are in the solid, why can be oriented by continuous laser light with power as low as ~20μW? We thus proposed 2 answers: 1) it is not in solid but the luminophore is weakly bound or it is not exactly oriented 2) the distribution of luminophore orientations is dis-symmetrized through bleaching.

FUTURE WORK AND PROSPECTS

Even though we have already contributed to opening up the subject of creating of optical functions in organic materials, there are still many studies to pursue in order 1) to consolidate the findings, 2) to develop this new domain and 3) to reach performing applications.

1) the main works that can be consolidated are the following:

- **For thermal model**: the proposed simple thermal calculation that allows an understanding of many thermal problems in spherical geometry, it will be more practical to extend it to cylindrical geometry in the cases of ellipsoidal energy deposition volume and materials with anisotropic diffusion. A useful tool for the technologist can be also developed based on that.
- **For the origin of PL induced by fs laser:** from the similar properties of luminescence that we have pointed out, we got the idea that similar species are at the root of the optical function. It will be necessary to engage in new experiments to precise the molecules produced by fs irradiation and see if they can be generalized.
- **For PL properties:** it would be necessary to measure the lifetimes and the relations between luminophores. To precise the thermal stability of the luminophores. To precise the bleaching mechanism of the PL excitable in the visible. And also to measure the quantum yields.
- **For the orientability of the luminescence property:** it is probably based on a special structure or in a liquid environment. The analysis of the property according to the excitation wavelength will allow an understanding if it is general or specific to one luminophore.
- Furthermore, for the generality of photonluminescence creation, it would be interesting to apply the method to other organic materials.
- **For SHG control:** SHG induced by some laser parameters present high contrast with respect to the polarisation of the

fundamental light, there are even some results that seem to correlate with the laser polarization of the irradiation. However, the reproducibility of the experiment is not good. The situation is more complex and perhaps we have not yet found the right irradiation parameters.

2) Nevertheless, the present work contributes already to opening new possibilities for the control of the functionalization of organic material and even adding another functionality like the orientation coding of the information or the imaging. It contributes to progress in the photonics field, considering that the future will be supported by organic substrates arising from natural products like sugar or natural polymer. Especially, the use of natural substrates, biodegradable, sustainable, and nontoxic is a dream that excites the imagination as illustrated in the scheme below. It contributes to the move from inorganic optics that are not sustainable to organic ones, completely renewable and preserving the planet.

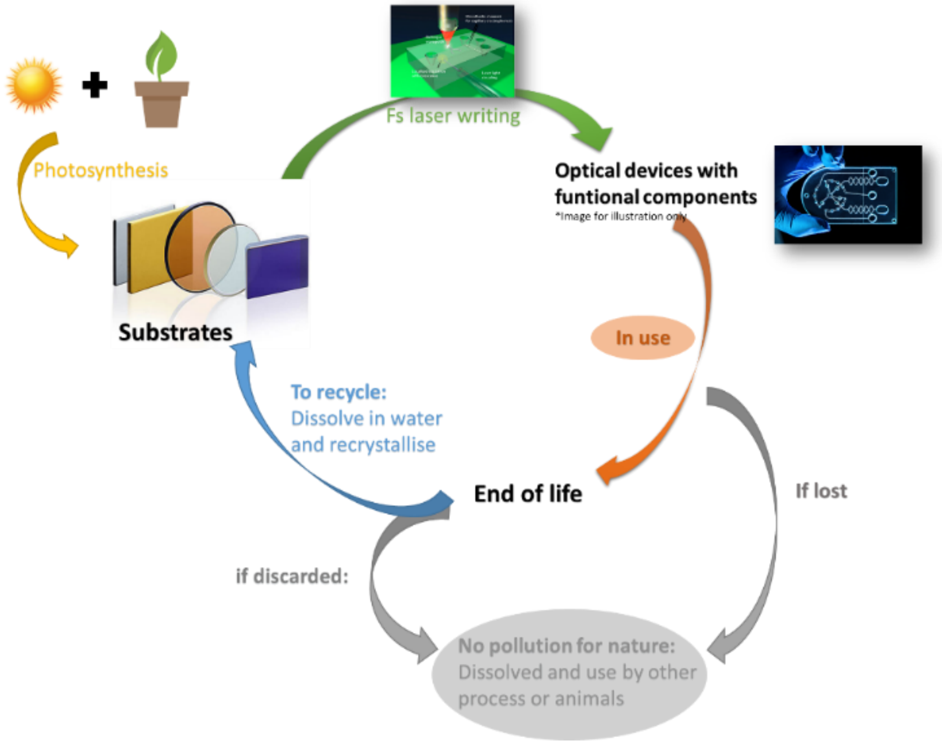

3) The prospects of our study are also manifold for the applications:

- FLDW allows 3D writing of Integrated optical circuits in the bulk thin film or the core of the fibers in organic materials (PMMA, plastic optical fibers such as Zeonex, CYTOP, etc.).
- Organic emitters such as OLEDs, and CDs are widely studied nowadays for their stability, selectivity, and biocompatibility. Luminescent properties accompanied with FLDW technology with simplicity and spatial precision will promise applications in, but not limited to sensing, labeling, etc., which will be widely used in the Internet of Things (IoT) field in the future.
- Short lifetime (<1ns and a few ns) is in a useful range for modern pico- and nanosecond time-domain or mega- to gigahertz frequency-domain instrumentation or technology such as LiFi.

Many other applications are reported in the reference[1]. Therefore, it is a domain with a great future.

REFERENCES

1. Tan, D., et al., *Photonic circuits written by femtosecond laser in glass: improved fabrication and recent progress in photonic devices*. Advanced Photonics, 2021. **3**(2): p. 024002.
2. Li, Y., et al., *Fabrication of magneto-optical microstructure by femtosecond laser pulses*. Chinese Optics Letters, 2012. **10**(10): p. 102201-102201.
3. Choi, J., et al. *Femtosecond laser written embedded diffractive optical elements and their applications*. in *Frontiers in Ultrafast Optics: Biomedical, Scientific, and Industrial Applications X*. 2010. SPIE.
4. McCulloch, Q., J. Gigax, and P. Hosemann, *Femtosecond laser ablation for mesoscale specimen evaluation*. Jom, 2020. **72**(4): p. 1694-1702.
5. Anderson, T., et al. *Integrating optics and micro-fluidic channels using femtosecond laser irradiation*. in *Commercial and Biomedical Applications of Ultrafast Lasers IX*. 2009. SPIE.
6. Berlich, R., et al., *Spatially resolved measurement of femtosecond laser induced refractive index changes in transparent materials*. Optics letters, 2012. **37**(14): p. 3003-3005.
7. Bhardwaj, V.R., et al., *Femtosecond laser-induced refractive index modification in multicomponent glasses*. Journal of applied physics, 2005. **97**(8): p. 083102.
8. Scully, P., D. Jones, and D. Jaroszynski, *Femtosecond laser irradiation of polymethylmethacrylate for refractive index gratings*. Journal of Optics A: Pure and Applied Optics, 2003. **5**(4): p. S92.
9. Sakakura, M. and M. Terazima, *Initial temporal and spatial changes of the refractive index induced by focused femtosecond pulsed laser irradiation inside a glass*. Physical Review B, 2005. **71**(2): p. 024113.
10. Bricchi, E., B.G. Klappauf, and P.G. Kazansky, *Form birefringence and negative index change created by femtosecond direct writing in transparent materials*. Optics letters, 2004. **29**(1): p. 119-121.
11. Yang, P., et al., *Femtosecond laser-pulse-induced birefringence in optically isotropic glass*. Journal of applied physics, 2004. **95**(10):

p. 5280-5283.

12. Zhang, B., L. Wang, and F. Chen, *Recent advances in femtosecond laser processing of LiNbO3 crystals for photonic applications.* Laser & Photonics Reviews, 2020. **14**(8): p. 1900407.
13. Kallepalli, D.L., et al., *Ultra-high density optical data storage in common transparent plastics.* Scientific Reports, 2016. **6**(1): p. 1-10.
14. Hnatovsky, C., et al., *Pulse duration dependence of femtosecond-laser-fabricated nanogratings in fused silica.* Applied Physics Letters, 2005. **87**(1): p. 014104.
15. Baum, A., et al., *Pulse-duration dependency of femtosecond laser refractive index modification in poly (methyl methacrylate).* Optics letters, 2008. **33**(7): p. 651-653.
16. Muzi, E., et al., *Towards a Rationalization of Ultrafast Laser-Induced Crystallization in Lithium Niobium Borosilicate Glasses: The Key Role of the Scanning Speed.* Crystals, 2021. **11**(3): p. 290.
17. Cao, J., et al., *Femtosecond laser-induced crystallization in glasses: growth dynamics for orientable nanostructure and nanocrystallization.* Crystal Growth & Design, 2019. **19**(4): p. 2189-2205.
18. Tian, J., et al., *Study of femtosecond laser-induced circular optical properties in silica by Mueller matrix spectropolarimetry.* Optics letters, 2017. **42**(20): p. 4103-4106.
19. Muzi, E., et al., *Towards a Rationalization of Ultrafast Laser-Induced Crystallization in Lithium Niobium Borosilicate Glasses: The Key Role of The Scanning Speed.* Crystals, 2021. **11**(3).
20. Nishikawa, M., B. Taheri, and J.L. West, *Mechanism of unidirectional liquid-crystal alignment on polyimides with linearly polarized ultraviolet light exposure.* Applied Physics Letters, 1998. **72**(19): p. 2403-2405.
21. Cao, J., et al., *Form birefringence induced in multicomponent glass by femtosecond laser direct writing.* Optics Letters, 2016. **41**(12): p. 2739-2742.
22. Weber, M.J., *Handbook of laser wavelengths*. 2018: CRC press.
23. Silfvast, W.T., *Laser fundamentals*. 2004: Cambridge university press.
24. Taylor, N., *LASER: The inventor, the Nobel laureate, and the thirty-year patent war*. 2002: Simon and Schuster.

25. Shank, C.V., *Generation of ultrashort optical pulses*, in *Ultrashort Laser Pulses and Applications*. 1988, Springer. p. 5-34.
26. Strickland, D. and G. Mourou, *Compression of amplified chirped optical pulses.* Optics communications, 1985. **55**(6): p. 447-449.
27. Tan, D., et al., *Femtosecond laser induced phenomena in transparent solid materials: Fundamentals and applications.* Progress in Materials Science, 2016. **76**: p. 154-228.
28. Gamaly, E.G., *Femtosecond laser-matter interaction: theory, experiments and applications*. 2011: Jenny Stanford Publishing.
29. Guo, B., et al., *Femtosecond Laser Micro/Nano-manufacturing: Theories, Measurements, Methods, and Applications.* Nanomanufacturing and Metrology, 2020. **3**(1): p. 26-67.
30. Wang, R., et al., *Identification of tunneling and multiphoton ionization in intermediate Keldysh parameter regime.* Optics Express, 2019. **27**(5): p. 6471-6482.
31. Keldysh, L., *ZhETF 47, 1515 (1964).* Sov. Phys. JETP, 1965. **20**: p. 1018.
32. Schaffer, C.B., A. Brodeur, and E. Mazur, *Laser-induced breakdown and damage in bulk transparent materials induced by tightly focused femtosecond laser pulses.* Measurement Science and Technology, 2001. **12**(11): p. 1784.
33. Dehareng, D. and G. Dive, *Vertical ionization energies of α-L-amino acids as a function of their conformation: an Ab Initio study.* International Journal of Molecular Sciences, 2004. **5**(11): p. 301-332.
34. Moliton, A. and R.C. Hiorns, *Review of electronic and optical properties of semiconducting π - conjugated polymers: applications in optoelectronics.* Polymer International, 2004. **53**(10): p. 1397-1412.
35. Le Drogoff, B., et al., *Influence of the laser pulse duration on laser-produced plasma properties.* Plasma Sources Science and Technology, 2004. **13**(2): p. 223.
36. Tien, A.-C., et al., *Short-pulse laser damage in transparent materials as a function of pulse duration.* Physical Review Letters, 1999. **82**(19): p. 3883.
37. Poumellec, B., et al., *Modification thresholds in femtosecond laser processing of pure silica: review of dependencies on laser parameters.* Optical Materials Express, 2011. **1**(4): p. 766-782.

38. Salaminia, A., et al., *The influence of self-focusing and filamentation on refractive index modifications in fused silica using intense femtosecond pulses*. Optics Communications, 2004. **241**: p. 529-538.
39. Marburger, J.H., *Self-focusing: Theory*. Progress in Quantum Electronics, 1975. **4, Part 1**: p. 35-110.
40. Jia, T., et al., *Ultraviolet-infrared femtosecond laser-induced damage in fused silica and CaF 2 crystals*. Physical Review B, 2006. **73**(5): p. 054105.
41. Gattass, R.R. and E. Mazur, *Femtosecond laser micromachining in transparent materials*. Nature photonics, 2008. **2**(4): p. 219-225.
42. Bloembergen, N., *Laser-induced electric breakdown in solids*. IEEE Journal of Quantum Electronics, 1974. **10**(3): p. 375-386.
43. Streltsov, A. and N. Borrelli, *Study of femtosecond-laser-written waveguides in glasses*. Journal of the Optical Society of America B, 2002. **19**(10): p. 2496-2504.
44. Rudenko, A., J.-P. Colombier, and T.E. Itina, *Nanopore-mediated ultrashort laser-induced formation and erasure of volume nanogratings in glass*. Physical Chemistry Chemical Physics, 2018. **20**(8): p. 5887-5899.
45. Lancry, M., et al., *Nanogratings formation in multicomponent silicate glasses*. Applied Physics B-Lasers and Optics, 2016. **122**(3): p. 1-8.
46. Temnov, V., et al., *Multiphoton ionization in dielectrics: Comparison of circular and linear polarization*. Physical review letters, 2006. **97**(23): p. 237403.
47. Little, D.J., et al., *Femtosecond laser modification of fused silica: the effect of writing polarization on Si-O ring structure*. Optics Express, 2008. **16**(24): p. 20029-20037.
48. Liu, D., et al., *The polarization-dependence of femtosecond laser damage threshold inside fused silica*. Applied Physics B, 2008. **91**(3): p. 597-599.
49. Shimotsuma, Y., et al., *Self-organized nanogratings in glass irradiated by ultrashort light pulses*. Physical Review Letters, 2003. **91**(24): p. 247405.
50. Shimotsuma, Y., et al., *Tunability of form birefringence induced by femtosecond laser irradiation in anion-doped silica glass*.

Journal of the American Ceramic Society, 2017. **100**(9): p. 3912-3919.

51. Shimotsuma, Y., et al., *Self-assembled glass/crystal periodic nanostructure in Al 2 O 3 - Dy 2 O 3 binary glass*. Applied Physics A, 2018. **124**(1): p. 82.

52. Muzi, E., et al., *Polarization-oriented LiNbO 3 nanocrystals by femtosecond laser irradiation in LiO 2–Nb 2 O 5–SiO 2–B 2 O 3 glasses*. Optical Materials Express, 2021. **11**(4): p. 1313-1320.

53. Taylor, R., E. Simova, and C. Hnatovsky, *Creation of chiral structures inside fused silica glass*. Optics Letters, 2008. **33**(12): p. 1312-1314.

54. Ravi-Kumar, S., et al., *Laser Ablation of Polymers: A Review*. Procedia Manufacturing, 2019. **34**: p. 316-327.

55. Vázquez, R.M., et al., *Fabrication of binary Fresnel lenses in PMMA by femtosecond laser surface ablation*. Optics express, 2011. **19**(12): p. 11597-11604.

56. Wang, L., et al., *Formation of deep-subwavelength structures on organic materials by femtosecond laser ablation*. IEEE Journal of Quantum Electronics, 2017. **54**(1): p. 1-7.

57. Ni, X., et al., *The study of nanojoule femtosecond laser ablation on organic glass*. Chinese Optics Letters, 2003. **1**(7): p. 429-431.

58. Hu, X., et al., *Bragg grating inscription in PMMA optical fibers using 400-nm femtosecond pulses*. Optics Letters, 2017. **42**(14): p. 2794-2797.

59. Cho, S.-H., et al., *Femtosecond laser embedded grating micromachining of flexible PDMS plates*. Optics Communications, 2009. **282**(7): p. 1317-1321.

60. Lacraz, A., et al. *Bragg grating inscription in CYTOP polymer optical fibre using a femtosecond laser*. in *Micro-structured and specialty optical fibres IV*. 2015. SPIE.

61. Lacraz, A., et al., *Femtosecond laser inscribed Bragg gratings in low loss CYTOP polymer optical fiber*. IEEE Photonics Technology Letters, 2015. **27**(7): p. 693-696.

62. Nan, Y.-G., et al., *Ultra-fast fiber Bragg grating inscription in CYTOP polymer optical fibers using phase mask and 400 nm femtosecond laser*. Optics Express, 2021. **29**(16): p. 25824-25835.

63. Kallepalli, D.L., et al., *Multiphoton laser-induced confined chemical changes in polymer films*. Optics Express, 2020. **28**(8):

p. 11267-11279.
64. Ye, L., et al., *NUV femtosecond laser inscription of volume Bragg gratings in poly (methyl) methacrylate with linear and circular polarizations*. Laser Physics, 2013. **23**(12): p. 126004.
65. Chae, S., et al., *Selective chain alignment of conducting polymer blend films by an ultrafast laser*. Macromolecular Chemistry and Physics, 2016. **217**(4): p. 537-542.
66. Martinez-Rubi, Y., et al., *Self-assembly and visualization of poly (3-hexyl-thiophene) chain alignment along boron nitride nanotubes*. The Journal of Physical Chemistry C, 2015. **119**(47): p. 26605-26610.
67. Garetz, B., et al., *Nonphotochemical, polarization-dependent, laser-induced nucleation in supersaturated aqueous urea solutions*. Physical review letters, 1996. **77**(16): p. 3475.
68. Yuyama, K.-i., et al., *Selective Fabrication of α- and γ-Polymorphs of Glycine by Intense Polarized Continuous Wave Laser Beams*. Crystal Growth & Design, 2012. **12**(5): p. 2427-2434.
69. Sun, X., B.A. Garetz, and A.S. Myerson, *Polarization switching of crystal structure in the nonphotochemical laser-induced nucleation of supersaturated aqueous l-histidine*. Crystal Growth and Design, 2008. **8**(5): p. 1720-1722.
70. Ikni, A., et al., *Experimental demonstration of the carbamazepine crystallization from Non-Photochemical LASER-Induced Nucleation in acetonitrile and methanol*. Crystal Growth & Design, 2014. **14**(7): p. 3286-3299.
71. Iftime, G., et al., *Control of chirality of an azobenzene liquid crystalline polymer with circularly polarized light*. Journal of the American Chemical Society, 2000. **122**(51): p. 12646-12650.
72. Dirac, P.A.M., *Quantum mechanics of many-electron systems*. Proceedings of the Royal Society of London. Series A, Containing Papers of a Mathematical and Physical Character, 1929. **123**(792): p. 714-733.
73. Schaffer, C.B., A. Brodeur, and E. Mazur, *Laser-induced breakdown and damage in bulk transparent materials induced by tightly focused femtosecond laser pulses*. Measurement Science and Technology, 2001. **12**: p. 1784.
74. Chichkov, B.N., et al., *Femtosecond, picosecond and nanosecond laser ablation of solids*. Applied physics A, 1996. **63**(2): p. 109-

115.

75. Davis, K.M., et al., *Writing waveguides in glass with a femtosecond laser*. Optics Letters, 1996. **21**: p. 1729-1731.
76. Glezer, E.N. and E. Mazur, *Ultrafast-laser driven micro-explosions in transparent materials*. Applied physics letters, 1997. **71**(7): p. 882-884.
77. Fernandez, T.T., et al., *Bespoke photonic devices using ultrafast laser driven ion migration in glasses*. Progress in Materials Science, 2018. **94**: p. 68-113.
78. Schaffer, C.B., et al., *Micromachining bulk glass by use of femtosecond laser pulses with nanojoule energy*. Optics Letters, 2001. **26**: p. 93.
79. Minoshima, K., et al., *Photonic device fabrication in glass by use of nonlinear materials processing with a femtosecond laser oscillator*. Opt. Lett, 2001. **26**(19): p. 1516-1518.
80. Schaffer, C., J. García, and E. Mazur, *Bulk heating of transparent materials using a high-repetition-rate femtosecond laser*. Applied Physics A: Materials Science & Processing, 2003. **76**(3): p. 351-354.
81. Eaton, S.M., et al., *Heat accumulation effects in femtosecond laser-written waveguides with variable repetition rate*. Optics Express, 2005. **13**(12): p. 4708-4716.
82. Eaton, S., et al., *Transition from thermal diffusion to heat accumulation in high repetition rate femtosecond laser writing of buried optical waveguides*. Optics Express, 2008. **16**(13): p. 9443-9458.
83. Bérubé, J.-P., M. Bernier, and R. Vallée, *Femtosecond laser-induced refractive index modifications in fluoride glass*. Optical Materials Express, 2013. **3**(5): p. 598-611.
84. Sakakura, M., et al., *Heating and rapid cooling of bulk glass after photoexcitation by a focused femtosecond laser pulse*. Optics Express, 2007. **15**(25): p. 16800-16807.
85. Yin Liu, B.Z., Li Wang, Jianrong Qiu, Ye Dai, and Hongliang Ma, *Femtosecond laser induced coordination transformation and migration of ions in sodium borate glasses*. Applied Physics Letters 2008. **92,** : p. 121113.
86. Liu, Y., et al., *Micromodification of element distribution in glass using femtosecond laser irradiation*. Optics Letters, 2009. **34**(2):

p. 136-138.

87. Shimizu, M., et al., *Formation mechanism of element distribution in glass under femtosecond laser irradiation.* Optics Letters, 2011. **36**: p. 2161-2163.
88. Zhu, B., et al., *Femtosecond laser induced space-selective precipitation of nonlinear optical crystals in rare-earth-doped glasses.* Optics Express, 2007. **15**(10): p. 6069-6074.
89. Dai, Y., et al., *Direct writing three-dimensional Ba2TiSi2O8 crystalline pattern in glass with ultrashort pulse laser.* Applied Physics Letters, 2007. **90**(18).
90. Zhang, B., et al., *Self‐organized periodic crystallization in unconventional glass created by an ultrafast laser for optical attenuation in the broadband near‐infrared region.* Advanced Optical Materials, 2019. **7**(20): p. 1900593.
91. Miyamoto, I., K. Cvecek, and M. Schmidt, *Evaluation of nonlinear absorptivity in internal modification of bulk glass by ultrashort laser pulses.* Optics Express, 2011. **19**(11): p. 10714-10727.
92. Eaton, S.M., et al., *Transition from thermal diffusion to heat accumulation in high repetition rate femtosecond laser writing of buried optical waveguides.* Optics express, 2008. **16**(13): p. 9443-9458.
93. Miyamoto, I., et al., *Characterization of plasma in microwelding of glass using ultrashort laser pulse at high pulse repetition rates.* Physics Procedia, 2014. **56**: p. 973-982.
94. Fernandez, T., et al., *Bespoke photonic devices using ultrafast laser driven ion migration in glasses.* Progress in Materials Science, 2018. **94**: p. 68-113.
95. Lax, M., *Temperature rise induced by a laser beam.* Journal of Applied Physics, 1977. **48**(9): p. 3919-3924.
96. Sanders, D.J., *Temperature distributions produced by scanning Gaussian laser beams.* Applied Optics, 1984. **23**(1): p. 30-35.
97. Haba, B., B.W. Hussey, and A. Gupta, *Temperature distribution during heating using a high repetition rate pulsed laser.* Journal of Applied Physics, 1991. **69**(5): p. 2871-2876.
98. Zhang, H., et al., *Heat accumulation during high repetition rate ultrafast laser interaction: Waveguide writing in borosilicate glass.* Journal of Physics: Conference Series, 2007. **59**: p. 682-686.
99. Miyamoto, I., et al., *Fusion Welding of Glass Using Femtosecond*

Laser Pulses with High-repetition Rates. Journal of Laser Micro Nanoengineering, 2007. **2**(1): p. 57-63.

100. Beresna, M., et al., *Three-dimensional modeling of the heat-affected zone in laser machining applications*. Laser Chemistry, 2008. **2008**.
101. Shimizu, M., et al., *Three-dimensional temperature distribution and modification mechanism in glass during ultrafast laser irradiation at high repetition rates*. Optics Express, 2012. **20**(2): p. 934-940.
102. Rahaman, A., A. Kar, and X. Yu, *Thermal effects of ultrafast laser interaction with polypropylene*. Optics express, 2019. **27**(4): p. 5764-5783.
103. Rahaman, A., et al., *Absorption and temperature distribution during ultrafast laser microcutting of polymeric materials*. Journal of Laser Applications, 2020. **32**(2): p. 022044.
104. Svelto, O. and D.C. Hanna, *Principles of lasers*. 5th ed. Vol. 4. 1998: Springer. 153-155.
105. Gbur, G. and E. Wolf, *The Rayleigh range of Gaussian Schell-model beams*. journal of modern optics, 2001. **48**(11): p. 1735-1741.
106. Burakov, I.M., et al., *Spatial distribution of refractive index variations induced in bulk fused silica by single ultrashort and short laser pulses*. Journal of Applied Physics, 2007. **101**: p. 043506.
107. Sun, Q., et al., *Effect of spherical aberration on the propagation of a tightly focused femtosecond laser pulse inside fused silica*. Journal of Optics A: Pure and Applied Optics, 2005. **7**: p. 655.
108. Couairon, A. and A. Mysyrowicz, *Femtosecond filamentation in transparent media*. Physics reports, 2007. **441**(2-4): p. 47-189.
109. Wang, X., *Convergence-Divergence of p-Series*. The College Mathematics Journal, 2002. **33**(4): p. 314-316.
110. Weideman, J.A.C., *Numerical integration of periodic functions: A few examples*. The American mathematical monthly, 2002. **109**(1): p. 21-36.
111. Atkinson, K.E., *An introduction to numerical analysis*. 2008: John wiley & sons.
112. Tool, A.Q. and C. Eicitlin, *Variations caused in the heating curves of glass by heat treatment 1*. Journal of the American Ceramic

Society, 1931. **14**(4): p. 276-308.

113. Tool, A.Q., *Relaxation of stresses in annealing glass.* J. Res. Natl. Bur. Stand.(US), 1945. **34**(2): p. 199-211.
114. Tool, A.Q., *Relation between inelastic deformability and thermal expansion of glass in its annealing range.* Journal of the American Ceramic society, 1946. **29**(9): p. 240-253.
115. Tool, A.Q., *Viscosity and the extraordinary heat effects in glass.* J. Am. Ceram. Soc, 1946. **29**(9): p. 240-253.
116. Maxwell, J.C., *IV. On the dynamical theory of gases.* Philosophical transactions of the Royal Society of London, 1867(157): p. 49-88.
117. Doñate-Buendía, C., et al. *Pulsed laser ablation in liquids for the production of gold nanoparticles and carbon quantum dots: from plasmonic to fluorescence and cell labelling*. in *Journal of Physics: Conference Series*. 2020. IOP Publishing.
118. Xie, Q., et al., *Application and validation of a viscosity approach to the existence of nanogratings in oxide glasses.* Optical Materials, 2022. **130**: p. 112576.
119. Que, R., et al., *Space-selective creation of photonics functions in a new organic material: Femtosecond laser direct writing in Zeonex glass of refractive index change and photoluminescence.* Optical Materials, 2022. **133**: p. 112651.
120. Fernandez, T.T., et al., *Controlling plasma distributions as driving forces for ion migration during fs laser writing.* Journal of Physics D: Applied Physics, 2015. **48**(15): p. 155101.
121. Miyamoto, I., A. Horn, and J. Gottmann, *Local Melting of Glass Material and Its Application to Direct Fusion Welding by Ps-laser Pulses.* Journal of Laser Micro Nanoengineering, 2007. **2**(1): p. 7-14.
122. Dawson, A., et al., *Effect of high pressure on the crystal structures of polymorphs of glycine.* Crystal growth & design, 2005. **5**(4): p. 1415-1427.
123. Pilling, S., et al., *The influence of crystallinity degree on the glycine decomposition induced by 1 MeV proton bombardment in space analog conditions.* Astrobiology, 2013. **13**(1): p. 79-91.
124. Power, L., K. Turner, and F. Moore, *The crystal and molecular structure of α-glycine by neutron diffraction–a comparison.* Acta Crystallographica Section B: Structural Crystallography and

Crystal Chemistry, 1976. **32**(1): p. 11-16.

125. Sivakumar, N., et al., *Synthesis, growth and characterization of γ-glycine–A promising material for optical applications*. Optical Materials, 2014. **37**: p. 780-787.
126. Uma, J. and V. Rajendran, *Growth and characterization of γ-glycine single crystals from cadmium chloride for optoelectronic applications*. Optik, 2014. **125**(2): p. 816-819.
127. Latha, A.A., et al., *Synthesis and characterization of γ-glycine–a nonlinear optical single crystal for optoelectronic and photonic applications*. Materials Science-Poland, 2017. **35**(1): p. 140-150.
128. Vijayalakshmi, V. and P. Dhanasekaran, *Growth and characterization of γ-glycine single crystals for photonics and optoelectronic device applications*. Journal of Crystal Growth, 2019. **506**: p. 117-121.
129. Bulutoglu, P.S., et al., *Exploring New Crystal Structures of Glycine via Electric Field-Induced Structural Transformations with Molecular Dynamics Simulations*. Processes, 2019. **7**(5): p. 268.
130. Yang, X., et al. *Polymorphism in the crystallization of glycine*. in *AICHE annual meeting, San Fransisco, CA*. 2006.
131. Chongprasert, S., S.A. Knopp, and S.L. Nail, *Characterization of frozen solutions of glycine*. Journal of pharmaceutical sciences, 2001. **90**(11): p. 1720-1728.
132. Towler, C.S., et al., *Impact of molecular speciation on crystal nucleation in polymorphic systems: The conundrum of γ glycine and molecular 'self poisoning'*. Journal of the American Chemical Society, 2004. **126**(41): p. 13347-13353.
133. Srinivasan, K., *Crystal growth of α and γ glycine polymorphs and their polymorphic phase transformations*. Journal of Crystal Growth, 2008. **311**(1): p. 156-162.
134. Bhat, M.N. and S. Dharmaprakash, *Growth of nonlinear optical γ-glycine crystals*. Journal of crystal growth, 2002. **236**(1-3): p. 376-380.
135. Peter, M.E. and P. Ramasamy, *Growth of gamma glycine crystal and its characterisation*. Spectrochimica Acta Part A: Molecular and Biomolecular Spectroscopy, 2010. **75**(5): p. 1417-1421.
136. Dhanaraj, P. and N. Rajesh, *Growth and characterization of nonlinear optical γ-glycine single crystal from lithium acetate as solvent*. Materials Chemistry and Physics, 2009. **115**(1): p. 413-

417.

137. Selvarajan, P., J.G. Arulraj, and S. Perumal, *Structural, mechanical, optical, dielectric and SHG studies of undoped and urea-doped γ-glycine crystals.* Physica B: Condensed Matter, 2010. **405**(2): p. 738-743.
138. Sakai, H., et al., *Transformation of alpha-glycine to gamma-glycine*. Journal of crystal growth, 1992. **116**: p. 421-426.
139. Oró, J., *Mechanism of synthesis of adenine from hydrogen cyanide under possible primitive Earth conditions.* Nature, 1961. **191**(4794): p. 1193-1194.
140. Chyba, C. and C. Sagan, *Endogenous production, exogenous delivery and impact-shock synthesis of organic molecules: an inventory for the origins of life*. Nature, 1992. **355**(6356): p. 125-132.
141. Herd, C.D., et al., *Origin and evolution of prebiotic organic matter as inferred from the Tagish Lake meteorite*. Science, 2011. **332**(6035): p. 1304-1307.
142. Ioppolo, S., et al., *A non-energetic mechanism for glycine formation in the interstellar medium.* Nature Astronomy, 2021. **5**(2): p. 197-205.
143. Dai, Y., et al., *Femtosecond laser-induced oriented precipitation of Ba2TiGe2O8 crystals in glass*. Optics Express, 2008. **16**(6): p. 3912-3917.
144. Cao, J., et al., *Modifications in lithium niobium silicate glass by femtosecond laser direct writing: morphology, crystallization, and nanostructure*. Journal of the Optical Society of America B, 2017. **34**(1): p. 160-168.
145. Zhang, B., et al., *Ultrafast Laser Inducing Continuous Periodic Crystallization in the Glass Activated via Laser‐Prepared Crystallite‐Seeds*. Advanced Optical Materials, 2021: p. 2001962.
146. Cao, J., et al., *Angular dependence of the second harmonic generation induced by femtosecond laser irradiation in silica-based glasses: variation with writing speed and pulse energy.* World Journal of Nano Science and Engineering, 2015. **5**(03): p. 96.
147. Weiss, I.M., et al., *Thermal decomposition of the amino acids glycine, cysteine, aspartic acid, asparagine, glutamic acid,*

glutamine, arginine and histidine. BMC biophysics, 2018. **11**(1): p. 2.

148. Bērziņš, K.r. and R. Suryanarayanan, *Compression-induced crystallization in sucrose-polyvinylpyrrolidone amorphous solid dispersions.* Crystal Growth & Design, 2018. **18**(2): p. 839-848.
149. Langrish, T. and S. Wang, *Crystallization rates for amorphous sucrose and lactose powders from spray drying: A comparison.* Drying Technology, 2009. **27**(4): p. 606-614.
150. Starzak, M. and M. Mathlouthi, *Formation of amorphous sugar in the syrup film–a key factor in modelling of industrial sugar drying.* Food chemistry, 2010. **122**(2): p. 394-409.
151. Simperler, A., et al., *Glass transition temperature of glucose, sucrose, and trehalose: an experimental and in silico study.* The Journal of Physical Chemistry B, 2006. **110**(39): p. 19678-19684.
152. Urbach, F., *The long-wavelength edge of photographic sensitivity and of the electronic absorption of solids.* Physical Review, 1953. **92**(5): p. 1324.
153. Skuja, L., et al., *Urbach absorption edge of silica: reduction of glassy disorder by fluorine doping.* Journal of Non-Crystalline Solids, 2004. **345**: p. 328-331.
154. Hariharan, P., *Optical Interferometry, 2e*. 2003: Elsevier.
155. de Groot, P., *Principles of interference microscopy for the measurement of surface topography.* Advances in Optics and Photonics, 2015. **7**(1): p. 1-65.
156. Echlin, P., et al., *Advanced scanning electron microscopy and X-ray microanalysis*. 2013: Springer Science & Business Media.
157. Salh, R., *Defect related luminescence in silicon dioxide network: a review.* Crystalline Silicon-Properties and Uses, 2011: p. 135-172.
158. Kim, K., et al., *Polymorphism control of nanosized glycine crystals on engineered surfaces.* CrystEngComm, 2011. **13**(4): p. 1127-1131.
159. Surovtsev, N., V. Malinovsky, and E. Boldyreva, *Raman study of low-frequency modes in three glycine polymorphs.* The Journal of chemical physics, 2011. **134**(4): p. 01B626.
160. Surovtsev, N., et al., *Glycine phases formed from frozen aqueous solutions: Revisited.* The Journal of chemical physics, 2012. **137**(6): p. 065103.
161. Childres, I., et al., *Raman spectroscopy of graphene and related*

materials. New developments in photon and materials research, 2013. **1**: p. 1-20.

162. Choi, J., et al., *Laser-Induced Graphene on a Quartz Crystal Microbalance for Humidity Sensing*. Crystals, 2021. **11**(3): p. 289.
163. Holtom, P.D., et al., *A combined experimental and theoretical study on the formation of the amino acid glycine (NH2CH2COOH) and its isomer (CH3NHCOOH) in extraterrestrial ices*. The Astrophysical Journal, 2005. **626**(2): p. 940.
164. Guan, Y.Y., et al., *UVolution: compared photochemistry of prebiotic organic compounds in low Earth orbit and in the laboratory*. Planetary and Space Science, 2010. **58**(10): p. 1327-1346.
165. Chen, F. and J.R.V. de Aldana, *Optical waveguides in crystalline dielectric materials produced by femtosecond-laser micromachining*. Laser & Photonics Reviews, 2014. **8**: p. 251-275.
166. Barty, A., et al., *Quantitative optical phase microscopy*. Optics Letters, 1998. **23**(11): p. 817-819.
167. Ossikovski, R., *Differential matrix formalism for depolarizing anisotropic media*. Optics letters, 2011. **36**(12): p. 2330-2332.
168. Arwin, H., et al., *Structural circular birefringence and dichroism quantified by differential decomposition of spectroscopic transmission Mueller matrices from Cetonia aurata*. Optics Letters, 2016. **41**(14): p. 3293-3296.
169. Arteaga, O., *Number of independent parameters in the Mueller matrix representation of homogeneous depolarizing media*. Optics Letters, 2013. **38**(7): p. 1131-1133.
170. Nie, Z., et al., *Femtosecond laser induced photoluminescence in poly (methyl methacrylate) and three-dimensional optical storage*. Journal of luminescence, 2011. **131**(2): p. 266-270.
171. Nie, Z., et al., *Multilayered optical bit memory with a high signal-to-noise ratio in fluorescent polymethylmethacrylate*. Applied Physics Letters, 2009. **94**(11): p. 111912.
172. Green, U., et al., *Exploring the radical nature of a carbon surface by electron paramagnetic resonance and a calibrated gas flow*. JoVE (Journal of Visualized Experiments), 2014(86): p. e51548.
173. Ishikawa, K., et al., *Absolute chirality of the γ-polymorph of glycine: correlation of the absolute structure with the optical rotation*. Chemical Communications, 2012. **48**(48): p. 6031-6033.

174. Cao, J., et al., *Tunable angular-dependent second-harmonic generation in glass by controlling femtosecond laser polarization.* Journal of the Optical Society of America B, 2016. **33**(4): p. 741-747.

175. Jung, C., B.K. Rhee, and D. Kim, *Simple method for determining the crystalline axes of nonlinear uniaxial crystal with second-harmonic generation.* Applied optics, 2000. **39**(28): p. 5142-5146.

176. Wang, Z., K.K. Tan, and Y.C. Lam, *Electrical Resistance Reduction Induced with CO2 Laser Single Line Scan of Polyimide.* Micromachines, 2021. **12**(3): p. 227.

177. Serrano, J., J. Moros, and J.J. Laserna, *Molecular signatures in femtosecond laser-induced organic plasmas: comparison with nanosecond laser ablation.* Physical Chemistry Chemical Physics, 2016. **18**(4): p. 2398-2408.

178. Gan, Z., et al., *Mechanism of photoluminescence from chemically derived graphene oxide: role of chemical reduction.* Advanced Optical Materials, 2013. **1**(12): p. 926-932.

179. Dekaliuk, M.O., et al., *Fluorescent carbon nanomaterials:"quantum dots" or nanoclusters?* Physical Chemistry Chemical Physics, 2014. **16**(30): p. 16075-16084.

180. Cheng, Z., et al., *Fabrication of silver dendrite fractal structures for enhanced second harmonic generation and surface-enhanced Raman scattering.* Optical Materials Express, 2019. **9**(2): p. 860-869.

181. Therien, D.A., R. Hou, and F. Lagugné-Labarthet, *Second-Harmonic Generation from Dendritic Fractal Structures.* Plasmonics, 2020. **15**(2): p. 507-515.

182. Das, S.C., A. Majumdar, and R. Hippler, *Electronic and chemical property of amorphous carbon, hydrocarbon, hydrogenated/hydrogen free carbon nitride: spectroscopic study.* IJISR, 2014. **12**(1): p. 148-156.

183. Abdulhafez, M., G.N. Tomaraei, and M. Bedewy, *Fluence-Dependent Morphological Transitions in Laser-Induced Graphene Electrodes on Polyimide Substrates for Flexible Devices.* ACS Applied Nano Materials, 2021. **4**(3): p. 2973-2986.

184. Tajik, S., et al., *Carbon and graphene quantum dots: A review on syntheses, characterization, biological and sensing applications for neurotransmitter determination.* RSC Advances, 2020. **10**(26):

p. 15406-15429.

185. Li, X., et al., *Transfer of Large-Area Graphene Films for High-Performance Transparent Conductive Electrodes*. Nano Letters, 2009. **9**: p. 4359-4363.

186. Tuinstra, F. and J.L. Koenig, *Raman Spectrum of Graphite*. The Journal of Chemical Physics, 1970. **53**(3): p. 1126-1130.

187. Brown, G.M. and H.A. Levy, *Further refinement of the structure of sucrose based on neutron-diffraction data*. Acta Crystallographica Section B: Structural Crystallography and Crystal Chemistry, 1973. **29**(4): p. 790-797.

188. Patyk, E., et al., *High ‐ Pressure (+) ‐ Sucrose Polymorph*. Angewandte Chemie International Edition, 2012. **51**(9): p. 2146-2150.

189. Kröll, J., J. Darmo, and K. Unterrainer, *Terahertz optical activity of sucrose single-crystals*. Vibrational Spectroscopy, 2007. **43**(2): p. 324-329.

190. Halbout, J.-M. and C. Tang, *Phase-matched second-harmonic generation in sucrose*. IEEE Journal Of Quantum Electronics, 1982. **18**(3): p. 410-415.

191. Szostak, M.M., et al., *Optical nonlinearity and electric conductivity origin study on sucrose crystal by using IR, Raman, INS, NMR, and EPR spectroscopies*. Carbohydr Res, 2014. **395**: p. 29-37.

192. Dillip, G., et al., *Effect of magnesium chloride on growth, crystalline perfection, structural, optical, thermal and NLO behavior of γ-glycine crystals*. Materials Chemistry and Physics, 2012. **134**(1): p. 371-376.

193. Hurtta, M., I. Pitkänen, and J. Knuutinen, *Melting behaviour of D-sucrose, D-glucose and D-fructose*. Carbohydrate research, 2004. **339**(13): p. 2267-2273.

194. Carstensen, J.T. and K. Van Scoik, *Amorphous-to-crystalline transformation of sucrose*. Pharmaceutical research, 1990. **7**(12): p. 1278-1281.

195. Nunes, C., A. Mahendrasingam, and R. Suryanarayanan, *Quantification of crystallinity in substantially amorphous materials by synchrotron X-ray powder diffractometry*. Pharmaceutical research, 2005. **22**(11): p. 1942-1953.

196. Belhamri, R. and M. Mathlouthi, *Effects of impurities on sucrose*

crystal shape and growth. Curr. Top. Cryst. Growth Res., 2004. **7**: p. 63-70.

197. Lee, S., et al., *Laser-induced defect centers and valence state change of Mn ions in sodium borate glasses*. Journal of Luminescence, 2007. **122**: p. 142-145.
198. Lee, S., M. Lee, and K. Lim, *Femtosecond laser induced PL change in Sm-doped sodium borate glass and 3D optical memory*. Journal of Luminescence, 2007. **122-123**: p. 990-992.
199. Bricchi, E. and P. Kazansky, *Extraordinary stability of anisotropic femtosecond direct-written structures embedded in silica glass*. Applied Physics Letters, 2006. **88**(11): p. 111119-111119.
200. Podlipensky, A., et al., *Femtosecond laser assisted production of dichroitic 3D structures in composite glass containing Ag nanoparticles*. Applied Physics a-Materials Science & Processing, 2005. **80**(8): p. 1647-1652.
201. Podlipensky, A., et al., *Second-harmonic generation from ellipsoidal silver nanoparticles embedded in silica glass*. Optics Letters, 2003. **28**(9): p. 716-718.
202. Fan, C., et al., *Gold Nanoparticles Reshaped by Ultrafast Laser Irradiation Inside a Silica-Based Glass, Studied Through Optical Properties*. Journal of Physical Chemistry C, 2012. **116**(4): p. 2647-2655.
203. Ha, J.M., et al., *Recent advances in organic luminescent materials with narrowband emission*. NPG Asia Materials, 2021. **13**(1): p. 53.
204. Kallepalli, D.L.N., et al., *Multiphoton laser-induced confined chemical changes in polymer films*. Optics Express, 2020. **28**(8): p. 11267-11279.
205. Krasovitskii, B.M.B.B.M.V.V.G., *Organic luminescent materials*. 1988, Weinheim: VCH.
206. Friedrich, J. and D. Haarer, *Photochemical Hole Burning: A Spectroscopic Study of Relaxation Processes in Polymers and Glasses*. Angewandte Chemie International Edition in English, 1984. **23**(2): p. 113-140.
207. Berezin, M.Y. and S. Achilefu, *Fluorescence lifetime measurements and biological imaging*. Chemical reviews, 2010. **110**(5): p. 2641-2684.
208. Zhang, H., et al., *A mini-review on recent progress of new*

sensitizers for luminescence of lanthanide doped nanomaterials. Nano Research, 2020. **13**(7): p. 1795-1809.

209. DeLuca, J.A., *An introduction to luminescence in inorganic solids.* Journal of Chemical Education, 1980. **57**(8): p. 541.
210. Brockman, J.M., et al., *Mapping the 3D orientation of piconewton integrin traction forces.* Nature methods, 2018. **15**(2): p. 115-118.
211. Kallepalli, D.L.N., et al., *Ultra-high density optical data storage in common transparent plastics.* Scientific Reports, 2016. **6**(1): p. 26163.
212. Woolfson, M.M., *How to use groups by J. W. Leech and D. J. Newman.* Acta Crystallographica Section A, 1969. **25**(5): p. 641-641.